JANUARY–MARCH 2024 VOL. 16 № 1 (60)

ISSN 2075-8251

ActaNaturae

Streptomyces phaeochromogenes BV-204, K-1115A Anthraquinone-Producing Strain: A New Protein Biosynthesis Inhibitor

A. R. Belik, Yu. V. Zakalyukina, V. A. Alferova, Y. A. Buyuklyan, I. A. Osterman, M. V. Biryukov

The use of advanced mechanism-oriented approaches to classical screening makes it possible to not only discover new biologically active substances, but also identify new promising properties of previously discovered yet poorly studied molecules and potentially rediscover them as new drugs. Despite the fact that the K-1115A compound has been discovered over 25 years ago, and some data have been obtained with regard to the antibacterial activity of its homologs, the activity of and action mechanism of this substance still remain understudied. The study using dual reporter system pDualrep2 has discovered a K-1115A producer that turned out to be a protein synthesis inhibitor.

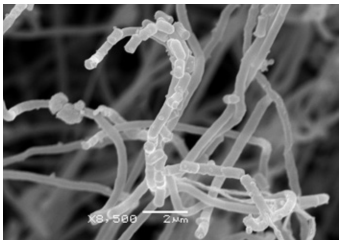

Electron micrography of *S. phaeochromogenes* BV-204

Ultrastructural 3D Microscopy for Biomedicine: Principles, Applications, and Perspectives

K. E. Mochalov, D. S. Korzhov, A. V. Altunina, O. I. Agapova, V. A. Oleinikov

Modern biomedical research often requires a three-dimensional microscopic analysis of the ultrastructure of biological objects and materials. This review discusses the principles and potential applications of such techniques as serial section transmission electron microscopy; techniques based on scanning electron microscopy (SEM) (array tomography, focused ion beam SEM, and serial block-face SEM). 3D analysis techniques based on modern super-resolution optical microscopy methods are described. A comparative analysis of the advantages and shortcomings of the discussed approaches is performed.

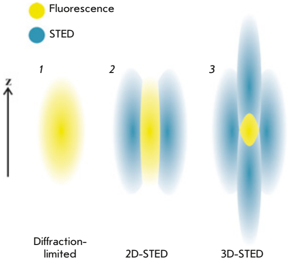

Narrowing of the effective radiation area due to STED suppression of peripheral radiation

Studying Signaling Pathway Activation in TRAIL-Resistant Macrophage-Like Acute Myeloid Leukemia Cells

Y. V. Lomovskaya, K. S. Krasnov, M. I. Kobyakova, A. A. Kolotova, A. M. Ermakov, A. S. Senotov, I. S. Fadeeva, E. I. Fetisova, A. I. Lomovsky, A. I. Zvyagina, V. S. Akatov, R. S. Fadeev

Acute myeloid leukemia (AML) is a malignant neoplasm characterized by extremely low curability and survival. The inflammatory microenvironment and maturation (differentiation) of AML cells induced by it contribute to the evasion of these cells from effectors of antitumor immunity. One of the key molecular effectors of immune surveillance, the cytokine TRAIL, is considered a promising platform for developing selective anticancer drugs. For the first time, bioinformatic analysis of the transcriptome revealed the main regulator, the *IL1B* gene, which triggers proinflammatory activation and induces resistance to TRAIL in THP–1ad macrophage-like cells.

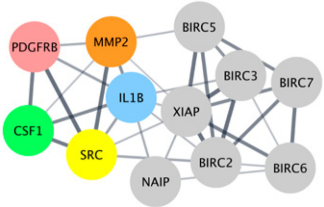

The discovered *IL1B*, *SRC*, *PDGFRB*, *MMP 2*, and *CSF1* hub genes are connected in PPI networks with antiapoptotic members of the IAPs

Broadly Reactive Nanobody Targeting the H3 Hemagglutinin of the Influenza A Virus

D. V. Shcheblyakov, D. V. Voronina, I. A. Favorskaya, I. B. Esmagambetov, I. A. Alekseeva, A. I. Korobkova, E. I. Ryabova, A. A. Derkaev, V. Yu. Kan, A. Sh. Dzharullaeva, A. I. Tukhvatulin, A. S. Bandelyuk, M. M. Shmarov, D. Yu. Logunov, A. L. Gintsburg

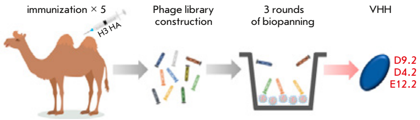

The schematic process of VHH isolation. Animal immunization and VHH selection

Monoclonal antibodies and recombinant antibody fragments are a very promising therapeutic tool to combat infectious diseases. Due to their unique paratope structure, nanobodies (VHHs) hold several advantages over conventional monoclonal antibodies, especially in relation to viral infections. In this study, three broadly reactive nanobodies to H3N2 influenza strains were isolated and Fc-fusion proteins (VHH-Fcs) were obtained and characterized *in vitro*.

ActaNaturae
JANUARY—MARCH 2024 VOL. 16 № 1 (60)
since april 2009, 4 times a year

Founders
Acta Naturae, Ltd,
National Research University
Higher School of Economics

Project Head: N.V. Soboleva
Editor: N.Yu. Deeva
Designer: K.K. Oparin
Art and Layout: K. Shnaider
Copy Chief: Daniel M. Medjo
Web Content Editor: O.B. Semina

Adress: 101000, Moscow, Myasnitskaya Ulitsa, 13, str. 4
Phone/Fax: +7 (495) 727 38 60
E-mail: actanaturae@gmail.com

Номер подписан в печать 30 марта 2024 г.
Тираж 15 экз. Цена свободная.
Отпечатано в типографии: НИУ ВШЭ,
г. Москва, Измайловское шоссе, 44, стр. 2

Founder and Chairman
of the Editorial Board (from 2009 to 2023)
of the journal Acta Naturae
Academician Grigoriev Anatoly Ivanovich

Indexed in PubMed, Web of Science,
Scopus, and RISC

Impact Factor: 2.0 (WOS); 3.5 (Scopus)

CONTENTS

REVIEWS

RESEARCH ARTICLES

CONTENTS

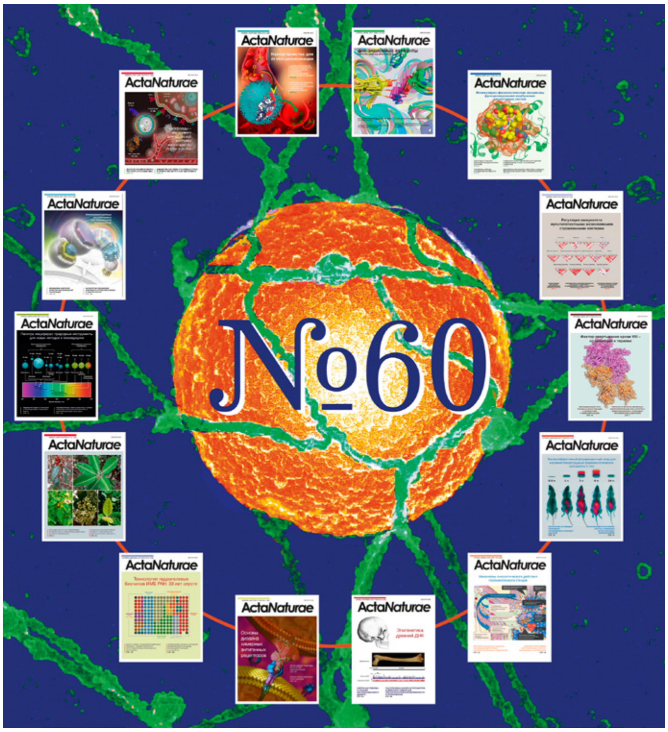

IMAGE ON THE COVER PAGE

Post-transcriptional Regulation of Gene Expression via Unproductive Splicing

L. G. Zavileyskiy[1,2], D. D. Pervouchine[2*]
[1]Lomonosov Moscow State University, Moscow, 119192 Russian Federation
[2]Skolkovo Institute of Science and Technology, Moscow, 121205 Russian Federation
[*]E-mail: d.pervouchine@skoltech.ru

Received: December 03, 2023; in final form, March 01, 2024
DOI: 10.32607/actanaturae.27337

ABSTRACT **Unproductive splicing is a mechanism of post-transcriptional gene expression control in which premature stop codons are inserted into protein-coding transcripts as a result of regulated alternative splicing, leading to their degradation via the nonsense-mediated decay pathway. This mechanism is especially characteristic of RNA-binding proteins, which regulate each other's expression levels and those of other genes in multiple auto- and cross-regulatory loops. Deregulation of unproductive splicing is a cause of serious human diseases, including cancers, and is increasingly being considered as a prominent therapeutic target. This review discusses the types of unproductive splicing events, the mechanisms of auto- and cross-regulation, nonsense-mediated decay escape, and problems in identifying unproductive splice isoforms. It also provides examples of deregulation of unproductive splicing in human diseases and discusses therapeutic strategies for its correction using antisense oligonucleotides and small molecules.**

KEYWORDS **unproductive splicing, nonsense-mediated decay, splicing, regulation, antisense oligonucleotides.**

ABBREVIATIONS **NMD – Nonsense-mediated decay; PTC – premature termination codon; EEJ – exon–exon junction; AS – alternative splicing; RBP – RNA-binding protein; UTR – untranslated region; SSO – splice-switching antisense oligonucleotides; nt – nucleotide.**

INTRODUCTION

Eukaryotic gene expression is controlled by a large number of factors that regulate a balance between mRNA synthesis and degradation [1, 2]. Nonsense mutations and frameshifting splicing errors lead to the emergence of mRNA isoforms containing premature termination codons (PTC). Eukaryotes have a system for selective degradation of such transcripts, called the nonsense-mediated decay (NMD) [3].

It has long remained unclear how the NMD pathway recognizes PTCs and distinguishes them from the normal stop codons [4]. The current model suggests that PTC recognition occurs in the cytoplasm, with the participation of the exon–exon junction (EEJ) complexes that are deposited on pre-mRNA during splicing [5, 6]. After the first round of translation, EEJ proteins located within the reading frame are displaced from pre-mRNA by ribosome (*Fig. 1A*) [7–9]. Since the normal translation termination site is usually located in the last exon [10], the EEJ proteins that remain bound to the pre-mRNA outside of the reading frame serve as a signal that a PTC has appeared (*Fig. 1B*). The presence of an EEJ 50–55 or more nucleotides downstream of the stop codon activates a cascade of transcript degradation, the central role in which is played by the UPF1 protein. The phosphorylated form of this protein attracts the endonuclease SMG6 and other factors that cause deadenylation and removal of the 5'-cap in pre-mRNA, which, in turn, triggers transcript decay by cellular exonucleases [9, 11–13]. There are other models in which PTCs are determined by the distance to the poly(A) tail, as well as models in which PTC causes mRNA degradation independently of EEJ proteins [14–18]. The existence of an EEJ-independent NMD mechanism explains the presence of a large number of NMD targets despite the almost complete lack of splicing in yeast [19, 20].

The primary function of NMD was originally believed to consist in preventing the emergence of truncated and, therefore, deleterious proteins [21]. However, it has become increasingly evident that NMD is ubiquitously used by the cell to regulate gene expression levels [22, 23]. For example, many RNA-binding proteins (RBPs) employ NMD to control their own expression through a negative feedback loop in which the protein product binds to its cognate mRNA and induces alternative splicing (AS) that leads to the generation of a PTC [24, 25]. Many splicing factors cross-regulate each other's expression levels in this way [26, 27]. The mechanism in which alternative splicing and NMD cooperate to post-transcriptionally regulate mRNA expression levels occurs in all known eukaryotes and is evolutionarily conserved [26, 28]. In the literature, it is referred to as regulated unproductive splicing and translation (RUST) or simply unproductive splicing [22, 29].

TYPES OF UNPRODUCTIVE SPLICING

Regulated transcript degradation through NMD depends on alternative splicing (AS), in which multiple mature mRNA isoforms are generated from the same pre-mRNA. AS events are usually categorized into few simple classes, such as exon skipping, alternative 5'- or 3'-splice sites, intron retention, mutually exclusive exons, but there are also more complex types of AS events [30, 31].

AS can generate PTCs in several ways. The best known are the so-called poison exons, which are skipped in the coding isoform but induce a PTC when included in the transcript (*Fig. 2A*) [29, 32, 33]. Poison exons can contain a stop codon within the exon itself or induce a PTC downstream through a frameshift (*Fig. 2B*). The reciprocal case is the so-called essential exon, which is normally included in the coding isoform but induces a PTC when skipped (*Fig. 2C*) [24]. It should be noted that essential exons are usually not a multiple of three in length and cause a frameshift inducing PTCs downstream. However, some essential exons are a multiple of three in length, and the PTC appears at the EEJ formed by their skipping (*Fig. 2D*). Activation of an alternative 5'- or 3'-splice site can also induce a PTC, both due to a frameshift and the formation of a new EEJ (*Fig. 2E,F*). Pairs of mutually exclusive exons can induce a frameshift if both exons are included or both are skipped at the same time (*Fig. 2G*). Thus, PTCs can arise as a result of stop codon insertion at the site of the AS event or somewhere downstream in the transcript.

Of particular interest are splicing events in the 3'-untranslated regions (3'-UTRs). The stop codon preceding the 3'-UTR is not premature; however, splicing of an intron located 50 nts or more downstream creates an NMD target. For example, expression of the AU-rich RNA binding factor AUF1 is regulated by conserved alternatively spliced elements in the 3'-UTR [34]. The 3'-UTRs of transcripts whose expression increases upon inactivation of the NMD system have a larger median length and are enriched in introns [35]. Moreover, most mRNAs encoding NMD factors themselves have long 3'-UTRs and are targets of NMD, which indicates that their expression is autoregulated [35, 36]. Splicing activ-

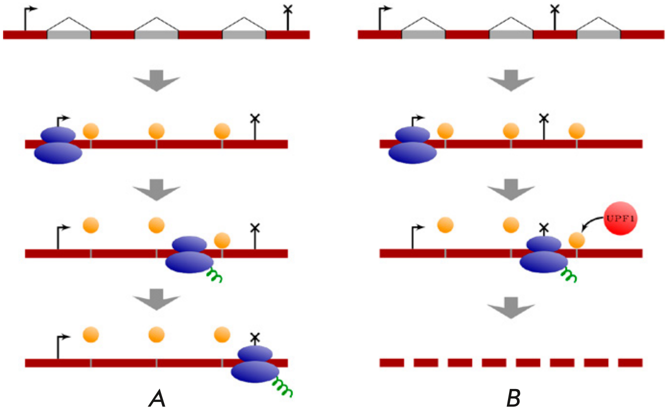

Fig. 1. The EEJ-dependent mechanism of NMD. (*A*) EEJ complexes (orange circles) are displaced from the mRNA by the ribosome during the first round of translation. (*B*) The EEJ complexes that remain bound to mRNA outside of the reading frame serve as a signal that a PTC has appeared

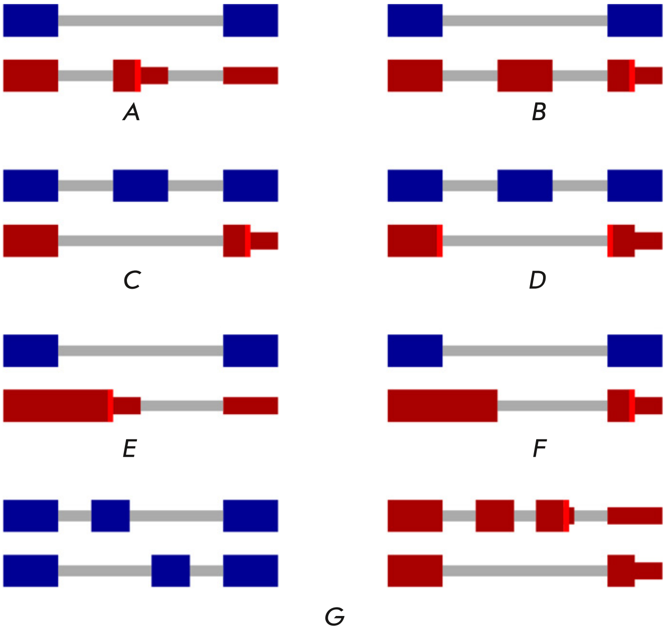

Fig. 2. Types of unproductive splicing events. Protein-coding isoforms are shown in blue. Unproductive isoforms are shown in red. PTCs are indicated with bright vertical red lines. (*A*) A poison exon carrying a PTC. (*B*) A poison exon inducing a PTC via frameshift. (*C*) An essential exon inducing a PTC via frameshift. (*D*) An essential exon inducing a PTC on the EEJ. (*E*) An alternative 5'-splice site inducing a PTC via intron retention. (*F*) An alternative 5'-splice site inducing a PTC via frameshift. (*G*) A pair of mutually exclusive exons

ity in 3'-UTRs significantly increases in tumors, correlates with poor prognosis, and affects many oncogenes [37, 38]. Therefore, unproductive splicing is not limited to premature translation termination within the coding frame and has a remarkable regulatory role in the 3'-UTR.

ANNOTATION OF UNPRODUCTIVE SPLICING

Current databases contain manually curated and automatically annotated lists of the transcripts that are NMD targets. Tools also exist to systematically classify AS events leading to the generation of NMD isoforms [39].

In databases such as ENSEMBL and GENCODE, NMD targets are annotated using the so-called 50-nt rule. Indeed, the presence of an EEJ 50 nt or more downstream of the stop codon has the greatest predictive power among the features that distinguish NMD transcripts [40, 41]. However, a significant proportion of transcripts that respond to NMD inactivation do not obey this rule [40, 42]. Some genes sensitive to NMD inactivation are annotated as non-coding [40]. According to the data obtained in experiments on NMD inactivation, the presence of upstream open reading frames (uORFs) may be the second most important feature determining the sensitivity of a transcript to NMD [40].

Incompleteness of the existing annotation of NMD transcripts has to do with the fact that their expression levels are normally quite low, hence they fall out of the annotation in databases. Long-read RNA sequencing has shown that many NMD substrates are unstable, and that their expression can be detected at a significant level only when the NMD pathway is inactivated [43]. There is an experimental approach to identifying lowly expressed NMD transcripts, which is based on sequencing of the RNA fraction enriched in EEJ complexes [44]. This fraction contains RNA that is partially spliced but not yet translated. A large number of previously unannotated, conserved EEJs were discovered using this method, with 70% of the exons being not a multiple of three in length and many remaining ones containing stop codons [44].

Unannotated unproductive splicing events can be predicted based on the evolutionary conservation of nucleotide sequences. For example, the *BRD3* gene contains a conserved intronic region which turns out to be a cryptic poison exon with strong evidence of expression in human tissue transcriptomes [44]. Remarkably, its paralog *BRD2* also contains a poison exon but in a non-homologous intron, and both these poison exons are surrounded and regulated by conserved RNA structures [44].

AUTO- AND CROSS-REGULATORY UNPRODUCTIVE SPLICING

Autoregulatory unproductive splicing is often triggered by the accumulation of the gene's protein product. For example, excess RBM10 protein binds to its own pre-mRNA and induces skipping of two essential exons, which shifts the balance of splice isoforms to NMD targets, and the expression level of RBM10 decreases [45]. This principle governs the expression of many of the genes involved in splicing such as the members of the serine-arginine-rich (SR) gene family [46–50], *CLK* [51, 52], *TIAL1* [53], *PTB* [54, 55], *hnRNPD* [56], and some ribosomal proteins [57, 58].

In cross-regulatory unproductive splicing, one protein binds to the pre-mRNA of another and promotes or suppresses NMD isoforms. This type of regulation is also common among RBPs from the SR family [59]. For example, the SRSF3 protein, along with the autoregulatory inclusion of a poison exon in its own pre-mRNA, causes inclusion of poison exons in the transcripts of its paralogs *SRSF2*, *SRSF5*, and *SRSF7* [48]. Besides SR proteins, other pairs of paralogs are regulated in the same way, such as *PTBP1*/*PTBP2* [60], *RBM10*/*RBM5* [45], *RBFOX2*/*RBFOX3* [61], *hnRNPD*/*hnRNPDL* [56], and *hnRNPL*/*hnRNPLL* [62]. Generally, cross-regulation among paralogs is a very common phenomenon for RBPs and is characterized by rapid evolutionary dynamics, particularly in regard to acquisition or loss of poison exons [26].

Cross-regulatory unproductive splicing is important not only for RBPs. For example, it causes tissue-specific expression of the *MID1* gene, which encodes microtubule-associated ubiquitin ligase, whose dysfunction leads to severe embryonic pathologies [27, 63]. Regulated unproductive splicing is important for many physiological processes, such as embryonic development [64], cellular differentiation [65], stress response [66–68], pathogenesis of neurodegenerative diseases [69, 70], etc.

Both splicing activators and repressors can participate in unproductive splicing regulation. An increase in the concentration of the repressor or a decrease in the concentration of the activator of poison exon inclusion leads to its skipping, thus raising the expression level of the target gene (*Fig. 3A*). Similarly, reduced concentration of the repressor or increased concentration of the activator of an essential exon suppresses its skipping, which also leads to upregulation of the target gene (*Fig. 3B*). It should be noted that some RBPs can serve as both activators and repressors, where the choice between activation and repression depends on the position of their binding site on the mRNA [71]. For example, PTBP1 stimulates

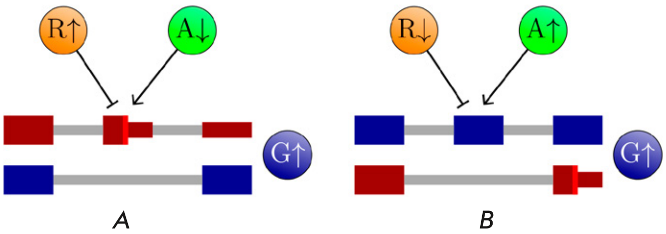

Fig. 3. Regulation of unproductive splicing. 'R' denotes a splicing repressor. 'A' denotes a splicing activator. 'G' denotes the target gene. Exon colors are as in *Fig. 2*. (*A*) An increase in R or a decrease in A leads to poison exon skipping, and expression of G increases. (*B*) A decrease in R or an increase in A suppresses essential exon skipping, and expression of G also increases

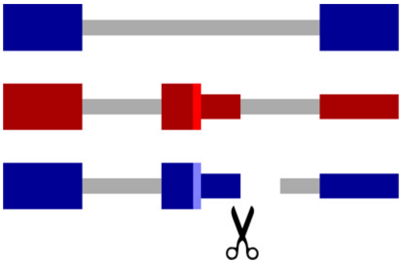

Fig. 4. Alternative polyadenylation promotes NMD escape by cutting off a part of the UTR that contains EEJ. This converts a PTC into a normal stop codon (bright vertical blue line)

the inclusion of a poison exon in the *DCLK2* gene causing its upregulation in neuronal tissues where expression of PTBP1 is reduced [72]. At the same time, PTBP1 suppresses the inclusion of a poison exon in the *IQGAP1* gene, thus reducing its expression level in the brain [72].

Many unproductive splicing targets are RBPs, which regulate splicing in other RBPs, creating multiple regulatory loops with positive and negative feedbacks. Negative feedbacks provide autoregulatory mechanisms to maintain homeostasis, while positive feedbacks can create bistable systems to turn on expression [73]. For example, the Drosophila *Sxl* gene employs both these mechanisms for autoinduction at low concentrations and, at the same time, to prevent harmful overproduction of the protein [74]. To achieve such regulation, RBPs can act simultaneously as splicing activators and splicing repressors by binding to multiple sites on the same pre-mRNA. This may explain the high level of evolutionary conservation of nucleotide sequences around unproductive splicing events [75].

NMD ESCAPE

It was discovered that not all PTCs necessarily cause NMD. A process called NMD escape plays an important role in the pathogenesis of many diseases [76–78]. NMD escape can be caused by PTC readthrough during translation. The frequency of PTC readthrough depends on the type of the stop codon (UAA, UAG or UGA), and in some NMD-escaping cell populations it can be as high as 20% [79, 80]. NMD escape can also be caused by translation reinitiation [81]. The difference is that translational readthrough produces a full-length protein, while translation reinitiation produces an N-terminal truncated protein and a short C-terminal peptide.

An interesting feature of NMD escape in the human homeostatic iron regulator (HFE) gene is the coordination between NMD and intronic polyadenylation [82]. HFE mRNA contains four alternative polyadenylation sites, one of which mediates NMD escape by pruning the EEJ-containing fragment. Thus, alternative polyadenylation may contribute to NMD escape if premature transcription termination cuts off a part of the untranslated region that contains EEJs, which converts the PTC into a normal stop codon (*Fig. 4*). Transcriptomic studies confirmed that transcripts escaping NMD by alternative polyadenylation are indeed expressed in human tissues [83]. The presence of an intronic polyadenylation site in the human *TAU* gene, which is associated with Alzheimer's disease, promotes NMD escape [84]. It should be noted that cotranscriptional splicing can prevent premature transcription termination at intronic polyadenylation sites, its functional outcome also being the N-terminal truncated protein [85].

The efficacy of NMD depends on the PTC position in the transcript and other properties. Studies of a large panel of tumor transcriptomes confirmed that the canonical EEJ model is the most important determinant of NMD efficacy [41]. However, the length of the 3'-UTR, proximity to the start codon, the distance between the PTC and the normal stop codon, the length of the exon in which the PTC is located, and other factors have a significant impact. One of them is the RNA structure, which can change the effective distances between cis-elements in the transcript and the binding sites of protein factors such as PABPC1, which apparently has an evolutionarily conserved function in maintaining correct translation termination and counteracting NMD activation [86]. The presence of *cis*-regulatory motifs of splicing factors, such as SRSF1, PABPN1, SNRPB2 and ACO1, also influences the efficacy of NMD [41].

NMD depends on the displacement of EEJ complexes by the ribosome, hence translation control mechanisms may influence its activity. Because miRNAs inhibit translation, they also may affect NMD targets [87], but specific examples of miRNAs that stabilize NMD substrates through this mechanism are currently unknown. In naturally occurring nonsense mutants, microRNAs can, on the contrary, suppress transcripts that escape NMD by binding to the extended 3'-UTR formed after PTC [88]. Interestingly, microRNAs can suppress the activity of the NMD cascade as a whole. For example, the mir-128 microRNA, whose expression level increases in differentiating neuronal cells, suppresses the expression of *UPF1* and the main component of the EEJ complex *MLN51*, thereby attenuating the response of the NMD system and increasing the expression of the proteins that control neuronal development [89].

DISEASES ASSOCIATED WITH UNPRODUCTIVE SPLICING AND NMD

Many diseases are associated with malfunctioning of the NMD system and unproductive splicing (*Table 1*). For example, nonsense mutations in the *CFTR* and *hERG* genes cause cystic fibrosis and long QT syndrome, respectively, as a result of the degradation of their transcripts by NMD [90, 91]. Deletions that cause frameshifts also lead to deficiency in important proteins. A well-known example is Duchenne muscular dystrophy, which is often caused by out-of-frame deletions in the *DMD* gene [92–94].

Mutations in splice sites can cause alternative splicing to switch to the NMD isoform. This happens in the *SYNGAP1* gene whose unproductive splicing is regulated by PTBP1/2 in a tissue-specific manner. Activation of an alternative 3'-splice site generates a NMD target causing the expression level to decrease, thus leading to the development of autism and mental retardation [96, 97].

However, not only mutations in the coding region and splice sites can generate NMD targets. Pathological states can arise due to mutations in introns and non-coding exons, while the mechanism of these pathologies is not always clear. For example, mutations in intron 20 of the *SCN1A* gene promote poison exon inclusion, leading to Dravet syndrome [95, 96]. Mutations in the poison exon of the *SNRPB* gene cause cerebro-costo-mandibular syndrome [101]. It is believed that they create or destroy a binding site of an RBP that activates or suppresses the inclusion of a poison exon, but it currently remains unknown which specific factors regulate these processes. A mutation in the cryptic poison exon of the *PCCA* gene, causing propionic acidemia, is a rare case when the mechanism of unproductive splicing deregulation is known [99]. This mutation is located in the binding site of the HNRNPA factor, which normally suppresses poison exon inclusion, but the mutation destroys this site and simultaneously creates a splicing enhancer, resulting in a decreased *PCCA* expression [99].

Not only mutations splicing cis-elements, but also improper functioning of the regulatory proteins can lead to a disease. A point mutation in the splicing factor SRSF2, which is observed at high frequency in patients with acute myeloid leukemia [103, 108], causes inclusion of a poison exon into histone methylase EZH2 transcripts, leading to its downregulation and, consequently, to the development of myeloid neoplasms, which are normally suppressed by EZH2 [103]. Mutations in the splicing factor SF3B1, which are often observed in myelodysplastic syndromes [109], promote inclusion of a poison exon in the *BRD9* gene, causing a decline in its expression, which results in accelerated growth and metastasis of melanomas [102]. Methylation of the SRSF3, SRSF6, and SRSF11 transcripts due to increased expression of methyltransferase METTL3, which is often observed in glioblastomas, promotes poison exon skipping that causes upregulation of these genes [105]. Remarkably, suppression of METTL3 expression in glioblastoma cell lines reduces cell proliferation and migration by altering splicing of SR protein targets such as BCL-X and NCOR2 [105].

In some cases, pathological changes in unproductive splicing are induced by the tissue condition, while a specific splicing regulator is unknown. For example, hypoxia, which is quite characteristic of many solid tumors, leads to excision of intron 3 from pre-mRNA of the angiogenesis inducer CYR61, a protein promoting cell proliferation and migration in tumors [110–112]. Under physiological conditions, intron 3 is retained, resulting in expression of the NMD target [106]. Under hypoxia, the activity of the NMD system and regulation through unproductive splicing are disrupted, and CYR61 expression increases, promoting tumor vascularization. Hypoxia also reduces the expression of the alternative isoform of the *LDHA* gene due to unproductive splicing, but the physiological consequence of this decrease is not clear [107].

MODULATION OF UNPRODUCTIVE SPLICING

Modulation of unproductive splicing is a promising therapeutic strategy for the treatment of many

Table 1. Disorders associated with unproductive splicing and NMD

Gene	Disease	Cause, regulators, and therapy	Refs
SCN1A	Dravet syndrome and other epilepsies	SCN1A haploinsufficiency due to mutations, including the ones in intron 20, that promote poison exon inclusion. SSOs switch to the productive isoform (in mouse models)	[95, 96]
SYNGAP1	Autism and mental retardation	Haploinsufficiency of SYNGAP1 due to mutations, including the ones in the splice site. PTBP1 and PTBP2 promote the NMD isoform. SSOs switch to the productive isoform (in mouse models and organoids)	[96, 97]
HTT	Huntington's disease	Expansion of CAG repeats. Reducing HTT expression by promoting poison exon inclusion using SSOs or small molecules branaplam (NCT05111249) and PTC518 (NCT05358717)	[98]
DMD	Duchenne muscular dystrophy	Frameshift due to a deletion. Eteplirsen (SSO) induces exon 51 skipping to restore the reading frame and to express a truncated but functional dystrophin (FDA approved)	[92, 93]
CFTR	Cystic fibrosis	Nonsense mutation in exon 23. CFTR expression restored by suppressing the inclusion of the mutated coding exon using SSO	[90]
hERG	Long QT syndrome	Nonsense mutation in the penultimate exon. hERG expression restored by retaining the last intron with SSO	[91]
PCCA	Propionic acidemia	Mutation in a cryptic poison exon. HNRNPA1 normally suppresses its inclusion, but the mutation disrupts the HNRNPA1 site and creates a splicing enhancer. PCCA expression restored by switching to a productive isoform using SSO	[99]
FUS	Amyotrophic lateral sclerosis (ALS)	Mutations in the localization signal cause accumulation of FUS in the cytoplasm. FUS suppresses the inclusion of an essential exon in its mRNA, but the autoregulatory loop is disrupted when mutant FUS is localized in the cytoplasm. SSO at the 5'-end of the essential exon switches splicing to unproductive isoform in cell lines	[100]
SNRPB	Cerebro-costo-mandibular syndrome	Mutations in the poison exon increase its inclusion level and reduce SNRPB expression	[101]
BRD9	Melanoma and other tumors	Mutant SF3B1 promotes poison exon inclusion in BRD9	[102]
EZH2	Myeloid leukemia	Mutant SRSF2 promotes poison exon inclusion in EZH2	[103]
SRSF1	Various tumors	KHDRBS1 switches SRSF1 splicing to the productive isoform	[104]
SRSF3,6,11	Glioblastoma	Increased level of METTL3 leads to the inclusion of the m^{6}A tag in SRSF3,6,11 mRNA and switches their splicing to the productive isoform	[105]
CYR61	Breast cancer	Deregulation of NMD due to hypoxia	[106]
LDHA	Breast cancer	Deregulation of NMD due to hypoxia	[107]

diseases. Splicing can be altered by the so-called splice-switching antisense oligonucleotides (SSO) [113]. The SSOs block the splice sites and/or binding sites of RBPs by complementarily binding to the pre-mRNA sequence and promoting the desired splicing outcome [113].

The SSOs for unproductive splicing modulation can be divided into three groups: SSOs that increase expression of the full-length protein (e.g. by promoting poison exon skipping), SSOs that maintain the expression of a truncated protein when the expression of the full-length protein is impossible (e.g. by promoting exon skipping or intron retention), and SSOs that reduce the expression level (e.g. by promoting poison exon inclusion).

The SSOs belonging to the first group can be used to treat diseases caused by deficiency in a functional protein; for example, due to mutations in genes such as *SYNGAP1*, *SCN1A*, *PCCA*, and *SNRNPB* [95–97, 99, 101]. SSOs of the second group can be used when a nonsense mutation or a frameshifting deletion renders a PTC, namely to avoid transcript degradation and maintain the expression of the truncated protein. Technically, SSOs of the second group can promote skipping of an exon carrying a nonsense mutation (as in the *PCCA* gene) or retention of an intron downstream of a PTC (as in the *hERG* gene). Coding exon skipping can be useful in the case of a frameshifting deletion to restore the frame (as in the *DMD* gene). A number of SSO drugs for the treatment of Duchenne muscular dystrophy have already been approved [94]. Third-group SSOs can be employed when protein accumulation needs to be suppressed. For example, mutations in the *FUS* gene, which destroy its nuclear localization signal and cause export into the cytoplasm, are associated with amyotrophic lateral sclerosis [114, 115]. To suppress the expression of *FUS* via unproductive splicing, its protein product must be located in the nucleus; however, the export of the mutant protein from the nucleus destroys the autoregulation loop, which aggravates its accumulation in the cytoplasm and promotes the formation of aggregates exhibiting cytotoxic effects [100, 116–118].

Despite all the positive aspects of SSO, there are many difficulties related to their delivery to target organs and tissues. The need to develop a delivery system and high drug doses in order to achieve the required concentration lead to higher prices and an increased risk of side effects [119]. Small molecule splicing modulators, which are more bioavailable, offer a powerful alternative to SSO.

A number of low-molecular-weight compounds that bind to splicing factors are currently known; however, they simultaneously modulate splicing of many genes [119]. Several small molecules have been found that specifically bind to target RNAs [98, 119–122]. The best studied of these, risdiplam, modulates splicing of the *SMN2* gene and can be used to treat spinal muscular atrophy [121]. Branaplam, similar in structure and mechanism of action to risdiplam, promotes the inclusion of the cryptic poison exon in the *HTT* gene, which reduces its expression and slows down the progression of Huntington's disease [122]. The small molecule PTC518, which is currently in phase 2 clinical trials, has a similar effect [120].

CONCLUSION

Unproductive splicing, an evolutionarily conserved mechanism of post-transcriptional regulation of gene expression, arose as a result of interaction between alternative splicing and nonsense-mediated decay. Unproductive splicing intricately maintains the balance of gene expression levels through the auto- and cross-regulatory cascades containing both positive and negative feedback loops. It is closely related to many other cellular processes, such as intronic polyadenylation, regulation of translation, and interactions with microRNAs. Deregulation of unproductive splicing is the cause of many human diseases, for which splice-switching antisense oligonucleotides offer a promising therapeutic strategy. ●

The authors would like to thank Dmitry Skvortsov for his critical comments.

This work was supported by the Russian Science Foundation (grant No. 22-14-00330).

REFERENCES

1. Borbolis F., Syntichaki P. // Mech. Ageing Dev. 2015. V. 152. P. 32–42.
2. Dassi E. // Front. Mol. Biosci. 2017. V. 4. P. 67.
3. Lykke-Andersen S., Jensen T.H. // Nat. Rev. Mol. Cell Biol. 2015. V. 16. № 11. P. 665–677.
4. He F., Peltz S.W., Donahue J.L., Rosbash M., Jacobson A. // Proc. Natl. Acad. Sci. USA. 1993. V. 90. № 15. P. 7034–7038.
5. Le Hir H., Gatfield D., Izaurralde E., Moore M.J. // EMBO J. 2001. V. 20. № 17. P. 4987–4997.
6. Le Hir H., Izaurralde E., Maquat L.E., Moore M.J. // EMBO J. 2000. V. 19. № 24. P. 6860–6869.
7. Nagy E., Maquat L.E. // Trends Biochem. Sci. 1998. V. 23. № 6. P. 198–199.
8. Karousis E.D., Nasif S., Mühlemann O. // Wiley Interdiscip. Rev. RNA. 2016. V. 7. № 5. P. 661–682.
9. Popp M.W., Maquat L.E. // Cell. 2016. V. 165. № 6.

P. 1319–1322.
10. Kurosaki T., Popp M.W., Maquat L.E. // Nat. Rev. Mol. Cell. Biol. 2019. V. 20. № 6. P. 384.
11. Isken O., Maquat L.E. // Genes Dev. 2007. V. 21. № 15. P. 1833–1856.
12. Loh B., Jonas S., Izaurralde E. // Genes Dev. 2013. V. 27. № 19. P. 2125–2138.
13. Unterholzner L., Izaurralde E. // Mol. Cell. 2004. V. 16. № 4. P. 587–596.
14. Fang Y., Bateman J.F., Mercer J.F., Lamandé S.R. // J. Cell Sci. 2013. V. 126. Pt 12. P. 2551–2560.
15. Kurosaki T., Maquat L.E. // Proc. Natl. Acad. Sci. USA. 2013. V. 110. № 9. P. 3357–3362.
16. Hogg J.R., Goff S.P. // Cell. 2010. V. 143. № 3. P. 379–389.
17. Hurt J.A., Robertson A.D., Burge C.B. // Genome Res. 2013. V. 23. № 10. P. 1636–1650.
18. Singh G., Rebbapragada I., Lykke-Andersen J. // PLoS Biol. 2008. V. 6. № 4. P. e111.
19. Lopez P.J., Séraphin B. // RNA. 1999. V. 5. № 9. P. 1135–1137.
20. Malabat C., Feuerbach F., Ma L., Saveanu C., Jacquier A. // Elife. 2015. V. 4. P. e06722.
21. Maquat L.E. // Nat. Rev. Mol. Cell Biol. 2004. V. 5. № 2. P. 89–99.
22. Lewis B.P., Green R.E., Brenner S.E. // Proc. Natl. Acad. Sci. USA. 2003. V. 100. № 1. P. 189–192.
23. Lareau L.F., Brooks A.N., Soergel D.A., Meng Q., Brenner S.E. // Adv. Exp. Med. Biol. 2007. V. 623. P. 190–211.
24. Pervouchine D., Popov Y., Berry A., Borsari B., Frankish A., Guigó R. // Nucl. Acids Res. 2019. V. 47. № 10. P. 5293–5306.
25. Nasif S., Contu L., Mühlemann O. // Semin. Cell Dev. Biol. 2018. V. 75. P. 78–87.
26. Lareau L.F., Brenner S.E. // Mol. Biol. Evol. 2015. V. 32. № 4. P. 1072–1079.
27. García-Moreno J.F., Romao L. // Int. J. Mol. Sci. 2020. V. 21. № 24. P. 9424.
28. Kalyna M., Simpson C.G., Syed N.H., Lewandowska D., Marquez Y., Kusenda B., Marshall J., Fuller J., Cardle L., McNicol J., et al. // Nucl. Acids Res. 2012. V. 40. № 6. P. 2454–2469.
29. Lareau L.F., Inada M., Green R.E., Wengrod J.C., Brenner S.E. // Nature. 2007. V. 446. № 7138. P. 926–929.
30. Wang Y., Liu J., Huang B.O., Xu Y.M., Li J., Huang L.F., Lin J., Zhang J., Min Q.H., Yang W.M., Wang X.Z. // Biomed. Rep. 2015. V. 3. № 2. P. 152–158.
31. Nilsen T.W., Graveley B.R. // Nature. 2010. V. 463. № 7280. P. 457–463.
32. Carvill G.L., Mefford H.C. // Curr. Opin. Genet. Dev. 2020. V. 65. P. 98–102.
33. Leclair N.K., Anczuków O. // Nat. Rev. Mol. Cell Biol. 2022. V. 23. № 12. P. 777.
34. Wilson G.M., Sun Y., Sellers J., Lu H., Penkar N., Dillard G., Brewer G. // Mol. Cell Biol. 1999. V. 19. № 6. P. 4056–4064.
35. Yepiskoposyan H., Aeschimann F., Nilsson D., Okoniewski M., Mühlemann O. // RNA. 2011. V. 17. № 12. P. 2108–2118.
36. Huang L., Lou C.H., Chan W., Shum E.Y., Shao A., Stone E., Karam R., Song H.W., Wilkinson M.F. // Mol. Cell. 2011. V. 43. № 6. P. 950–961.
37. Chan J.J., Zhang B., Chew X.H., Salhi A., Kwok Z.H., Lim C.Y., Desi N., Subramaniam N., Siemens A., Kinanti T., et al. // Nat. Cell Biol. 2022. V. 24. № 6. P. 928–939.
38. Guo T., You K., Chen X., Sun Y., Wu Y., Wu P., Jiang Y. // Cell Death Discov. 2022. V. 8. № 1. P. 320.
39. Hsu M.K., Lin H.Y., Chen F.C. // PLoS One. 2017. V. 12. № 4. P. e0174798.
40. Colombo M., Karousis E.D., Bourquin J., Bruggmann R., Mühlemann O. // RNA. 2017. V. 23. № 2. P. 189–201.
41. Lindeboom R.G., Supek F., Lehner B. // Nat. Genet. 2016. V. 48. № 10. P. 1112–1118.
42. Tani H., Imamachi N., Salam K.A., Mizutani R., Ijiri K., Irie T., Yada T., Suzuki Y., Akimitsu N. // RNA Biol. 2012. V. 9. № 11. P. 1370–1379.
43. Karousis E.D., Gypas F., Zavolan M., Mühlemann O. // Genome Biol. 2021. V. 22. № 1. P. 223.
44. Kovalak C., Donovan S., Bicknell A.A., Metkar M., Moore M.J. // Genome Biol. 2021. V. 22. № 1. P. 132.
45. Sun Y., Bao Y., Han W., Song F., Shen X., Zhao J., Zuo J., Saffen D., Chen W., Wang Z., et al. // Nucl. Acids Res. 2017. V. 45. № 14. P. 8524–8540.
46. Änkö M.L., Morales L., Henry I., Beyer A., Neugebauer K.M. // Nat. Struct. Mol. Biol. 2010. V. 17. № 8. P. 962–970.
47. Sureau A., Gattoni R., Dooghe Y., Stévenin J., Soret J. // EMBO J. 2001. V. 20. № 7. P. 1785–1796.
48. Änkö M.L., Müller-McNicoll M., Brandl H., Curk T., Gorup C., Henry I., Ule J., Neugebauer K.M. // Genome Biol. 2012. V. 13. № 3. P. R17.
49. Sun S., Zhang Z., Sinha R., Karni R., Krainer A.R. // Nat. Struct. Mol. Biol. 2010. V. 17. № 3. P. 306–312.
50. Stoilov P., Daoud R., Nayler O., Stamm S. // Hum. Mol. Genet. 2004. V. 13. № 5. P. 509–524.
51. Hillman R.T., Green R.E., Brenner S.E. // Genome Biol. 2004. V. 5. № 2. P. R8.
52. Duncan P.I., Stojdl D.F., Marius R.M., Bell J.C. // Mol. Cell. Biol. 1997. V. 17. № 10. P. 5996–6001.
53. Le Guiner C., Gesnel M.C., Breathnach R. // J. Biol. Chem. 2003. V. 278. № 12. P. 10465–10476.
54. Wollerton M.C., Gooding C., Wagner E.J., Garcia-Blanco M.A., Smith C.W. // Mol. Cell. 2004. V. 13. № 1. P. 91–100.
55. Rahman L., Bliskovski V., Reinhold W., Zajac-Kaye M. // Genomics. 2002. V. 80. № 3. P. 245–249.
56. Kemmerer K., Fischer S., Weigand J.E. // RNA. 2018. V. 24. № 3. P. 324–331.
57. Takei S., Togo-Ohno M., Suzuki Y., Kuroyanagi H. // Nucl. Acids Res. 2016. V. 44. № 12. P. 5585–5596.
58. Cuccurese M., Russo G., Russo A., Pietropaolo C. // Nucl. Acids Res. 2005. V. 33. № 18. P. 5965–5977.
59. Leclair N.K., Brugiolo M., Urbanski L., Lawson S.C., Thakar K., Yurieva M., George J., Hinson J.T., Cheng A., Graveley B.R., Anczuków O. // Mol. Cell. 2020. V. 80. № 4. P. 648–665.
60. Spellman R., Llorian M., Smith C.W. // Mol. Cell. 2007. V. 27. № 3. P. 420–434.
61. Jangi M., Boutz P.L., Paul P., Sharp P.A. // Genes Dev. 2014. V. 28. № 6. P. 637–651.
62. Rossbach O., Hung L.H., Schreiner S., Grishina I., Heiner M., Hui J., Bindereif A. // Mol. Cell. Biol. 2009. V. 29. № 6. P. 1442–1451.
63. Winter J., Lehmann T., Krauss S., Trockenbacher A., Kijas Z., Foerster J., Suckow V., Yaspo M.L., Kulozik A., Kalscheuer V., et al. // Hum. Genet. 2004. V. 114. № 6. P. 541–552.
64. McIlwain D.R., Pan Q., Reilly P.T., Elia A.J., McCracken S., Wakeham A.C., Itie-Youten A., Blencowe B.J., Mak T.W. // Proc. Natl. Acad. Sci. USA. 2010. V. 107. № 27. P. 12186–12191.
65. Wong J.J., Ritchie W., Ebner O.A., Selbach M., Wong J.W., Huang Y., Gao D., Pinello N., Gonzalez M., Baidya K.,

et al. // Cell. 2013. V. 154. № 3. P. 583–595.
66. Karam R., Lou C.H., Kroeger H., Huang L., Lin J.H., Wilkinson M.F. // EMBO Rep. 2015. V. 16. № 5. P. 599–609.
67. Li Z., Vuong J.K., Zhang M., Stork C., Zheng S. // RNA. 2017. V. 23. № 3. P. 378–394.
68. Gardner L.B. // Mol. Cell. Biol. 2008. V. 28. № 11. P. 3729–3741.
69. Qiu H., Lee S., Shang Y., Wang W.Y., Au K.F., Kamiya S., Barmada S.J., Finkbeiner S., Lui H., Carlton C.E., et al. // J. Clin. Invest. 2014. V. 124. № 3. P. 981–999.
70. Polymenidou M., Lagier-Tourenne C., Hutt K.R., Huelga S.C., Moran J., Liang T.Y., Ling S.C., Sun E., Wancewicz E., Mazur C., et al. // Nat. Neurosci. 2011. V. 14. № 4. P. 459–468.
71. Hamid F.M., Makeyev E.V. // Nucl. Acids Res. 2017. V. 45. № 21. P. 12455–12468.
72. Mironov A., Petrova M., Margasyuk S., Vlasenok M., Mironov A.A., Skvortsov D., Pervouchine D.D. // Nucl. Acids Res. 2023. V. 51. № 7. P. 3055–3066.
73. Müller-McNicoll M., Rossbach O., Hui J., Medenbach J. // J. Mol. Cell. Biol. 2019. V. 11. № 10. P. 930–939.
74. Moschall R., Gaik M., Medenbach J. // FEBS Lett. 2017. V. 591. № 11. P. 1471–1488.
75. Ni J.Z., Grate L., Donohue J.P., Preston C., Nobida N., O'Brien G., Shiue L., Clark T.A., Blume J.E., Ares M. // Genes Dev. 2007. V. 21. № 6. P. 708–718.
76. Litchfield K., Reading J.L., Lim E.L., Xu H., Liu P., Al-Bakir M., Wong Y.N.S., Rowan A., Funt S.A., Merghoub T., et al. // Nat. Commun. 2020. V. 11. № 1. P. 3800.
77. Dyle M.C., Kolakada D., Cortazar M.A., Jagannathan S. // Wiley Interdiscip. Rev. RNA. 2020. V. 11. № 1. P. e1560.
78. Cheng M.M., Cao Y.Y. // Yi Chuan. 2020. V. 42. № 4. P. 354–362.
79. Bidou L., Hatin I., Perez N., Allamand V., Panthier J.J., Rousset J.P. // Gene Ther. 2004. V. 11. № 7. P. 619–627.
80. Tate W.P., Poole E.S., Mannering S.A. // Prog. Nucl. Acid. Res. Mol. Biol. 1996. V. 52. P. 293–335.
81. Zhang J., Maquat L.E. // EMBO J. 1997. V. 16. № 4. P. 826–833.
82. Martins R., Proença D., Silva B., Barbosa C., Silva A.L., Faustino P., Romão L. // PLoS One. 2012. V. 7. № 4. P. e35461.
83. Gilat R., Shweiki D. // Biochem. Biophys. Res. Commun. 2007. V. 353. № 2. P. 487–492.
84. Ngian Z.K., Tan Y.Y., Choo C.T., Lin W.Q., Leow C.Y., Mah S.J., Lai M.K., Chen C.L., Ong C.T. // Proc. Natl. Acad. Sci. USA. 2022. V. 119. № 37. P. e2204179119.
85. Vlasenok M., Margasyuk S., Pervouchine D. // Nucl. Acids Res. Genom. Bioinform. 2023. V. 5. № 2. P. lqad051.
86. Eberle A.B., Stalder L., Mathys H., Orozco R.Z., Mühlemann O. // PLoS Biol. 2008. V. 6. № 4. P. e92.
87. Choe J., Cho H., Lee H.C., Kim Y.K. // EMBO Rep. 2010. V. 11. № 5. P. 380–386.
88. Zhao Y., Lin J., Xu B., Hu S., Zhang X., Wu L. // Elife. 2014. V. 3. P. e03032.
89. Bruno I.G., Karam R., Huang L., Bhardwaj A., Lou C.H., Shum E.Y., Song H.W., Corbett M.A., Gifford W.D., Gecz J., et al. // Mol. Cell. 2011. V. 42. № 4. P. 500–510.
90. Kim Y.J., Sivetz N., Layne J., Voss D.M., Yang L., Zhang Q., Krainer A.R. // Proc. Natl. Acad. Sci. USA. 2022. V. 119. № 3. e2114858118.
91. Gong Q., Stump M.R., Zhou Z. // J. Mol. Cell. Cardiol. 2011. V. 50. № 1. P. 223–229.
92. Mendell J.R., Rodino-Klapac L.R., Sahenk Z., Roush K., Bird L., Lowes L.P., Alfano L., Gomez A.M., Lewis S., Kota J., et al. // Ann. Neurol. 2013. V. 74. № 5. P. 637–647.
93. McDonald C.M., Shieh P.B., Abdel-Hamid H.Z., Connolly A.M., Ciafaloni E., Wagner K.R., Goemans N., Mercuri E., Khan N., Koenig E., et al. // J. Neuromuscul. Dis. 2021. V. 8. № 6. P. 989–1001.
94. Aartsma-Rus A., Corey D.R. // Nucl. Acid Ther. 2020. V. 30. № 2. P. 67–70.
95. Carvill G.L., Engel K.L., Ramamurthy A., Cochran J.N., Roovers J., Stamberger H., Lim N., Schneider A.L., Hollingsworth G., Holder D.H., et al. // Am. J. Hum. Genet. 2018. V. 103. № 6. P. 1022–1029.
96. Lim K.H., Han Z., Jeon H.Y., Kach J., Jing E., Weyn-Vanhentenryck S., Downs M., Corrionero A., Oh R., Scharner J., et al. // Nat. Commun. 2020. V. 11. № 1. P. 3501.
97. Yang R., Feng X., Arias-Cavieres A., Mitchell R.M., Polo A., Hu K., Zhong R., Qi C., Zhang R.S., Westneat N., et al. // Neuron. 2023. V. 111. № 10. P. 1637–1650.
98. Keller C.G., Shin Y., Monteys A.M., Renaud N., Beibel M., Teider N., Peters T., Faller T., St-Cyr S., Knehr J., et al. // Nat. Commun. 2022. V. 13. № 1. P. 1150.
99. Spangsberg Petersen U.S., Dembic M., Martínez-Pizarro A., Richard E., Holm L.L., Havelund J.F., Doktor T.K., Larsen M.R., Færgeman N.J., Desviat L.R., Andresen B.S. // Mol. Ther. Nucl. Acids. 2024. V. 35. № 1. P. 102101.
100. Zhou Y., Liu S., Liu G., Oztürk A., Hicks G.G. // PLoS Genet. 2013. V. 9. № 10. P. e1003895.
101. Lynch D.C., Revil T., Schwartzentruber J., Bhoj E.J., Innes A.M., Lamont R.E., Lemire E.G., Chodirker B.N., Taylor J.P., Zackai E.H., et al. // Nat. Commun. 2014. V. 5. P. 4483.
102. Inoue D., Chew G.L., Liu B., Michel B.C., Pangallo J., D'Avino A.R., Hitchman T., North K., Lee S.C., Bitner L., et al. // Nature. 2019. V. 574. № 7778. P. 432–436.
103. Rahman M.A., Lin K.T., Bradley R.K., Abdel-Wahab O., Krainer A.R. // Genes Dev. 2020. V. 34. № 5–6. P. 413–427.
104. Ghigna C., Giordano S., Shen H., Benvenuto F., Castiglioni F., Comoglio P.M., Green M. R., Riva S., Biamonti G. // Mol. Cell. 2005. V. 20. № 6. P. 881–890.
105. Li F., Yi Y., Miao Y., Long W., Long T., Chen S., Cheng W., Zou C., Zheng Y., Wu X., et al. // Cancer Res. 2019. V. 79. № 22. P. 5785–5798.
106. Hirschfeld M., zur Hausen A., Bettendorf H., Jäger M., Stickeler E. // Cancer Res. 2009. V. 69. № 5. P. 2082–2090.
107. Han J., Li J., Ho J.C., Chia G.S., Kato H., Jha S., Yang H., Poellinger L., Lee K.L. // Sci. Rep. 2017. V. 7. № 1. P. 4108.
108. Kim E., Ilagan J.O., Liang Y., Daubner G.M., Lee S.C., Ramakrishnan A., Li Y., Chung Y.R., Micol J.B., Murphy M.E., et al. // Cancer Cell. 2015. V. 27. № 5. P. 617–630.
109. Jiang M., Chen M., Liu Q., Jin Z., Yang X., Zhang W. // Front. Oncol. 2023. V. 13. P. 1116438.
110. Chen Y., Du X.Y. // J. Cell. Biochem. 2007. V. 100. № 6. P. 1337–1345.
111. Chen C.C., Mo F.E., Lau L.F. // J. Biol. Chem. 2001. V. 276. № 50. P. 47329–47337.
112. Huang Y.T., Lan Q., Lorusso G., Duffey N., Rüegg C. // Oncotarget. 2017. V. 8. № 6. P. 9200–9215.
113. Bennett C.F. // Annu. Rev. Med. 2019. V. 70. P. 307–321.
114. Kino Y., Washizu C., Aquilanti E., Okuno M., Kurosawa M., Yamada M., Doi H., Nukina N. // Nucl. Acids Res. 2011. V. 39. № 7. P. 2781–2798.
115. Dormann D., Rodde R., Edbauer D., Bentmann E., Fischer I., Hruscha A., Than M.E., Mackenzie I.R., Capell A.,

Schmid B., et al. // EMBO J. 2010. V. 29. № 16. P. 2841–2857.
116. Maharana S., Wang J., Papadopoulos D.K., Richter D., Pozniakovsky A., Poser I., Bickle M., Rizk S., Guillén-Boixet J., Franzmann T.M., et al. // Science. 2018. V. 360. № 6391. P. 918–921.
117. Patel A., Lee H. O., Jawerth L., Maharana S., Jahnel M., Hein M.Y., Stoynov S., Mahamid J., Saha S., Franzmann T.M., et al. // Cell. 2015. V. 162. № 5. P. 1066–1077.
118. Sun Z., Diaz Z., Fang X., Hart M.P., Chesi A., Shorter J., Gitler A.D. // PLoS Biol. 2011. V. 9. № 4. P. e1000614.
119. Schneider-Poetsch T., Chhipi-Shrestha J.K., Yoshida M. // J. Antibiot. (Tokyo). 2021. V. 74. № 10. P. 603–616.
120. Estevez-Fraga C., Tabrizi S.J., Wild E.J. // J. Huntingtons Dis. 2022. V. 11. № 4. P. 351–367.
121. Paik J. // CNS Drugs. 2022. V. 36. № 4. P. 401–410.
122. Krach F., Stemick J., Boerstler T., Weiss A., Lingos I., Reischl S., Meixner H., Ploetz S., Farrell M., Hehr U., et al. // Nat. Commun. 2022. V. 13. № 1. P. 6797.

Ultrastructural 3D Microscopy for Biomedicine: Principles, Applications, and Perspectives

K. E. Mochalov[1], D. S. Korzhov[1,2], A. V. Altunina[1,3], O. I. Agapova[4], V. A. Oleinikov[1,2*]
[1]Shemyakin–Ovchinnikov Institute of Bioorganic Chemistry, Russian Academy of Sciences, Moscow, 117997 Russian Federation
[2]National Research Nuclear University MEPhI (Moscow Engineering Physics Institute), Moscow, 115409 Russian Federation
[3]Moscow Institute of Physics and Technology (National Research University), Dolgoprudny, Moscow Region, 141701 Russian Federation
[4]Academician V.I. Shumakov National Medical Research Center of Transplantology and Artificial Organs, Ministry of Health of the Russian Federation, Moscow, 123182 Russian Federation
[*]E-mail: voleinik@mail.ru
Received November 8, 2023; In final form, December 29, 2023
DOI: 10.32607/actanaturae.27323

ABSTRACT **Modern biomedical research often requires a three-dimensional microscopic analysis of the ultrastructure of biological objects and materials. Conceptual technical and methodological solutions for three-dimensional structure reconstruction are needed to improve the conventional optical, electron, and probe microscopy methods, which to begin with allow one to obtain two-dimensional images and data. This review discusses the principles and potential applications of such techniques as serial section transmission electron microscopy; techniques based on scanning electron microscopy (SEM) (array tomography, focused ion beam SEM, and serial block-face SEM). 3D analysis techniques based on modern super-resolution optical microscopy methods are described (stochastic optical reconstruction microscopy and stimulated emission depletion microscopy), as well as ultrastructural 3D microscopy methods based on scanning probe microscopy and the feasibility of combining them with optical techniques. A comparative analysis of the advantages and shortcomings of the discussed approaches is performed.**

KEYWORDS **ultrastructural 3D microscopy; electron microscopy; tomography; super-resolution optical microscopy; scanning probe microscopy; biomedical research.**

ABBREVIATIONS **EM – electron microscopy; SEM – scanning electron microscopy; TEM – transmission electron microscopy; OM – optical microscopy; SPM – scanning probe microscopy; STORM – stochastic optical reconstruction microscopy; STED – stimulated emission depletion; ssTEM – serial section transmission electron microscopy; AT – array tomography; ATUM-SEM – automated tape collecting ultramicrotome scanning electron microscopy; SBF-SEM – serial block-face scanning electron microscopy; FIB-SEM – focused ion beam scanning electron microscopy; ET – electron tomography; ECT – electron cryotomography; STA – subtomogram averaging; AECs – alveolar epithelial cells; SMLM – single-molecule localization microscopy; PBS – polarizing beam splitter; WS – wave selector; PM – phase modulator; SMF – single-mode optical fiber; DC – dichroic mirror; DF – dichroic filter; EF – extracting filter; MMF – multi-mode optical fiber; APD – avalanche photodiode; EMCCD – electron multiplying charge-coupled device; PALM – photo-activated light microscopy; PAINT – point accumulation for imaging in nanoscale topography; MINFLUX – minimal photon fluxes; SPNT – scanning probe nanotomography; PSF – point spread function.**

INTRODUCTION

Methods for the three-dimensional nanoscale analysis of the spectral, morphological, and optical properties of nanostructured specimens need to be improved or elaborated to conduct modern research into biological objects and nanomaterials.

Techniques based on three fundamental microscopy techniques have conventionally been employed for 2D visualization: electron microscopy (EM) [1], optical microscopy (OM) [2], and scanning probe microscopy (SPM) [3]. These approaches have a rather broad scope of application but differ in their key characteristics and provide different types of information about the investigated objects. Thus, EM and SPM allow one to record images with a spatial resolution of several nanometers, making it possible to identify various components of the internal cell structure. The significant drawbacks of these methods include the small field of view and the infeasibility of obtaining information about specimen composition. In contrast, the use of highly specific immunostaining (including multicolor immunostaining) in OM allows for a specific reconstruction of the spatial distribution of the objects of interest (e.g., membrane proteins responsible for any cell–cell interaction process). In many cases, OM can be employed to work with living tissues. Diffraction-limited resolution is the main shortcoming of this method. The Abbe criterion $d > \lambda/2n$ suggests that a high spatial resolution is achieved at small wavelengths and high refractive index of the medium. An axial (Z-axis) resolution of up to 500 nm and up to 250 nm in the lateral (XY) plane can be achieved when using confocal optical microscopy. Nevertheless, this limitation can be obviated by modern computer processing software and the use of multibeam illumination, which underlies such methods as stochastic optical reconstruction microscopy (STORM) [4] and stimulated emission depletion (STED) microscopy [5].

Transition to three-dimensional analysis is the next stage in developing the aforementioned techniques, since the features of the 3D organization of biological objects and materials have a crucial impact on their functional activity and biological properties in most cases. For this reason, a number of studies focusing on different approaches to solving this problem have recently been published. Therefore, this review aimed to summarize the latest achievements in obtaining three-dimensional images with a nanoscale resolution.

EM-BASED ULTRASTRUCTURAL 3D MICROSCOPY METHODS

The key electron microscopy methods include scanning electron microscopy (SEM) and transmission electron microscopy (TEM); each of them has been modified in its own way to obtain 3D images. Acquisition of these images relies on obtaining multiple 2D images of a specimen's cross sections and merging them into a single 3D image (*Fig. 1*).

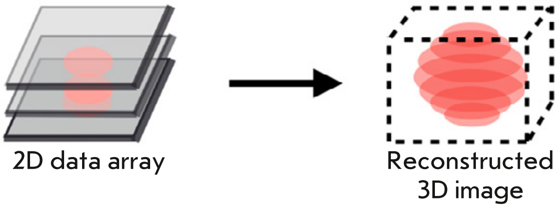

Fig. 1. The fundamental principle applied in obtaining three-dimensional images

Figure 2 shows the most advanced 3D image acquisition methods employing this approach. The key differences determining which approach will be selected for a particular task [6] include the method used for creating the serial section images [7], the volume being analyzed, and the maximum spatial resolution.

Serial sectioning TEM (ssTEM) [10], which is TEM involving serial examination of thin sections cut on an ultramicrotome, was a pioneering EM-based 3D microscopy method. The key advantage of ssTEM is that the specimen examination depth is not limited. This method has been pushed to the limit of its capabilities and is intensively employed in a large number of studies [11, 12]. *Figure 3* shows an example of the use of this method.

The main shortcomings of ssTEM involve its labor intensity [13] (as a large number of sections need to be fabricated and examined individually) and technical complexity. The sections have numerous artifacts: mechanical impurities [14], holes, cracks, compressions [15], folds, and uneven the thickness of the section or carrier film [16], which can render adequate data processing arduous. An even bigger problem is the possibility of losing part of the sections due to folds or damage [17, 18]. In such cases, the recorded image can be incorrect and requires separate efforts to eliminate losses.

Array tomography (AT) is similar to ssTEM in many respects but employs SEM instead of TEM. This change has made it possible to use microscope slides, silicon wafers, and conductive coating coverslips as substrates [19, 20]. Unlike SEM grids, these substrates have a manifold larger size, and thus allow one to collect more sections. *Figure 4* shows an example of the use of this method.

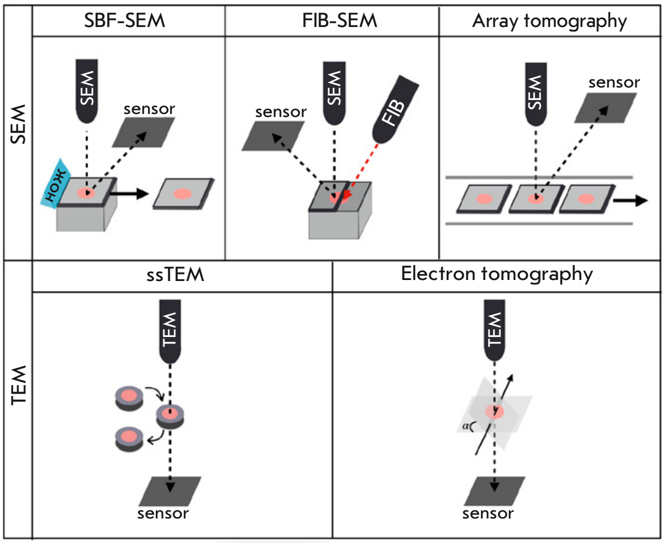

Fig. 2. Methods for obtaining three-dimensional images using TEM and SEM. Regardless of the type of microscopy, the first step is specimen preparation, which involves using polymer media to immobilize the specimen and then cut it into sections. Among specimen immobilization methods, the most popular techniques include fixation using methacrylate [8], cryofixation, freeze-fixation, and Tokuyasu cryosectioning [9]. The next step involves accumulating an array of 2D images using TEM or SEM. The recorded images should be aligned with the XY axes and potential rotation should be eliminated, being especially important for systems that study individual sections (ssTEM and array tomography). Next, the area that will be shown in the final image is selected from the resulting array. The final step is creating a full-fledged 3D image from the recorded 2D segments using specialized software

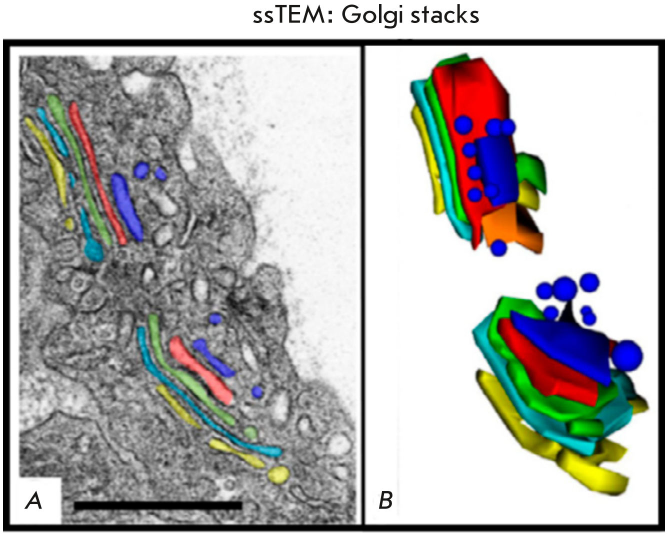

Fig. 3. An ssTEM image of Golgi stacks in the mouse lung cell AE1. (*A*) One of the EM microphotographs of the series with color manual segmentation. (*B*) A 3D model of Golgi stacks obtained in TEM based on nine consecutive sections with manually segmented tanks of both stacks. Scale range: 500 nm. The figure was taken from ref. [6]

A special tape can also be used as a substrate, enabling automated acquisition of thousands of sections for a single specimen. This approach is known as automated tape collecting ultramicrotome SEM (ATUM-SEM) [21]. Sections are obtained using an ultramicrotome equipped with a special UMT knife and a water bath. Fragments floating in water are collected by a moving tape, which can be coiled up into a spool if desired. The tape is then cut into pieces, attached to silicon wafers, and SEM images are recorded [19]. The noteworthy advantage of this technique is that post-staining can be used to enhance contrast [22]. Among all the EM techniques, ATUM-SEM boasts the largest field of view, limited only by the width of the ultramicrotome knife. The shortcomings of this technique are generally the same as those for ssTEM; however, they are not as significant because of larger arrays and automated section collection.

SEM images can be obtained not only from sections, but also from the surface of the remaining specimen portion, which underlies the technique known as serial block-face scanning electron microscopy (SBF-SEM). The upper portion of the resin-filled specimen is removed, and the remaining surface is scanned by SEM. This approach eliminates problems such as position alignment, distortion, compression, and section damage. Meanwhile, a problem with this approach is that the charge accumulates in the insulating resin, thus negatively affecting image quality. Additional metallization is required for this reason. When using a high-intensity electron beam, there is a risk of damaging the polymer, which reduces the resolution and plasticity needed for cutting a good-quality surface section [23, 24]. Furthermore, post-staining cannot be used in this approach; so, the original specimen must be characterized by good contrast and conductivity. *Figure 5A* shows an example of the use of this method.

A focused ion beam can be applied for surface sectioning. This approach is known as focused ion beam scanning electron microscopy (FIB-SEM). In all other aspects, the principle of workstation operation is simi-

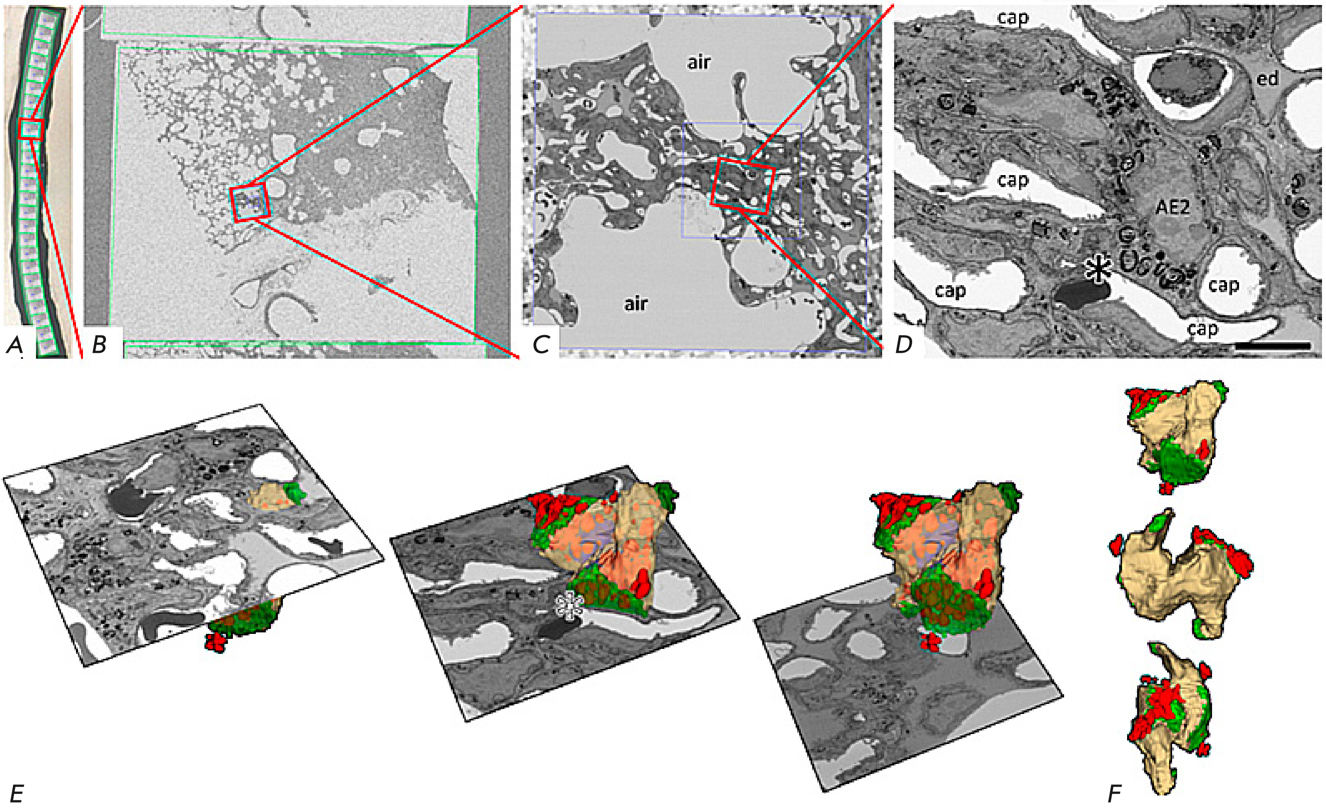
Array tomography: AE2 cells in the fibrotic parenchyma of mouse lung

Fig. 4. An AT image of an AE2 cell in the fibrotic parenchyma of the mouse lung. (*A*–*D*) Sequential magnification of the SEM image from one of the sections of the tape (*A*). The asterisk on (*D*) corresponds to one AE2 cell in the fibrotic tissue area. Scale bar: 5 μm. (*E*) 3D reconstruction of the AE2 cell. Three separate cross-sectional planes from the sequence of recorded images are shown. (*F*) 3D reconstruction of the AE2 cell at different tilts. The figure was borrowed from ref. [6]

lar to that for SBF-SEM. Structurally, a focused ion beam scanning electron microscope consists of two radiation sources: the top-mounted electron optics for the scanning beam and the side-mounted ion optics for the cutting beam. Both beams focus at a single point, and the entire specimen volume is therefore continuously scanned [25]. Depending on the ion beam current, it is possible to either finely cut a small area or coarsely cut large layers. This method allows one to increase axial resolution from 20 nm for ultramicrotomy to 5 nm for FIB-SEM. Lateral resolution has to be sacrificed for such an increase in axial resolution, since refocusing is only feasible in a region several tens of micrometers in size. Another advantage of ion beam is that it allows one to cut into harder and unstable materials, as well as specimens not embedded in resin. FIB-SEM has already been used for detailed examination of subcellular structures and has demonstrated a high degree of detail of images [26, 27]. The result of this study can be seen in *Fig. 5B*.

Electron tomography (ET) is another three-dimensional-analysis technology [28]. In contrast to all the techniques described above, ET provides virtual, rather than physical, sections of a specimen. The specimen preparation method is similar to that used in TEM and SEM; it involves chemical fixation or cryofixation, and staining or antibody labeling [29]. Therefore, any investigation takes place both at room temperature for specimens embedded in resin and at a cryotemperature for frozen specimens. Below, special attention will be devoted to the aspects of using ET at cryogenic temperatures, which has given rise to a separate technique called electron cryotomography (ECT) [30]. It is also possible to study suspen-

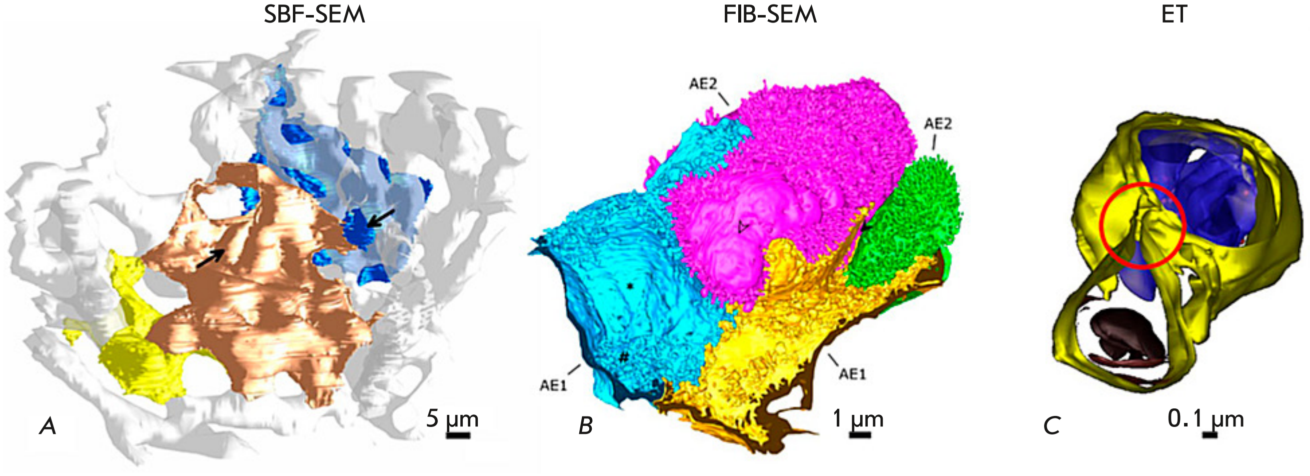

Fig. 5. 3D reconstructions obtained using serial block-face scanning electron microscopy (SBF-SEM), SEM with layer-by-layer etching with a focused ion beam (FIB-SEM), and electron tomography (ET). (*A*) 3D reconstruction of human alveolar epithelial type 1 cells (AE1) (yellow, gold, and blue) and the alveolar capillary network (white) based on the SBF-SEM dataset. Arrows indicate the position of the nuclei of AE1 cells. (*B*) 3D reconstruction of virtually the entire human alveolar epithelial type 2 (AE2) cell (pink) with portions of adjacent AE1 cell domains (blue and yellow) and an additional AE2 cell (green) based on the FIB-SEM dataset. (*C*) 3D reconstruction of the lamellar body (top) and the autophagosome (bottom) inside an AE2 cell (mouse lung) based on the ET dataset. Separate lipid membranes are distinguishable, which in this case is indicative of a connection of two organelles (a red circle). The figure was taken from ref. [6]

sions of particles smaller than hundreds of nanometers (e.g., viruses, organelles, and macromolecules) by applying them onto a carbon film or a layer of frozen water [31].

In terms of its operation principle, ET is similar to computed tomography, where radiation is directed at different angles, and virtual sections are created. The difference between these two techniques is that an X-ray tube and a camera rotate around the specimen in CT, while the specimen rotates and the camera remains stationary in ET. Because of this design modification, an image is recorded not 360°, but only at 70° with respect to the normal to the specimen at the initial position. This limitation has been termed the “missing wedge” [32] or “missing cone” in the case of using multiple tilt directions [33]. A significantly higher resolution is achieved using this method compared to other EM-based 3D analysis approaches, but it is highly dependent on parameters such as object thickness, accelerating voltage, goniometer tilt calibration, and alignment of the acquired images. The need to achieve a minimum signal-to-noise ratio that suffers from inelastic scattering imposes limitations on the possible specimen size. Thus, accelerating voltages of 200–300 kV are conventionally applied in ET, which allows one to examine specimens up to 300 nm in size. Thicker specimens reduce the achievable resolution [34]. This limitation can be partially obviated either by using the energy filtering approach [35] or by increasing the accelerating voltage. Thus, Vanhecke et al. [36] demonstrated that application of a 400 kV accelerating voltage enabled the examination of a 1 µm thick specimen. Because of the limitations put on the size of the region being investigated, this method is best suited to the study of subcellular structures smaller than 100 nm (*Fig. 5C*). Thicker structures can be examined by ET when making a series of sections and stacking them as it was done in previous methods [27, 37]. Despite the aforementioned limitations, ET, and ECT in particular, produce an absolutely record-breaking performance for all 3D microscopy types in terms of the achieved spatial resolution. Thus, the record-breaking value of the spatial resolution of 3D reconstruction (2.8 Å) was achieved using the subtomogram averaging (STA) procedure; however, for it to be used, there needs to be a large number of identical nanoscale objects (e.g., protein molecules) available for averaging [30].

Nevertheless, the widespread implementation of ET and ECT remains substantially hampered by their considerable complexity; so, these methods are being

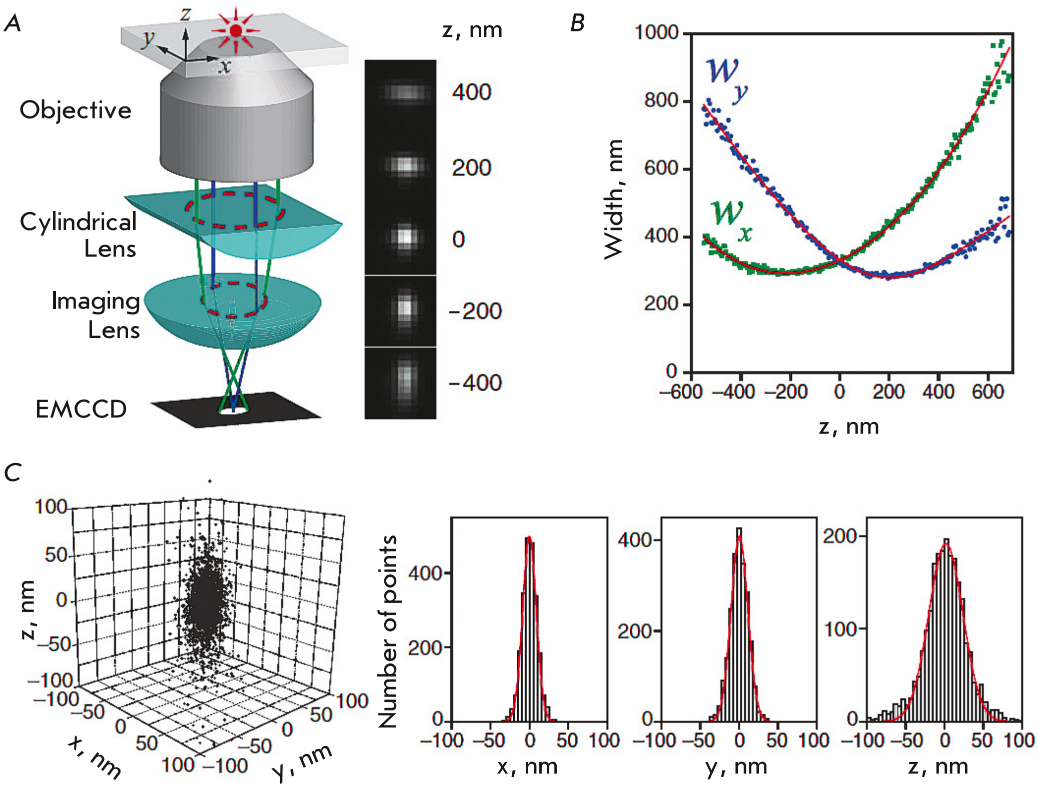

Fig. 6. The principle of the 3D STORM technique. (*A*) An optical scheme for determining the axial coordinate of a radiating object by analyzing the ellipticity of its image. The right panel shows images of the radiating object in the X and Y planes depending on its axial position. (*B*) Examples of the dependence of the ellipticity of the image of the emitting object (Alexa 647) for X and Y coordinates on focusing along the Z axis. (*C*) An example of the 3D distribution of single emitting objects and the corresponding histograms of the distribution in the X, Y, and Z directions. The figure was taken from ref. [45]

developed and used by only a few research groups [28, 30, 38–40].

ULTRASTRUCTURAL 3D MICROSCOPY METHODS BASED ON SUPER-RESOLUTION OPTICAL MICROSCOPY

Optical imaging of biological structures has conventionally been performed using confocal microspectrometry [41], as well as its modifications such as 4Pi microscopy [42–44]. The main shortcoming of all these techniques is that they come with low spatial resolution. For this reason, various super-resolution optical microscopy methods have been developed over the past two decades and adapted for 3D analysis; the most prominent of those are stochastic optical reconstruction microscopy (STORM) [4] and stimulated emission depletion microscopy (STED) [5]. The practical importance of these techniques is that they enable not only a nanometer resolution structural analysis of specimens, but also the reconstruction of the spatial distribution of target objects thanks to highly specific fluorescent immunostaining, which is an integral step in specimen preparation in any super-resolution OM method.

3D-STORM is the first super-resolution 3D microscopy technique [45]. It belongs to the single-molecule localization microscopy (SMLM) class. This group of techniques relies on the fact that certain fluorophores spontaneously “light up” and “go down,” which can be detected by fast frame-by-frame imaging. In this way, the emission of different subsets of fluorescent molecules will be caught in each frame. The resulting images are still diffraction-limited; however, the positions of individual molecules are determined with a high accuracy from multiple frames using a special mathematical apparatus employing the Delaunay triangulation [46]. The final 3D image is reconstructed using the data obtained by a statistical analysis of thousands of localizations.

Myosin was the first single molecule spatially localized by STORM [47]. For recording images, the molecules (fluorescent probes) were rarefied to such an extent that their signals did not overlap. In this way, it became possible to find the positions of each probe with great accuracy. A fundamentally different approach employing photoswitchable cyanine dyes was developed in ref. [48]. Measurements were conducted as follows: low-intensity radiation switched on a small number of probes; the image was then recorded and probe positions were calculated; radiation with a different wavelength switched

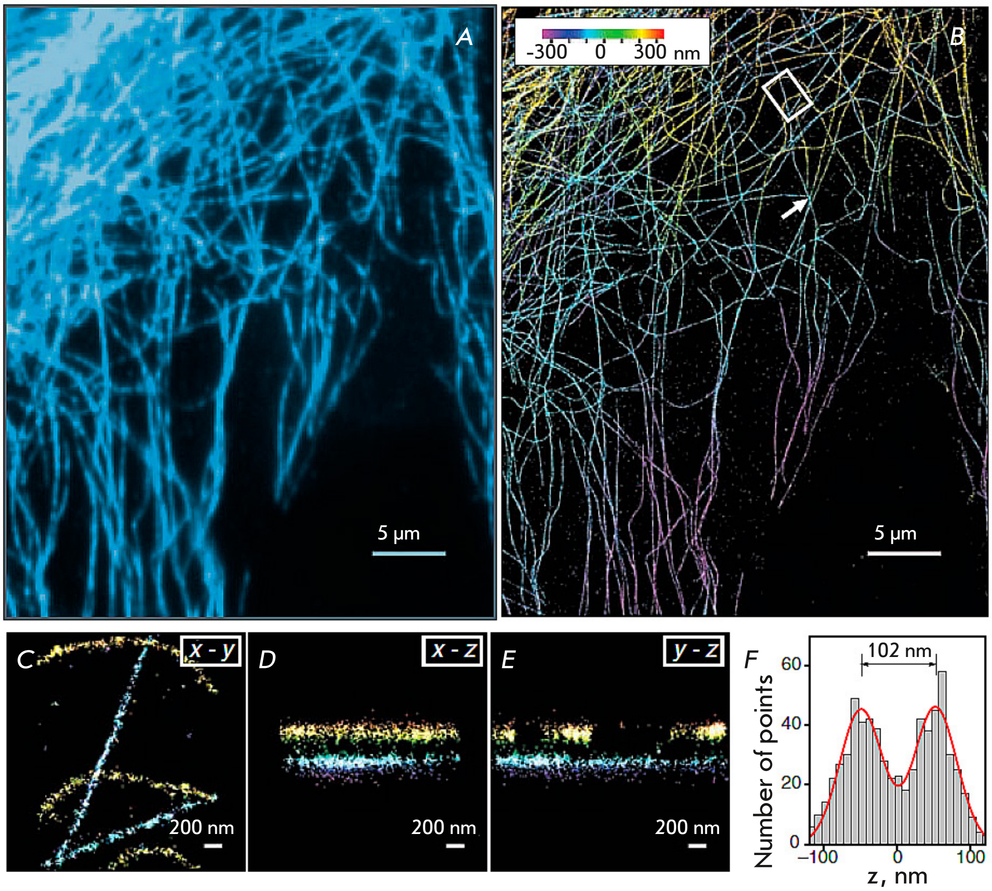

Fig. 7. Results obtained using the 3D STORM technique. (*A*) A widefield fluorescent image of microtubules in a BS-C-1 cell. (*B*) An image obtained in the 3D STORM mode of the same section of the BSC-1 cell as that shown in panel (*A*). Data on the axial coordinates of the occurrence are presented in the pseudo-color scale. (*C–E*) The cross sections corresponding to the five microtubule strands in the X-Y, X-Z, and Y-Z directions in the BS-C-1 cell area are shown with a white rectangle in (*B*). (*F*) Z-profile histogram of two microtubules intersecting in the X-Y projection, plotted in the area indicated with a white arrow in panel (*B*). The figure was taken from ref. [45]

this set of probes off and switched another one on. This procedure was repeated many times, yielding a complete 3D image of the specimen. The spatial resolution achieved using this method ranges from 20 to 30 nm. Photo-activated light microscopy is a variation of STORM; it is based on a similar approach, but photoactivated proteins are used instead of dyes [49]. In general, the differences in SMLM techniques also come down to the fluorophores used for specific labeling. For example, the direct STORM (dSTORM) method utilizes cyanine dyes (Cy5 and Alexa 647) switched on by adding a special buffer containing thiol and glucose oxidase [50]; a wide range of fluorescent labels for SMLM have been described in refs. [51, 52]. Another SMLM technique, the point accumulation for imaging in nanoscale topography (PAINT) method, uses diffusible dyes that are switched on only when being transiently bound to the target structure [53, 54].

Elaboration of the STORM-based 3D-SMLM method is based on allowance for the astigmatism of the images obtained at different specimen depths [55]. It is achieved by using a special cylindrical lens with a small radius of curvature in the optical scheme so that focal planes differ for the X and Y directions. The fluorophore occurrence depth is calculated according to changes in the ellipticity of the spatial distribution of its emission. The operating principle of this approach is shown in *Fig. 6*. Thus, *Fig. 6B* illustrates the difference in the ellipticity minima for the X and Y coordinates and the method for determining the true specimen position on the Z coordinate according to the intersection of the X and Y ellipticity dependences. *Figure 6C* also shows an example

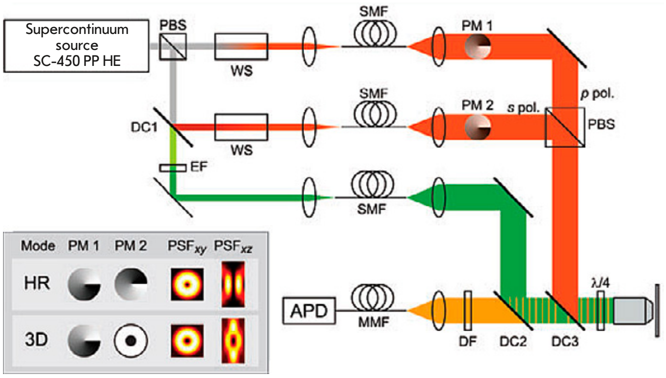

Fig. 8. Schematic diagram of the setup for implementing the 3D-STED technique using a supercontinuum laser. The figure was borrowed from ref. [61]

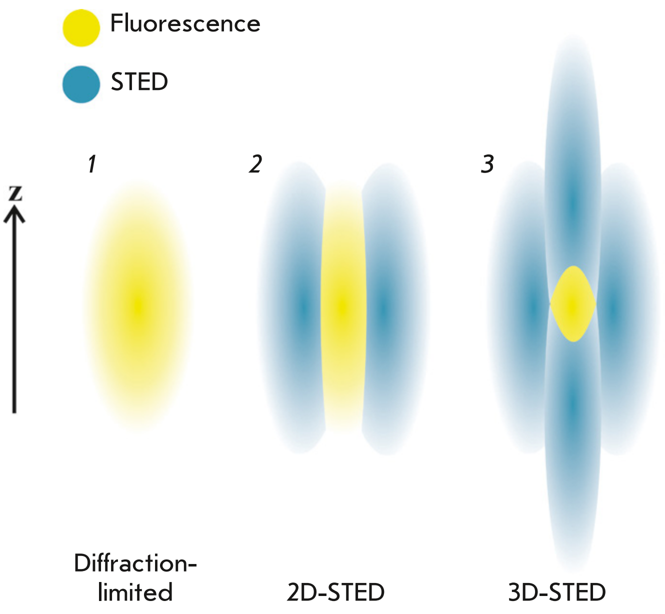

Fig. 9. Narrowing of the effective radiation area due to STED suppression of peripheral radiation. *1* – diffraction-limited fluorescent PSF. *2* – the torus-shaped STED beam narrows the diameter of the fluorescent PSF. *3* – fluorescent PSF in the case of 3D-STED

of 3D localization distribution of single molecules (in this case, Alexa 647 fluorophore). The experimentally observed cluster of localizations (intersections of ellipticity curves) of the same molecule is related to its multiple activation/deactivation. Therefore, it is necessary to localize a sufficiently large number of clusters (145 in this case) that are further statistically aligned with respect to the center of mass to obtain the overall three-dimensional distribution of the localizations (left panel in *Fig. 6C*).

Imaging of a BS-C-1 cell stained with primary and secondary antibodies, as well as Cy3 and Alexa 647 dyes, can be reported as an example of a practical application of this technique [56]. The result of using this approach is demonstrated in *Fig. 7*.

Unlike for 3D-SMLM, in the case of 3D optical imaging by STED, the investigated area is illuminated not completely but pointwise using two focused lasers. The first laser scans the surface in a way similar to a conventional confocal microscope, while the beam profile of the second laser in the focal plane is shaped as a torus projection and used to suppress spontaneous emission at the margins of the investigated area, using stimulated emission. A resolution of several tens of nanometers is achieved due to the fact that the recorded radiation originates exactly from the center of the excitation laser beam [57]. The near-zero intensity in the center of the suppressing beam is an essential factor in this case; otherwise, STED efficiency decreases because of a suppression of radiation in the investigated region [58]. Several types of STED can be differentiated depending on the light distribution in the suppressing beam: 1D-STED (X or Y directions) [59], 2D-STED (X and Y simultaneously) [60], z-STED (along the optical axis Z), and, finally, 3D-STED [61, 62]. The major technical challenge for 3D-STED consists in a noncoherent integration of two suppressing beams, one having a profile identical to that for 2D-STED and the other one identical to that for z-STED. This approach also allows one to separately adjust the axial and lateral resolutions. The shape of the suppressing beam is set by creating certain phase patterns. Fixed phase delay plates or spatial light modulators are used for this purpose.

Strictly synchronized pulsed laser sources have conventionally been used in STED microscopy; their operating principle is as follows: a fluorescence-exciting pulse (~ 80 ps, shorter than the fluorescence lifetime) is followed by a STED pulse with a duration of ~ 250 ps, narrowing the spatial region. However, extension of STED microscopy to the visible spectrum necessitated the use of sophisticated nonlinear optics for pulse shaping and synchronization. It has been shown recently [63] that STED microscopy can be conducted using supercontinuum lasers, which greatly simplifies the hardware assemblies for STED microscopy and may contribute to wider implementation of this technique. *Figure 8* shows a schematic diagram of the 3D-STED setup on a supercontinuum laser.

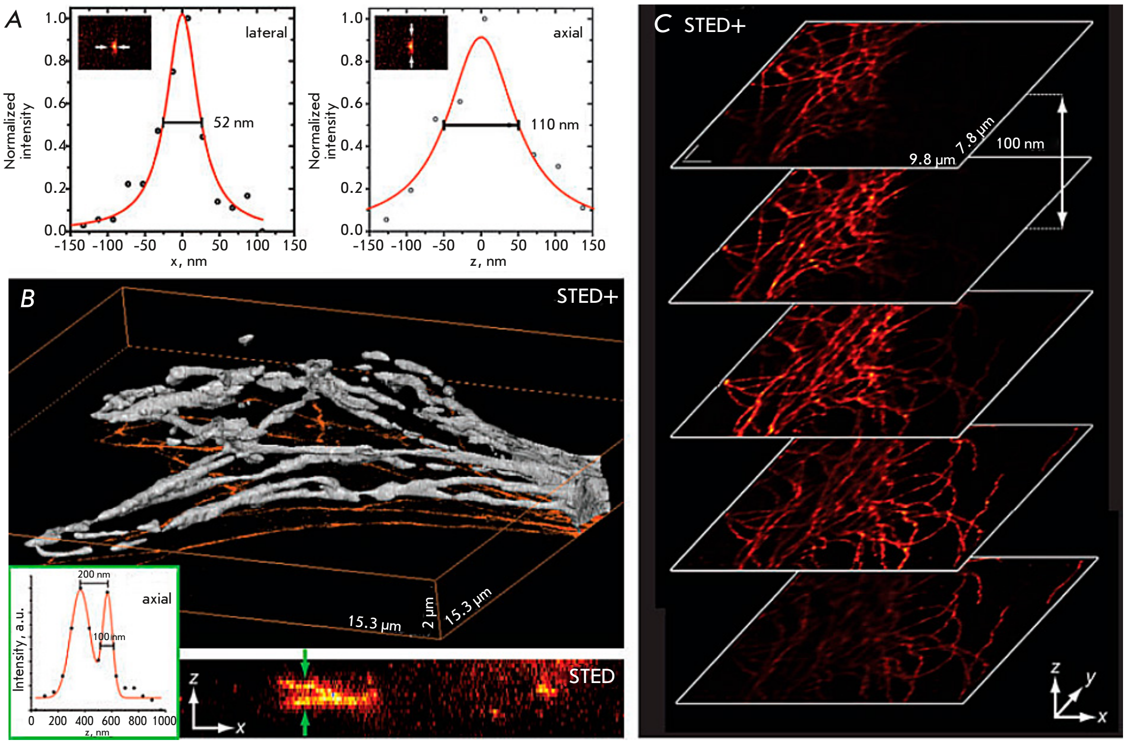

Fig. 10. The results obtained using the 3D-STED technique. (*A*) Spatial resolution of fluorescent nanoparticles 44 nm in diameter: 52 nm in the X-direction and 110 nm in the axial (Z) direction. (*B*) A 3D image of fluorescently labeled microtubules: visualization of the isosurface (top) and projection of maximum intensity along the Y axis (bottom) – 30 sections. The inset shows the intensity profile at the specified location. (*C*) Sections obtained at a 100 nm increment in the Z direction. The figure was taken from ref. [61]

A polarizing beam splitter (PBS) divides laser radiation into two orthogonally (*s* and *p*) polarized beams. The required wavelength is extracted from each beam using a wave selector (WS), and the beam is spatially filtered by single-mode optical fibers (SMFs). The profile of suppressing beams (highlighted in red in the figure) is then set by phase plates (modulators) (PM1 and PM2), and the final beams are summed up by a polarizing beam splitter and directed to the lens entrance by a dichroic mirror (DC3). Portion *s* of the polarized beam that has passed through the dichroic mirror (DC1) is used as the exciting radiation. The extracting filter (EF) isolates the desired wavelength (highlighted in green in the figure); the beam is then also spatially filtered and directed to the lens entrance by the dichroic mirror (DC2). A quarter-wavelength plate in front of the lens makes all the incoming beams circularly polarized. The Stokes fluorescence signal (highlighted in yellow in the figure) passes through both dichroic mirrors, is filtered from the exciting radiation by an optical (dichroic) filter (DF), is focused into a multi-mode optical fiber (MMF) acting as a confocal aperture, and detected by an avalanche photodiode (APD). Scanning takes place as the sample is moved with a three-axis piezo positioner. *Figure 8* also shows the point spread functions (PSFs) in multiple directions when using phase plates for ultra-high lateral resolution (HR) and acquiring 3D images [64]. Details of the narrowing of the effective radiation area for 3D-STED are shown in *Fig. 9*.

Laser intensity and optical aberrations are the key parameters affecting the spatial resolution of STED. For biological specimens, this value is several tens of nanometers. Work is currently underway aiming to eliminate aberrations arising from the use of long-focus lenses and optical windows, which have enabled aberration-free 3D images with a depth of tens of nanometers [65]. *Figure 10* shows an example of the operation of 3D-STED.

An important feature of the method is that nanoscale resolution is achieved without mathematical signal processing. However, studies focusing on combining STED and SMLM are currently underway; an example is the 3D-MINFLUX (minimal photon fluxes) technique with a resolution of several nanometers, which is record-breaking for fluorescence microscopy [66, 67].

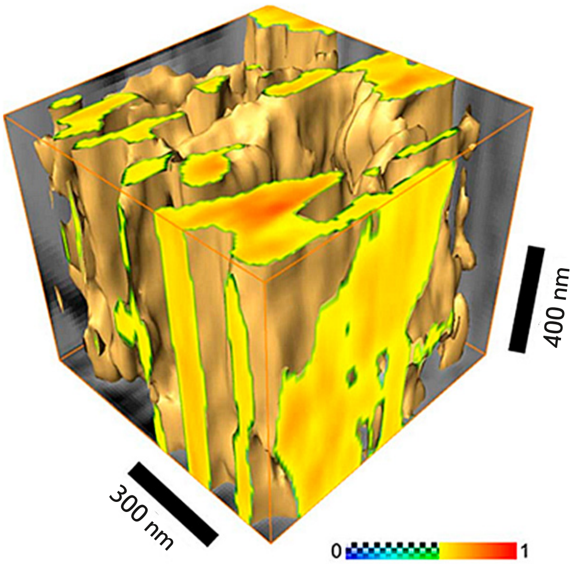

Fig. 11. Tomographic reconstruction of a section of human bone, 256 × 256 × 19 voxels, step-by-step chemical etching of 80 nm. The color scale is the value of the phase shift of the SPM probe oscillations normalized to unity. The figure is borrowed from ref. [70]

SPM-BASED ULTRASTRUCTURAL 3D MICROSCOPY METHODS

The approach to 3D analysis based on scanning probe microscopy is in many respects similar to another surface mapping method described previously, scanning electron microscopy, and requires removing the scanned nanolayer from the material surface. The principle of 3D reconstruction is the same as that for FIB-SEM: merging 2D SPM images into a 3D one. The most essential difference between SPM and EM consists in the slightly lower average lateral (XY) spatial resolution that depends on the probe's radius of curvature. The radius of curvature of standard SPM probes specified by the manufacturer is ~ 10 nm; however, there are quite a few specialized probes (e.g., those with grown diamond whiskers (https://tipsnano.ru/catalog/afm-special/super-sharp/nsg10-dlc/) whose radius of curvature is ~ 1 nm). SPM was first applied when performing a 3D study of the microdomains of the polystyrene-block-butadiene-block-styrene-type triblock copolymer [68]. Controlled plasma etching was used to remove the layers in this case, which allowed for the removal of 7.5 nm of the material after each etching run. As a result, a 200 × 160 × 45 nm area was reconstructed. A significant drawback of this method was that the

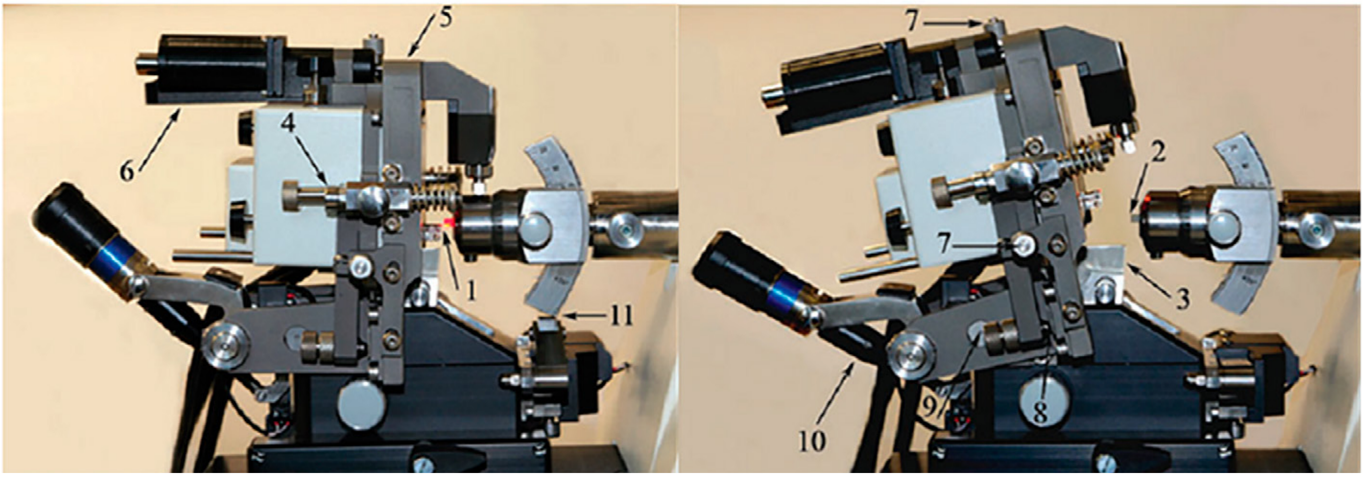

Fig. 12. A setup for implementing the SPM-UMT procedure: Ntegra Tomo unification methodology (NT-MDT, Russia). The left panel is the working position for carrying out SPM measurements; the right panel – the SPM head is reserved for performing the UMT cut. (1) SPM probe holder; (2) test specimen; (3) UMT knife holder; (4) SPM-head supports; (5) SPM-head support platform; (6) SPM-head motorized supply system; (7) micrometer screws of the SPM-head positioner; (8) polycorundum support plates; (9) SPM-head hinge fastening system; (10) the system of motorized removal of the SPM-head to bring it to the position of the UMT-cut; and (11) The restrictive support of the UMT console. The figure was taken from ref. [73]

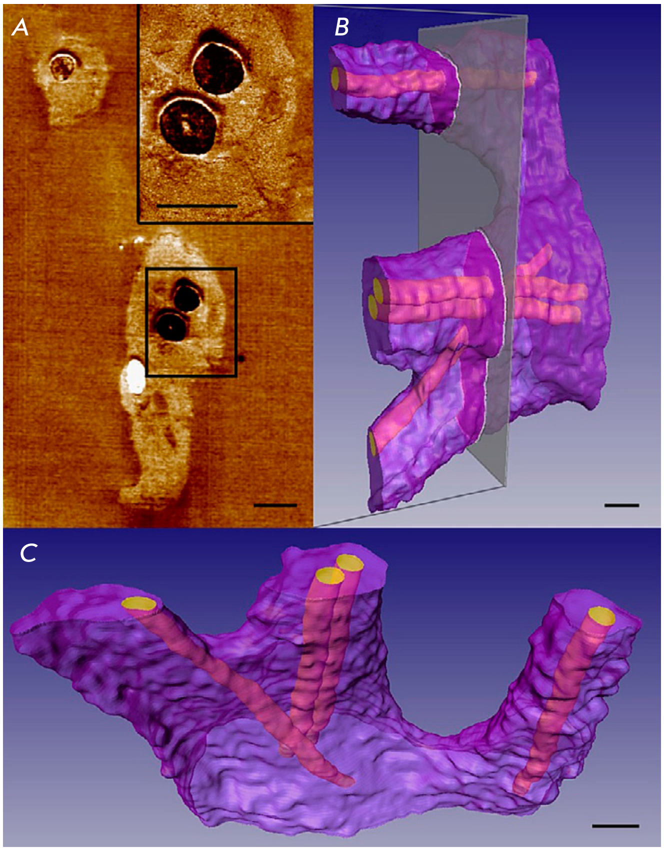

Fig. 13. 3D SPNT reconstruction of a cardiomyocyte enveloping nanofibers. (*A*) One of the topographic SPM images (phase contrast) used for 3D reconstruction. Insert: a zoomed-in area, shown with a rectangle, including fibers and a membrane fold; (*B*, *C*) 3D models of a cardiomyocyte enveloping nanofibers (16.0 × 16.0 × 6.5 μm, 54 sections, 120 nm section thickness). The selected plane in (*B*) corresponds to the position of the SPM image in (*A*). The dimensional bar is 1 μm. The figure was taken from ref. [83]

sample had to be removed after each scan, but this was corrected as the technique was further improved [69, 70]. Its important feature is that conventional topography cannot be used to acquire a series of 2D images for subsequent 3D reconstruction as signals depending on the X- and Y-coordinates, since in actual life, a conventional atomic force microscopy image is already a 3D object. Therefore, such signals as phase, conductivity, magnetic response, etc. are used to acquire a 2D dataset.

This technique was used to reconstruct the structure of polymer composites [71, 72], as well as a human bone fragment [70] in the phase-contrast imaging mode (*Fig. 11*). The image was obtained after acquiring 19 scans in the phase-contrast imaging mode with etching in hydrochloric acid.

The most significant shortcoming of this method is related to etching, the process used to remove the material, making it impossible to study porous materials, as well as nanocomposites (for them, different reaction rates of the components cause distortions during surface scanning and, therefore, incorrect volume reconstruction). This drawback can be partially compensated for by using special data processing algorithms [70], but the final resolution will differ for some areas, having a negative effect on the analysis of the results.

Using an ultramicrotome is another approach to 3D SPM [73, 74]. The minimal section thickness depends on the ultramicrotome characteristics and is 20 nm for modern setups. It does not matter how the sample was immobilized: using polymer resin or by cryofreezing.

A device for conducting SPNT is shown in *Fig. 12*. It consists of the SPM scanning head attached by special hinges to the UTM knife holder. The design allows for two positions: for scanning (*Fig. 12*, right) and for measurements (*Fig. 12*, left). In the former position, the scanning head is moved away from the movable UTM console, which in turn moves to cut a section. In the latter position, the UTM console returns to its original state, the SPM is brought in, and the remaining specimen portion is scanned [73]. A similar approach has previously been described for SEM; it prevents mechanical distortions of the scanned object such as compression, stretching, and deformation.

The acquired series of successive SPM images are used for the reconstruction and imaging of 3D nanostructures in the bulk of the studied specimens. Application of different SPM measurement techniques allows one to collect information on morphology, as well as local electrical [75], mechanical [76], and many other properties. The technique enables reconstruction of the 3D distribution of nanoparticles in the bulk of nanomaterials [75, 76] and 3D topology of nanoporous structures [77–80].

In particular, the SPNT method can be efficiently used for 3D reconstruction of micro- and nanofiber cellular scaffolds based on biopolymers [81, 82] and determining their volumetric porosity, surface area to volume ratio, and other 3D morphology parameters. Reconstruction of the 3D structures of cell-engineered constructs allows one to study the topology and numerical morphological parameters of cells and cell–scaffold interfaces, which can act as indicators of the state and biological activity of the cells [83, 84].

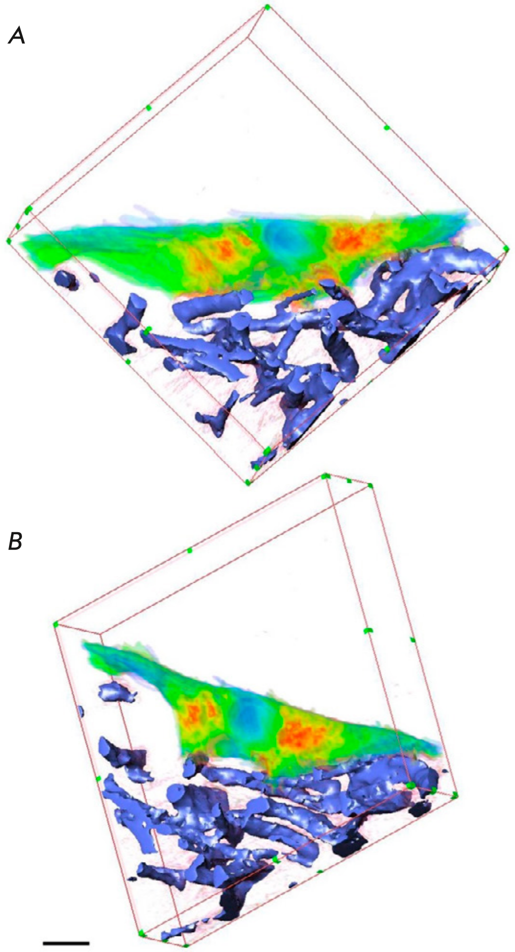

Fig. 14. Visualization of the 3D SPNT reconstruction of a fibroblast fragment (shown with green and red) and surrounding polyurethane fibers (blue), 23 sections 150 nm thick, reconstructed volume 32.0 × 32.0 × 3.3 μm, scale bar is 3 μm. The reconstructed fibroblast fragment is shown in two views (*A* and *B*). The measurements were carried out in the phase contrast mode under normal atmospheric conditions at room temperature. The figure was taken from ref. [84]

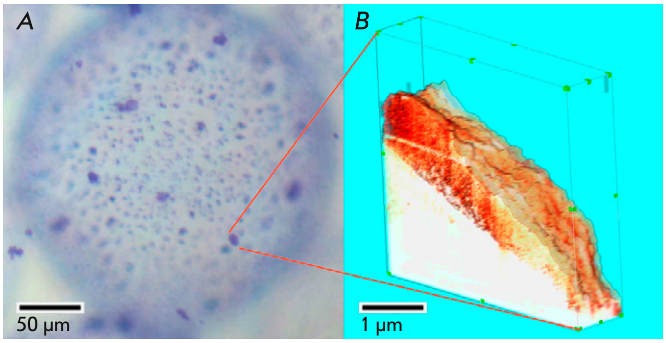

Fig. 15. Cryo-SPNT reconstruction of a single microparticle of the rat liver extracellular matrix on the surface of an alginate microcarrier performed at –120°C: (*A*) optical microscopy, Coomassie Brilliant Blue R-250 staining; (*B*) 3D cryo-SPM reconstruction of a single rat liver extracellular matrix microparticle obtained from 13 sequential cryo-SPM images of the microparticle surface on a spherical alginate microcarrier after successive 80-nm thick cryosections. The reconstructed volume is 5.0 × 5.0 × 1.1 μm. The resolution of each 2D SPM scan is 400 × 400 pixels. The pseudocolor palette corresponds to the phase shift of the SPM probe oscillations normalized to unity. The figure was taken from ref. [87]

Thus, the characteristic features of the interaction between neonatal rat cardiomyocytes and polymeric nanofiber matrices were revealed by SPNT: it was found that cardiomyocytes, unlike fibroblasts, completely envelop nanofibers in most cases, thus significantly increasing the area of the cell–fiber contact zone. *Figure 13* shows a 3D SPNT reconstruction of the region of a cardiomyocyte enveloping suspended polylactide nanofibers. A total of 54 segmented SPM images of the specimen surface were used for this 3D reconstruction. Each image was acquired sequentially after each UTM cut 120 nm thick [83].

Another example is the 3D structure of a fibroblast fragment shown in *Fig. 14* (primary human fibroblast culture) contacting several fibers of the microfibrillar polyurethane matrix to form the typical cell membrane protrusions partially enveloping the fibers [84].

In order to study soft biopolymeric materials and biological objects without embedding them into an epoxy medium, they need to be preliminarily frozen; for this purpose, we have designed a setup combining SPM and a cryo-ultramicrotome chamber [85]. This setup allows one to perform successive SPM measurements on the surface of frozen specimens immediately after cutting with a diamond cryo-ultramicrotome knife in the cryochamber. In this case, the measurements are performed in the semi-contact mode using cantilevers mounted on quartz resonators and not requiring an optical deflectometer to be used, which is important for working with a cryochamber. *Figure 15* shows the 3D cryo-SPNT reconstruction of a single microparticle of a rat liver extracellular matrix on the surface of an alginate

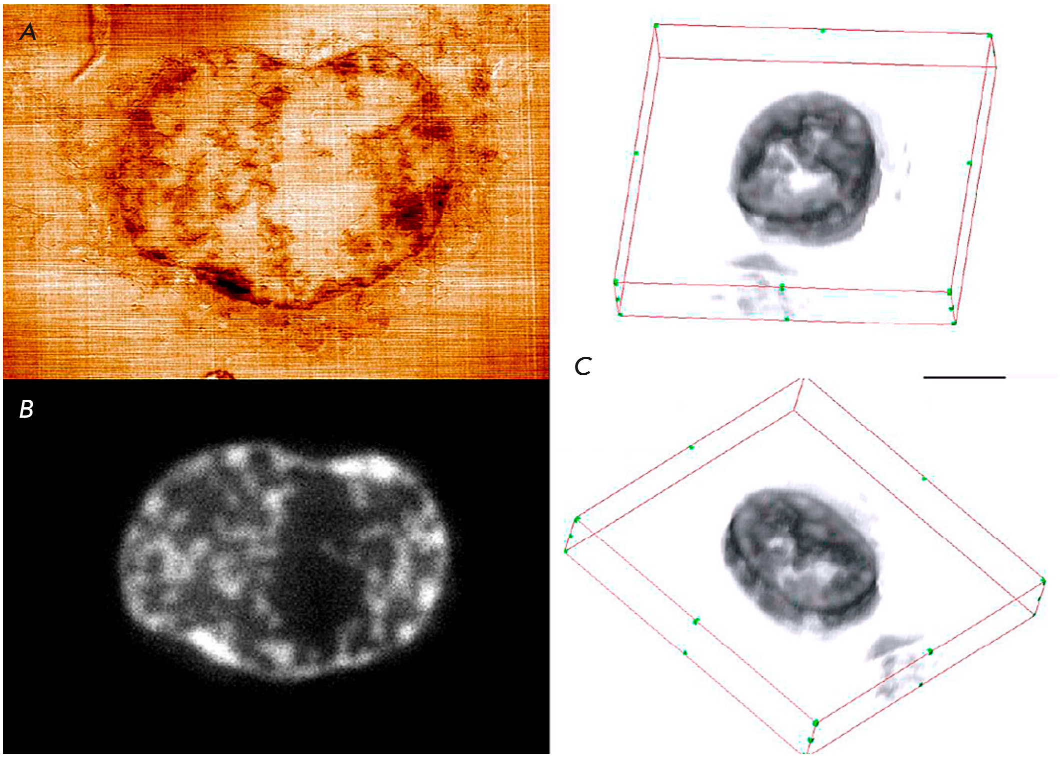

Fig. 16. Analysis of human breast adenocarcinoma MCF-7 cell samples with doxorubicin. (*A*) An SPM image of the topography of the cut surface of the MCF-7 cell, scan size 13.8 × 9.5 μm; height variation range, 33.5 nm; (*B*) fluorescent image of a cut of the same area of the MCF-7 cell; (*C*) 3D reconstruction of doxorubicin distribution in the volume of the MCF-7 cell sample, 22.5 × 18.7 × 2.4 μm; section thickness, 120 nm; the dimensional segment, 5 μm; visualization is presented in two views. The figure was taken from ref. [92]

microcarrier shown as an example of the operation of this setup performed at –120°C, since sectioning at higher temperatures disrupts the structure of hydrogel microcarriers [86, 87].

A detailed protocol for obtaining specimens of rat liver extracellular matrix microparticles was reported in ref. [86]. Using this protocol, cells were completely removed from the extracellular matrix, whose fragments were comminuted in liquid nitrogen; this procedure yielded extracellular matrix microparticles 1–5 μm in size. The resulting microparticles were then covalently crosslinked to alginate microspheres 200–300 μm in size (*Fig. 15A*).

Capabilities in analyzing the 3D nanostructures of biological objects can be substantially broadened by combining SPNT and high-resolution optical microscopy techniques, and fluorescence microscopy in particular, into a single correlative optical probe nanotomography technique [88–91], which can be implemented using a unique research setup (http://ckp-rf.ru/usu/486825/).

Figure 16 shows an example of correlative fluorescence and SPM images of an MSF-7 cell and visualization of the 3D reconstruction of the doxorubicin distribution in the cell based on the data obtained. The 3D reconstruction shows a coherent distribution structure that can be used as a successful measure of the employed 3D method. Resolution of the reconstruction along the Z coordinate (in the axial direction) corresponds to the section thickness (120 nm) in this case [92].

CONCLUSIONS

Among the 3D structural reconstruction methods discussed in this review, one cannot be singled out, as the best since each of these techniques has its own advantages and shortcomings.

The key advantage of electron microscopy-based methods is the very high spatial resolution (< 1 nm) and the possibility of acquiring images from significant depths thanks to the layer-by-layer scanning mode; however, the use of vacuum, as well as the electron and ion beams in them, can damage the specimen and alter the native structures of polymers and protein compounds. Furthermore, these methods provide no information other than sample morphology.

The STORM and STED optical methods have a lower spatial resolution (several nanometers), but they allow one to both conduct an ultrastructural analysis of a specimen and reconstruct the spatial distribution of target objects thanks to highly specific fluorescent immunostaining. Meanwhile, significant limitations are imposed on the size of the area being analyzed. Aberrations must be eliminated to obtain high-quality images, making it necessary to use complex optical systems.

Similar to EM, the application of scanning probe microscopes for 3D reconstruction allows one to reconstruct images of specimens with a large depth by removing some material, as well as obtain information on the chemical structure, electrical, and magnetic properties using the phase contrast method and special conductive, magnetic, or functionalized probes. Meanwhile, this technique is inferior to electron and optical microscopy in terms of lateral resolution.

Simultaneous use of SPM correlative measurement techniques and high-resolution fluorescence microscopy for the 3D reconstruction of the ultrastructure of biological objects is promising for enhancing the information value of the 3D data obtained (in particular, the 3D distributions of fluorescent markers and nanoscale morphological features). ●

This work was supported by the Russian Science Foundation (grant No. 22-14-00168), https://rscf.ru/project/22-14-00168/

REFERENCES

1. Franken L.E., Grünewald K., Boekema E.J., Stuart M.C.A. // Small. 2020. V. 16. № 14. P. e1906198.
2. Northover A.S., Keatley S., Elliot A.D., Hobbs R.P., Yang R., Lymbery A.J., Godfrey S.S., Wayne A.F., Thompson R.C.A. // Syst. Parasitol. 2019. V. 96. № 7. P. 553–563.
3. Bian K., Gerber C., Heinrich A., Müller D., Scheuring S., Jiang Y. // Nat. Rev. Meth. Primers. 2021. V. 1. № 1. P. 1–36. https://doi.org/10.1038/s43586-021-00033-2
4. Rust M.J., Bates M., Zhuang X. // Nat. Meth. 2006. V. 3. № 10. P. 793–795.
5. Hell S.W., Wichmann J. // Opt. Lett. 1994. V. 19. № 11. P. 780–782.
6. Schneider J.P., Hegermann J., Wrede C. // Histochem. Cell Biol. 2021. V. 155. № 2. P. 241–260.
7. Müller-Reichert T., Mancuso J., Lich B., McDonald K. // Meth. Cell Biol. 2010. V. 96. P. 331–361.
8. Borrett S., Hughes L. // J. Microscopy. 2016. V. 263. № 1. P. 3–9.
9. Bogers J., Nibbeling H., Deelder A., van Marck E. // J. Histochem. Cytochem. 1996. V. 44. № 1. P. 43–48.
10. Tokuyasu K.L. // J. Cell Biol. 1973. V. 57. P. 551–565.
11. Gay H., Anderson T.F. // Science. 1954. V. 120. № 3130. P. 1071–1073.
12. Miranda K., Girard-Dias W., Attias M., de Souza W., Ramos I. // Mol. Reprod. Dev. 2015. V. 82. P. 530–547.
13. Hegermann J., Wrede C., Fassbender S., Schliep R., Ochs M., Knudsen L., Mühlfeld C. // Am. J. Physiol. Lung Cell Mol. Physiol. 2019. V. 317. P. 778–784.
14. Kremer A., Lippens S., Bartunkova S., Asselbergh B., Blanpain C., Fendrych M., Goossens A., Holt M., Janssens S., Krols M. // J. Microscopy. 2015. V. 259. № 2. P. 80–96.
15. Harris K.M., Perry E., Bourne J., Feinberg M., Ostroff L., Hurlburt J. // J. Neurosci. 2006. V. 26. № 47. P. 12101–12103.
16. Peter G., Lee D. // J. Biophys. Biochem. 1958. V. 4. № 3. P. 345–349.
17. Aescht E., Büchl-Zimmermann S., Burmester A. Romeis Mikroskopische Technik. Berlin Heidelberg: Spektrum Akademischer Verlag, 2010. 551 p.
18. Saalfeld S., Fetter R., Cardona A., Tomancak P. // Nat. Meth. 2012. V. 9. № 7. P. 717–720.
19. Young S.L., Fram E.K., Craig B.L. // Am. J. Anatomy. 1985. P. 174–175.
20. Baena V., Schalek R.L., Lichtman J.W., Terasaki M. // Meth. Cell Biol. 2019. V. 152. P. 41–67.
21. Beike L., Wrede C., Hegermann J., Lopez-Rodriguez E., Kloth C., Gauldie J., Kolb M., Maus U. A., Ochs M., Knudsen L. // Lab. Invest. 2019. V. 99. № 6. P. 830–852.
22. Schalek R., Hayworth K., Kasthuri N., Morgan J.L., Berger D., Wilson A.M., Anger P., Aderhold D., Seung H.S., Lichtman J.W. // Microscopy Microanalysis. 2012. V. 18. P. 572–573.
23. Kasthuri N., Hayworth K., Berger D., Schalek R., Conchello J., Knowles-Barley S., Lee D., Vázquez-Reina A., Kaynig V., Jones T. // Cell. Cell Press. 2015. V. 162. № 3. P. 648–661.
24. Smith D., Starborg T. // Tissue Cell. 2019. V. 57. P. 111–122.
25. Titze B., Genoud C. // Biol. Cell. 2016. V. 108. № 11. P. 307–323.
26. Knott G., Rosset S., Cantoni M. // J. Visual. Exp. 2011. V. 53. e2588.
27. Schneider J.P., Wrede C., Mühlfeld C. // Int. J. Mol. Sci. 2020. V. 21. № 3. 1089.
28. Mühlfeld C., Wrede C., Molnár V., Rajces A., Brandenberger C. // Histochem. Cell. Biol. 2021. V. 155. № 2. P. 261–269.
29. McIntosh R., Nicastro D., Mastronarde D. // Trends Cell Biol. 2005. V. 15. № 1. P. 43–51.
30. Ni T., Frosio T., Mendonça L., Sheng Y., Clare D., Himes B.A., Zhang P. // Nat. Protoc. 2022. V. 17. P. 421–444.
31. Al-Amoudi A., Chang J., Leforestier A., McDowall A., Salamin L., Norlén L., Richter K., Blanc N., Studer D., Dubochet J. // EMBO J. 2004. V. 23. № 18. P. 3583–3588.
32. Dubochet J., McDowall A.W.V. // J. Microsc. 1981. V. 124. № 3. P. 3–4.
33. Saghi Z., Midgley P.A. // Ann. Rev. Materials Res. 2012.

V. 42. P. 59–79.
34. Neumüller J. // Wien Med. Wochenschr. 2018. V. 168. № 11–12. P. 322–329.
35. Ercius P., Alaidi O., Rames M.J., Ren G. // Adv. Materials. 2015. V. 27. № 38. P. 5638–5663.
36. Vanhecke D., Asano S., Kochovski Z., Fernandez-Busnadiego R., Schrod N., Baumeister W., Lučić V. // J. Microsc. 2011. V. 242. № 3. P. 221–227.
37. West J.B., Fu Z., Deerinck T.J., Mackey M.R., Obayashi J.T., Ellisman M.H. // Respir. Physiol. Neurobiol. 2010. V. 170. № 2. P. 202–209.
38. Höög J.L., Schwartz C., Noon A.T., O'Toole E.T., Mastronarde D.N., McIntosh J.R., Antony C. // Dev. Cell. 2007. V. 12. № 3. P. 349–361.
39. Lučić V., Förster F., Baumeister W. // Annu. Rev. Biochem. 2005. V. 74. P. 833–865.
40. Gan L., Jensen G.J. // Quarterly Rev. Biophys. 2012. V. 45. № 1. P. 27–56.
41. Frey T.G., Perkins G.A., Ellisman M.H. // Annu. Rev. Biophys. Biomol. Struct. Annu. Rev. 2006. V. 35. № 1. P. 199–224.
42. Zipfel W.R., Williams R.M., Webb W.W. // Nat. Biotechnol. 2003. V. 21. № 11. P. 1369–1377.
43. Gugel H., Bewersdorf J., Jakobs S., Engelhardt J., Storz R., Hell S.W. // Biophys. J. 2004. V. 87. № 6. P. 4146–4152.
44. Min Gu. Principles of Three-Dimensional Imaging in Confocal Microscopes. Singapore: World Scientific Publishing Co Pte Ltd, 1996. 352 p.
45. Huang B., Wenqin W., Bates M., Zhuang X. // Science. 2008. V. 319. № 5864. P. 807–810.
46. Skvortsov A.V. Delaunay triangulation and its application. Tomsk: University Press, 2002. 128 p.
47. Yildiz A., Forkey J.N., McKinney S.A., Ha T., Goldman Y.E., Selvin P.R. // Science. 2003. V. 300. № 5628. P. 2061–2065.
48. Rust M.J., Bates M., Zhuang X. // Nat. Meth. 2006. V. 3. № 10. P. 793–795.
49. Betzig E., Patterson G., Sougrat R., Lindwasser W., Olenych S., Bonifacino J., Davidson M., Lippincott-Schwartz J., Hess H. // Science. 2006. V. 313. № 5793. P. 1642–1645.
50. Heilemann M., van de Linde S., Schüttpelz M., Kasper R., Seefeldt B., Mukherjee A., Tinnefeld P., Sauer M. // Angewandte Chemie. 2008. V. 47. № 33. P. 6172–6176.
51. Vogelsang J., Cordes T., Forthmann C., Steinhauer C., Tinnefeld P. // Proc. Natl. Acad. Sci. USA. 2009. V. 106. № 20. P. 8107–8112.
52. Cordes T., Strackharn M., Stahl S.W., Summerer W., Steinhauer C., Forthmann C., Puchner E.M., Vogelsang J., Gaub H.E., Tinnefeld P. // Nano Lett. 2010. V. 10. № 2. P. 645–651.
53. Jungmann R., Avendaño M., Woehrstein J., Dai M., Shih W., Yin P. // Nat. Meth. 2014. V. 11. № 3. P. 313–318.
54. Sharonov A., Hochstrasser R. // Proc. Natl. Acad. Sci. USA. 2006. V. 103. № 50. P. 18911–18916.
55. Holtzer L., Meckel T., Schmidt T. // Appl. Phys. Lett. 2007. V. 90. № 5. 053902.
56. Bates M., Huang B., Dempsey G.T., Zhuang X. // Science. 2007. V. 317. P. 1749–1753.
57. Bianchini P., Peres C., Oneto M., Galiani S., Vicidomini G., Diaspro A. // Cell Tissue Res. 2015. V. 360. № 1. P. 143–150.
58. Galiani S., Harke, B., Vicidomini G., Lignani G., Benfenati F., Diaspro A., Bianchini P., Vicidomini G., Moneron G., Han K. // Proc. Natl. Acad. Sci. USA. 2010. V. 143. № 7. P. 3361–3371.
59. Klar T., Jakobs S., Dyba M., Egner A., Hell S. // Proc. Natl. Acad. Sci. USA. 2000. V. 97. № 15. P. 8206–8210.
60. Willig K., Keller J., Bossi M., Hell S. // New J. Phys. 2006. V. 8. № 6. 106.
61. Wildanger D., Medda R., Kastrup L., Hell S. // J. Microsc. 2009. V. 236. № 1. P. 35–43.
62. Harke B., Ullal C., Keller J., Hell S. // Nano Lett. 2008. V. 8. № 5. P. 1309–1313.
63. Willig K., Harke B., Medda R., Hell S. // Nat. Meth. 2007. V. 4. № 11. P. 915–918.
64. Finzel L., Reuss M. // Micros. Today. 2022. V. 30. № 4. P. 26–33.
65. Heine J., Wurm C.A., Keller-Findeisen J., Schönle A., Harke B., Reuss M., Winter F.R., Donnert G. // Rev. Sci. Instr. 2018. V. 89. № 5. P. 053701.
66. Gwosch C.C., Pape J.K., Balzarotti F., Hoess P., Ellenberg J., Ries J., Hell S.W. // Nat. Meth. 2020. V. 17. № 2. P. 217–224.
67. Schmidt R., Weihs T., Wurm C.A., Jansen I., Rehman J., Sahl S.J., Hell S.W. // Nat. Commun. 2021. V. 12. № 1. P. 1478.
68. Magerle R. // Phys. Rev. Lett. 2000. V. 85. № 13. P. 2749.
69. Hund M., Herold H. // Rev. Sci. Instr. 2007. V. 78. № 6. 063703.
70. Dietz C., Röper S., Scherdel S., Bernstein A., Rehse N., Magerle R. // Rev. Sci. Instr. 2007. V. 78. № 5. 053703.
71. Rehse N., Marr S., Scherdel S., Magerle R. // Adv. Materials. 2005. V. 17. № 18. P. 2203–2206.
72. Liedel C., Hund M., Olszowka V., Böker A. // Soft Matter. 2012. V. 8. № 4. P. 995–1002.
73. Efimov A., Tonevitsky A., Dittrich M., Matsko N. // J. Microsc. 2007. V. 226. № 3. P. 207–216.
74 Efimov A., Agapov I., Agapova O., Oleinikov V., Mezin A., Molinari M., Nabiev I., Mochalov K. // Rev. Sci. Instr. 2017. V. 88. № 2. P. 023701.
75. Alekseev A., Efimov A., Lu K., Loos J. // Adv. Materials. 2009. V. 21. № 48. P. 4915–4919.
76. Alekseev A., Efimov A., Loos J., Matsko N., Syurik J. // Eur. Polymer J. 2014. V. 52. № 1. P. 154–165.
77. Mochalov K., Efimov A., Bobrovsky A., Agapov I., Chistyakov A., Oleinikov V., Sukhanova A., Nabiev I. // ACS Nano. 2013. V. 7. P. 8953–8962.
78. Efimov A., Agapova O., Mochalov K., Agapov I. // Physics Procedia. 2015. V. 73. P. 173–176.
79. Efimov A., Moisenovich M., Bogush V., Agapov I. // RSC Adv. Royal Soc. Chem. 2014. V. 4. № 105. P. 60943–60947.
80. Efimov A.E., Agapov I.I. // Bulletin of transplantology and artificial organs. 2014. V. 16. № 3. P. 109–116.
81. Safonova L., Bobrova M., Efimov A., Lyundup A., Agapova O., Agapov I. // Pharmaceutics. 2021. V. 13. P. 1561.
82. Safonova L., Bobrova M., Efimov A., Davydova L., Tenchurin T., Bogush V., Agapova O., Agapov I. // Pharmaceutics. 2021. V. 13. P. 1704.
83. Balashov V., Efimov A., Agapova O., Pogorelov A., Agapov I., Agladze K. // Acta Biomater. 2018. V. 68. P. 214–222.
84. Efimov A.E., Agapova O.I., Safonova L.A., Bobrova M.M., Parfenov V.A., Koudan E.V., Pereira F.D.A.S., Bulanova E.A., Mironov V.A., Agapov I.I. // Express Polym. Lett. 2019. V. 13. P. 632–641.
85. Efimov A.E., Gnaegi H., Schaller R., Grogger W., Hofer F., Matsko N. // Soft Matter. 2012. V. 8. № 38. P. 9756–9760.
86. Efimov A.E., Agapova O.I., Safonova L.A., Bobrova

M.M., Volkov A.D., Khamkhash L., Agapov I.I. // RSC Adv. 2017. V. 7. P. 8808–8815.
87. Efimov A., Agapova O., Safonova L., Bobrova M., Agapov I. // Russian Journal of Transplantology and Artificial Organs. 2017. V. 19. № 4. P. 78–87.
88. Efimov A.E., Agapov I.I., Agapova O.I., Oleinikov V.A., Mezin A.V., Molinari M., Nabiev I., Mochalov K.E. // Rev. Sci. Instrum. 2017. V. 88. P. 023701.
89. Mochalov K.E., Chistyakov A.A., Solovyeva D.O., Mezin A.V., Oleinikov V.A., Vaskan I.S., Molinari M., Agapov I.I., Nabiev I., Efimov A.E. // Ultramicroscopy. 2017. V. 182. P. 118–123.
90. Efimov A.E., Bobrovsky A.Y., Agapov I.I., Agapova O.I., Oleinikov V.A., Nabiev I.R., Mochalov K.E. // Technical Physics Lett. 2016. V. 42. № 2. P. 171–174.
91. Agapova O.I., Efimov A.E., Safonova L.A., Bobrova M.M., Agapov I.I., Gautier S.V. // Dokl Biochem Biophys. 2021. V. 500. № 1. P. 331–334.
92. Agapova O.I., Efimov A.E., Mochalov K.E., Solovyova D.O., Gileva A.M., Markvicheva E.A., Yakovlev D.V., Lundup A.V., Oleinikov V.A., Agapov I.I., Gauthier S.V. // Dokl Biol Sci. 2023. V. 509. № 1. P. 103–106.

Streptomyces phaeochromogenes BV-204, K-1115A Anthraquinone-Producing Strain: A New Protein Biosynthesis Inhibitor

A. R. Belik[1], Yu. V. Zakalyukina[1,2], V. A. Alferova[3], Y. A. Buyuklyan[1], I. A. Osterman[1,4], M. V. Biryukov[1,2*]
[1]Sirius University of Science and Technology, Sochi, 354340 Russian Federation
[2]Lomonosov Moscow State University, Moscow, 119234 Russian Federation
[3]Shemyakin–Ovchinnikov Institute of Bioorganic Chemistry, Moscow, 117997 Russian Federation
[4]Skolkovo Institute of Science and Technology, Moscow, 121205 Russian Federation
*E-mail: metrim@gmail.com

Received: November 02, 2023; in final form, January 16, 2024
DOI: 10.32607/actanaturae.27315

ABSTRACT **In the search for new antibiotics, it is a common occurrence that already known molecules are "rediscovered" while new promising ones remain unnoticed. A possible solution to this problem may be the so-called "target-oriented" search, using special reporter microorganisms that combine increased antibiotic sensitivity with the ability to identify a molecule's damaging effect. The use of such test organisms makes it possible to discover new promising properties even in known metabolites. In this study, we used a high-throughput screening method based on the pDualrep2 dual reporter system, which combines high sensitivity through the use of modified strains of test organisms and makes it possible to easily and accurately identify the interaction mechanisms of a substance and a bacterial cell at the initial stages of screening. This reporter system is unknown in Russia and is significantly superior to its global analogues. In the system, translation inhibition induces the expression of the fluorescent protein Katushka2s, while DNA damage is induced by TurboRFP. Using pDualrep2, we have isolated and described BV-204, an** ***S. phaeochromogenes*** **strain producing K-1115A, the biologically active substance that we have previously described. In our study, K-1115A for the first time has demonstrated antibiotic activity and an ability to inhibit bacterial translation, which was confirmed** ***in vitro*** **in a cell-free translation system for FLuc mRNA. K-1115A's antibacterial activity was tested and confirmed for** ***S. aureus*** **(MRSA) and** ***B. subtilis*****, its cytotoxicity measured against that for the HEK293 cell line. Its therapeutic index amounted to 2 and 8, respectively. The obtained results open up prospects for further study of K-1115A; so, this can be regarded as the basis for the production of semi-synthetic derivatives with improved therapeutic properties to be manufactured in dosage forms.**

KEYWORDS **actinomycetes, K-1115A, antibiotics, reporter system pDualrep2, inhibition of protein biosynthesis, in vitro translation, citizen science.**

ABBREVIATIONS **BGC – biosynthetic gene cluster; CF – culture fluid; SPE – solid phase extraction; MIC – minimum inhibitory concentration; CMSA – chromatography-mass spectrometric analysis; HPLC – high-efficiency liquid chromatography; LPS – lipopolysaccharide; FLuc mRNA – messenger RNA encoding firefly luciferase.**

INTRODUCTION

Pathogens becoming more resistant to antibiotics is one of the most pressing problems of modern medicine, because the potential of the molecules already found and long ago introduced into medical practice is now almost exhausted, and the rate of discovery of new ones has significantly slowed compared to what it was during the "Golden Age" of antibiotics in the middle of the twentieth century. Most antibiotics discovered during large-scale screening [1–3] turn out to be "rediscoveries" of previously discovered molecules, but the new tools for investigating action mechanisms have enabled us to look at these substances from a new angle and discover new potential in them [4–6].

Such new tools are target-based screening and the methods for determining the action mechanism of a molecule at the initial stages of research. These tools allow one to focus a search on the antibacterial agents specific to the most promising targets and may even accelerate molecule identification. Currently, we are successfully utilizing a reporter system in which compounds that inhibit protein or DNA biosynthesis are detected by fluorescent protein reporter gene expression in response to this inhibition. The relevance of this approach lies in that a ribosome is a key element in the functioning of a living cell, and considering the significant differences in the structures of the ribosomes of pro- and eukaryotes, it creates an opportunity to produce a highly specific effect on bacterial ribosomes and significantly increase the chances of developing drugs with good therapeutic properties.

Actinomycetes of the genus *Streptomyces* are the richest source of biologically active substances and produce approximately 50% of the antibacterial substances used in pharmaceutics [7–9]. Actinomycetes are among the prokaryotes of the largest genomes and have a large coding potential imparting a structural diversity to the secondary metabolites they produce. Tens of thousands of such molecules have been described so far, and even “rediscovered” ones often show new, unique properties.

Previously, thanks to the mentioned reporter system, we were able to establish the action mechanism of tetracenomycin X [10], a molecule whose antibacterial properties were first described in the 1960s. Tetracenomycin X has a structure similar to that of doxorubicin, so it was believed that its effect was also based on intercalation into the double-stranded DNA structure. But our study showed that this molecule inhibits protein biosynthesis by interacting with the ribosome in a new, previously unexplored binding center, giving hope that new, promising semi-synthetic derivatives may be developed from it.

In the present study, we detected a strain producing K-1115A, a substance whose antibacterial action mechanism is based on protein biosynthesis inhibition. This was confirmed by a test in a cell-free translation system. The results obtained have allowed us to conclude that the substance acts as an inhibitor of protein biosynthesis.

EXPERIMENTAL

Microorganisms sampling, isolation and culturing

S. phaeochromogenes BV-204 was isolated from soil samples collected at the Sirius Federal Territory. The samples were collected in the spring of 2021 in a park area on the Black Sea coast (43°23’53.7″N 39°57’48.2″E). Sampling was carried out following the method described in [11, 12]. The top layer of the soil (0–5 cm) was removed with a sterile spatula and placed in a sterile specimen collection container. Actinobacteria were isolated by surface seeding on agarized nutrient media from serial dilutions of soil suspensions as per [13]. ISP3 [13] combined with nystatin (250 μg/mL) and nalidixic acid (10 μg/mL) was used as a nutrient medium to inhibit the development of fungi and Gram-negative bacteria, respectively. The culture was incubated for 14 days at 28°C.

Strain BV-204 was selected on the basis of morphological characters, isolated in pure culture from primary inoculation on the Gauze 1 mineral agar for micromorphological studies [14]. For *in vitro* maintenance, the strain was cultured on the ISP3 medium; for long-term storage, it was grown in a liquid ISP3 medium for 14 days with constant stirring (200 rpm at 28°C), and then the resulting suspension was mixed with an equal volume of a 50% glycerol solution and frozen in liquid nitrogen; the samples were stored at -80°C.

Polyphase strain identification

The culture attributes of the strain (presence and color of aerial mycelium, release of soluble pigments) were evaluated on dense media recommended by the International Streptomyces Project (ISP) after 14 days of cultivation at 28°C [15]. The morphological characteristics (presence and shape of reproductive spore chains, character of the spore surface) were evaluated using a Zeiss Axiolab A1 light Zeiss (Carl Zeiss Microscopy GmbH, Germany) and a scanning electron microscope JSM-6380LA (JEOL Ltd., Japan) after 14 days of growth at 28°C in the ISP3 medium. The samples for electron microscopy were prepared as described in [16]. The utilization of carbon sources (mono- and polysaccharides, alcohols) was evaluated on a ISP9 mineral agar with the addition of bromocresol purple at 28°C during 14 days [15]; the ability to degrade starch, cellulose, and casein by the size of polymer hydrolysis zones, as per [17, 18]. The sensitivity to different antibiotics was determined using antibiotic-impregnated paper disks (HiMedia Laboratories Pvt. Ltd., India).

Whole-genome sequencing, phylogenetic analysis and BGC analysis

DNA from the producer strain was isolated as per [19]. The genome of strain BV-204 was sequenced *de novo* on an Illumina HiSeq 4000 platform (Illumina, USA) and assembled using SPAdes v3.13.0 [20]. It was annotated using the RASTtk pipeline based on the PATRIC web service [21]. The genome’s integrity and quality, as well as average nucleotide identity (ANI), were assessed using the MiGA web service (http://microbial-genomes.org). Its phylogenetic affiliation was investigated using full-genome sequencing on the Type (Strain) Genome Server (TYGS) (https://tygs.dsmz.de/). The genome was automatically compared to all the genomes represented in the TYGS database using the MASH algorithm [22]. Its phylogenetic tree was obtained using FastME 2.1.6.1 based on GBDP distances calculated from the genome's nucleotide sequences. The branch lengths were scaled by applying the GBDP d5 distance formula [23]. The BGCs of its bioactive compounds were identified using the bacterial version of the antiSMASH 6.1.0 browser (https://antismash.secondarymetabolites.org). Homologous regions in each genome were identified using NCBI Blastn (https://blast.ncbi.nlm.nih.gov).

Antimicrobial action screening

The primary antibacterial activity was determined on *E. coli* BW25113, whose codons 330–352 of the lptD gene were deleted, so it is hereinafter referred to as *E. coli* SS_lptd. This mutation leads to disruption of the normal lipopolysaccharide envelope synthesis of Gram-negative bacteria, making it more permeable to low molecular weight compounds [11]. The strain contains the pDualrep2 plasmid [10]. In the presence of DNA replication or protein biosynthesis inhibitors, the strain expresses the fluorescent protein TurboRFP or Katushka2S (Supplementary, *Fig. S*7). Screening was performed by the agar diffusion method described previously [16]. Along with other strains, strain BV-204 was grown on ISP3 and tested on days 3, 6, and 9; for this purpose, a 5-mm-diameter agar block was cut from a lawn area with distinct growth and placed on cups containing an agarized LB medium pre-cultured with the test organisms. The fluorescent signal was detected the next day after culturing using a ChemiDoc MP (Bio-Rad) in SU 3 and SU 5 channels. To study the strain's action spectrum, BV-204 was tested on other test organisms, such as *S. aureus* ATCC 29213, *S. aureus* ATCC 25923, *S. aureus* SS01, *S. aureus* (MRSA) INA00761, *B. subtilis* ATCC 6633, *C. albicans* CBS 8836, and *M. smegmatis* Ac-1171. The antibacterial activity was evaluated by applying the agar diffusion technique described above. To form a bacterial lawn, an Agarized LB medium was utilized. As for yeast, it was glucose-peptone-yeast agar [24], incubated at 37°C for 24 h to evaluate the size of growth suppression zones.

Separation and identification of active components

Initial screening established BV-204 ability to exhibit antagonistic activity when grown on the ISP3 medium. To obtain the CF containing the active ingredient, the strain was cultured on a ISP3 liquid nutrient medium (7 days, 28°C in a New Brunswick Innova shaker (Eppendorf) at 200 rpm). The CF was separated from the biomass by centrifugation at 4, 000 g, concentrated and purified by SPE. For this purpose, CF was applied to a Poly-Prep Econo-Pac chromatographic column (Bio-Rad) containing 1 ml of LPS-500H sorbent (Tekhnosorbent, Russia), then eluted with a stepwise gradient of water-acetonitrile (v/v) for fractional collection of the eluate. The antagonistic activity of the collected fractions was investigated, and their active fractions were purified using HPLC.

HPLC analysis and fractionation were performed in a Vanquish Flex system with a diode array detector (Thermo Fisher Scientific, USA) equipped with a 5 μm C18(2) 100 Å, 250 × 4.6 mm Luna column (Phenomenex), flow rate 1 mL/min, injection volume 20 μL. A 0.1% aqueous THF solution was used as eluent A and acetonitrile with 0.1% THF as eluent B. Elution was performed by increasing the eluent B concentration from 25 to 95% for 10 min and then maintaining it at 95% for 2 min. Fractions of 1 mL were collected to analyze their antibacterial activity (*Fig. S8*).

The active fractions were analyzed using a UltiMate 3000 chromatograph (Thermo Fisher Scientific, USA) equipped with an Acclaim RSLC 120 C18 2.2 μm 2.1 × 100 mm column (Thermo Fisher Scientific) and an amaXis II 4G ETD qTof-mass spectrometer (Bruker Daltonics). Measurements were performed in the 100–1,500 m/z spectrum recording mode to register the three most intense ions, dissociation type CID 10–40 eV, in nitrogen. The mass spectra were analyzed using OpenChrom Lablicate Edition (1.4.0.202201211106), TOPPView v.2.6.0 [25]. Chemical structures were identified using the GNPS [26], NPAtlas [27, 28], and the Dictionary of Natural Products 31.1 databases.

The active HPLC fraction (1 mL) was concentrated using a CentriVap vacuum bioconcentrator (Labconco) and dissolved in 500 μL of a 10% aqueous DMSO solution; the resulting solution was referred to as the "antibiotic working solution."

Translation inhibition *in vitro*

Translation suppression was studied in a cell-free system using a commercial *E. coli* T7 S30 Extract System for Circular DNA kit (Promega) as per the manufacturer's instructions. The Antibiotic solution (0.5 μL) was added to the reaction mixture (4 μL) followed by 0.5 μL of 200 ng/μL FLuc mRNA and incubated for 1 h at 37°C.

The luciferase activity was measured by chemiluminescence intensity at a wavelength of 580(80) nm using the Luciferase Assay Reagent kit (Promega) in a ClarioStar plate reader (BMG Labtech).

MIC and cytotoxicity

Overnight cultures of *E. coli* SS_lptd, *S. aureus* INA00761 (MRSA), *S. aureus* SS01, and *B. subtilis* ATCC 6633 were diluted with a fresh LB medium to OD_{600} = 0.6, and then the resulting inoculum was diluted 1,000-fold to obtain a working suspension. Some 100 µl of the suspension was added to the wells of a sterile 96-well plate, except for the first and last rows. The first row was filled with 180 µl of the suspension each, and the last row was filled with 100 µl of a sterile nutrient medium to be used as a negative control. Then, 20 µl of the antibiotic solution was added to the first row of the plate and a series of twofold dilutions were obtained by sequentially transferring 100 µl from the well of one row to the well of the next row. The penultimate row, where no antibiotic was delivered, was used as a positive control. The plate was then incubated under stirring (200 rpm, 37°C). Cell growth was recorded in 24 h at a wavelength of 590 nm in the ClarioStar tablet reader. The substance concentration completely suppressing bacterial growth was considered as MIC.

To determine the cytotoxicity, the cell lines were prepared as per [29]. The HEK293 cells were cultured on the DMEM nutrient medium containing 10% FBS, 4 mM of L-glutamine, and 4.5 g/L of glucose. A row of prepared microcentrifuge tubes was filled with 100 µl of the nutrient medium each, then 80 µl of the medium and 20 µl of the antibiotic solution were added to the first tube, followed by two-fold serial dilutions, transferring 100 µl each from the first tube to the second tube and then throughout the row. Double dilutions of doxorubicin ranging from 75.9 to 0.16 µM were used as negative controls; a number of wells with cells without antibiotics were left as positive controls. The contents of the tubes were transferred to the corresponding wells of a pre-arranged plate with cells and incubated for 3 days in a CO_2 incubator at 37°C. After the incubation, 20 µL of a resazurin solution (0.15 mg/mL) was added to the wells containing a nutrient medium, stirred by rocking to distribute the dye evenly and incubated in a CO_2 incubator at 37°C for 3 h. Fluorescence intensity was then measured in the ClarioStar plate reader (Ex = 545 nm, Em = 600 nm).

RESULTS

Genetic and phylogenetic analyses

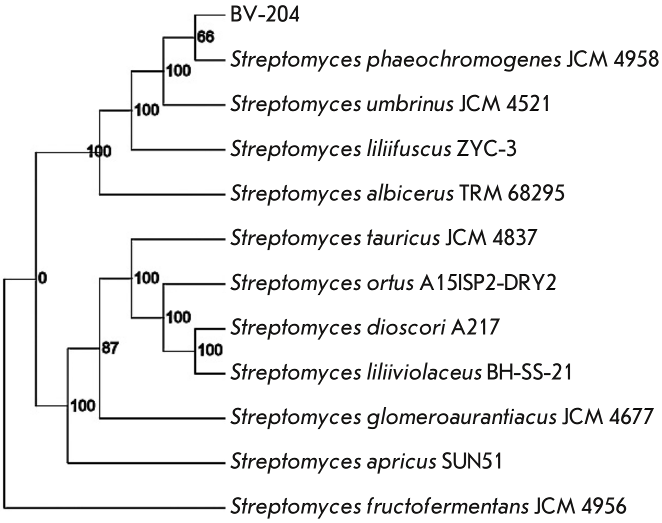

Fig. 1. Phylogenetic tree based on the complete genome of *S. phaeochromogenes* BV-204. The bootstrap analysis values are above 60%

The results of full-genome sequencing and subsequent assembly demonstrated the genome size of BV-204 cells to be typical for representatives of the genus *Streptomyces* [30] and comprised 11,380,121 bp at the G+C content of 70.2%. Phylogenetic analysis showed that BV-204 clustered most closely with *S. phaeochromogenes* JCM 4958 (formerly *S. ederensis* JCM 4958) and together with it, as well as with *S. umbrinus* JCM 4521, *S. liliifuscus* ZYC-3, and *S. albicerus* TRM 68295, formed a monophyletic group with a maximum branching support value of 100% (*Fig. 1*).

Phenotypic and morphological properties of BV-204

The strain is a Gram-positive aerobic bacterium with immobile cells growing actively on the ISP2 and ISP3 and moderately on the ISP5 and ISP6 nutrient media. The substrate mycelium coloration varies from dark-brown to beige, the aerial mycelium is pale with pink shades, and no aerial mycelium is formed on the ISP6 medium. In addition, the strain growing on the ISP3 medium produces a dark brown soluble pigment (Supplementary, *Table S1*).

BV-204 cells have the same spectrum of carbohydrate utilization as previously described *S. phaeochromogenes* JCM 4958(T) and *S. umbrinus* JCM 4521: they show no differences in their ability to utilize mono-, disaccharides, and alcohols. We also found that BV-204 was able to hydrolyze carboxymethylcellulose; i.e., this strain possesses cellulase activity not previously encountered in other representatives of this taxon (Supplementary, *Table S2*).

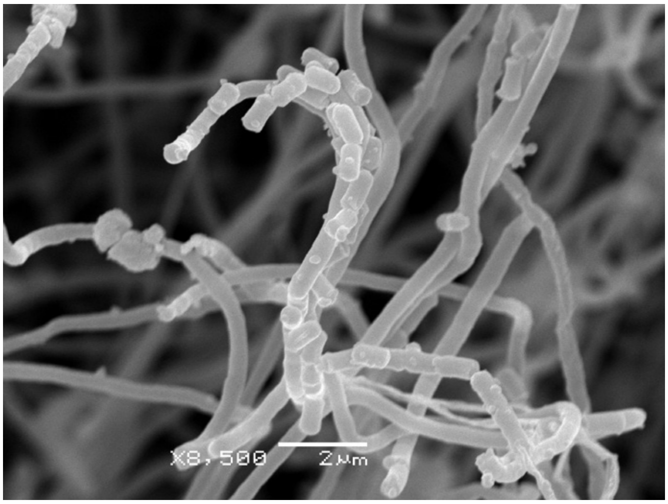

Fig. 2. Electron micrography of *S. phaeochromogenes* BV-204 on the 14th day of incubation on the ISP3 medium at 28°C. The dimensional cutoff is 2 μm

BV-204 forms straight, long chains of spores with a smooth surface, typical for strains of its kind [14] (*Fig. 2*).

Therefore, the results of the phylogenetic analysis based on the polyphasic taxonomic approach and comparison of phenotypic traits enabled us to assign BV-204 to the species *S. phaeochromogenes.*

Antibacterial activity

Initial screening revealed the strain's antibacterial activity against *E. coli* SS_lptd pDualrep2. The substance secreted by the producer induced Katushka2S expression that could possibly inhibit protein synthesis (*Fig. 3*). As positive controls, we used 0.05 μg of erythromycin (protein biosynthesis inhibitor) inducing Katushka2S expression, and 1 ng of norfloxacin (DNA gyrase inhibitor) inducing TurboRFP expression. For convenience, the Katushka2S and TurboRFP signals were visualized in respective red and green by the ChemiDoc MP software. In *E. coli* JW5503 ΔtolC pDualrep2 no inhibition or induction of reporter fluorescent proteins was registered.

BV-204 was found to inhibit the growth of Gram-positive bacteria *B. subtilis* ATCC 6633, *S. aureus* SS01, and *S. aureus* INA00761 (MRSA); however, it did not inhibit *S. aureus* ATCC 29213, *S. aureus* ATCC 25923, *C. albicans* CBS8836, or *M. smegmatis* Ac-1171. Both the agarized and liquid ISP3 media were deemed optimal for the strain to synthesize active metabolites.

Active substance identification

Pure active metabolites were obtained by solid-phase extraction from *S. phaeochromogenes* BW-204 CF and detected in fractions containing 30–40% acetonitrile. The fractions were concentrated and subjected to further separation and fractionation by HPLC. The activity was found to be associated with a component eluted at 9.47 min (Supplementary, *Figs. S10* and *S11*) and with absorption maxima at 276 and 407 nm. CMS analysis of this substance showed that it almost did not get ionized in the positive ion detection mode but yielded an intense [M–N] adduct corresponding to an accurate mass of 326.0805 Da (Supplementary, *Fig. S12*). Considering the characteristic absorption spectrum of the isolated compound in the NPAtlas, Dictionary of Natural Products, and PubChem databases, a candidate with the gross formula C18H14O (accurate mass 326.0790, deviation 4.5 m.d.) and the structural formula shown in *Fig. 4* was found.

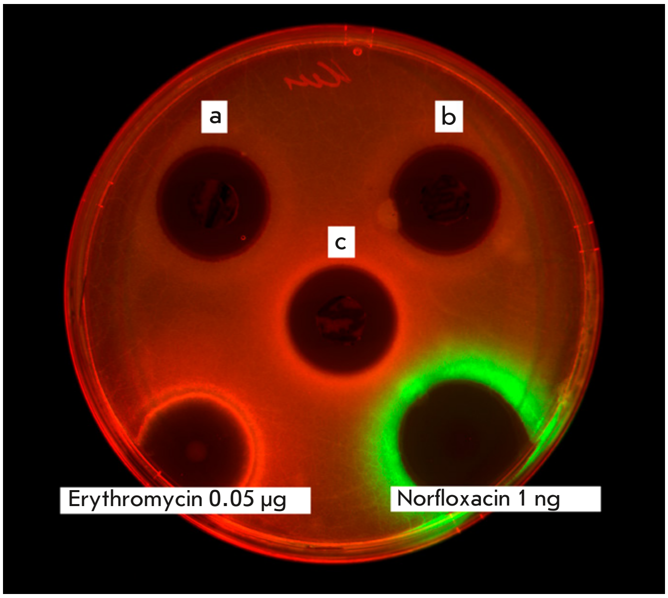

Fig. 3. Activity of the agar blocks containing *S. phaeochromogenes* BV-204 in the presence of *E. coli* lptd pDualrep2 on (a) the 3rd, (b) 6th, (c) and 9th days of growth

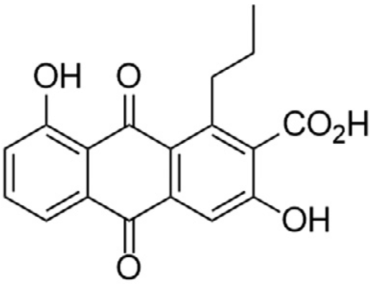

Fig. 4. Structure of the identified active component K-1115A (3,8-dihydroxy-9,10-dioxo-1-propylanthracene-2-carboxylic acid)

As alnumycin, K-1115A is of biosynthetic origin and produced by streptomycetes [31]. The fragmentation spectrum of the adduct with *m/z* 325.07 showed a major fragment ion [M–44] with *m/z* 281.08, consistent with the carboxyl group present in the molecule.

Inhibition of protein biosynthesis by K-1115A *in vitro*

The ability of the HPLC-purified fraction of K-1115A to inhibit cell-free translation was investigated with erythromycin used as a reference translation inhibitor. The experiments were carried out in triplicate; the results of determining the dose-effect concentration dependence are presented in *Fig. 5*. The EC_{50} values were 0.004 and 0.606 μg/mL for erythromycin and K-1115A, respectively.

BGC analysis

The bioinformatic methods applied enabled us to detect alnumycin BGC in the genome of BV-204 with K-1115A as a bypass product, which was homologous to the gene cluster previously annotated in *Streptomyces* sp. CM020 (*Fig. 6*) [32]. The BGC contains 32 open reading frames that may participate in the biosynthesis of alnumycin and K-1115A. It presumably consists of 22 structural and 10 regulatory and transport genes. The cluster's total length is 31,030 bp. The antibiotic is synthesized by a type-II polyketide synthase.

DISCUSSION

The genus *Streptomyces* is the most extensive among actinomycetes, so most of the known and clinically relevant antibiotics, starting from streptomycin, have been isolated from the members of this taxon. Through the efforts of numerous scientific teams, data on tens of thousands of compounds exhibiting antagonistic activity had been published by 1980; most of them, however, were not fully characterized due to the limited methodological base of that time. One such compounds turned out to be K-1115A produced by the BV-204 strain that we detected during a large-scale citizen-science screening using the pDualrep2 target-based reporter system.

The BV-204 producer strain, attributed from a polyphase analysis to the *S. phaeochromogenes* species, demonstrated the ability to inhibit model strains and cause induction of a reporter system, suppressing protein synthesis when grown on an oat medium.

Successive stages of CF solid-phase extraction followed by HPLC fractionation resulted in the isolation of the pure active substance. Subsequent CMSA suggested K-1115A (3,8-dihydroxy-9,10-dioxo-1-propylanthracene-2-carboxylic acid) as a candidate, as evidenced by the exact mass match and characteristic UV spectrum consistent with previously published data [33]. The bioinformatic analysis revealed that the BV-204 genome had a BGC responsible for the production of alnumycin and other related substances, including K-1115A, which also confirmed the strain's ability to synthesize K-1115A. Moreover, the antibacterial activity of K-1115A had not been previously reported.

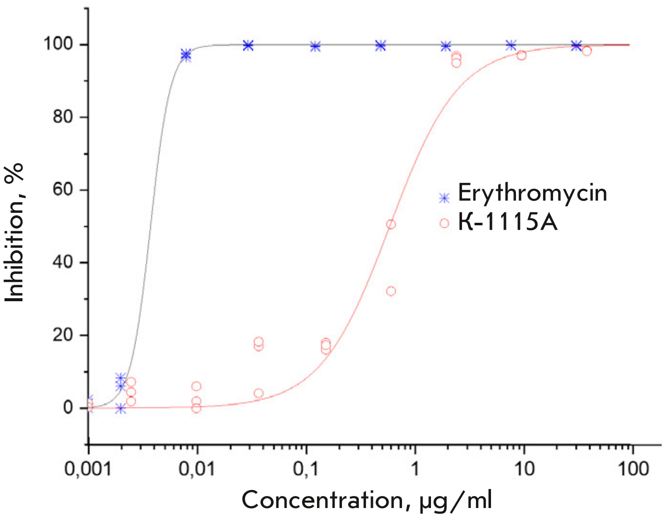

Fig. 5. *In vitro* inhibition of luciferase gene translation by K-1115A and erythromycin

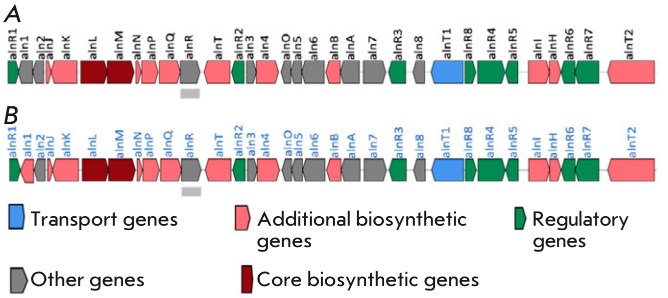

Fig. 6. Alnumycin and K-1115A BGC in the genomes of (*A*) *Streptomyces sp*. CM020; (*B*) *S. phaeochromogenes* BV-204

Some products of alnumycin BGC are known to have antibacterial activity [31], but their action mechanism has not been studied yet. Analysis of the reference genome (GenBank RefSeq:GCF_026343615.1) of *S. phaeochromogenes* NBC 00034 also revealed it to have an alnumycin BGC and conjugated compounds. This cluster had been annotated previously based on *Streptomyces* sp. CM020 [32], whose phylogenetic attribution data have not been published. However, considering the high homologic and phenotypic similarity of the alnumycin BGCs from *Streptomyces* sp. CM020, *S phaeochromogenes* NBC 00034, and *S phaeochromogenes* BV-204, it can be assumed that *Streptomyces* sp. CM020 also belongs to the *S. phaeochromogenes* taxon.

According to published data, *S. phaeochromogenes* NBC 00034 produces various isomers of phaeochromacetin (A, B, C, D, E) [34–38], as well as moenomycin and bambermycin [38], but CMSA did not detect these products in the spectrum of the BV-204 metabolites. It is noteworthy that no alnumycin was detected either. Disruption of the *aln4* and *aln5* genes can affect alnumycin biosynthesis [34] and transform it to K-1115A as a major product [32]. Gene alignment demonstrated that *aln4* in *Streptomyces sp.* CM020 and *S. phaeochromogenes* NBC 00034 were fully identical, whereas the nucleotide sequence of the *aln4* gene of BV-204 differs from them by several substitutions. The genetic sequences of the *aln5* gene in the analyzed strains differ much more strongly (Supplementary, *Fig. S9*). This is probably the reason why our strain produces only K-1115A.

Analysis of the BV-204 genome revealed the regions responsible for the synthesis of many secondary metabolites, such as siderophore coelichelin, but investigating the strain's ability to form iron-chelating compounds using the agar diffusion method [39] yielded negative results.

3,8-dihydroxy-9,10-dioxo-1-propylanthracene-2-carboxylic acid was first isolated from the *S. griseorubiginosus* strain (Mer-K1115A). It was described as an anthraquinone-series compound and named K-1115A [33]. The compound's anti-inflammatory properties have been studied, but no data on its antimicrobial activity have been reported in the literature. However, there have been publications reports on the antagonistic activity against Gram-positive bacteria of a structurally similar molecule (3,8-dihydroxy-1-propylanthraquinone-2-carboxylic acid) [40]. Discs loaded with 40 μg of the active agent were placed on the *S. aureus* and *S. viridochromogenes* lawns, with inhibition zones of 14 and 12 mm in diameter, respectively, and no activity against yeasts and micromycetes was detected [40]. Here, it should be noted that, probably by mistake, the authors named the molecule they studied "K-1115A" despite it having a different formula. Another closely related compound (3,8-dihydroxy-l-methylanthraquinone-2-carboxylic acid) inhibited the biofilms formed by methicillin-resistant *S. aureus* at EC_{50} at 200 μg/mL [41]. It appears necessary to mention that this study was referenced in the recent paper erroneously attributing the antibacterial activity to K-1115A. However, the present paper is where for the first time the antibacterial activity of K-1115A has been reliably demonstrated. There is evidence that alnumycin and some other BGC products, such as 6-dihydro-8-propylanthraquinone, are active against *E. coli* ΔtolC [42], but in our experiments K-1115A showed no activity against this pathogen. K-1115A affected a variant of the *E. coli* SS_lptd strain with impaired synthesis of envelope lipopolysaccharides and increased cell membrane permeability. According to published data, anthraquinone compounds mainly affect Gram-positive microorganisms, in particular *Staphylococcus, Bacillus, Streptomyces,* etc., but not Gram-negative bacteria or fungi [40].

Anthraquinone substances generally inhibit the processes involved in DNA biosynthesis, but the products and intermediates of alnumycin BGC, in particular alnumycin itself and 1,6-dihydro-8-propylanthraquinone, do not bind to double-stranded DNA and do not inhibit DNA gyrase [43]. Examination of K-1115A using the pDualrep2 reporter system also found no inhibitory effect on DNA synthesis but revealed its ability to inhibit protein biosynthesis.

We studied the effect K-1115A had on translation in a cell-free system *in vitro* and demonstrated that this compound acts as an inhibitor of protein biosynthesis. For K-1115A, EC_{50} was found to be 97% of its MIC, while that of erythromycin in this study was 0.8%. In other words, the concentration of erythromycin must be 125-fold higher to inhibit cell growth than to inhibit translation, whereas in the case of K-1115A these concentrations are almost identical. This property somehow distinguishes K-1115A from common translation inhibitors, but it does not make it unique. For example, chloramphenicol, a well-known translation inhibitor having additional action mechanisms besides binding to the ribosome, has a similar effect [44]. This may suggest that inhibition of bacterial translation is not the only mechanism of antimicrobial action that K-1115A possesses. For instance, some enzyme systems in a microbial cell may modify K-1115A in such a way that the resulting molecule has a significantly greater inhibitory effect that cannot be observed *in vitro*.

It may also be assumed that disrupting bacterial cell membrane synthesis is not an alternative action mechanism, since in our case the substance affects a strain with already disrupted LPS synthesis, but not a strain in which this structure is preserved. Another assumption is that the additional target is not related to the interaction with DNA, even though this is typical for anthraquinone derivatives; otherwise, we would have observed an additional induction of TurboRFP in the experiment, indicative of an SOS response.

It should be noted that K-1115A's specificity against Gram-positive bacteria and a recombinant *E. coli*

Table 1. K-1115A capability to inhibit model pathogenic strains

Tested strain	MIC, μg/mL	TI
E. coli SS_lptd	0.625	8
S. aureus (MRSA) INA00761	2.5	2
B. subtilis ATCC 6633	1.25	4
S. aureus SS01	0.625	8
S. aureus 29213	No*	–
S. aureus ATCC 25923	No	–
M. smegmatis Ac-1171	No	–
C. albicans CBS 8836	No	–

*No inhibition in the range investigated.

SS_lptd strain with a deletion in the lptD gene indicates that its activity against bacterial cells is largely determined by cellular barriers permeability.

For a compound to be considered as a perspective agent of antimicrobial therapy, it is its therapeutic index (TI) indicating the specificity of the effect a compound has on pathogenic and animal cells that plays the major role. For that purpose, we examined the ability of K-1115A to inhibit the HEK293 cell line (EC_{50} of 5 μg/mL) and several model pathogens (*Table 1*) to calculate its TI as the ratio of HEK293 EC_{50} and microbial-strain MICs.

For the inhibited strains, TI varied from 2 to 8, which gives hope that semi-synthetic derivatives with good clinical prospects can be developed based on K-1115A.

We also obtained evidence that that the products and intermediates of alnumycin BGC had antitumor activity through paraptosis [45], autophagy [45], prevention of aberrant cellular metabolism [46], increased radiosensitivity of cancer cells [47], apoptosis, etc. [48]. K-1115A was shown to have anti-inflammatory properties; it inhibited direct binding of the AP-1 transcription factor to the AP-1 oligonucleotide and collagenase production in IL-1a-stimulated rat synovial cells *in vitro*. It was also found that K-1115A attenuates the AR-1-mediated inflammatory response by reducing the activity of ornithine decarboxylase in mice induced by phorbolmyristate acetate [31]. Patterson et al. have used substance K-1115A to produce physiologically active conjugates [49].

CONCLUSION

The use of modern mechanism-oriented approaches in classical screening makes it possible to identify not only new biologically active substances, but also to discover new promising properties of previously discovered, but poorly studied, molecules, giving them a chance to become potential drugs. Despite the fact that K-1115A was discovered more than 25 years ago and that data on the antibacterial activity of its homologs have long been available, the activity of this substance and its action mechanism have not yet been studied. In this study, using the pDualrep2 dual reporter system, we were able to detect a K-1115A producer, establish that this compound inhibits protein synthesis, and confirm this effect by inhibiting translation *in vitro* using FLuc mRNA.

K-1115A, an anthraquinone derivative produced by *S. phaeochromogenes* BV-204, has been shown to affect the *E. coli* SS_lptd strain with an attenuated cell membrane and subsequently a number of clinically relevant *S. aureus* isolates, including MRSA and *B. subtilis*. No activity against *S. aureus* ATCC 29213, *S. aureus* ATCC 25923, *C. albicans* CBS 8836, *M. smegmatis* Ac-1171 gives hope K-1115A may turn out to be effective (in terms of specificity) against bacterial targets. K-1115A has also demonstrated a novel property for alnumycin BGC products; namely, the ability to inhibit protein biosynthesis.

The substance's TI is relatively small (2–8 in different strains), but K-1115A may become the basis for the development of semi-synthetic derivatives for antimicrobial therapy. Earlier studies found K-1115A and its semi-synthetic derivatives to have an anti-inflammatory effect, which, together with its antimicrobial properties, allows us to consider them as promising compounds for the development of preparations for complex antimicrobial and anti-inflammatory therapy (e.g., for wound treatment).

High-throughput screening using the pDualrep2 system has significantly improved efficiency when searching for new protein-synthesis inhibitors even among known compounds, opening up new properties and perspectives for entire classes of molecules. ●

This study was funded by the Ministry of Science and Higher Education of the Russian Federation under Agreement No. 075-10-2021-093, Project [BTH-RND-2127].

Supplementaries are available on the website https://doi.org/10.32607/actanaturae.27315.

REFERENCES

1. Abdel-Razek A.S., El-Naggar M.E., Allam A., Morsy O.M., Othman S.I. // Processes. 2020. V. 8. № 4. P. 470.
2. Newman D.J., Cragg G.M. // J. Nat. Prod. 2020. V. 83. № 3. P. 770–803.
3. Dai J., Han R., Xu Y., Li N., Wang J., Dan W. // Bioorganic Chem. 2020. V. 101. P. 103922.
4. Wright G.D. // Chem. Biol. 2012. V. 19. № 1. P. 3–10.
5. Zhu Y., Huang W.E., Yang Q. // Infect. Drug Resist. 2022. V. Volume 15. P. 735–746.
6. Alferova V.A., Maviza T.P., Biryukov M.V., Zakalyukina Y.V., Lukianov D.A., Skvortsov D.A., Vasilyeva L.A., Tashlitsky V.N., Polshakov V.I., Sergiev P.V., et al. // Biochimie. 2022. V. 192. P. 63–71.
7. Mahajan G.B. // Front. Biosci. 2012. V. E4. № 1. P. 240–253.
8. Sousa J.A.D.J., Olivares F.L. // Chem. Biol. Technol. Agric. 2016. V. 3. № 1. P. 24.
9. Tian X., Zhang Z., Yang T., Chen M., Li J., Chen F., Yang J., Li W., Zhang B., Zhang Z., et al. // Front. Microbiol. 2016. V. 7. № 5. P.17-18.
10. Osterman I.A., Komarova E.S., Shiryaev D.I., Korniltsev I.A., Khven I.M., Lukyanov D.A., Tashlitsky V.N., Serebryakova M.V., Efremenkova O.V., Ivanenkov Y.A., et al. // Antimicrob. Agents Chemother. 2016. V. 60. № 12. P. 7481–7489.
11. Volynkina I.A., Zakalyukina Y.V., Alferova V.A., Belik A.R., Yagoda D.K., Nikandrova A.A., Buyuklyan Y.A., Udalov A.V., Golovin E.V., Kryakvin M.A., et al. // Antibiotics. 2022. V. 11. № 9. P. 1198.
12. ISO. https://www.iso.org/standard/65223.html. (Accessed November 1, 2023).
13. Baranova A.A., Chistov A.A., Tyurin A.P., Prokhorenko I.A., Korshun V.A., Biryukov M.V., Alferova V.A., Zakalyukina Y.V. // Microorganisms. 2020. V. 8. № 12. P. 1948.
14. Gause G.F., Preobrazhenskaya T.P., Terekhova L.P., Maksimova T.S. Guide for Determination of Actinomycetes: Genera Streptomyces, Streptoverticillium, and Chainia. 1st ed. M.: Nauka, 1983. P. 84–89.
15. Shirling E.B., Gottlieb D. // Int. J. Syst. Bacteriol. 1966. V. 16. № 3. P. 313–340.
16. Zakalyukina Y.V., Osterman I.A., Wolf J., Neumann-Schaal M., Nouioui I., Biryukov M.V. // Antonie Van Leeuwenhoek. 2023. V. 116. № 6. P. 597–598.
17. Williams S.T., Goodfellow M., Alderson G., Wellington E.M.H., Sneath P.H.A., Sackin M.J. // Microbiology. 1983. V. 129. № 6. P. 1743–1813.
18. Zakalyukina Y.V., Birykov M.V., Lukianov D.A., Shiriaev D.I., Komarova E.S., Skvortsov D.A., Kostyukevich Y., Tashlitsky V.N., Polshakov V.I., Nikolaev E., et al. // Biochimie. 2019. V. 160. P. 93–99.
19. Zakalyukina Yu.V., Biryukov M.V., Golichenkov M.V., Netrusov A.I. // Mosc. Univ. Biol. Sci. Bull. 2017. V. 72. № 1. P. 13–19.
20. Prjibelski A., Antipov D., Meleshko D., Lapidus A., Korobeynikov A. // Curr. Protoc. Bioinforma. 2020. V. 70. № 1. P. e102.
21. Brettin T., Davis J.J., Disz T., Edwards R.A., Gerdes S., Olsen G.J., Olson R., Overbeek R., Parrello B., Pusch G.D., et al. // Sci. Rep. 2015. V. 5. № 1. P. 8365.
22. Ondov B.D., Treangen T.J., Melsted P., Mallonee A.B., Bergman N.H., Koren S., Phillippy A.M. // Genome Biol. 2016. V. 17. № 1. P. 132.
23. Lefort V., Desper R., Gascuel O. // Mol. Biol. Evol. 2015. V. 32. № 10. P. 2798–2800.
24. Zakalyukina Y.V., Pavlov N.A., Lukianov D.A., Marina V.I., Belozerova O.A., Tashlitsky V.N., Guglya E.B., Osterman I.A., Biryukov M.V. // Insects. 2022. V. 13. № 11. P. 1042.
25. Kohlbacher O., Reinert K., Gröpl C., Lange E., Pfeifer N., Schulz-Trieglaff O., Sturm M. // Bioinformatics. 2007. V. 23. № 2. P. e191–e197.
26. Wang M., Carver J.J., Phelan V.V., Sanchez L.M., Garg N., Peng Y., Nguyen D.D., Watrous J., Kapono C.A., Luzzatto-Knaan T., et al. // Nat. Biotechnol. 2016. V. 34. № 8. P. 828–837.
27. van Santen J.A., Poynton E.F., Iskakova D., McMann E., Alsup T.A., Clark T.N., Fergusson C.H., Fewer D.P., Hughes A.H., McCadden C.A., et al. // Nucleic Acids Res. 2022. V. 50. № D1. P. D1317–D1323.
28. Van Santen J.A., Jacob G., Singh A.L., Aniebok V., Balunas M.J., Bunsko D., Neto F.C., Castaño-Espriu L., Chang C., Clark T.N., et al. // ACS Cent. Sci. 2019. V. 5. № 11. P. 1824–1833.
29. Segeritz C.-P., Vallier L. In: Basic Science Methods for Clinical Researchers. // Elsevier. Academic Press. 2017. P. 151–172
30. Nouioui I., Carro L., García-López M., Meier-Kolthoff J.P., Woyke T., Kyrpides N.C., Pukall R., Klenk H.-P., Goodfellow M., Göker M. // Front. Microbiol. 2018. V. 9. P. 2007.
31. Goto M., Masegi M.-A., Yamauchi T., Chiba K.-I., Kuboi Y., Harada K., Naruse N. // J. Antibiot. (Tokyo). 1998. V. 51. № 6. P. 539–544.
32. Oja T., Palmu K., Lehmussola H., Leppäranta O., Hännikäinen K., Niemi J., Mäntsälä P., Metsä-Ketelä M. // Chem. Biol. 2008. V. 15. № 10. P. 1046–1057.
33. Naruse N., Goto M., Watanabe Y., Terasawa T., Dobashi K. // J. Antibiot. (Tokyo). 1998. V. 51. № 6. P. 545–552.
34. Ritacco F.V., Eveleigh D.E. // J. Ind. Microbiol. Biotechnol. 2008. V. 35. № 9. P. 931–945.
35. Graziani E.I., Ritacco F.V., Bernan V.S., Telliez J.-B. // J. Nat. Prod. 2005. V. 68. № 8. P. 1262–1265.
36. Bycroft B.W., Higton A.A., Roberts A.D. // Dictionary of antibiotics and related substances. // London ; New York. 1988. P.944.
37. Van Pée K.-H., Lingens F. // FEBS Lett. 1984. V. 173. № 1. P. 5–8.
38. Söhngen C., Podstawka A., Bunk B., Gleim D., Vetcininova A., Reimer L.C., Ebeling C., Pendarovski C., Overmann J. // Nucleic Acids Res. 2016. V. 44. № D1. P. D581–D585.
39. Schwyn B., Neilands J.B. // Anal. Biochem. 1987. V. 160. № 1. P. 47–56.
40. Poumale H.M.P., Ngadjui B.T., Helmke E., Laatscha H. // Z. Für Naturforschung B. 2006. V. 61. № 11. P. 1450–1454.
41. Song Z.-M., Zhang J.-L., Zhou K., Yue L.-M., Zhang Y., Wang C.-Y., Wang K.-L., Xu Y. // Front. Microbiol. 2021. V. 12. P. 709826.
42. Sagurna L., Heinrich S., Kaufmann L.-S., Rückert-Reed C., Busche T., Wolf A., Eickhoff J., Klebl B., Kalinowski J., Bandow J.E. // Antibiot. Basel Switz. 2023. V. 12. № 7. P. 1116.
43. Tian W., Wang C., Li D., Hou H. // Future Med. Chem. 2020. P. fmc-2019-0322.
44. Pavlova J.A., Khairullina Z.Z., Tereshchenkov A.G., Nazarov P.A., Lukianov D.A., Volynkina I.A., Skvortsov D.A., Makarov G.I., Abad E., Murayama S.Y., et al. // Anti-

biotics. 2021. V. 10. № 5. P. 489.
45. Liu Y., Zhong Y., Tian W., Lan F., Kang J., Pang H., Hou H., Li D. // Anticancer. Drugs. 2019. V. 30. № 10. P. 1038–1047.
46. Hitosugi T., Zhou L., Elf S., Fan J., Kang H.-B., Seo J.H., Shan C., Dai Q., Zhang L., Xie J., et al. // Cancer Cell. 2012. V. 22. № 5. P. 585–600.
47. Wang D., Wang S., Liu Q., Wang M., Wang C., Yang H. // Oncol. Rep. 2013. V. 29. № 6. P. 2341–2347.
48. Stanojković T., Marković V., Matić I.Z., Mladenović M.P., Petrović N., Krivokuća A., Petković M., Joksović M.D. // Bioorg. Med. Chem. Lett. 2018. V. 28. № 15. P. 2593–2598.
49. Ijaz T., Tran P., Ruparelia K.C., Teesdale-Spittle P.H., Orr S., Patterson L.H. // Bioorg. Med. Chem. Lett. 2001. V. 11. № 3. P. 351–353.

The Effect of Calcium Ions on the Electrophysiological Properties of Single ANO6 Channels

D. O. Kolesnikov, E. R. Grigorieva, M. A. Nomerovskaya, D. S. Reshetin, A. V. Shalygin*, E.V. Kaznacheyeva**
Institute of Cytology of the Russian Academy of Sciences, St. Petersburg, 194064 Russian Federation
*E-mail: shalygin.alexey@gmail.com
**E-mail: evkazn@incras.ru

Received December 5, 2023; in final form, December 12, 2023
DOI: 10.32607/actanaturae.27338

ABSTRACT **Proteins belonging to the anoctamin (ANO) family form calcium-activated chloride channels (CaCCs). The most unusual member of this family, ANO6 (TMEM16F), simultaneously exhibits the functions of calcium-dependent scramblase and the ion channel. ANO6 affects the plasma membrane dynamics and phosphatidylserine transport; it is also involved in programmed cell death. The properties of ANO6 channels remain the subject of debate. In this study, we investigated the effect of variations in the intracellular and extracellular concentrations of calcium ions on the electrophysiological properties of endogenous ANO6 channels by recording single ANO6 channels. It has been demonstrated that (1) a high calcium concentration in an extracellular solution increases the activity of endogenous ANO6 channels, (2) the permeability of endogenous ANO6 channels for chloride ions is independent of the extracellular concentration of calcium ions, (3) that an increase in the intracellular calcium concentration leads to the activation of endogenous ANO6 channels with double amplitude, and (4) that the kinetics of the channel depend on the plasma membrane potential rather than the intracellular concentration of calcium ions. Our findings give grounds for proposing new mechanisms for the regulation of the ANO6 channel activity by calcium ions both at the inner and outer sides of the membrane.**

KEYWORDS **ANO6, TMEM16F, calcium-activated chloride channels, patch-clamp technique, recording currents through single channels.**

ABBREVIATIONS **CaCC – calcium-activated chloride channels; ANO – anoctamins; $[Ca^{2+}]_i$ – calculated intracellular concentration of free calcium ions.**

INTRODUCTION

Calcium-activated chloride channels are involved in the regulation of critical intracellular processes related to chloride transport and cellular membrane dynamics.

One of the isoforms of anoctamin, ANO6 (TMEM16F), simultaneously exhibits the functions of scramblase and the ion channel. Impaired functioning of ANO6 causes pathologic formation of the skeleton and placenta, miscarriage, cancer, and bleeding [1–4]. Reduction of ANO6 activity is an effective approach to treating inflammatory respiratory diseases [5, 6].

Most of the studies focusing on channel functions have concerned ANO6 overexpression, which significantly alters the state of the cellular membrane, thus affecting channel properties. Furthermore, electrophysiological properties such as the open state lifetime of the channel, its single amplitude, and conductance can be adequately assessed only by recording the current flowing through single ion channels. The lack of these data obscures our understanding of the principles of ion channel functioning.

Being calcium-activated (EC50 = 10 μM at +40 mV), the ANO6 channel is not only regulated by intracellular calcium ions but can also conduct Ca^{2+} ions [4]. Thus, anionic conductance has been detected in some studies, while others have demonstrated that the channel has cationic conductance [4, 7]. Data on the effect of the extracellular calcium concentration on the electrophysiological properties of endogenous

ANO6 channels is quite scarce. Furthermore, it is unclear how changes in the intracellular concentration of free calcium ions ($[Ca^{2+}]_i$) or membrane potential affect the kinetics and substates of single endogenous ANO6 channels.

This work aims to shed light on the dependence between the electrophysiological properties of single endogenous ANO6 channels and two major activity-modulating factors: the calcium concentration and potential.

MATERIALS AND METHODS

Cell culture

The work was conducted using a HEK293T cell line from the collection of the Institute of Cytology, Russian Academy of Sciences (St. Petersburg, Russia). The cells were cultured in a liquid Dulbecco's modified Eagle medium (DMEM) (PanEco, Russia) supplemented with 10% fetal bovine serum, 1% penicillin, 1% streptomycin, and 1% L-glutamine. The cells were re-inoculated onto coverslip fragments 16–48 h before the experiments.

Reagents

The reagents used in electrophysiological experiments were purchased from Sigma Aldrich (USA).

Electrophysiological measurements of the current

The currents flowing through single channels were recorded by the patch-clamp technique in the inside-out configuration using an Axopatch 200B (Axon Instruments, USA). The data were digitized using a Digidata 1322A analog-to-digital converter (Axon Instruments) with a discretization frequency of 5 kHz. The signal was passed through a built-in low-frequency (2 kHz) Bessel filter. In order to analyze the amplitude and the open state probability, as well as present the data, the recordings were additionally filtered at 110 Hz. No additional filtering was needed when analyzing the open-state lifetime of the channels; events shorter than 0.5 ms were not taken into account.

The composition of the extracellular solution (recording pipette solution) was as follows:

1) 105 mM $CaCl_2$, 10 mM Tris-HCl, pH 7.4;
2) 1.5 mM $CaCl_2$, 126 mM NaCl, 10 mM TeaCl, 10 mM glucose, 10 mM Tris-HCl, pH 7.4; and
3) 140 mM NaCl, 5 mM EGTA-Na, 10 mM Tris-HCl, pH 7.4.

The free calcium concentration $[Ca^{2+}]_i$ was calculated using the Max Chelator software (Stanford University, USA). An intracellular solution with the calculated concentration of free calcium ions $[Ca^{2+}]_i$ = 100 nM contained 130 mM CsGlutamate, 3.3 mM $CaCl_2$, 5 mM $MgCl_2$, 1 mM MgATP, 10 mM EGTA, and 10 mM HEPES. pH 7.2.

Solutions with calculated concentrations of free calcium ions of 0.2, 1 and 10 μM were obtained by adding $CaCl_2$ at concentrations of 5, 8.5, and 9.82 mM, respectively, to the initial solution. The experiments were conducted at room temperature. The glass micropipettes had a resistance of 7–15 mΩ.

Channel activity was quantified using the (NP_o) value, where N is the number of channels and P_o is the open channel probability. $NP_o = (I)/i$, where (I) is the average current through a membrane fragment; i is the amplitude of the open channel current. Since channel activity significantly varied over time, the average $NP_o max_{30}$ value (i.e., the average NP_o measured during a 30s interval when channel activity was maximal) was used for our analysis.

Statistical analysis

The data were analyzed using the OriginPro2018 (Originlab, USA) and Clampfit 10.3 (Molecular Devices, USA) software. Data normality was tested using the Shapiro–Wilk test; the homogeneity of variance was assessed using Levene's test for the equity of variances. Outliers, if any, were detected using the Grubbs' test and expunged from the dataset. The frequencies of observation of CaCC were compared using the Fisher's exact test. The open state probabilities for independent and constrained data were compared using the Student's test and paired Student's test, respectively. Multiple comparisons were conducted by ANOVA, with the Bonferroni correction. The data are presented as the Mean ± Standard error of the mean. Differences were considered significant at $p < 0.05$.

RESULTS AND DISCUSSION

Increasing activity of endogenous CaCCs ANO6 at higher extracellular concentrations of calcium

Previously, we had recorded and described single CaCC channels formed by ANO6 proteins [8, 9]. An extracellular solution containing 105 mM Ca^{2+} or 1.5 mM Ca^{2+} was used to study the effect of the extracellular calcium concentration on ANO6. Experiments were conducted in the inside-out configuration at a fixed membrane potential of +40 mV. Activation of endogenous ANO6 CaCCs was induced by adding a 10 μM $[Ca^{2+}]_i$ solution to the intracellular side of the membrane (*Fig. 1A,B*).

In the presence of a physiological concentration of $CaCl_2$ (1.5 mM) in the extracellular solution, channel activation was observed in 28.5% of the experiments

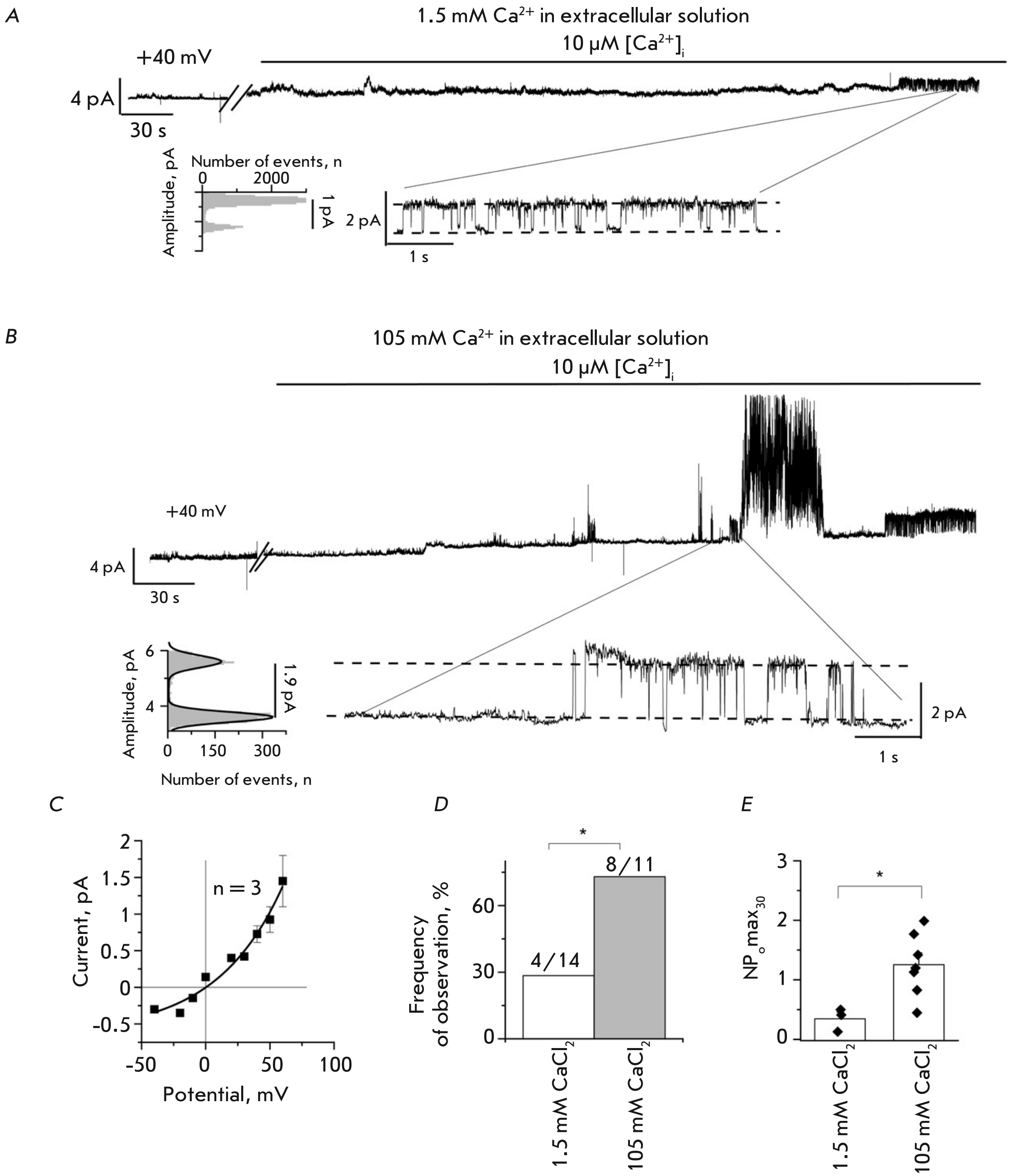

Fig. 1. Activity of endogenous ANO6 CaCCs induced by application of 10 μM $[Ca^{2+}]_i$ to the intracellular side of the plasma membrane in the inside-out configuration in the presence of 1.5 mM or 105 mM Ca^{2+} in the extracellular solution. Representative fragments of the recordings are shown, with expanded current traces and corresponding amplitude histograms at the bottom. (*A*) A fragment of the current recording through endogenous ANO6 CaCCs activated by application of 10 μM $[Ca^{2+}]_i$ with 1.5 mM Ca^{2+} in the extracellular solution. (*B*) A fragment of the current recording through endogenous ANO6 CaCCs activated by application of 10 μM $[Ca^{2+}]_i$ with 105 mM Ca^{2+} in the extracellular solution. (*C*) The average current–voltage relationship of endogenous ANO6 CaCCs in the presence of 1.5 mM Ca^{2+} in the extracellular solution. (*D*) The frequency of experiment observations with endogenous ANO6 CaCCs activated by application of 10 μM $[Ca^{2+}]_i$ with 1.5 mM or 105 mM Ca^{2+} in the extracellular solution ($p < 0.05$). (*E*) $NP_o max_{30}$ of endogenous ANO6 CaCCs activated by application of 10 μM $[Ca^{2+}]_i$ in the extracellular solutions of 1.5 mM and 105 mM Ca^{2+} ($p < 0.05$)

(4/14); the average $NP_o max_{30}$ was 0.35 ± 0.11 ($n = 3$) (*Figs. 1A,C,D,E*). Meanwhile, in the presence of a high calcium concentration in the extracellular solution (105 mM $CaCl_2$), channel activation was observed reliably more frequently: in 73% of the experiments with $NP_o max_{30} = 1.26 \pm 0.2$ ($n = 7$) ($p < 0.05$) (*Fig. 1D,E*). Earlier, we demonstrated that a high concentration of calcium ions in a pipette solution could not activate endogenous ANO6 channels without additional stimulation by intracellular Ca^{2+} ions [8]. Therefore, the increase in channel activity correlates with a rising concentration of extracellular Ca^{2+}.

Endogenous ANO6 channels are known both to be activated by calcium ions and to conduct them [4]. It can be assumed that at increased intracellular calcium concentrations, calcium ions permeate through a pore of the endogenous ANO6 channel, which can lead to the activity self-maintenance mode and further potentiation of channel activity.

Therefore, we demonstrated that both the open state probability and frequency of observation of endogenous ANO6 CaCCs in HEK293T cells increase with the concentration of calcium ions in the extracellular solution.

The extracellular calcium concentration has no effect on the anionic conductance of channels

The data on the anionic conductance of ANO6 are controversial. ANO6 has been described as anion-conducting [7] or cation-conducting [4] in different studies. The permeability of the channel for chloride ions depends on $[Ca^{2+}]_i$ [10]. It was demonstrated that at low $[Ca^{2+}]_i$, the channel will preferably conduct cations rather than anions. The effect of the extracellular calcium concentration on anionic conductance remains poorly understood.

In order to study this aspect, we removed all free calcium ions from the extracellular solution using the EGTA chelator. CaCC activation was induced by adding 10 μM $[Ca^{2+}]_i$ to the intracellular side of the membrane (*Fig. 2A*). We observed activation of endogenous ANO6 CaCCs in the experiments (*Fig. 2B*).

In the presence of 140 mM NaCl, 5 mM EGTA in the extracellular solution, endogenous ANO6 CaCCs were observed in 26% of the experiments (6/23), the open-state probability being 1.17 ± 0.43 ($n = 6$). The activity of channels in the extracellular solution containing 140 mM NaCl, 5 mM EGTA showed no statistically significant differences compared to that in the presence of calcium at a physiological concentration (1.5 mM Ca^{2+}) (*Fig. 1E, Fig. 2D*) ($p > 0.05$). These findings indicate that the physiological calcium concentration in the extracellular solution *per se* does not potentiate the activity of endogenous ANO6 CaCCs in HEK293T cells.

The variation in channel permeability for chloride ions can be assessed based on the changes in reversal potential as the Cl^- concentration in the extracellular solution is varied. For this purpose, in the experiments with a calcium-free extracellular solution, we replaced the intracellular solution containing 130 CsGlutamate (10 mM $[Cl^-]$) with a solution containing 130 CsCl (140 mM $[Cl^-]$). When the intracellular solution containing 10 mM $[Cl^-]$ was replaced with that containing 140 mM $[Cl^-]$, the reversal potential shifted rightward by 12.7 ± 3.9 mV ($n = 3$) (*Fig. 2E*). Earlier, we demonstrated that the presence of 105 mM $CaCl_2$ in the extracellular solution shifted the reversal potential rightward by 16 ± 2 mV when the intracellular solution was replaced in the same manner [8]. Hence, no statistically significant differences in the shift in the reversal potential were observed when using extracellular solutions containing or not containing calcium ions (*Fig. 2E*) [8].

Therefore, Ca^{2+} ions in extracellular solutions have no effect on the permeability of endogenous ANO6 channels for chloride ions.

An increase in $[Ca^{2+}]_i$ leads to preferential activation of endogenous ANO6 channels with double amplitude

Channels belonging to the anoctamin family of proteins are known to exist as homodimers. Each subunit contains a conducting pore. Inside each pore, there are two binding sites of calcium ions differing in their affinity [11].

It has been demonstrated that at low $[Ca^{2+}]_i$, when only one $[Ca^{2+}]_i$ binding site is occupied, two pores of ANO1 channels function independently [12]. As $[Ca^{2+}]_i$ increases, both binding sites of the $[Ca^{2+}]_i$ ions in the pore are occupied, thus causing synchronous functioning of ion conduction pores in the channel [12]. However, it is currently unknown whether ANO6 also exhibits this property.

In order to answer this question, we recorded the activity of endogenous ANO6 channels in intracellular solutions with low (1 μM) and high (10 μM) $[Ca^{2+}]_i$ in the inside-out configuration at a membrane potential of +40 mV. A pipette solution containing 105 mM $CaCl_2$ was used to increase the frequency of observation of ANO6 CaCCs.

We discovered that channels with amplitude 0.95 ± 0.06 pA ($n = 10/11$) were typically activated in the presence of 1 μM $[Ca^{2+}]_i$ (*Fig. 3A*). When using the solution containing 10 μM $[Ca^{2+}]_i$, we observed activation of channels with a similar amplitude (1 ± 0.12 pA

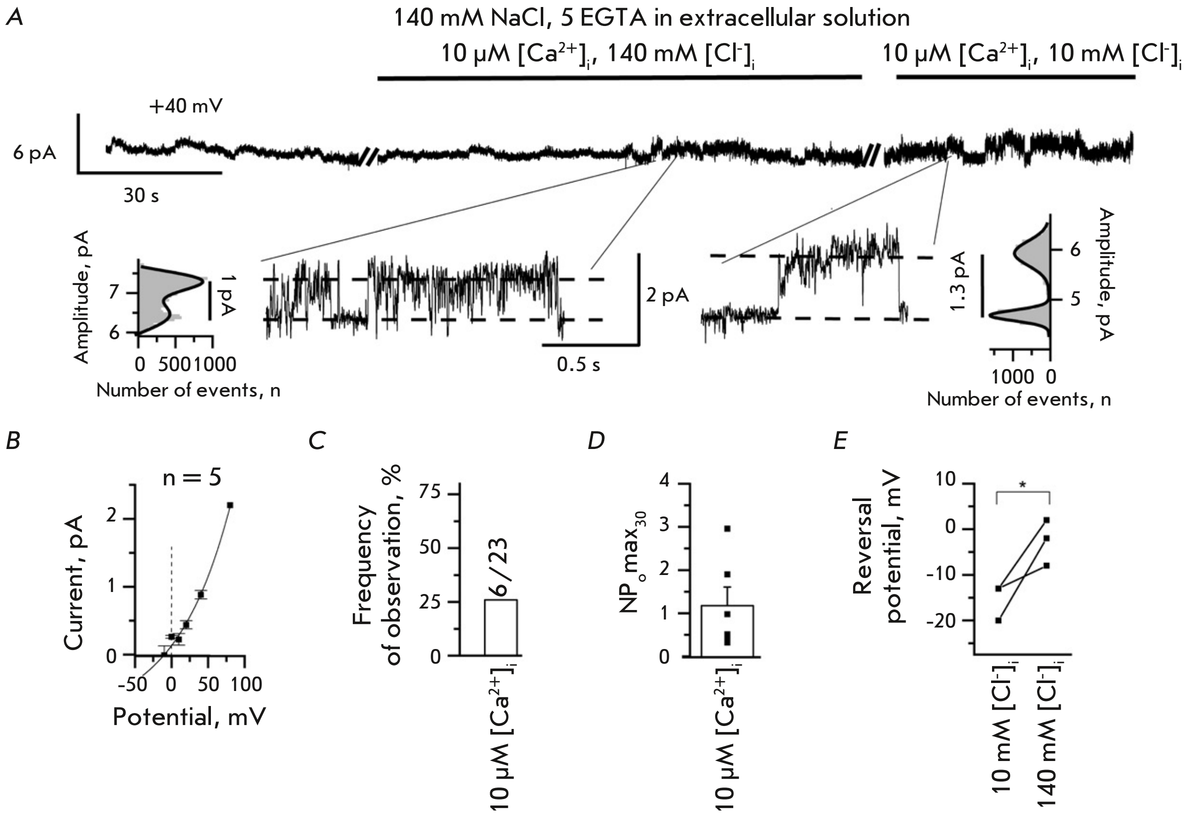

Fig. 2. Activity of endogenous ANO6 CaCCs in the absence of divalent ions in the external solution. (*A*) A fragment of current recording through endogenous ANO6 CaCCs in an external solution containing 140 mM NaCl, 5 mM EGTA. Representative fragments of the recordings are shown, with expanded current traces and corresponding amplitude histograms at the bottom. (*B*) The average current–voltage relationship of endogenous CaCCs in an external solution containing 140 mM NaCl, 5 mM EGTA and intracellular solution based on CsGlutamate. (*C*) Frequency of observation of endogenous ANO6 CaCCs at 140 mM NaCl, 5 mM EGTA in an external solution. (*D*) The open state probability of endogenous ANO6 CaCCs at 140 mM NaCl, 5 mM EGTA in an external solution. (*E*) A shift in the reversal potential of endogenous CaCCs when one replaces an intracellular CsGlutamate solution with CsCl at 140 mM NaCl, 5 mM EGTA in the extracellular solution

(n = 3/7)), as well as channels with double amplitude (1.79 ± 0.14 pA (n = 4/7)) (*Fig. 3B*). In the solution containing 1 μM $[Ca^{2+}]_i$, activation of channels with double amplitude was observed only in 9% of the experiments (n = 1/11) ($p < 0.05$) (*Fig. 3C,D*).

Hence, it can be inferred from our data that as $[Ca^{2+}]_i$ increases, two conduction pores of endogenous ANO6 CaCCs start conducting current synchronously. Therefore, we can assume that the mechanisms of regulation by intracellular calcium ions are similar for ANO1 and ANO6 CaCCs.

The open-state lifetime of the endogenous ANO6 CaCC depends on the membrane potential rather than on $[Ca^{2+}]_i$

The current through an endogenous ANO6 CaCC is known to increase with the intracellular calcium concentration and membrane depolarization [10]. We have previously demonstrated that this is related to a higher open state probability of the channels, their amplitude, and conductance [8]. However, the increase in the current can also be related to changes in the open state lifetime of the channel.

In order to study this question, we analyzed the open state lifetime of endogenous ANO6 channels as a function of the $[Ca^{2+}]_i$ concentration on the intracellular side of the membrane at a fixed membrane potential of +40 mV.

At 0.2 μM $[Ca^{2+}]_i$, the open state lifetime of channels was 1.07 ± 0.21 ms (n = 5); at 1 μM $[Ca^{2+}]_i$, – 0.77 ± 0.14 ms (n = 4); at 10 μM $[Ca^{2+}]_i$ – 1.18 ± 0.31 ms (n = 4); and at 100 μM $[Ca^{2+}]_i$ – 1.07 ± 0.15 ms (n = 4) ($p > 0.05$) (*Fig. 4A*). Therefore, the open state lifetime of channels was in-

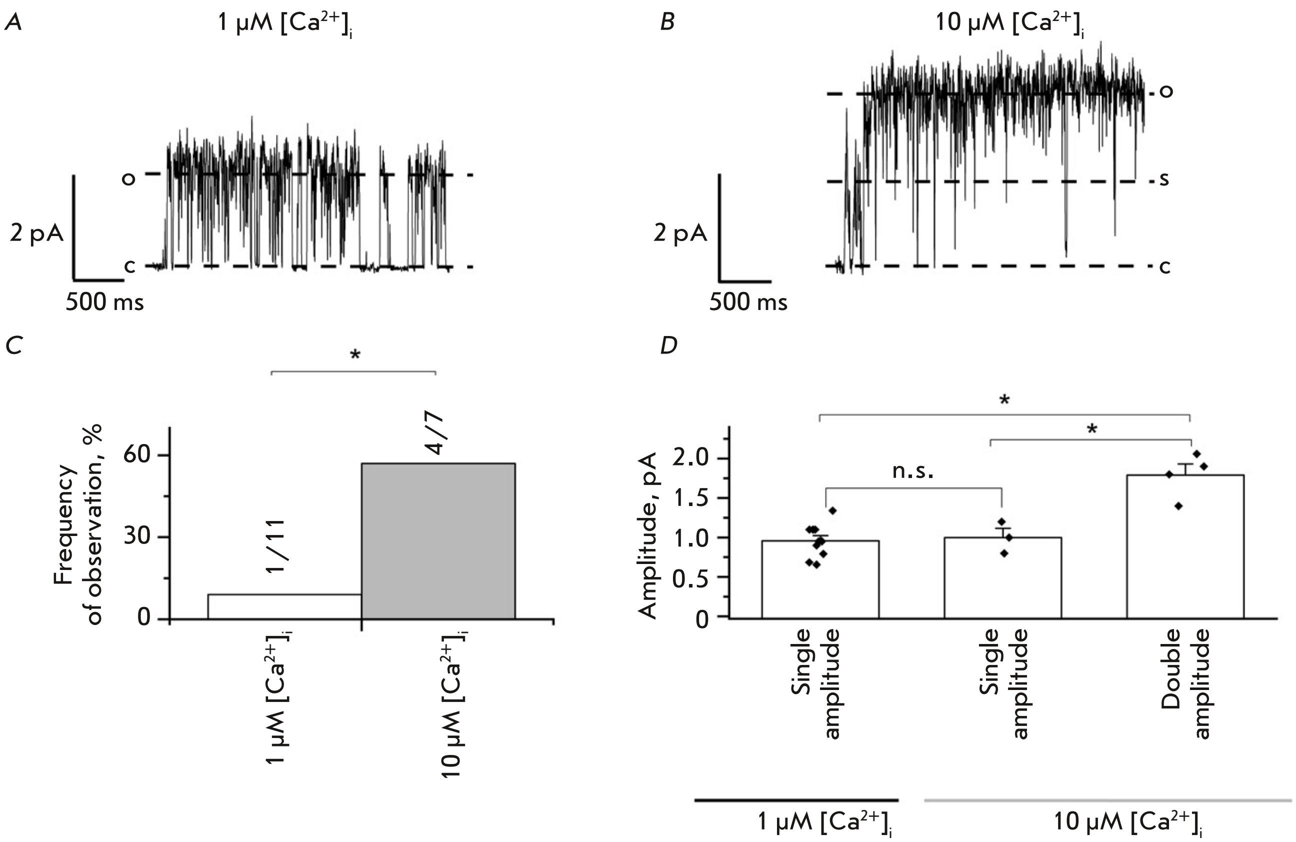

Fig. 3. Amplitude of endogenous CaCC at 1 and 10 μM $[Ca^{2+}]_i$. The extracellular solution contained 105 mM $CaCl_2$. The channels were activated by application of a solution with 1 or 10 μM $[Ca^{2+}]_i$. (*A*) A fragment of current recording through endogenous single-amplitude CaCC activated by application of 1 μM $[Ca^{2+}]_i$. c is the closed state of the channel; o is the open state of the channel. (*B*) A fragment of current recording through endogenous double amplitude CaCC activated by application of 10 μM $[Ca^{2+}]_i$. c is the closed state of the channel; o is the open state of the channel; and s is the substate. (*C*) The frequency of observation of endogenous CaCC ANO6 with double amplitude activated by 1 μM $[Ca^{2+}]_i$ (white) or 10 μM $[Ca^{2+}]_i$ (gray), $p < 0.05$. (*D*) The amplitude of endogenous ANO6 channels activated by 1 or 10 μM $[Ca^{2+}]_i$ ($p < 0.05$)

dependent of variations in $[Ca^{2+}]_i$. An analysis of the dependence of the open state lifetime of endogenous ANO6 channels on the membrane potential at a fixed intracellular concentration of 100 μM $[Ca^{2+}]_i$ demonstrated that the open state lifetime of CaCC increases linearly with increasing potential upon membrane depolarization (*Fig. 4B*).

Therefore, the increase in the current through endogenous CaCCs upon membrane depolarization is related not only to the higher conductance and open state probability of the channels (which was described earlier), but also to the longer open state lifetime of endogenous ANO6 channels. Meanwhile, variation in $[Ca^{2+}]_i$ does not alter the open state lifetime of channels.

Activity of ANO6 increases after transient switching to the negative membrane potential and back

We have found that the activity of ANO6 channels at a potential of +40 mV increases after transient membrane potential switching to a negative potential and back to +40 mV. The experimental scheme is presented below: channels were activated by adding 1 μM $[Ca^{2+}]_i$ to the intracellular side of the membrane at a potential of +40 mV; then the potential was maintained negative during 30 s, and a +40 mV voltage was reapplied. Potential switching back to +40 mV increased activity, on average from 0.23 ± 0.06 to 0.81 ± 0.26 ($n = 7$, $p < 0.05$, *Fig. 5*). This effect was not observed at higher calcium concentrations (10 or 100 μM): presumably, the channels had been induced

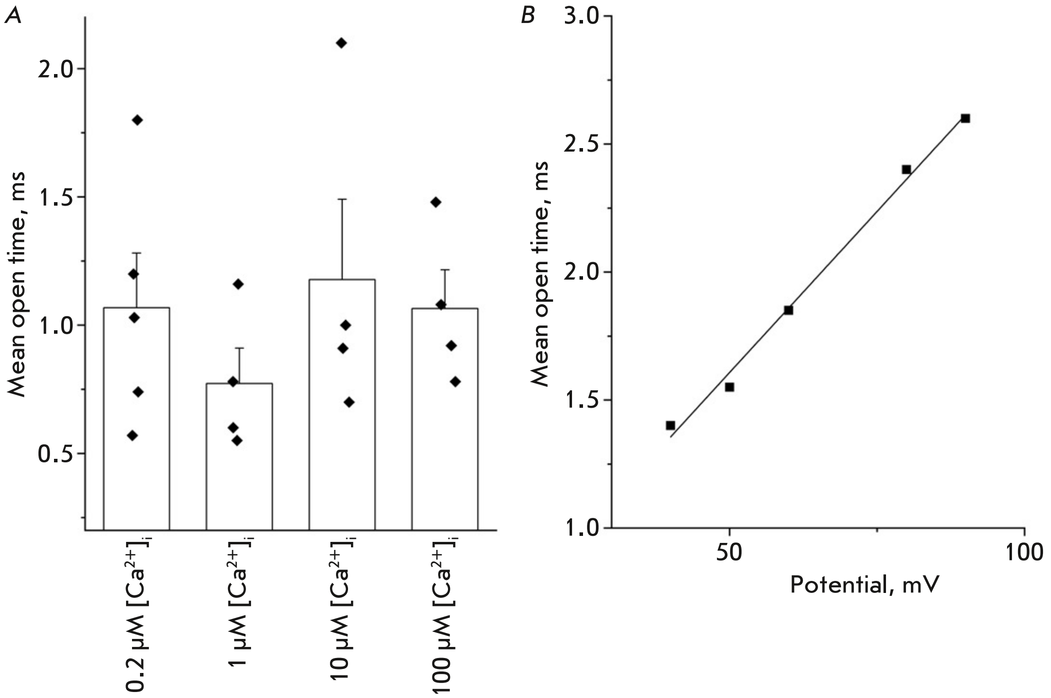

Fig. 4. Effect of $[Ca^{2+}]_i$ and the membrane potential on the open state lifetime of endogenous ANO6 channels in HEK293T cells. For the analysis, experiments were conducted in an inside-out configuration with 105 mM $CaCl_2$ in the extracellular solution. (*A*) The average open state lifetime of endogenous CaCCs at +40 mV at various intracellular calcium concentrations ($p > 0.05$). (*B*) The dependence of the open state lifetime of endogenous CaCCs on the membrane potential at an intracellular calcium concentration of 100 μM (the data from a representative experiment are presented)

to the maximum extent and activity could not be increased any further.

It is known that there exists synergy between increasing the intracellular calcium concentration and plasma membrane depolarization in the activation of ANO6 channels. Thus, for overexpressed ANO6 channels, depolarization facilitates the interaction between calcium ions and intracellular binding sites, which increases channel activity [10]. In this study, we demonstrated for the first time that potential switching *per se* increases ANO6 activity. It is fair to believe that changes in the electric field at the instant when the membrane potential is switched from a negative value to +40 mV contributes to the conformational changes in endogenous ANO6 channels, which enable efficient binding of calcium ions in the channel pore vestibule. This regulation will presumably be particularly pronounced under physiological conditions upon membrane potential fluctuations (hyperpolarization followed by depolarization), since it theoretically reduces the calcium concentration needed to increase channel activity. It would be interesting to further study whether this effect depends on the rate of the switching from a negative potential to a positive one.

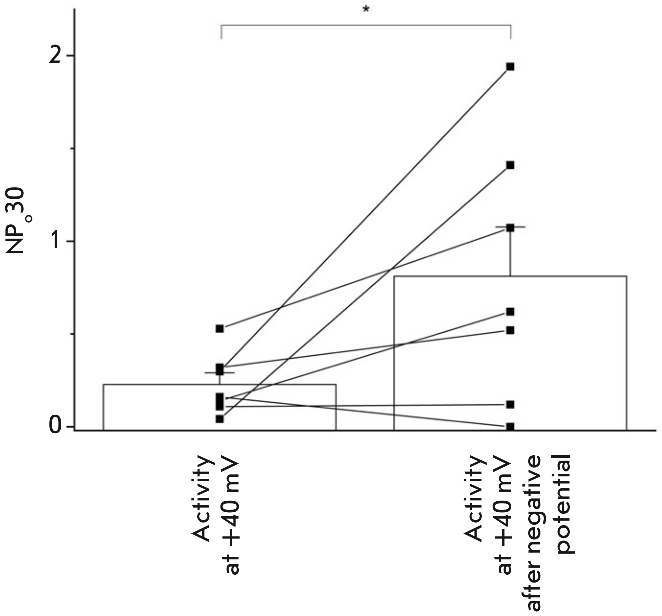

Fig. 5. Activity of ANO6 channels at +40 mV before and after transient membrane potential switching to a negative value. The channels were pre-activated by adding 1 μM calcium to the intracellular side of the membrane. After the development of activity at +40 mV, the membrane potential was switched to negative and then returned to +40 mV

CONCLUSIONS

By analyzing the kinetics of the functioning of single CaCCs, we have, for the first time, detected lengthening of the open state lifetime of the channel induced by an increase in membrane potential. Along with the previously reported increase in conductance and open state probability of the channels, this property seems to be responsible for the characteristic outward rectification of CaCCs. The intracellular calcium concentration had no effect on channel lifetime; however, an analysis of the channel amplitude demonstrated that increasing calcium concentration synchronizes functioning of the pores of the anoctamin dimer, thus increasing the current twofold.

Under experimental conditions, ANO6 channels are activated at high concentrations of intracellular calcium (several tens of micromoles), whereas the physiological calcium concentration in the cytoplasm is two orders of magnitude lower. We revealed that the cycle of membrane potential changes (hyperpolarization followed by depolarization) increases channel activity at a calcium ion concentration as low as 1 μM. This regulation can potentially also be observed under physiological conditions upon local membrane potential fluctuations.

High concentration of extracellular calcium ions increased channel activity, probably via nonselective entry of calcium ions and self-maintenance of channel activity. Since this effect was observed only in the presence of excessive calcium concentration (being almost two orders of magnitude higher than the physiological one), the physiological role of this process still needs to be elucidated. Channel permeability for chloride ions was independent of extracellular calcium concentration.

The identified mechanisms of regulation of ANO6 channel activity illustrate the potential pathways for fine-tuning of channel functioning under normal physiological and pathological conditions. ●

This work was supported by the Russian Science Foundation (grant No. 22-24-00761).

REFERENCES

1. Ehlen H.W.A., Chinenkova M., Moser M., Munter H.M., Krause Y., Gross S., Brachvogel B., Wuelling M., Kornak U., Vortkamp A. // J. Bone Mineral Res. 2013. V. 28. № 2. P. 246–259.
2. Zhang Y., Le T., Grabau R., Mohseni Z., Kim H., Natale D.R., Feng L., Pan H., Yang H. // Sci. Advanc. 2020. V. 6. P. eaba0310.
3. Ousingsawat J., Wanitchakool P., Schreiber R., Wuelling M., Vortkamp A., Kunzelmann K. // J. Biol. Chem. 2015. V. 290. № 10. P. 6270–6280.
4. Yang H., Kim A., David T., Palmer D., Jin T., Tien J., Huang F., Cheng T., Coughlin S.R., Jan Y.N., et al. // Cell. 2012. V. 151. № 1. P. 111–122.
5. Cabrita I., Benedetto R., Schreiber R., Kunzelmann K. // JCI Insight. 2019. V. 4. № 15. P. e128414.
6. Braga L., Ali H., Secco I., Chiavacci E., Neves G., Goldhill D., Penn R., Jimenez-Guardeño J.M., Ortega-Prieto A.M., Bussani R., et al. // Nature. 2021. V. 594. № 7861. P. 88–93.
7. Martins J.R., Faria D., Kongsuphol P., Reisch B., Schreiber R., Kunzelmann K. // Proc. Natl. Acad. Sci. USA. 2011. V. 108. № 44. P. 18168–18172.
8. Kolesnikov D., Perevoznikova A., Gusev K., Glushankova L., Kaznacheyeva E., Shalygin A. // Int. J. Mol. Sci. 2021. V. 22. № 9. P. 4767
9 Kolesnikov D.O., Nomerovskaya M.A., Grigorieva E.R., Reshetin D.S., Skobeleva K.V., Gusev K.O., Shalygin A.V., Kaznacheyeva E.V. // Biochem. Biophys. Res. Commun. 2024. V. 693. P. 149378.
10. Ye W., Han T.W., He M., Nung Jan Y., Yeh Jan L. // eLife. 2019. V. 8. P. e45187.
11. Kalienkova V., Clerico Mosina V., Paulino C. // J. Mol. Biol. 2021. V. 433. № 16. P. 166941.
12. Lim N.K., Lam A.K.M., Dutzler R. // J. Gen. Physiol. 2016. V. 148. № 5. P. 375–392.

Studying Signaling Pathway Activation in TRAIL-Resistant Macrophage-Like Acute Myeloid Leukemia Cells

Y. V. Lomovskaya[1*], K. S. Krasnov[1], M. I. Kobyakova[1,2], A. A. Kolotova[1], A. M. Ermakov[1], A. S. Senotov[1], I. S. Fadeeva[1], E. I. Fetisova[1], A. I. Lomovsky[1], A. I. Zvyagina[1], V. S. Akatov[1], R. S. Fadeev[1]
[1]Institute of Theoretical and Experimental Biophysics of the Russian Academy of Sciences, Pushchino, Moscow region, 142290 Russian Federation
[2]Institute of Clinical and Experimental Lymphology, Branch of the Institute of Cytology and Genetics SB RAS, Novosibirsk, 630060 Russian Federation
*E-mail: yannalomovskaya@gmail.com
Received: November 01, 2023; in final form, January 31, 2024
DOI: 10.32607/actanaturae.27317

ABSTRACT **Acute myeloid leukemia (AML) is a malignant neoplasm characterized by extremely low curability and survival. The inflammatory microenvironment and maturation (differentiation) of AML cells induced by it contribute to the evasion of these cells from effectors of antitumor immunity. One of the key molecular effectors of immune surveillance, the cytokine TRAIL, is considered a promising platform for developing selective anticancer drugs. Previously, under *in vitro* conditions of the inflammatory microenvironment (a three-dimensional high-density culture of THP-1 AML cells), we demonstrated the emergence of differentiated macrophage-like THP-1ad clones resistant to TRAIL-induced death. In the present study, constitutive activation of proinflammatory signaling pathways, associated transcription factors, and increased expression of the anti-apoptotic *BIRC3* gene were observed in TRAIL-resistant macrophage-like THP-1ad AML cells. For the first time, a bioinformatic analysis of the transcriptome revealed the main regulator, the *IL1B* gene, which triggers proinflammatory activation and induces resistance to TRAIL in THP–1ad macrophage-like cells.**
KEYWORDS **acute myeloid leukemia, TRAIL-induced apoptosis, transcriptome, inflammation.**

ABBREVIATIONS **AML – acute myeloid leukemia; TRAIL – tumor necrosis factor (TNF)-related apoptosis inducing ligand; TF – transcription factor; INF – interferon; IL – interleukin; FDR – false discovery rate; DEG – differentially expressed genes; PPI – protein–protein interactions.**

INTRODUCTION

Acute myeloid leukemia (AML) is a malignant blood disease characterized by extremely low curability and poor chance of survival [1]. Despite the progress made in therapeutic strategies over the past decade, the overall five-year survival rate is only 30% in patients diagnosed with AML [2]. AML is characterized by uncontrolled clonal expansion and accumulation (hypercellularity) of malignantly transformed hematopoietic progenitor cells in bone marrow and peripheral blood. It is well known that in acute myeloid leukemia, the bone marrow acquires the characteristics of damaged tissue, with signs of chronic inflammation [3, 4]. The inflammatory process in the bone marrow contributes to the avoidance of tumor cell death induced by both antitumor drugs and components of antitumor immunity; therefore, it is a marker of an unfavorable prognosis in the course of the disease [5–7]. It is also known that under inflammatory conditions, activation of proinflammatory intracellular signaling pathways can lead to myeloid differentiation of healthy hematopoietic progenitor cells [8–10]. Recently, there has appeared evidence that AML cells with a differentiated (mature) myeloid phenotype can suppress the activity of antitumor immunity and are more resistant to a number of antitumor drugs [11–13].

The apoptosis-inducing ligand (TRAIL), which is related to the tumor necrosis factor (TNF), is a key molecular component of antitumor immunity. Cytokine TRAIL binds to four membrane-bound receptors: pro-apoptotic DR4 and DR5, anti-apoptotic DcR1 and DcR2, and to the soluble anti-apoptotic "receptor" osteoprotegerin [14]. TRAIL is unique in its ability to selectively induce the death of tumors and transformed cells in the absence of cytotoxic effects on healthy cells. This property is very attractive and promising for the development of highly active agonists of pro-apoptotic TRAIL receptors, which, in turn, is extremely important for reducing any serious non-specific side effects of immunobiological antitumor drugs [15, 16].

Previously, we showed that in AML THP-1 cells under *in vitro* conditions, in a three-dimensional high-density culture simulating homotypic intercellular communication in the hyperplasia of leukemic blasts in the bone marrow, there was an increase in the production of proinflammatory cytokines, chemokines, and growth factors; activation of proinflammatory NF-kB-dependent signaling pathways; and a reversible increase in resistance to TRAIL-induced death and to the action of chemotherapeutic drugs [17, 18]. In addition, we have shown that macrophage-like clones THP-1ad with constitutive resistance to TRAIL-induced death appear in a three-dimensional high-density culture of these cells [19]. Differentiation of AML cells is also known to increase their resistance to TRAIL-induced death [20, 21].

Hence, based on the published data and our own results, we assume that the proinflammatory microenvironment of AML cells, simulated in a three-dimensional high-density cell culture *in vitro*, can induce cell maturation and lead to the emergence of new cell clones resistant to the cytotoxic effect of antitumor cytokine TRAIL. In this study, the bioinformatic analysis of the transcriptomes of macrophage-like THP-1ad cells that had formed under conditions of a proinflammatory microenvironment and were resistant to TRAIL-induced death identified the main signaling pathways and the key molecular participants associated with the activation of the survival pathways.

EXPERIMENTAL

Cell cultures

The THP-1 human AML cell line (TB-202) was procured from ATCC (Manassas, VA, USA). Proliferating macrophage-like clones THP-1ad were obtained as previously described [19]. The cells were cultured in a RPMI 1640/F12 medium (Sigma, USA) supplemented with 10% fetal bovine serum (FBS) (Gibco, USA) and 40 μg/mL gentamicin sulfate (Sigma) at 37°C in the presence of 5% CO_2. Non-proliferating macrophage-like THP-1PMA cells were obtained by incubating THP-1 cells with 200 nM phorbol-12-myristate-13-acetate (Sigma) for 96 h. For proinflammatory activation, THP-1 cells were cultured with 10 μg/mL LPS from *Escherichia coli* O111:B4 (Sigma) for 24 h.

Cell transcriptome sequencing

RNA sequencing for the analysis of cell transcriptomes was performed at Genoanalytika LLC using a HiSeq 1500 sequencer (Illumina, USA). RNA sequencing of each of the two groups of cells was performed in triplicate.

Analysis of differential gene expression

To identify differences in gene expression between macrophage-like clones THP-1ad and parent THP-1 cells, cluster analysis and principal component analysis using the Python programming language (v. 3.10.5) and the Scikit-learn package (v. 1.3.2) were performed (*Fig. 1*).

Gene set enrichment analysis (GSEA) was used to study the activation of signaling pathways in macrophage-like THP-1ad clones compared to parent THP-1 cells, since this method analyzes all the changing genes rather than only the genes with a multiplicity of changes above a certain threshold [22]. Gene sets from the H (Hallmark) and C3 collections (transcription factor target gene sets) of the MSigDB molecular signature database (https://www.gsea-msigdb.org/gsea/msigdb/human/collections.jsp) were analyzed using the Python programming language software package (v. 3.10) GSEApy (v. 1.0.5). The enrichment score was used as a criterion for the activation of signaling pathways and transcription factors (TF). Additionally, the normalized enrichment score (NES) was used to compare sets of genes containing different numbers of genes. The higher the value of the NES or enrichment score, the higher the probability of activation of the signaling pathway or TF is.

To identify differentially expressed genes (DEG), whose products can participate in the regulation of the studied signaling pathways, protein–protein interaction networks (PPIs) were constructed and their functional interactions were analyzed to identify the central regulatory elements. We used the STRING database (http://string-db. org), Cytoscape software (v. 3.10.0), and CytoHubba plugin [23].

Quantitative reverse transcription PCR

Total RNA was isolated using an innuPREP RNA Mini Kit 2.0 (Analytik Jena, Germany). cDNA was synthesized and amplified using the One Tube RT-PCR SYBR kit (Eurogen, Russia) on a QuantStudio 5 Real-Time PCR device (Thermo Scientific, USA), according to the manufacturer's instructions. The oligonucleotide primers used in this study were synthesized at Eurogen CJSC and are listed in *Table 1*.

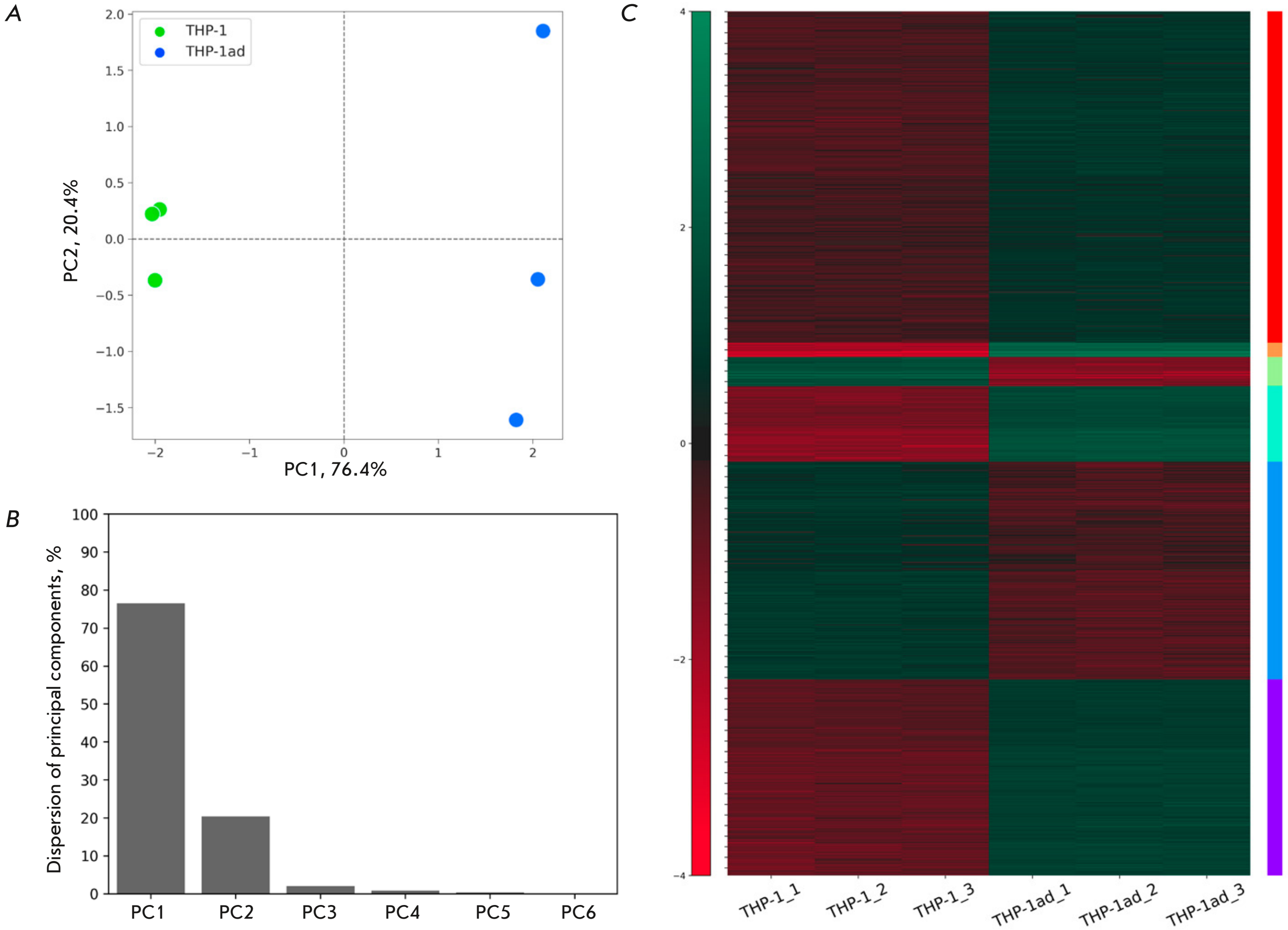

Fig. 1. Comparative analysis of gene expression variations between THP-1ad and THP-1 cells. An analysis using principal component analysis was conducted for gene expression data to identify changes in expression between two experimental groups (*A*). Allocation of variation among the major components (*B*). Clustering of differentially expressed genes (DEGs) with significant changes in expression (*C*)

Statistical analysis

Results are presented as a mean ± standard deviation (M ± SD). Experiments were performed with at least five repetitions ($n \geqslant 5$). The statistical significance of the differences was determined using one–sided ANOVA, followed by multiple Holm–Sidak comparisons ($p < 0.05$). The statistical significance of changes in gene expression was assessed using the Wald test adjusted for multiple Benyamini–Hochberg comparisons (FDR) $\leqslant 0.05$ [24].

RESULTS AND DISCUSSION

Identification of the most activated signaling pathways in macrophage-like clones THP-1ad

Previously, we demonstrated the formation of macrophage-like clones THP-1ad *in vitro* in three-dimensional high-density cultures of THP-1 AML cells with increased resistance to TRAIL-induced death [19]. To determine the main signaling pathways and potential mechanisms of TRAIL resistance in macrophage-like THP-1ad clones, the transcriptomes of these cells were sequenced, followed by an analysis of differential gene expression in comparison with the parent THP-1 cells.

To identify the activity of intracellular signaling pathways, gene set enrichment analysis (GSEA) of the MSigDB database [25] was performed on the entire transcriptome sequencing dataset, which allows one to analyze the activation/deactivation of the studied signaling pathway or all the target genes under study, because of the contribution of even minor changes in the transcriptional activity [22].

Gene set enrichment analysis using the H collection showed that in the macrophage-like clones THP-1ad,

Table 1. The oligonucleotide primers used in this study

Oligonucleotide	The nucleotide sequence 5’→3’
NAIP-F	GGGGACTTCGTCTGGGATTC
NAIP-R	CTGGCCAGTGGAAGGAAAGT
CIAP1-F	CTGATTCCCGGCTCTGCG
CIAP1-R	AGCACGAGCAAGACTCCTTT
CIAP2-F	TCCATGGGTTCAACATGCCA
CIAP2-R	CTCCTGGGCTGTCTGATGTG
XIAP-F	TGGCGCTCATCGAGGGA
XIAP-R	TGTCTGCAGGTACACAAGTTTTAG
Survivin-F	TTCAAGGAGCTGGAAGGCTG
Survivin-R	GCAACCGGACGAATGCTTTT
BRUCE-F	AGAAAGGGATGATGCAAGTACG
BRUCE-R	CTACCTGGGCTGCTGAACTC
Livin-F	GGCCTCCTTCTATGACTGGC
Livin-R	GCAGAAGAAGCACCTCACCT
ILP-2-F	GGAGAGGAAAAGCGTTGTGC
ILP-2-R	TCTTCACTATGCATGGCGGG
BCL2-F	CAACATCGCCCTGTGGATGA
BCL2-R	CCGTACAGTTCCACAAAGGC
BCL2L1-F	GGCTTGTTCGGGAGAGACG
BCL2L1-R	CACTGAGTCTCGTCTCTGGTT
MCL1-F	TGGAGACCTTACGACGGGTT
MCL1-R	AGCACATTCCTGATGCCACC
BCL2L2-F	CGACTGTGACTCTGCTGCAA
BCL2L2-R	TCTCCCTGACTCGAGCTTTG
BCL2A1-F	GGATAAGGCAAAACGGAGGC
BCL2A1-R	TCTTCTTGTGGGCCACTGAC

the sets of genes of the interferon alpha response (NES 2.13), IL6 JAK STAT3 signaling (NES 2.06), inflammatory response (NES 2.01), interferon gamma response (NES 1.98), and TNFA signaling via NF-KB (NES 1.96) had the highest positive normalized enrichment score (NES) (*Fig. 2A*), indicating activation of these signaling pathways. It is well known that the activity of the identified signaling pathways is characteristic of proinflammatory activation of cells [26–28]. We also found that in macrophage-like clones THP-1ad, the activity of the signaling pathways MYC targets V1 (NES -2.86), MYC targets V2 (NES -2.83), and oxidative phosphorylation (NES–2.03) was suppressed, as evidenced by the highest negative value of NES. Suppression of these signaling pathways is also characteristic of the proinflammatory activation of cells and increased resistance to TRAIL-induced death [29–31].

To identify the most probable TF controlling the expression of the genes from the sets with the highest positive NES value, that is, those directly involved in the activation of the aforementioned signaling pathways in macrophage-like clones THP-1ad, gene set enrichment analysis was performed using a C3 collection and sets of genes containing sequences for binding to TF of the IRF, STAT, and NF-kB families.

It was shown that of all the sets of the C3 collection (subcollections of TFT:TFT_LEGACY) containing genes binding TF of the IRF family, the sets of genes IRF_Q6 (ES 0.46), STTTCRNTTT_IRF_Q6 (ES 0.46), IRF1_Q6 (ES 0.45), and IRF7_01 (ES 0.45) were significantly ($FDR \leqslant 0.05$) enriched and had a positive enrichment score (ES), which indicates the transcriptional activity of IRF1 and IRF7 factors. When studying sets containing genes with sequences for binding TF of the STAT family, it was found that the sets of STAT3_02 (ES 0.48) and STAT6_02 (ES 0.42) genes were significantly enriched ($FDR \leqslant 0.05$) and had a positive ES, indicating the transcriptional activity of STAT3 and STAT6 factors. A study of the sets containing genes with sequences binding NF-kB showed that the sets GGGNNTTTCC_NFKB_Q6_01, NFKB_Q6_01, NFKAPPAB_01, NFKB_Q6, and NFKAPPAB65_01 were significantly enriched ($FDR \leqslant 0.05$) and had positive enrichment scores of 0.524001, 0.485919, 0.477002, 0.458895, and 0.44804, respectively, indicating an expressed NF-kB-dependent transcriptional activity (*Fig. 2A–2D*).

The regulatory factors interferon IRF1 and IRF7 are known to regulate the expression of interferons of the first (α and β) and second (γ) types, acting as inducers of inflammation in the development of tumor diseases [32–34]. STAT3 and STAT6 are also known to be activated during inflammation in the tumor mi-

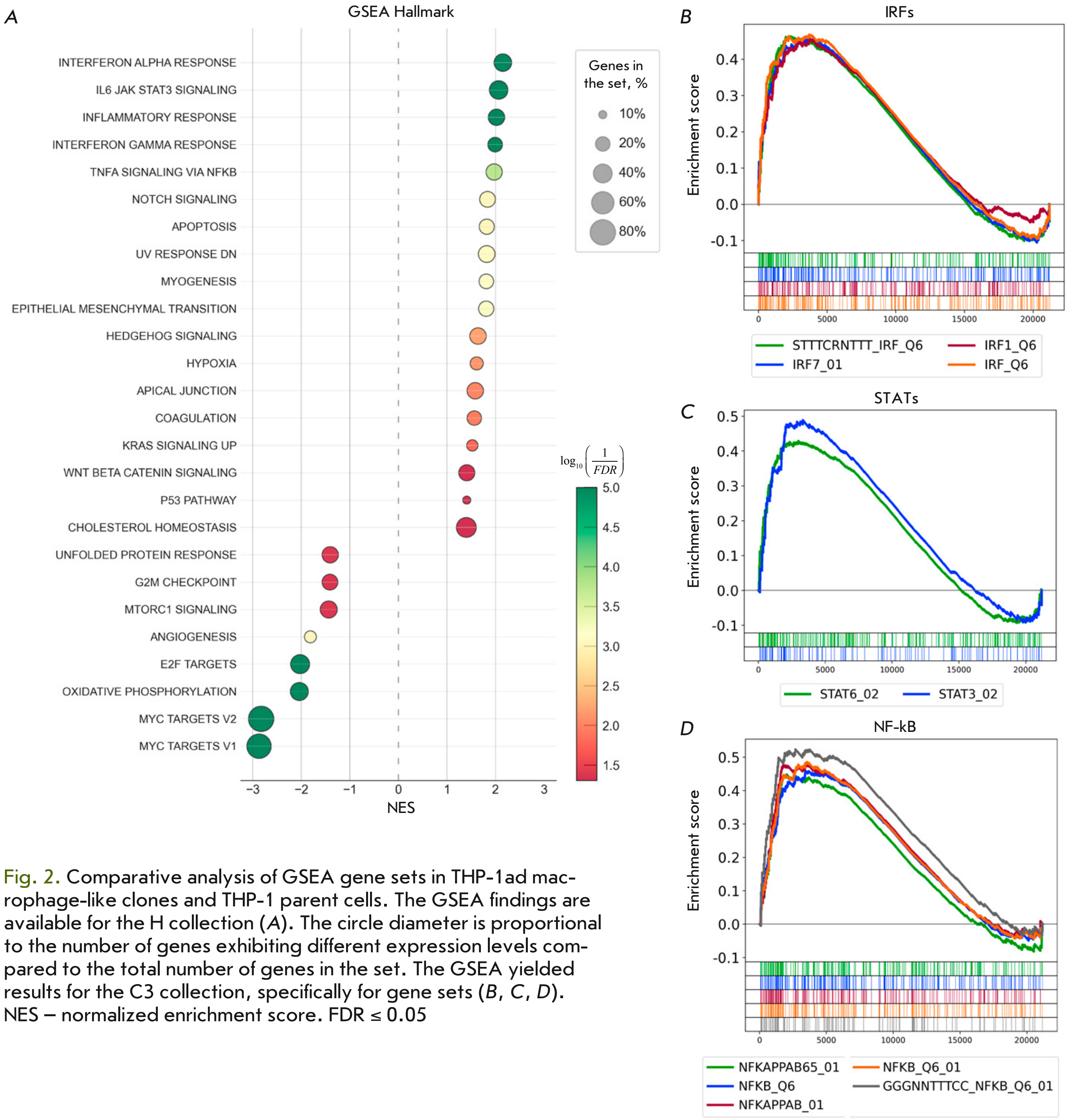

Fig. 2. Comparative analysis of GSEA gene sets in THP-1ad macrophage-like clones and THP-1 parent cells. The GSEA findings are available for the H collection (*A*). The circle diameter is proportional to the number of genes exhibiting different expression levels compared to the total number of genes in the set. The GSEA yielded results for the C3 collection, specifically for gene sets (*B*, *C*, *D*). NES – normalized enrichment score. FDR ≤ 0.05

croenvironment; their activity may be associated with an increased inflammatory response during leukemia progression [35–37]. It has been posited that NF-kB plays a role in the formation of a leukemic microenvironment during the stimulation of a chronic inflammation in the BM niche under the effect of the cytokine tumor necrosis factor-α (TNFα), which supports a favorable environment for the survival and production of leukemic cells [38–40].

Hence, it can be assumed that proinflammatory signaling pathways associated with IFNα, IFNγ, IL-6, and TNFα are constitutively active in macrophage-like clones THP-1ad. In addition, the data obtained indicate that IRF1, IRF7, STAT3, STAT6, and NF-kB, the

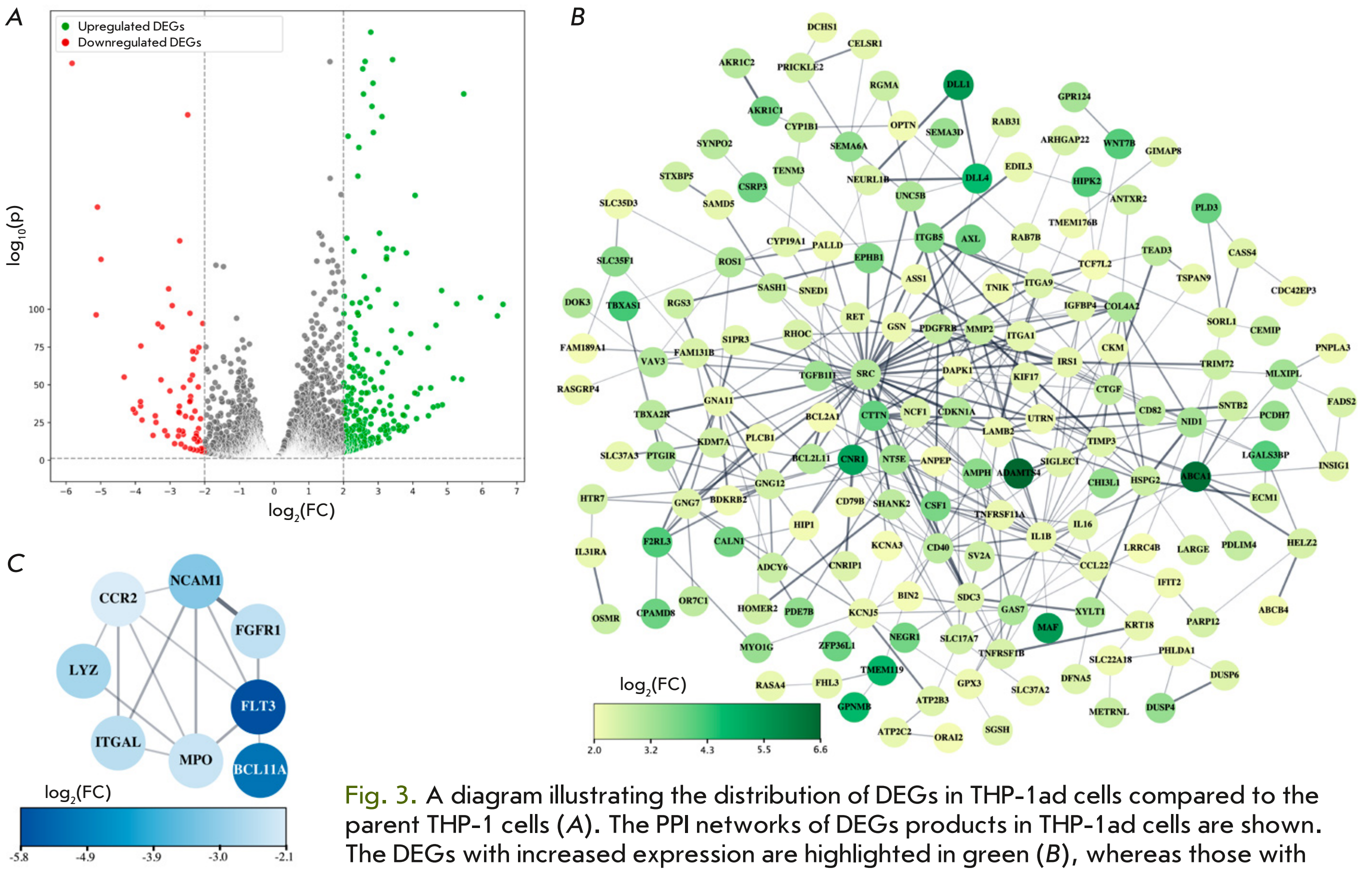

Fig. 3. A diagram illustrating the distribution of DEGs in THP-1ad cells compared to the parent THP-1 cells (*A*). The PPI networks of DEGs products in THP-1ad cells are shown. The DEGs with increased expression are highlighted in green (*B*), whereas those with decreased expression are highlighted in blue (*C*)

known modulators of tumor cell resistance, are involved in the activation of these processes.

Identification of the potential regulatory genes involved in TRAIL resistance in macrophage-like THP-1ad clones

To determine the DEGs whose products are most likely to act as regulatory elements of identifiable signaling pathways in macrophage-like clones THP-1ad from 21,511 transcribed genes, 355 DEGs were selected corresponding to the parameter $2 \leqslant \log_2(FC) \leqslant -2$. Identification of the selected DEGs showed increased expression of 286 genes and decreased expression of 69 genes compared to those in the parent THP-1 cells (*Fig. 3A*).

PPI networks were built for DEGs with increased and decreased expression in order to identify interactions between DEGs products using the STRINGdb database [41]. It was shown that 167 out of the 286 genes with increased expression formed an interconnected network (*Fig. 3B*), whereas only eight out of the 69 genes with reduced expression formed a connected network (*Fig. 3C*).

We analyzed the PPI network only for DEGs with increased expression, because it contained more interconnected participants than the DEGs network with reduced expression did, which could potentially make a more significant contribution to the formation of TRAIL resistance in macrophage-like THP-1ad clones. Clustering was then performed among the genes with increased expression in the PPI network using the cytoHubba module plug-in in the Cytoscape software [23]. Clustering was performed using 12 available cytoHubba algorithms to identify the most likely hub genes that could potentially contribute more to the formation of the PPI network and, thus, become potential targets for reducing TRAIL resistance in macrophage-like clones THP-1ad. Using cytoHubba algorithms, 20 genes with the highest rank value were identified in the analyzed PPI network. The rank in the PPI network shows the degree of "importance" of a gene, and the higher the rank (the closer to zero), the more significant this gene is for the formation of the network (*Fig. 4*).

In the PPI network clusters shown in *Fig. 4*, the five most repetitive genes were selected with the

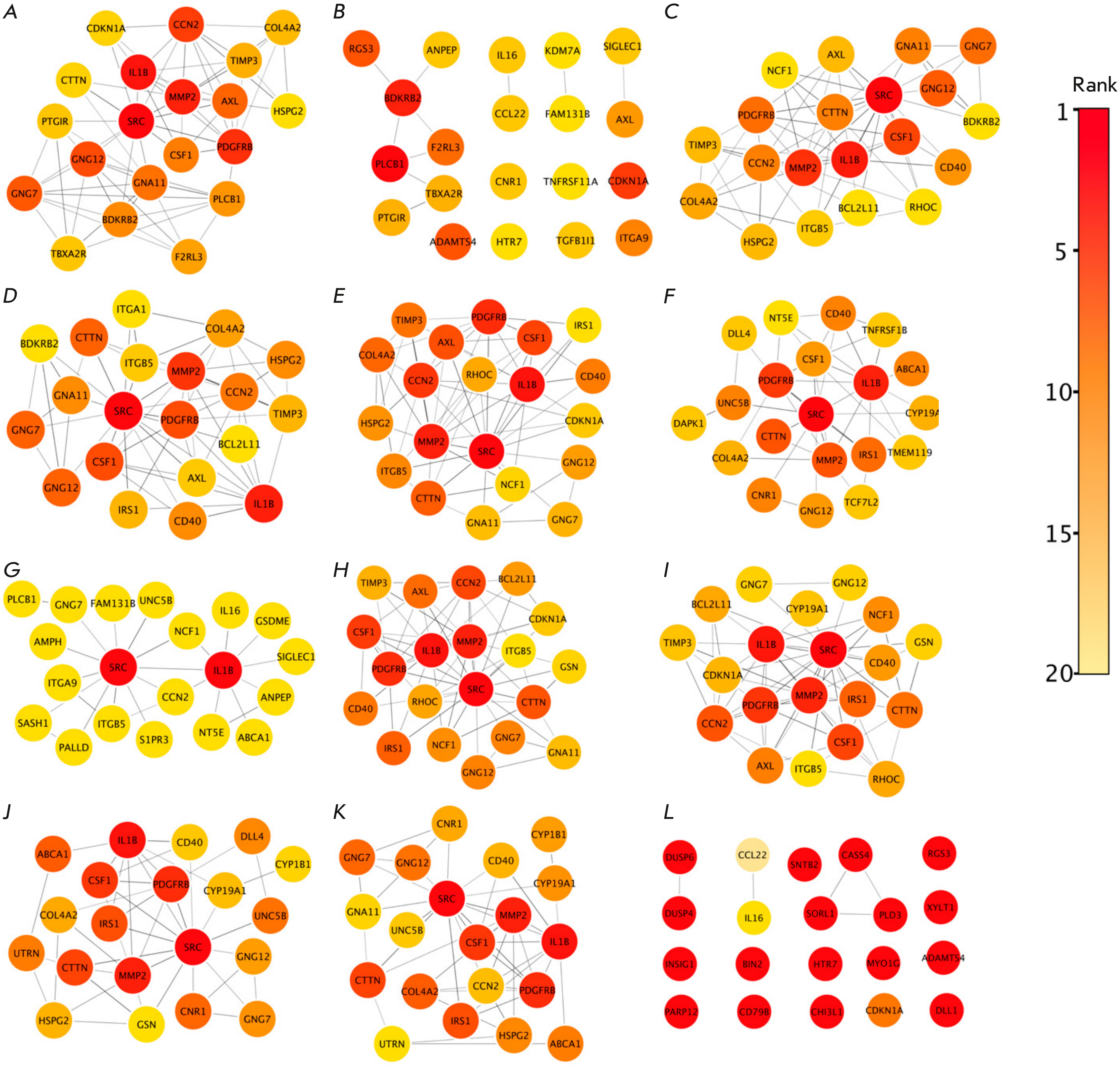

Fig. 4. Clustering of the PPI network of genes with increased expression using the cytoHubba module algorithms: MCC (*A*), DMNC (*B*), MNC (*C*), Degree (*D*), EPC (*E*), BottleNeck (*F*), EcCentricity (*G*), Closeness (*H*), Radiality (*I*), Betweenness (*J*), Stress (*K*), and ClusteringCoefficient (*L*)

highest rank value, namely *CSF1*, which encodes a macrophage colonystimulating factor (M-CSF); *PDGFRB*, encoding the platelet growth factor receptor (PDGF); *MMP2*, encoding matrix metalloproteinase 2; *SRC*, encoding non-receptor tyrosine kinase SRC; and *IL1B* encoding interleukin1ß (IL-1ß). The role of the products of identifiable hub genes is well known in myeloid maturation, proinflammatory activation of cells, and progression of AML. M-CSF is the main regulator of macrophage differentiation and a promising target for AML therapy [42, 43]. The PDGF receptor has been shown to participate in

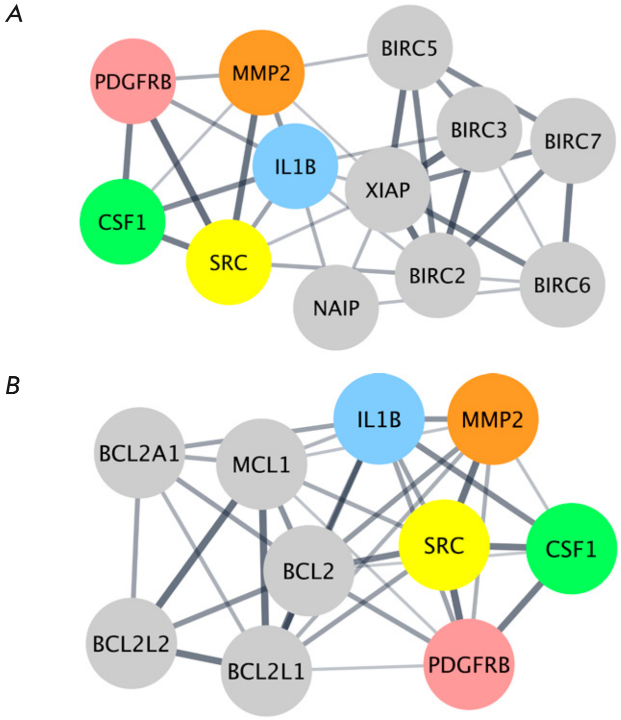

Fig. 5. The discovered *IL1B*, *SRC*, *PDGFRB*, *MMP 2*, and *CSF1* hub genes are connected in PPI networks with antiapoptotic members of the IAPs (*A*) and BCL-2 (*B*) families

the myeloid maturation of leukemic cells, activation of proto-oncogenic tyrosine kinases of the SRC family, and maintenance of the viability and proliferation of tumor cells [44–46]. SRC tyrosine kinases are the specific signaling integrators necessary for normal hematopoiesis and progression of acute leukemia [47, 48]. The role of IL-1β in the development of inflammatory processes and malignant neoplasms is well known. For example, chronic inflammation mediated by IL-1β is often associated with the emergence and progression of malignant tumors, as well as the direct regulation of myeloid cell differentiation and the signaling pathways that mediate the survival of leukemic cells [49–51]. Matrix metalloproteinases are involved in the migration of myeloid cells induced by an inflammation, and their suppression significantly reduces the viability and proliferation of AML cells [52, 53].

Therefore, the most probable regulatory genes of the signaling pathways activated in macrophage-like THP-1ad clones, such as *CSF1, PDGFRB, MMP2, SRC*, and *IL1B*, have been identified. The products of the identified genes can serve as promising targets for the suppression of TRAIL resistance in THP-1ad macrophage-like clones.

Investigation of the interaction of hub genes with members of the IAPs and BCL-2 families

It is well known that the main intracellular positive regulators of AML cell resistance to TRAIL-induced apoptosis are members of the BCL-2 and IAPs families, which block apoptosis at the mitochondrial and effector caspase levels [18, 54, 55]. PPI networks were built to determine the potential interaction of the identified hub genes with anti-apoptotic members of the IAPs and BCL-2 families.

Among the five identified hub genes, only *MMP2* (partners of *BIRC5* and *XIAP*), *IL1B* (partners of *BIRC2, BIRC3, NAIP*, and *XIAP*), and *SRC* (partners of *BIRC2* and *XIAP*) interacted with members of the IAPs family (*Fig. 5A*). Simultaneously, all the identified hub genes interacted with members of the BCL-2 family. The partners of the *IL1B* gene are *BCL2*, *BCL2A1*, and *MCL1*; the partners of the *SRC*, *PDGFRB*, and *MMP2* genes are *BCL2*, *BCL2L1*, and *MCL1*; and that of the *CSF1* gene is *BCL2* (*Fig. 5B*). Hence, all the identified concentrator genes can interact with anti-apoptotic members of the IAPs and BCL-2 families, which, in turn, indicates the potential participation of these families in the mechanism of resistance of macrophage-like THP-1ad cells to TRAIL-induced death.

Furthermore, expression of all the anti-apoptotic members of the IAPs and BCL-2 family in macrophage-like THP-1ad clones and in parent THP-1 cells was revealed by quantitative reverse transcription PCR. Additionally, expression of these genes was analyzed in THP-1 cells treated with forbol ether (THP-1PMA) and LPS (THP-1LPS), known inducers of macrophage differentiation and activation of proinflammatory signaling pathways, respectively [56, 57].

In THP-1ad cells, expression of only the *BIRC3* gene encoding the cIAP2 protein, an inhibitor of caspases 3, 7, 8, and 10, was significantly increased (63 ± 7 times) ($p \leqslant 0.05$) [58]. Similar results were obtained for THP-1LPS cells, and only the expression of the *BIRC3* gene was also significantly ($p \leqslant 0.05$) increased (42 ± 3 times). No significant increase in the expression of IAPs family members was observed in THP-1PMA cells (*Fig. 6A*). An analysis of the expression of the BCL-2 family anti-apoptotic genes revealed a significant ($p \leqslant 0.05$) increase (48 ± 6 times) in the expression of the *MCL1* gene. Inhibitors of the proapoptotic proteins Bax and Bak were expressed only in THP-1PMA cells (*Fig. 6B*) [59].

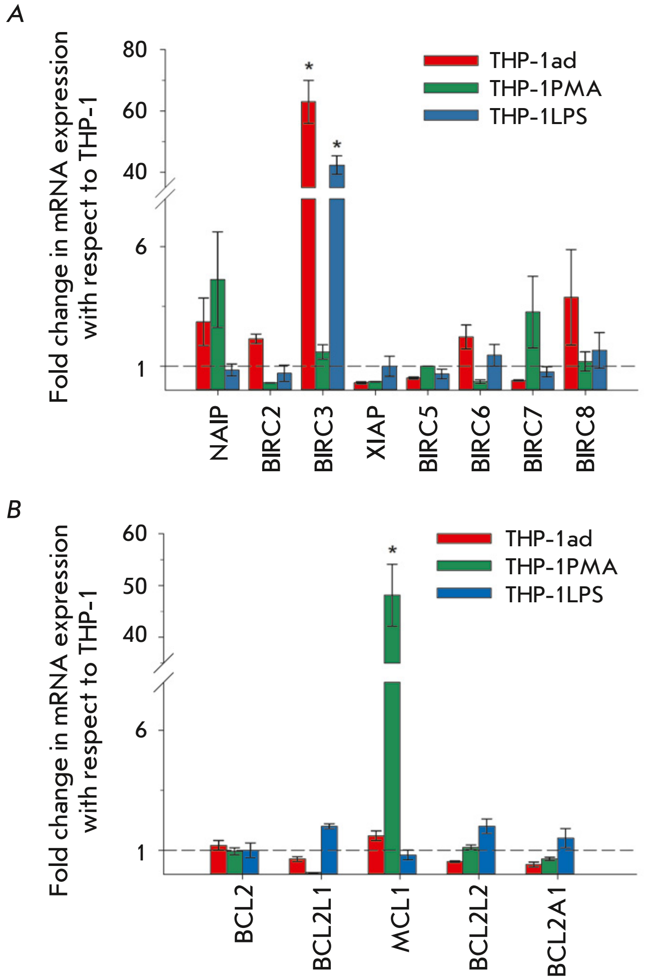

Fig. 6. Gene expression of IAPs (*A*) and BCL-2 (*B*) family members was analyzed in macrophage-like THP-1ad clones, THP-1 PMA, and THP-1LPS cells. The data are presented as the mean value ± SD ($n \geq 5$). Statistical significance ($^*p \leq 0.05$) was observed when comparing the parent cells of THP-1

Therefore, in macrophage-like THP-1ad clones, the increase in the expression of the *BIRC3* gene, which is a partner of the *IL1B* hub gene, is characteristic of proinflammatory activation, which most likely indicates the key role of this hub gene in increasing resistance to TRAIL-induced death.

The data on the activation of inflammatory processes in the bone marrow microenvironment in AML [5, 6, 60] and the role of cytokine IL1ß in the progression of myeloid leukemia have been reported [51, 61, 62]. In addition, macrophage differentiation is accompanied by increased expression of the cIAP2 protein [63]. However, these data on the possible participation of IL-1β-mediated proinflammatory activation in the development of the resistance of macrophage-like AML cells to cytotoxic TRAIL, potentially implemented through increased expression of *BIRC3*, were obtained here for the first time.

CONCLUSION

Transcriptomic analysis of macrophage-like TRAIL-resistant THP-1ad clone AML cells, which were obtained under model conditions of the proinflammatory microenvironment of leukemic cells, showed high constitutive activity of the intracellular proinflammatory signaling pathways associated with IFNα, IFNβ, IL-6, and TNFα. The most probable TF, such as IRF1, IRF7, STAT3, STAT6, and NF-kB, have also been identified, potentially determining the activation of these signaling pathways. When searching for potential regulators of the identified proinflammatory signaling pathways, the most probable participants in these pathways, *CSF1, PDGFRB, MMP2, SRC*, and *IL1B*, were identified. It was also revealed that in THP-1ad cells, with proinflammatory activation, expression of the *BIRC3* gene encoding cIAP2, an inhibitor of effector caspases, increased, which may mediate an increase in resistance to the cytotoxic TRAIL ligand. An important result is the discovery of a key molecular participant, the *IL1B* gene, which potentially links the processes of proinflammatory activation and the development of resistance to TRAIL in macrophage-like THP-1ad clones. Therefore, we believe that the mechanism of TRAIL resistance induction during the activation of inflammation in macrophage-like AML cells may consist of a IL-1β-associated, through NF-kB, increase in the expression of the inhibitor of apoptosis cIAP2. ●

This study was conducted as part of State Assignment No. 075-00224-24-01.

REFERENCES

1. Short N.J., Rytting M.E., Cortes J.E. // The Lancet. 2018. V. 392. № 10147. P. 593–606.
2. Kantarjian H., Kadia T., DiNardo C., Daver N., Borthakur G., Jabbour E., Garcia-Manero G., Konopleva M., Ravandi F. // Blood Cancer J. 2021. V. 11. № 2. P. 41.
3. Récher C. // Front. Oncol. 2021. V. 11. P. 623952.
4. Cook E.K., Luo M., Rauh M.J. // Exp. Hematol. 2020. V. 83. P. 85–94.
5. Zhong F.-M., Yao F.-Y., Liu J., Zhang H.-B., Li M.-Y., Jiang J.-Y., Xu Y.-M., Yang W.-M., Li S.-Q., Zhang J., et al. // Biosci. Rep. 2022. V. 42. № 5. P. BSR20220647.

6. Ellegast J.M., Alexe G., Hamze A., Lin S., Uckelmann H.J., Rauch P.J., Pimkin M., Ross L.S., Dharia N.V., Robichaud A.L., et al. // Cancer Discov. 2022. V. 12. № 7. P. 1760–1781.
7. Lasry A., Nadorp B., Fornerod M., Nicolet D., Wu H., Walker C.J., Sun Z., Witkowski M.T., Tikhonova A.N., Guillamot-Ruano M., et al. // Nat. Cancer. 2022. V. 4. № 1. P. 27–42.
8. Mysore V., Tahir S., Furuhashi K., Arora J., Rosetti F., Cullere X., Yazbeck P., Sekulic M., Lemieux M.E., Raychaudhuri S., et al. // J. Exp. Med. 2022. V. 219. № 5. P. e20210562.
9. Hernandez G., Mills T.S., Rabe J.L., Chavez J.S., Kuldanek S., Kirkpatrick G., Noetzli L., Jubair W.K., Zanche M., Myers J.R., et al. // Haematologica. 2020. V. 105. № 3. P. 585–597.
10. Maltby S., Hansbro N.G., Tay H.L., Stewart J., Plank M., Donges B., Rosenberg H.F., Foster P.S. // J. Immunol. 2014. V. 193. № 8. P. 4072–4082.
11. Yoyen-Ermis D., Tunali G., Tavukcuoglu E., Horzum U., Ozkazanc D., Sutlu T., Buyukasik Y., Esendagli G. // Sci. Rep. 2019. V. 9. № 1. P. 11697.
12. Van Galen P., Hovestadt V., Wadsworth Ii M.H., Hughes T.K., Griffin G.K., Battaglia S., Verga J.A., Stephansky J., Pastika T.J., Lombardi Story J., et al. // Cell. 2019. V. 176. № 6. P. 1265-1281.e24.
13. Bottomly D., Long N., Schultz A.R., Kurtz S.E., Tognon C.E., Johnson K., Abel M., Agarwal A., Avaylon S., Benton E., et al. // Cancer Cell. 2022. V. 40. № 8. P. 850-864.e9.
14. Montinaro A., Walczak H. // Cell Death Differ. 2023. V. 30. № 2. P. 237–249.
15. Artykov A.A., Yagolovich A.V., Dolgikh D.A., Kirpichnikov M.P., Trushina D.B., Gasparian M.E. // Front. Cell Dev. Biol. 2021. V. 9. P. 733688.
16. Di Cristofano F., George A., Tajiknia V., Ghandali M., Wu L., Zhang Y., Srinivasan P., Strandberg J., Hahn M., Sanchez Sevilla Uruchurtu A., et al. // Biochem. Soc. Trans. 2023. V. 51. № 1. P. 57–70.
17. Kobyakova M.I., Evstratova Ya.V., Senotov A.S., Lomovsky A.I., Minaychev V.V., Zvyagina A.I., Solovieva M.E., Fadeeva I.S., Akatov V.S., Fadeev R.S. // Membr. Cell Biol. 2021. V. 38. № 1. P. 61–70.
18. Kobyakova M., Lomovskaya Y., Senotov A., Lomovsky A., Minaychev V., Fadeeva I., Shtatnova D., Krasnov K., Zvyagina A., Odinokova I., et al. // Int. J. Mol. Sci. 2022. V. 23. № 14. P. 7881.
19. Lomovskaya Y.V., Kobyakova M.I., Senotov A.S., Lomovsky A.I., Minaychev V.V., Fadeeva I.S., Shtatnova D.Y., Krasnov K.S., Zvyagina A.I., Akatov V.S., et al. // Biomolecules. 2022. V. 12. № 2. P. 150.
20. Lomovskaya Ya.V., Kobyakova M.I., Senotov A.S., Fadeeva I.S., Lomovsky A.I., Krasnov K.S., Shtatnova D.Yu., Akatov V.S., Fadeev R.S. // Membr. Cell Biol. 2022. V. 39. № 6. P. 457–473.
21. Dijk M.V., Murphy E., Morrell R., Knapper S., O'Dwyer M., Samali A., Szegezdi E. // Cancers. 2011. V. 3. № 1. P. 1329–1350.
22. Subramanian A., Tamayo P., Mootha V.K., Mukherjee S., Ebert B.L., Gillette M.A., Paulovich A., Pomeroy S.L., Golub T.R., Lander E.S., et al. // Proc. Natl. Acad. Sci. 2005. V. 102. № 43. P. 15545–15550.
23. Chin C.-H., Chen S.-H., Wu H.-H., Ho C.-W., Ko M.-T., Lin C.-Y. // BMC Syst. Biol. 2014. V. 8. № S4. P. S11.
24. Benjamini Y., Hochberg Y. // J. R. Stat. Soc. Ser. B Methodol. 1995. V. 57. № 1. P. 289–300.
25. Liberzon A., Subramanian A., Pinchback R., Thorvaldsdóttir H., Tamayo P., Mesirov J.P. // Bioinformatics. 2011. V. 27. № 12. P. 1739–1740.
26. Kopitar-Jerala N. // Front. Immunol. 2017. V. 8. P. 873.
27. Hirano T. // Int. Immunol. 2021. V. 33. № 3. P. 127–148.
28. Zelová H., Hošek J. // Inflamm. Res. 2013. V. 62. № 7. P. 641–651.
29. Bae S., Park P.S.U., Lee Y., Mun S.H., Giannopoulou E., Fujii T., Lee K.P., Violante S.N., Cross J.R., Park-Min K.-H. // Cell Rep. 2021. V. 35. № 11. P. 109264.
30. Liu L., Lu Y., Martinez J., Bi Y., Lian G., Wang T., Milasta S., Wang J., Yang M., Liu G., et al. // Proc. Natl. Acad. Sci. 2016. V. 113. № 6. P. 1564–1569.
31. Lee H.Y., Cha J., Kim S.K., Park J.H., Song K.H., Kim P., Kim M.-Y. // Mol. Cancer Res. 2019. V. 17. № 2. P. 544–554.
32. Qing F., Liu Z. // Front. Immunol. 2023. V. 14. P. 1190841.
33. Holicek P., Truxova I., Rakova J., Salek C., Hensler M., Kovar M., Reinis M., Mikyskova R., Pasulka J., Vosahlikova S., et al. // Cell Death Dis. 2023. V. 14. № 3. P. 209.
34. Provance O.K., Lewis-Wambi J. // Breast Cancer Res. 2019. V. 21. № 1. P. 59.
35. Huang B., Lang X., Li X. // Front. Oncol. 2022. V. 12. P. 1023177.
36. Delgado-Ramirez Y., Ocaña-Soriano A., Ledesma-Soto Y., Olguín J.E., Hernandez-Ruiz J., Terrazas L.I., Leon-Cabrera S. // Int. J. Mol. Sci. 2021. V. 22. № 8. P. 4049.
37. Karpathiou G., Papoudou-Bai A., Ferrand E., Dumollard J.M., Peoc'h M. // Pathol. - Res. Pract. 2021. V. 223. P. 153477.
38. Di Francesco B., Verzella D., Capece D., Vecchiotti D., Di Vito Nolfi M., Flati I., Cornice J., Di Padova M., Angelucci A., Alesse E., et al. // Cancers. 2022. V. 14. № 14. P. 3557.
39. Zhang T., Ma C., Zhang Z., Zhang H., Hu H. // MedComm. 2021. V. 2. № 4. P. 618–653.
40. Zhang S., Yang X., Wang L., Zhang C. // Oncol. Lett. 2018. V.16. № 1. P. 679-686.
41. Szklarczyk D., Gable A.L., Lyon D., Junge A., Wyder S., Huerta-Cepas J., Simonovic M., Doncheva N.T., Morris J.H., Bork P., et al. // Nucleic Acids Res. 2019. V. 47. № D1. P. D607–D613.
42. Jones C.V., Ricardo S.D. // Organogenesis. 2013. V. 9. № 4. P. 249–260.
43. Sletta K.Y., Castells O., Gjertsen B.T. // Front. Oncol. 2021. V. 11. P. 654817.
44. Shah K., Vincent F. // Mol. Biol. Cell. 2005. V. 16. № 11. P. 5418–5432.
45. Reiterer G., Yen A. // Cancer Res. 2007. V. 67. № 16. P. 7765–7772.
46. Pandey P., Khan F., Upadhyay T.K., Seungjoon M., Park M.N., Kim B. // Biomed. Pharmacother. 2023. V. 161. P. 114491.
47. Voisset E., Brenet F., Lopez S., De Sepulveda P. // Cancers. 2020. V. 12. № 7. P. 1996.
48. Patel R.K., Weir M.C., Shen K., Snyder D., Cooper V.S., Smithgall T.E. // PloS One. 2019. V. 14. № 12. P. e0225887.
49. Mon N.N., Senga T., Ito S. // Oncol. Lett. 2017. V. 13. № 2. P. 955–960.
50. Liu S.T., Pham H., Pandol S.J., Ptasznik A. // Front. Physiol. 2014. V. 4. P. 416.
51. Arranz L., Arriero M.D.M., Villatoro A. // Blood Rev. 2017. V. 31. № 5. P. 306–317.
52. Chou J., Chan M.F., Werb Z. // Microbiol. Spectr. 2016. V. 4. № 2. P. 4.2.18.
53. Pirillo C., Birch F., Tissot F.S., Anton S.G., Haltalli M.,

Tini V., Kong I., Piot C., Partridge B., Pospori C., et al. // Blood Adv. 2022. V. 6. № 10. P. 3126–3141.
54. Saraei R., Soleimani M., Movassaghpour Akbari A.A., Farshdousti Hagh M., Hassanzadeh A., Solali S. // Biomed. Pharmacother. 2018. V. 107. P. 1010–1019.
55. Hao X.-S., Hao J.-H., Liu F.-T., Newland A.C., Jia L. // Apoptosis. 2003. V. 8. № 6. P. 601–607.
56. Chanput W., Mes J.J., Wichers H.J. // Int. Immunopharmacol. 2014. V. 23. № 1. P. 37–45.
57. Page M.J., Kell D.B., Pretorius E. // Chronic Stress. 2022. V. 6. P. 247054702210763.
58. Mohamed M.S., Bishr M.K., Almutairi F.M., Ali A.G. // Apoptosis. 2017. V. 22. № 12. P. 1487–1509.
59. Sancho M., Leiva D., Lucendo E., Orzáez M. // FEBS J. 2022. V. 289. № 20. P. 6209–6234.
60. Lasry A., Nadorp B., Fornerod M., Nicolet D., Wu H., Walker C.J., Sun Z., Witkowski M.T., Tikhonova A.N., Guillamot-Ruano M., et al. // Nat. Cancer. 2022.
61. Wang Y., Sun X., Yuan S., Hou S., Guo T., Chu Y., Pang T., Luo H.R., Yuan W., Wang X. // Cytotherapy. 2020. V. 22. № 3. P. 127–134.
62. Carey A., Edwards D.K., Eide C.A., Newell L., Traer E., Medeiros B.C., Pollyea D.A., Deininger M.W., Collins R.H., Tyner J.W., et al. // Cell Rep. 2017. V. 18. № 13. P. 3204–3218.
63. Morón-Calvente V., Romero-Pinedo S., Toribio-Castelló S., Plaza-Díaz J., Abadía-Molina A.C., Rojas-Barros D.I., Beug S.T., LaCasse E.C., MacKenzie A., Korneluk R., et al. // PLOS ONE. 2018. V. 13. № 3. P. e0193643.

A Method for the Production of Recombinant VSVs with Confirmation of Biological Activity

V. D. Moroz[1#*], N. B. Gasanov[1#*], A. D. Egorov[1], A. S. Malogolovkin[1,2], M. O. Nagornykh[1], E. N. Subcheva[1], E. S. Kolosova[1], A. Yu. Fizikova[1], R. A. Ivanov[1], A. V. Karabelsky[1]
[1]Sirius University of Science and Technology, Krasnodar Region, Sirius, 354340 Russian Federation
[2]First Moscow State Medical University (Sechenov University), Moscow, 119435 Russian Federation
[#]These authors contributed equally to this work.
[*]E-mail: moroz.vd@talantiuspeh.ru; gasanov.nb@talantiuspeh.ru

Received: November 01, 2023; in final form, January 30, 2024
DOI: 10.32607/actanaturae.27314

ABSTRACT **The design of new effective cancer treatment methods is a promising and important research field in translational medicine. Oncolytic viruses can induce immunogenic cell death by activating the body's immune system to recognize tumor cells. This work presents the results for optimizing the production of recombinant vesicular stomatitis viruses (rVSVs). To ensure the assembly of viral particles, we developed the HEK293TN-T7 cell line, which stably expresses DNA-dependent RNA polymerase 7 for viral genome transcription, and obtained helper plasmids encoding viral genes under the control of the CAG promoter. The oncolytic activity of the purified virus preparation was assessed in a murine model of B16F10Red melanoma cells expressing a red fluorescent protein. The presented method makes it possible to obtain purified viral preparations with a high titer and oncolytic activity. The amplification of viral particles in a HEK293 suspension culture allows for rapid scalability. Therefore, the developed approach can be used to obtain other recombinant VSV-based oncolytic viruses for tumor immunotherapy.**

KEYWORDS **oncolytic viruses, vesicular stomatitis virus, cancer, melanoma, cytopathic effect, recombinant vesicular stomatitis virus**

ABBREVIATIONS **VSV – vesicular stomatitis virus; rVSV – recombinant vesicular stomatitis virus; GFP – green fluorescent protein; CPE – cytopathic effect; MOI – multiplicity of infection; CF – centrifugation; UCF – ultracentrifugation; $TCID_{50}$/ml – tissue culture infectious dose of the virus; bp – base pairs; RFP – red fluorescent protein.**

INTRODUCTION

Oncolytic viruses have long been considered as a potent antitumor drug. To date, the development of new oncolytic viruses is one of the priority areas of tumor immunotherapy. According to recent data, there are currently more than 200 clinical trials on the safety and effectiveness of oncolytic virus-based drugs [1, 2]. The RNA-containing vesicular stomatitis virus (VSV) effectively infects different human and animal cells while being non-pathogenic to humans. Low virulence, a rapid replication cycle in the cytoplasm (without integration into the genome), possibilities to obtain high virus titers when producing VSV in mammalian (BHK-21 and HEK293) cells and genetically modify viruses, as well as the absence of neutralizing antibodies in the human population, make VSV an ideal candidate for producing viral vaccines, transgene delivery vectors, and oncolytic viruses [3–5]. Assembly of such rVSVs as rVSV-dG-GFP involves transfection of BHK-21 cells with five plasmids and co-infection of cells with either the vaccinia virus (VV) or another virus expressing T7 DNA-dependent RNA polymerase (T7 RNA polymerase) [6]. When generating biotechnological products for further use as drugs, it is necessary to minimize the number of helper viruses, in particular the replication-competent ones, since the latter can cause viral contamination. In addition, the resulting drug preparation should not contain VV or other virus particles [7]. There are currently few works with a comprehensive and detailed description of all stages of the production, purification, concentration of VSV-based oncolytic viruses, and assessment of their functional activity for further studies. This paper presents a method for the production of purified replication-competent model rVSV encoding the green fluorescent protein (rVSV-dM51-GFP) without the use of a helper virus.

EXPERIMENTAL

Plasmids and genetic engineering

The following commercial plasmids were used for cloning: pBS-N-ФT-Kan (cat# EH1013, Kerafast, USA), pBS-P-ФT-Amp (cat# EH1014, Kerafast), pBS-L-ФT-Amp (cat# EH1015, Kerafast), pBS-G-OT-Kan (cat# EH1016, Kerafast), pCAGGS-G-Kan (cat# EH1017, Kerafast), pVSV-dG-GFP 2.6 (cat# EH1026, Kerafast), and pCAG-T7pol (cat# 59926, Addgene). *Escherichia coli* strains (DH5-alpha, NEB® Stable (cat# C3040H, NEB, Great Britain)) were used for plasmid amplification. Genetic transformation, hydrolysis by restriction endonucleases, ligation, gel electrophoresis, and DNA isolation were performed using standard protocols and the recommendations of the enzyme manufacturers [8]. Commercial reagent kits (cat. # BC021L and cat. # BC124, Evrogen, Russia) were used for DNA isolation. Targeted mutagenesis of the *VSVM* gene encoding the VSVM protein was performed by inverse PCR using pVSV-dG-GFP 2.6 (cat# EH1026, Kerafast) as a template and specific primers:

forward GACACCTATGATCCGAATCAATTAAG-ATATGAGA;

reverse CTCGTCAACTCCAAAATAGGATTTGTCA-ATTGGA.

VSVG from the pCAGGS-G-Kan plasmid was cloned into the mutagenesis plasmid pVSV-dG-dM51-GFP at NheI/XbaI sites to generate the pVSV-dM51-GFP plasmid, which is required for the assembly of replication-competent rVSV-dM51-GFP. To obtain helper plasmids with the CAG promotor (pCAG-VSVL, pCAG-VSVN, and pCAG-VSVP), *N* and *P* gene sequences were cloned at the EcoRI/NotI sites and the *L* gene was cloned at the XbaI/NotI sites in pCAG-T7pol. The genes were amplified using specific primers; the plasmids pBS-N-ФT-Kan, pBS-P-ФT-Amp, and pBS-L-ФT-Amp were used as templates for the amplification of *VSVN*, *VSVP*, and *VSVL*, respectively. The correct assembly of vectors was verified by Sanger sequencing using an ABI 3500 Genetic Analyzer (Applied Biosystems, USA) in standard conditions with the reagents recommended by the manufacturer.

Production of HEK293TN-T7 and BHK-21-T7 cells

The T7-RNApol gene encoding the T7 RNA polymerase was cloned in the retroviral vector pBabe-bleo (Plasmid #176) at BamHI/SalI sites. The accuracy of the pBabe-bleo vector assembly was verified by restriction enzyme analysis and Sanger sequencing.

To obtain the retrovirus, the resulting plasmid was used for the transfection of Phoenix-AMPHO (CRL-3213 – ATCC) cells with Lipofectamine® 3000 (cat# L3000015, Thermo Fisher Scientific) according to the manufacturer's instructions. HEK293TN and BHK-21 cells were infected with a cultural medium containing the obtained retrovirus for 3 h during each 12-h interval. Selection was performed within a week using 100 μg/ml of zeocin (cat# R25005, Invitrogen by Thermo Fisher Scientific). The surviving cells were seeded and screened 2 weeks after the start of selection based on the presence of a T7-RNApol insertion in the cell genome determined by PCR with specific primers. A clone of HEK293TN-T7 and BHK-21-T7 cells was selected for further studies. The activity of T7 RNA polymerase was confirmed in the clones by detecting luminescence using the Luciferase Assay System (Promega, USA). For this, the cells were transfected with the following expression vectors: plasmids pEGFPN3 (cat# 632515, Clontech), pSmart_5'-Mod-FFLuc-3'-Mod [9], pCAG-T7pol, and pSmart_5'-Mod-FFLuc-3'-Mod (positive control).

Production and amplification of rVSV-dM51-GFP

For rVSV-dM51-GFP assembly, 80–85% confluent HEK293TN-T7 cells in 12-well plates were transfected with pCAG-VSVN, pCAG-VSVP, pCAG-VSVL, pCAGGS-G, and pVSV-dM51-GFP at a 3:5:1:4:8 ratio, respectively, using PEI (a 5:1 ratio) and total DNA (10.5 μg). Cultural media, obtained 72 h after transfection, were used for further virus amplification in either adherent BHK-21 cells (cat# 85011433, ECACC General Collection) or suspension HEK293 cells in a serum-free medium (BalanCD HEK293, Irvine Scientific). Virus-containing supernatants (MOI = 10^{-4}) obtained by centrifugation (3,000 *g*) of the culture medium from the previous stages of rVSV-dM51-GFP production were added, and the cells were incubated for 72 h. The culture medium was collected at all stages of virus production, centrifuged at 3,000 *g* and either stored at –80°C or used immediately for repeated virus transduction, isolation, purification, analysis, etc. After virus amplification in HEK293 cells, virus-containing supernatants were passed through 0.45-μm filters, concentrated (300 kDa, Vivaspin 6, VS0651, Sartorius) 100- to 200-fold and mixed with the standard phosphate-buffered saline (PBS, pH 7.4) for storage, purification, and analysis.

Purification of rVSV-dM51-GFP by ultracentrifugation

For purification and concentration of rVSV-dM51-GFP by ultracentrifugation (UCF), viral particles were purified and precipitated through a sucrose cushion (20% sucrose solution in HEN buffer: 10 мM HEPES pH 7.4, 1 мM EDTA, and 100 мM NaCl). The virus-containing supernatant was transferred into UCF tubes (cat# 344061, Beckman Coulter), and 4 ml of a 20% sucrose solution was added under the supernatant layer. The tubes were ultracentrifuged at 120,000 *g* and 4°C for 1 h, the supernatant was removed, and the precipitate was resuspended in 500 µl of an ET buffer (1 mM Tris-HCl, pH 7.5, 1 mM EDTA, and 10% DMSO) and incubated for 2 h at 4°C. The second UCF stage was performed in a discontinuous sucrose-density gradient with a HEN buffer with three different densities (25, 45, and 60%). Samples were centrifuged at 130,000 *g* and 4°C for 16 h. The band at the boundary between the 25% and 45% layers was extracted. At the third stage, the resulting sample was diluted 12-fold in standard PBS (pH 7.4). The samples were centrifuged at 120,000 *g* and 4°C for 1 h. The precipitate containing the purified viral fraction was dissolved in the required volume of PBS (pH 7.4).

Analysis of rVSV-dM51-GFP samples by electron microscopy

A Crossbeam 550 scanning electron microscope (Carl Zeiss, Germany) was used in the scanning transmission electron microscopy (STEM) mode. The sample was applied onto copper grids pretreated with air plasma for 10 s (formvar/carbon (200 mesh), cat#BZ31022a, EMCN, China) using a Zepto Plasma Cleaner (Diener Electronic). The samples were incubated for 2 min, and the grid was washed with double-distilled water and contrasted with 1% aqueous uranyl acetate (cat#0379, Polysciences Inc.) for 1 min. The resulting sample grids were dried in air at room temperature. The samples were visualized at an accelerating voltage of 30 kV.

Analysis of rVSV-dM51-GFP samples

The protein composition of the samples was analyzed by polyacrylamide gel electrophoresis (PAGE) under denaturing conditions using sodium dodecyl sulfate (SDS-PAGE) according to the standard protocol [10]. The rVSV-dM51-GFP preparation titer ($TCID_{50}$/ml) was calculated using the Reed–Muench method [11].

Production of B16F10red cells

B16F10Red cells were obtained from B16F10 murine melanoma cells (third passage) from the Collection of Tumor Strains of the Federal State Budgetary Institution Blokhin National Medical Research Center of Oncology of the Russian Ministry of Health. B16F10 cells were obtained from murine C57BL/6 cells. B16F10 cells were transduced with viral particles from the culture medium of HEK293TN cells, previously transfected with the plasmids pMD2.G (cat# 12259, Addgene), pMDLg/pRRE (cat# 12251, Addgene), pRSV-REV (cat# 12253, Addgene), and a plasmid encoding the fusion protein H2B-Katushka2 under the EF1a promoter. Cells that survived in the selective medium were seeded in a 25 cm^2 culture flask. Colonies with the highest fluorescence intensity of the H2B-Katushka2 reporter were selected. The fluorescence intensity in the resulting B16F10Red cell subline was detected using a microscope with a fluorescence filter (Carl Zeiss Axio Vert.A1).

Monitoring of the B16F10Red cell number using lncuCyte S3

To study the changes in the number of fluorescent B16F10Red cells, cells infected with viral particles with different rVSV-dM51-GFP dilutions were incubated for 84 h according to the manufacturer's recommendations using a lncuCyte S3 Live Cell Analysis System. The number of fluorescent cells was counted every 2 h.

RESULTS AND DISCUSSION

The conventional method for rVSV assembly [6] includes transfection of BHK-21 cells with five plasmids expressing individual genes and the complete VSV genome and co-infection of cells with either the vaccinia virus or another virus expressing T7 RNA polymerase, which is required for rVSV assembly [6]. The use of individual viruses expressing T7 RNA polymerase for rVSV assembly has a number of disadvantages, which are mentioned above. Co-transfection of cells with rVSV assembly plasmids and a plasmid encoding the T7 RNA polymerase gene makes it possible to avoid the unadvisable use of a helper virus for rVSV assembly. The use of an additional plasmid for transfection increases the DNA load on cells, which can cause cytotoxicity and affect virus assembly. For this reason, we obtained HEK293TN-T7 and BHK-21-T7 cells expressing T7 RNA polymerase. To assess the effectiveness of polymerase expression, we measured the luminescence of the cells transfected with a plasmid carrying the firefly luciferase gene under the T7 RNA polymerase promoter. Luciferase expression under the T7 RNA polymerase promoter in HEK293TN-T7 cells reaches a level similar to that in the positive control (cells transfected with a plasmid carrying the T7 RNA

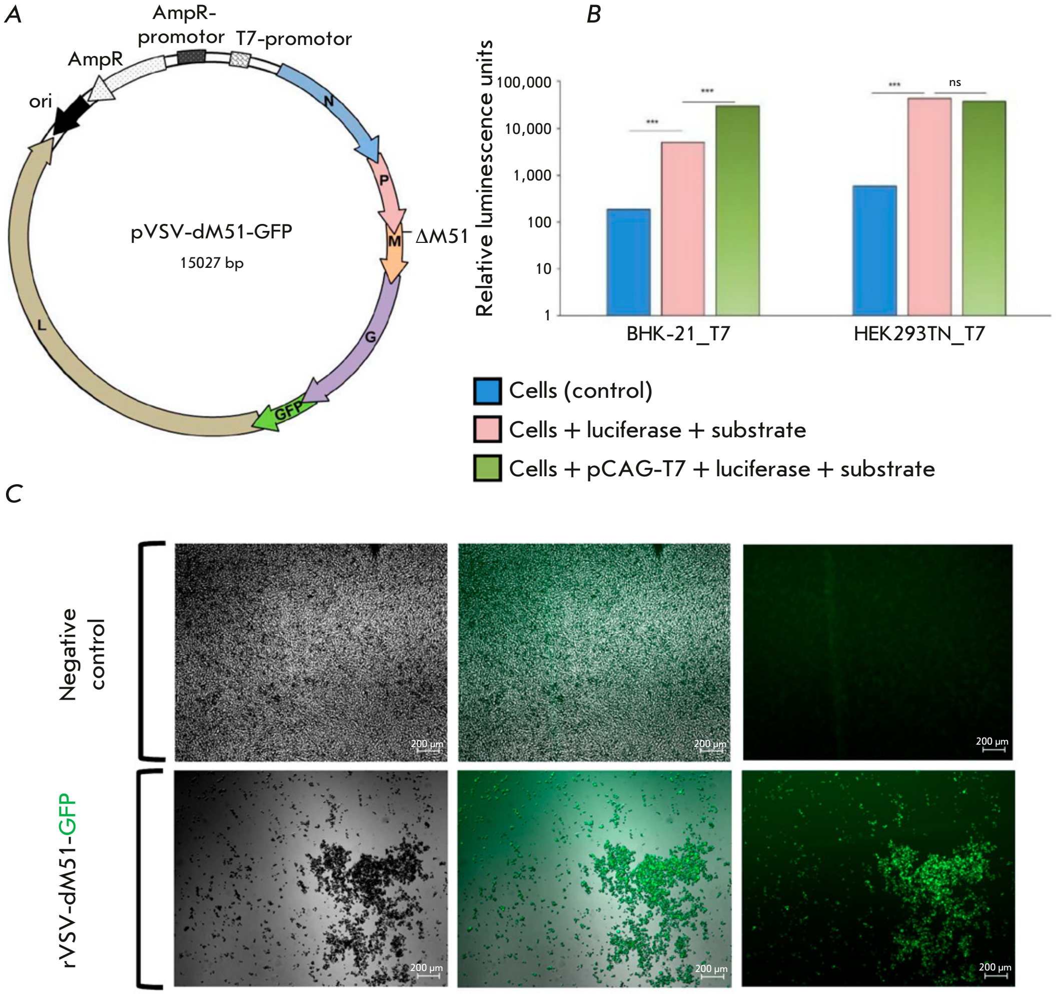

Fig. 1. Assembly of rVSV-dM51-GFP from plasmids.
(*A*) – Plasmid vector map for the assembly of replication-competent rVSV-dM51-GFP variants. The dM51 mutation and genes encoding VSV proteins are indicated, including the integrated VSV G gene.
(*B*) – Luminescence of BHK21-T7 and HEK293TN-T7 cells.
(*C*) – Micrographs of HEK293TN-T7 cells 72 h after transfection. The upper table presents the negative transfection control with the plasmids necessary for rVSV-dM51-GFP assembly from the plasmids in the absence of the vector encoding the viral genome (pCAG-VSVL, pCAG-VSVN, and pCAG-VSVP); the lower table shows the cells transfected with all plasmids (pCAG-VSVL, pCAG-VSVN, pCAG-VSVP, and pVSV-dM51-GFP) necessary for rVSV-dM51-GFP assembly

polymerase gene). However, at the same time, the luciferase expression level exceeds that in BHK-21-T7 cells (*Fig. 1B*). Therefore, we used HEK293TN-T7 cells in further studies for the assembly of model rVSV particles. The pVSV-dM51-GFP plasmid with a M51 deletion in VSV M (dM51) was used as a model virus to develop an optimized technique for obtaining purified rVSV preparations. It is known that rVSV with this deletion does not suppress interferon expression upon its entry in live cells, which makes this modification valuable in terms of the safety of rVSV-based drugs [12]. The model virus genome also contains *VSVG*, which encodes the envelope glycoprotein required for virus entry into the cell. This makes the virus replication-competent; in addition, it also makes it possible to avoid pre-transfection of cells with a *VSVG*-encoding plasmid for the production of virus preparations [6, 13]. To introduce modifications into the model virus genome, we obtained the pVSV-dM51-GFP plasmid carrying the dM51 deletion and *VSVG* (*Fig. 1A*). The plasmid was used for co-transfection with helper plasmids (pCAG-VSVL, pCAG-VSVN, and pCAG-VSVP) at the stage of virus assembly. To increase the effectiveness of model rVSV-dM51-GFP assembly, we also constructed helper plasmids with the CAG promoter based on the data on promoter use for rVSV assembly [14] and evidence of protein synthesis enhancement by the CAG promoter in HEK293F cells [15]. BHK-21 and Vero cells are usually used for rVSV production [16]. However, we observed efficient rVSV-dM51-GFP assembly only in HEK293TN-T7 cells (*Fig. 1C*). Neither the GFP nor CPE signal was observed in BHK-21-T7 cells, or even in BHK-21 and

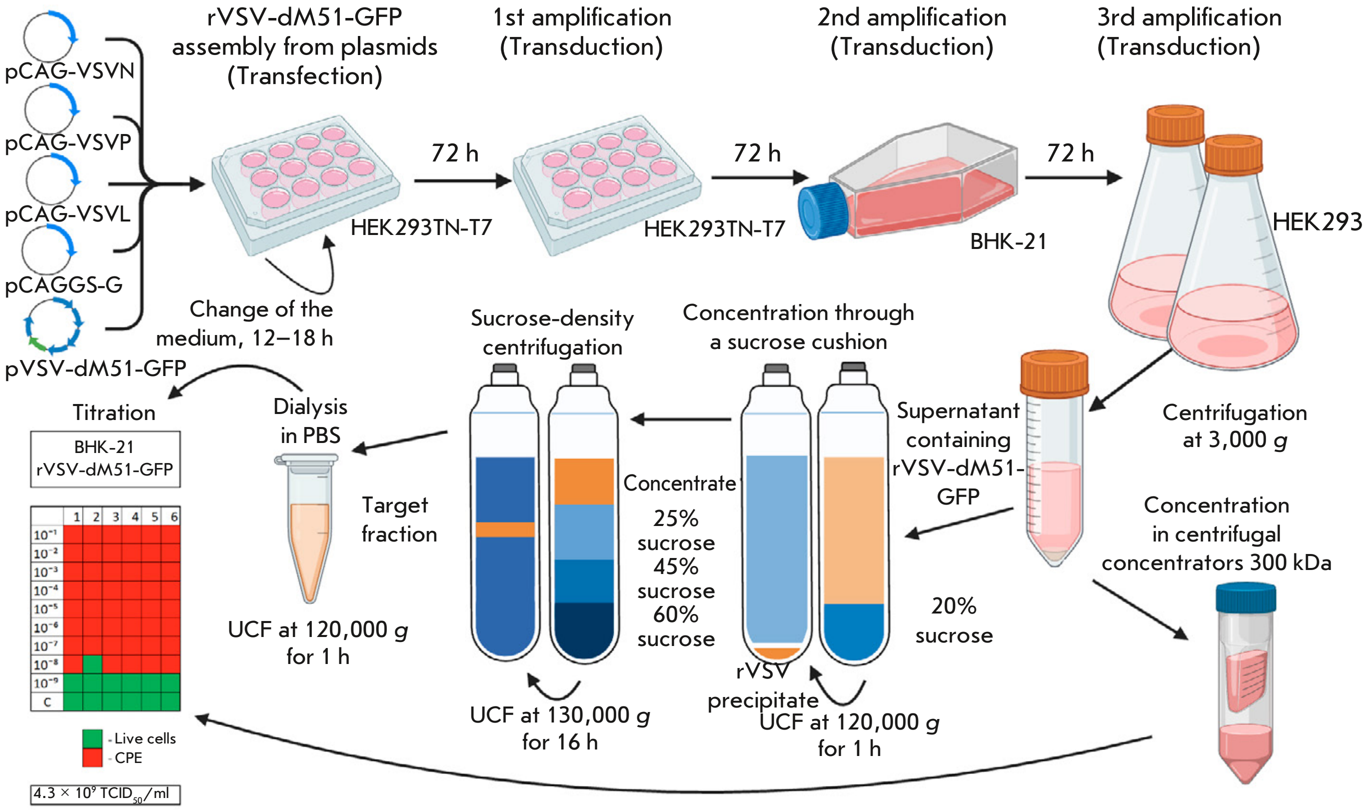

	1	2	3	4	5	6
10^{-1}	🟥	🟥	🟥	🟥	🟥	🟥
10^{-2}	🟥	🟥	🟥	🟥	🟥	🟥
10^{-3}	🟥	🟥	🟥	🟥	🟥	🟥
10^{-4}	🟥	🟥	🟥	🟥	🟥	🟥
10^{-5}	🟥	🟥	🟥	🟥	🟥	🟥
10^{-6}	🟥	🟥	🟥	🟥	🟥	🟥
10^{-7}	🟥	🟥	🟥	🟥	🟥	🟥
10^{-8}	🟥	🟩	🟥	🟥	🟥	🟥
10^{-9}	🟩	🟩	🟩	🟩	🟩	🟩
C	🟩	🟩	🟩	🟩	🟩	🟩

4.3 × 10^9 $TCID_{50}$/ml

Fig. 2. Schematic representation of the protocol for preparation of purified rVSV-dM51-GFP in adherent and suspension cell cultures

Vero-76 cells transfected with the additional plasmid pCAG-T7pol.

The ratio of plasmids used for HEK293TN-T7 transfection resulting in efficient rVSV-dM51-GFP assembly differs from the ones used in previously published protocols [6, 14]. At the same time, the plasmid ratios used in the study by Whitt M. [6] generated GFP and CPE signals similar to those in the negative control (data not shown, since they coincided with the negative control, as presented in *Fig. 1C*). We assume that the optimal plasmid ratios for the assembly of model rVSV-dM51-GFP particles vary under different conditions. Hence, when rVSV is not assembled, the plasmid ratio can be adjusted and the optimal ratio can be determined for the given conditions. Due to the lack of comprehensive protocols for rVSV production, we developed a method with in-detail description of all stages of the production of a purified preparation of the model rVSV virus, including titer determination and oncolytic activity evaluation (*Fig. 2–4*).

Production of the rVSV preparation in a cell suspension culture greatly facilitates the scaling up of the technological process and simplifies the scaling of laboratory technology to the use of industrial bioreactors and, therefore, the industrial production of rVSV batches [17]. The use of a serum-free medium for cultivation, e.g. a HEK293 suspension culture, eliminates the need to test the drug for the presence of components of animal origin [18]. Optimization of the HEK293 cultivation process, for instance, by using culture feeds, can significantly increase the virus titer [17]. To purify the rVSV-dM51-GFP preparation of contaminants and inhibitory particles and concentrate the preparation, we performed a three-step purification of samples by sucrose-density UCF (*Fig. 2*). The purification steps included concentration of viral particles and purification in a sucrose gradient, followed by isolation and dialysis of the target viral fraction in PBS (pH 7.4). In similar protocols for VSV purification, the order of the stages may vary; for example, the stage of concentration through the so-called sucrose cushion may be the final step [19] or even absent altogether [20]. In our study, we centrifuged the culture medium containing rVSV-dM51-GFP through 20% sucrose not only to concentrate the sample, but also to partially pre-purify it from contaminants and thereby increase the efficiency of the following second stage of purification in a sucrose gradient. The

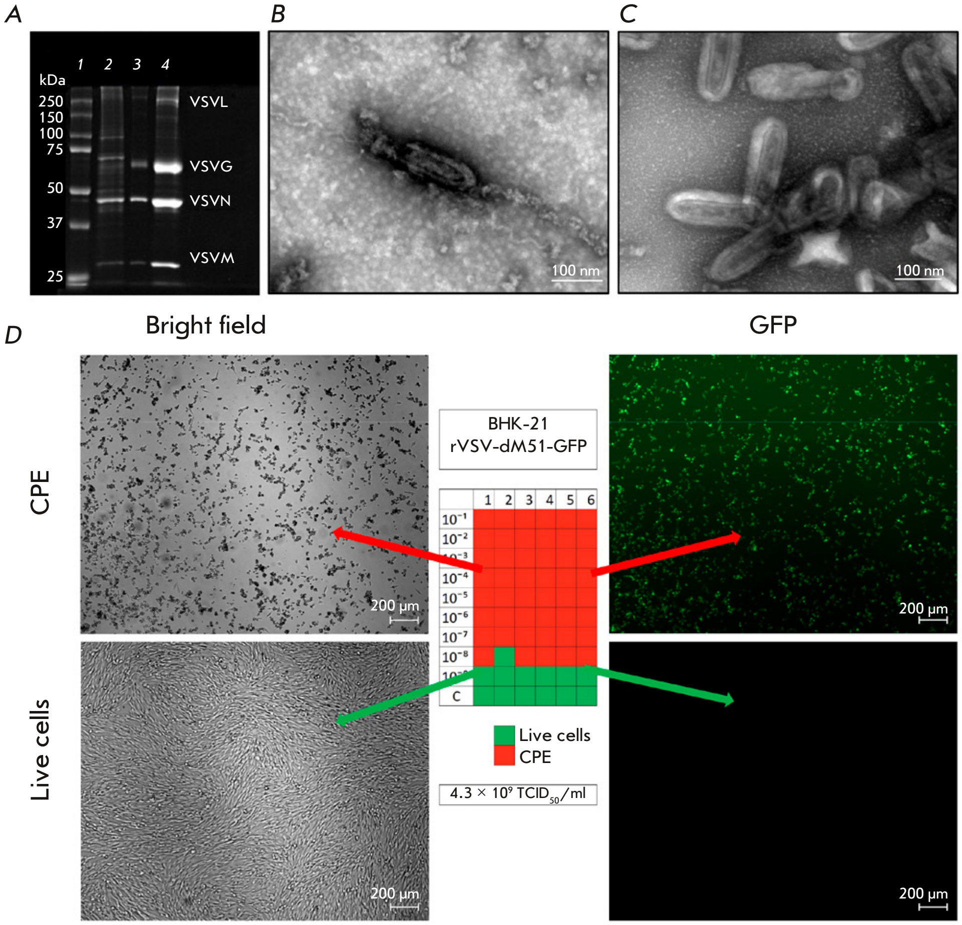

Fig. 3. Analysis of rVSV-dM51-GFP samples.
(*A*) – SDS-PAGE (from left to right):
1 – protein molecular weight marker (10–250 kDa),
2 – rVSV-dM51-GFP supernatant after CF at 3,000 *g*,
3 – rVSV-dM51-GFP fraction after the second UCF stage,
4 – purified rVSV-dM51-GFP after the third UCF stage;
(*B*) – STEM micrograph image of rVSV-dM51-GFP before UCF purification (magnification, × 130,000).
(*C*) – STEM micrograph of rVSV-dM51-GFP after UCF purification (magnification, × 130,000).
(*D*) – $TCID_{50}$/ml in BHK-21 cells and the micrographs of BHK-21 cells in the presence (top) and absence (bottom) of CPE

following sucrose concentrations were used at the second UFC stage: 25%, 45%, and 60% [21]. The final purification step included dialysis in PBS (pH 7.4) using re-precipitation by UCF (*Fig. 2*). UCF can lead to loss and damage to viral particles and, as a consequence, a decrease in the viral preparation titer. To verify the titer and purity of the rVSV-dM51-GFP preparations obtained by using the proposed protocol (*Fig. 2*), we analyzed the samples by SDS-PAGE, $TCID_{50}$, and STEM (*Fig. 3*). A change in the intensity of the SDS-PAGE bands corresponding to five rVSV proteins [22, 23] and the absence of non-specific bands indicate an increase in the viral concentration at each purification stage (*Fig. 3A*).

A STEM analysis of the viral samples also showed that UCF of the rVSV-dM51-GFP preparation resulted in an increase in the number of viral particles in the field of view and a decrease in the number of contaminants (*Fig. 3B,C*). To confirm the viability of the viral particles, we measured rVSV-dM51-GFP titers before and after UCF by using $TCID_{50}$ as a method that determines the number of infectious viral particles causing a cytopathic effect [11]. In addition to the SDS-PAGE and STEM data, the rVSV-dM51-GFP titer in the supernatants before the concentration stage (2 × 10^8 $TCID_{50}$/ml) was lower than that after viral purification and concentration by UCF (4.3 × 10^9 $TCID_{50}$/ml) (*Fig. 3D*). In addition to performing qualitative and quantitative analyses, we also studied the oncolytic properties and dose–response relationship of the model rVSV preparation obtained using the proposed approach in B16F10 murine melanoma cells (*Fig. 4B*). These cells are often used to evaluate the therapeutic properties of various drugs, including oncolytic viruses, and, in particular, in *in vivo* studies [24–26]. Visualization of living cells using fluorescent proteins makes it possible to monitor cancer cell growth both *in vitro* and *in vivo*. This, in turn, allows for an evaluation of the therapeutic effect of anticancer drugs. To assess the dose–response relationship *in vitro*, we obtained RFP-expressing B16F10 cells (B16F10Red) (*Fig. 4A*) and conducted intravital cell number monitoring on IncuCyte S3 (*Fig. 4B*). A similar growth trend was

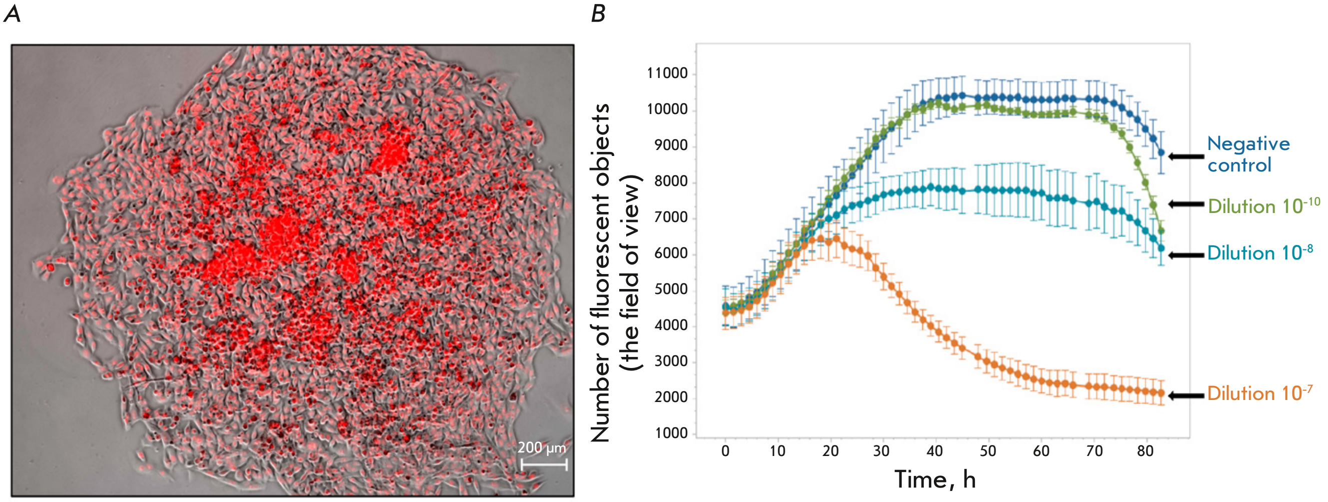

Fig. 4. The dose–response relationship for rVSV-dM51-GFP in B16F10Red cells. (*A*) – micrographs of B16F10Red cells; (*B*) – CPE in B16F10Red cells after addition of rVSV-dM51-GFP at different dilutions

observed in virus-free variants and variants containing high dilutions of the viral preparation (**10^8 and 10^{10}**): the growth (~0–40 h), plateau (~40–75 h), and cell death phases (⩾~75 h). In case of using the lowest dilution of the viral preparation (**10^7**), the cell growth pattern differed significantly: the cell death phase was observed approximately 25 h after the growth phase. We plotted the curves of the number of fluorescent objects on the viral preparation dilution and observed the dose–response relationship between the viral amount and the number of living cells (*Fig. 4B*). Based on those results, we conclude that the model virus particles do not lose their viability and oncolytic properties while they retain the ability to lyse cancer cells at high viral dilutions (**10^7–10^8**) after the abovementioned stages of virus assembly, amplification, and purification.

CONCLUSION

We have developed a scalable method for producing purified preparations of model rVSV-dM51-GFP without the use of a helper virus. The protocol includes the stages of production, purification, titer determination, and analysis of the virus oncolytic activity. The model virus preparation obtained by the above-described approach can be used to assess its therapeutic characteristic in *in vivo* syngeneic murine models with B16F10 cells and compare it with enhanced rVSV variants with immunostimulatory characteristics [12, 26, 27]. ●

This project was financially supported by the Ministry of Science and Higher Education of the Russian Federation (Agreement No. 075-10-2021-093; Project No. GTH-RND-2113).

REFERENCES

1. Pearl T., Markert J., Cassady K., Ghonime M. // Mol. Ther. Oncolytics. 2019. V. 13. P. 14–21.
2. Malogolovkin A., Gasanov N., Egorov A., Weener M., Ivanov R., Karabelsky A. // Viruses. 2021. V. 13. № 7. P. 1271.
3. Geisbert T., Feldmann H. // J. Infectious Dis. 2011. V. 204. № suppl_3. P. 1075–1081. https://www.jstor.org/stable/41329906.
4. Zemp F., Rajwani J., Mahoney D. // Biotechnol. Genet. Engin. Rev. 2018. V. 34. № 1. P. 122–138.
5. Velazquez-Salinas L., Naik S., Pauszek S., Peng K., Russell S., Rodriguez L. // Hum. Gene Ther. Clin. Dev. 2017. V. 28. № 2. P. 108–115.
6. Whitt M. // J. Virol. Methods. 2010. V. 169. № 2. P. 365–374.
7. Decision of the Council of the Eurasian Economic Commission dated November 3, 2016 № 89 “On approval of the Rules for conducting research on biological medicinal products of the Eurasian Economic Union” (as amended by decisions of the Council of the Eurasian Economic Commission dated July 15, 2022 No. 110, dated July 4, 2023 № 77)
8. Green M., Sambrook J. Mol. Cloning: A Laboratory Manual. 4th Edition. New York, 2012. V. 2.
9. Kirshina A., Vasileva O., Kunyk D., Seregina K., Muslimov A., Ivanov R., Reshetnikov V. // Biomolecules. 2023. V. 13. № 11. P. 1677. doi: 10.3390/biom13111677.

10. Laemmli U. // Nature. 1970. V. 227. № 5259. P. 680–685.
11. Lei C., Yang J., Hu J., Sun X. // Virologica Sinica. 2021. V. 36. № 1. P. 141–144.
12. Felt S., Grdzelishvili V. // J. Gen. Virol. 2017. V. 98. № 12. P. 2895–2911.
13. Finkelshtein D., Werman A., Novick D., Barak S., Rubinstein M. // Proc. Natl. Acad. Sci. USA. 2013. V. 110. № 18. P. 7306–7311.
14. Takahashi K., Yokobayashi Y. // ACS Synth. Biol. 2019. V. 8. № 9. P. 1976–1982.
15. Dou Y., Lin Y., Wang T., Wang X., Jia Y., Zhao C. // FEBS Open Bio. 2021. V. 11. № 1. P. 95–104.
16. Abdelmageed A., Ferran M. // Curr. Protoc. Microbiol. 2020 V. 58. № 1. e110.
17. Elahi S., Shen C., Gilbert R. // J. Biotechnol. 2019. V. 289. P. 144–149.
18. Van der Valk J., Bieback K., Buta C., Cochrane B., Dirks W., Fu J., Hickman J., Hohensee C., Kolar R., Liebsch M. // ALTEX. 2018. V. 35. № 1. P. 99–118.
19. Kim I., Jenni S., Stanifer M., Roth E., Whelan S., van Oijen A., Harrison S. // Proc. Natl. Acad. Sci. USA. 2017. V. 114. P. 28–36.
20. Sakata M., Tani H., Anraku M., Kataoka M., Nagata N., Seki F., Tahara M., Otsuki N., Okamoto K., Takeda M. // Sci. Rep. 2017. V. 7. № 1. P. 11607.
21. Moerdyk-Schauwecker M., Hwang S., Grdzelishvili V. // Virol. J. 2009. V. 6. P. 166.
22.Thomas D., Newcomb W., Brown J., Wall J., Hainfeld J., Trus B., Steven A. // J. Virol. 1985. V. 54. № 2. P. 598–607.
23. Buonocore L., Blight K., Rice C., Rose J. // J. Virol. 2002. V. 76. № 14. P. 6865–6872.
24. Durham N., Mulgrew K., McGlinchey K., Monks N., Ji H., Herbst R., Suzich J., Hammond S., Kelly E. // Mol. Ther. 2017. V. 25. № 8. P. 1917–1932.
25. Abdulal R., Malki J., Ghazal E., Alsaieedi A., Almahboub S., Khan M., Alsulaiman R., Ghaith M., Abujamel T., Ganash M. // Front. Mol. Biosci. 2023. V. 10. P. 1190669.
26. Isaeva A.S., Porozova N.O., Idota E., Volodina S.I., Lukashev A.N., Malogolovkin A.S. // Sechenov Med. J. 2023. V. 14. № 4. P. 17–30.
27. Cristi F., Gutiérrez T., Hitt M., Shmulevitz M. // Front. Mol. Biosci. 2022. V. 9. P. 831091.

The Effect of Liposomes of Various Compositions on the Skin and Its Derivatives After II–IIIA Degree Thermal Burns

N. I. Pashkevich[1*], D. V. Vilyanen[2], A. F. Marcinkevich[1], M. M. Borisova-Mubarakshina[2], S. S. Osochuk[1]
[1]Vitebsk State Order of Peoples' Friendship Medical University, Vitebsk, 210009 Republic of Belarus
[2]Institute of Basic Biological Problems, Russian Academy of Sciences, Pushchino, Moscow Region, 142290 Russian Federation
*E-mail: orekhova.ni93@gmail.com

Received: November 17, 2023; in final form, January 15, 2024
DOI: 10.32607/actanaturae.27329

ABSTRACT **This study examines the pathological processes and conditions arising from an experimental modeling of II–IIIA degree thermal burns in laboratory animals. These conditions are characterized by skin structure defects, diminished skin functions, especially the barrier function, and damage to skin derivatives like hair follicles and sebaceous glands. We compared the effect of liposomes composed of soybean lecithin of 90% phosphatidylcholine content and liposomes composed of lecithin of 26% phosphatidylcholine content on the epidermis, dermis and its capillaries, hair follicles, and the sebaceous glands of the laboratory animals 24 h after experimental modeling of II–IIIA degree thermal skin burns. We discuss the dependency of liposome effects on the skin and its derivatives on the fatty acid composition of the lecithin used, with particular focus on phosphatidylinositol, phosphatidic acids, as well as oleic and linoleic acids.**

KEYWORDS **burn, skin, phosphatidylcholine, polyunsaturated fatty acid, liposome.**

ABBREVIATIONS **PUFA – polyunsaturated fatty acid.**

INTRODUCTION

The skin is known to be the largest organ of the human and animal bodies, and it plays an important role in metabolism. Damage to the skin can cause significant abnormalities in the functioning and condition of all its layers and derivatives, leading to serious changes in the metabolic processes taking place in cells and tissues, or even death.

The human skin contains 3–4 million sweat glands [1]; their total weight is about 100 g [2], which is close to the mean weight of the kidney. Sweat glands are involved in the excretion of xenobiotics, exogenous and endogenous toxic/bioactive substances, such as metals [3], drugs [4, 5], cytokines [6], steroids [7], and lipids, in particular cholesterol [3, 5, 8–10]. The skin possesses a powerful antioxidant system [2] and is also considered as an independent endocrine organ [11].

Sebaceous glands can act as immunocompetent cells, because they are able to recognize pathogens and synthesize and release pro- and anti-inflammatory cytokines and chemokines, as well as antimicrobial peptides and lipids [12]. An isomer of palmitoleic acid (C16:1D6), sapienic acid in sebum, is known to exhibit antimicrobial activity [13]. Sebaceous gland secretion is a major physiological route of fat-soluble antioxidants to the upper layers of the skin [14]. Additionally, these glands can respond to leptin, linking them to the regulation of starvation and obesity mechanisms [15] and the release of pheromones [16].

Thus, sebaceous glands are considered to be the "brain of the skin" and the most important endocrine glands of the skin. The functional activity of sebaceous glands is closely related to the functioning of hair follicles.

The hair follicle acts as a sensor and immunologic sentinel for the skin. The hair detects stimuli above the skin surface, and the slightest bending of the hair activates neuroreceptors in the follicle, sending sensory information to the nervous system. In turn, Langerhans cells of hair follicles, acting as macrophages, detect surface pathogens and activate the immune system [17]. Hair follicle cells located near the insertion of the erector pili muscle possess the properties of epithelial stem cells and can act as a reserve of epidermal cells and sebaceous glands [18]. Therefore, damage to or preservation of hair follicle cells is an important indicator of the regenerative potential of the skin.

One of the most common skin injuries is burn injury. According to the Federal State Statistics Service of the Russian Federation, the number of burn injury cases in 2021 exceeded 220,000 people [19]. Accordingly, 70% of burn treatments should be performed on an outpatient basis [20]. In this regard, the development of novel drugs for the treatment of burns is of particular topicality.

Healing damaged skin involves four main stages: hemostasis, inflammation, proliferation, and remodeling. Each stage is controlled by a cascade of molecular biological processes [21]. The stage of inflammation and its resolution are considered crucial for wound healing. In this regard, prostaglandins, leukotrienes, and hydroxy- and keto-eicosatetraenoic acids are important [22] and their synthesis requires polyunsaturated fatty acids (PUFAs), mainly omega-3 and omega-6 fatty acids (ω-3 and ω-6, respectively). PUFAs are the preferred targets for free radical oxidation, and their enhanced oxidation can lead to devastating consequences of burn injury [23]. Given the smaller amount of essential PUFAs in phosphatidylcholine from sebaceous glands compared with that in phosphatidylcholine from other organs [24], enhancement of free radical oxidation during skin burns can cause a significant deficiency of essential ω-3 and ω-6 PUFAs. Under these conditions, there may be a partial or significant transition to the production of prostanoids from endogenously synthesized ω-9 series PUFAs capable, under a deficiency of ω-3 and ω-6 series essential fatty acids, of boosting the production of pro-inflammatory cytokines by macrophages [25]. Thus, it seems appropriate to use topical agents containing essential ω-3 and ω-6 PUFAs, such as phosphatidylcholine-based liposomes, in the treatment of burn injuries.

The history of liposome discovery and application began in the 1960s with the work of Alec Bangham and colleagues, who experimented with phospholipids in aqueous media and discovered their ability to form membrane-like structures [26]. Currently, liposomes are widely used as biological nanocontainers for drug delivery in oncology [27, 28], ophthalmology [29], dermatology [30], gene therapy [31], and other fields of medicine. The undeniable advantages of liposomes include their biodegradability, low immunogenicity, and ability to interact with the cell membrane, ensuring intracellular delivery of their contents [32]. However, despite the evidence of high metabolic activity of essential PUFAs constituting the phospholipids used for the production of liposomes, not enough attention is focused on the metabolic effects of such liposomes, depending on the spectrum of fatty acids included in their composition. In the scientific literature, there are only a few studies which compare the activities of liposomes with different fatty acid compositions. For example, L.J. Jenski et al. [33, 34] mentioned the ability of liposomes containing α-linolenic and docosahexaenoic acids to increase the survival chances of mice with experimental cancer. The effect was explained by the cytotoxicity of docosahexaenoic acid against tumor cells. The ability of liposomes composed of linolenic acid-containing phosphatidylcholine to inhibit the growth of *Helicobacter pylori* has been reported [35]. However, there are no systematic studies on the effect of liposomes with different contents and range of fatty acids on skin derivatives.

EXPERIMENTAL

Our studies were performed on the basis of a cooperation agreement between the Vitebsk State Medical University (VSMU) and the Pushchino Scientific Center for Biological Research of the Russian Academy of Sciences, in the research laboratory of VSMU.

Preparation of liposomes

Liposomes of two compositions were prepared from soybean lecithin (phosphatidylcholine) and cholesterol (Sigma, USA) at a 5:1 ratio according to the procedure described in [36]. Lecithin (7.78%) and cholesterol (1.5%) were dissolved in 15 mL of chloroform and 5 mL of methanol. A thin film layer of lipids was formed by vacuum drying the solution on a rotary evaporator. The film was slowly resuspended in 0.01 M phosphate buffer (pH 6) and shaken. The final liposome solution was extruded through a 400 nm filter using an Avanty laboratory mini-extruder (Avanti Polar Lipids, USA). To prepare liposomes of the first composition, we used pharmaceutical lecithin (Riceland Foods, Inc., USA) that contained 26% of phosphatidylcholine, 12–15% of phosphatidylinositol, 4–8% of phosphatidic acids, and 40–50% of

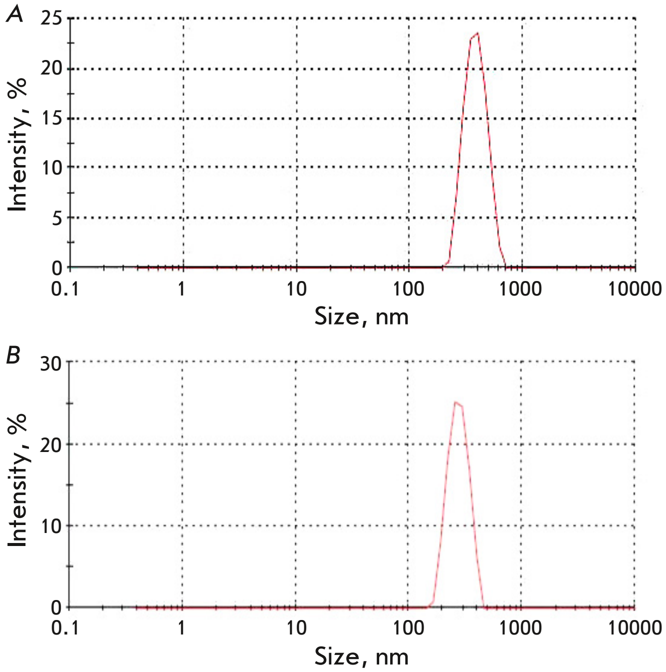

Fig. 1. Size distribution of liposomes. (*A*) Liposomes with 26% of phosphatidylcholine. (*B*) Liposomes with 90% of phosphatidylcholine

free fatty acids; also, 100 g of the compound contained 3,000 mg of P, 1,250 mg of K^+, 150 mg of Ca^{2+}, 4 mg of Fe, 150 mg of Mg^{2+}, 30 mg of Na^+, and 5 mg of vitamin E. Liposomes of the second composition were prepared using lecithin containing 90% of phosphatidylcholine (PanReac AppliChem, Spain).

The size of the liposomes was determined using a Zetasizer Nano ZS analyzer (Malvern Instruments Ltd, UK) (*Fig. 1A,B*). The mean size of the liposomes containing 26% and 90% of phosphatidylcholine was 486.7 nm and 523.2 nm, respectively.

Fatty acid methylation of both lecithins was performed using sodium methoxide (Sigma-Aldrich). The spectrum of fatty acids was studied by gas-liquid chromatography on a Thermo Focus GC chromatograph (USA) using a capillary column SGEBPX70 (60 m × 0.25 mm) and the temperature program: evaporator temperature – 200°C, flame ionization detector temperature – 280°C, the column thermostat temperature was elevated from 120°C to 245°C at a speed of 3°C/min, an isotherm step at 245°C was 5 min (total analysis time was 46.66 min). The carrier gas (He) rate was 1.3 mL/min. Fatty acids were identified with respect to the retention times of standard methyl esters (Sigma-Aldrich). The amount was estimated as a percentage of the total area of all identified peaks.

Laboratory animals

The experiments were carried out in two stages, on 92 white non-inbred male rats weighing 180–250 g divided into four groups: 1 – intact animals (n = 7 for the first liposome type and n = 12 for the second); 2 – stress control, so-called false stress (n = 7 for the first liposome type and n = 12 for the second) (unburned and untreated animals); 3 – thermal burn (n = 15 for the first liposome type and n = 12 for the second); and 4 – thermal burn + liposomes of the first type (n = 15) and liposomes of the second type (n = 12).

Simulation of thermal burns of the skin

A device for simulating thermal burns was manufactured by the design bureau Display (Vitebsk, Republic of Belarus) based on a cooperation agreement with VSMU.

To simulate burns, the rats were anesthetized with ketamine at a dose of 150 μL/rat [37–39]. The fur on the back was shaved, and the device heated to 150°C was applied to the skin for 4 min. The induced damage was morphologically assessed as II–IIIA degree burns (*Fig. 2*). The burn area was 8–9% of the body area. To calculate the burn area, we used the formula proposed by Meeh: S = k × W2/3, where S is the body surface area (cm^2); W is the body weight of the animal (kg); and k is a Meeh constant of 9.46 [40]. Immediately after burn induction, the damaged skin in the animals of the fourth experimental group was treated with 0.45 mL of a type 1 or type 2 liposome solution.

Histological examination of the skin

The animals were decapitated under ether anesthesia 24 h after the burn injury, and the skin was sampled for histological examination. Skin samples were fixed in a 10% neutral formaldehyde solution. Histological sections were stained with hematoxylin–eosin and examined on a Leica DM 2500 microscope (Germany, ×10 eyepiece, ×20 and ×40 objectives) equipped with a Leica DFC 320 digital camera. The number of damaged elements was counted in 10 fields of view, and the mean indicator of examined skin elements was calculated.

Statistical data analysis was performed using the R package, version 4.0.5 (2021-03-31). The distribution of analyzed indicators was assessed using the Shapiro–Wilk test; in the case of a Gaussian distribution, parametric statistics methods were used for comparison; otherwise, nonparametric methods were

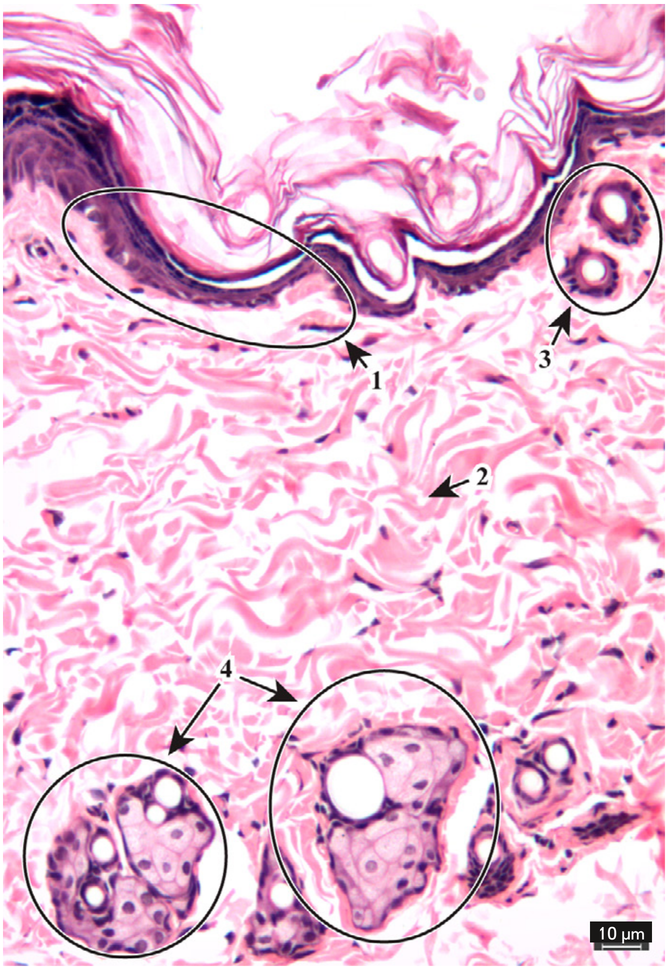

Fig. 2. Micrograph of intact animal skin. Hematoxylin and eosin stain. ×20 objective. 1 – epidermis, 2 – dermis, 3 – hair follicles, 4 – sebaceous glands

used. Pairwise comparisons were performed using the Student's *t* test or the Wilcoxon–Mann–Whitney test. Multiple comparisons were performed using ANOVA (in the case of heterogeneity of variances of the analyzed indicators, the Welch correction was applied) or the Kruskal–Wallis H test. *Post hoc* analysis was performed using the Tukey test or the Kruskal–Wallis H test and the Dunn test, corrected for multiple comparisons using the Benjamini–Iekutieli method. Differences were considered statistically significant at $p < 0.05$.

RESULTS

According to our measurements using gas-liquid chromatography, pharmaceutical lecithin (26% phosphatidylcholine) included the following fatty acids (of the total fatty acid content, %): C16:0 – 18.87, C18:0 – 3.86, C18:1n9c – 8.8, C18:2n6c – 56.95, and C18:3n3 – 6.81. Lecithin containing 90% of phosphatidylcholine included the following fatty acids (of the total fatty acid content, %): C16:0 – 13.63, C18:0 – 3.68, C18:1n9c – 11.36, C18:2n6c – 62.88, and C18:3n3 – 6.12. Therefore, lecithin containing 90% of phosphatidylcholine had a higher content of linoleic acid (C18:2n6c – 62.88% vs. 56.95% in pharmaceutical lecithin) and oleic acid (C18:1n9c 11.36% vs. 8.8% in pharmaceutical lecithin).

An assessment of the influence of the so-called false stress (see Experimental section) on the examined indicators did not reveal statistically significant deviations from the values characteristic of the intact animals (*Table 1*).

The epidermis of the intact animals and animals from the false stress group has a layered structure: the stratum corneum, basal, spinous, and granular layers are preserved (*Fig. 2*). The dermis is characterized by a fibrous structure; collagen fibers are crimped; the tissue is well structured. The integrity of hair and hair follicles is preserved; the outer and inner epidermal root sheath is clearly structured; and the medulla is not expanded. The integrity of sebaceous glands is preserved; secretion-containing vesicles are tightly adjacent to each other; and the stratified epithelium of the glands is preserved. Microvasculature vessels and papillary capillaries of the dermis are not hyperemic and, therefore, are poorly visualized.

Figure 3 shows the changes in the skin 24 h after the II–IIIA degree thermal burns. The structure of all epidermal layers had changed, which manifested itself as the destruction of the stratum corneum and necrosis of highly proliferating cells of the spinous and basal layers; the granular layer was preserved only in certain areas; the epidermal–dermal junction was flattened. There were no dermal papillae or dermal fiber bundle structure; the tissue was represented by a homogeneous structureless mass resulting from collagen denaturation. Destruction of the hair root, root sheath, and connective tissue follicle was not observed; the medulla of the hair root was significantly expanded, the shape of the hair root was changed, and there was a single-layer cell contour around the root. Sebaceous glands were deformed, secretory vesicles were destroyed, and epithelial cells were damaged. Hypodermal vessels were hyperemic, and the wall was destroyed.

A mathematical assessment of the burn impact on the assessed parameters revealed a statistically significant decrease in the thickness of the epidermis, stratum corneum of the epidermis, and epidermis without the stratum corneum compared with that in both in-

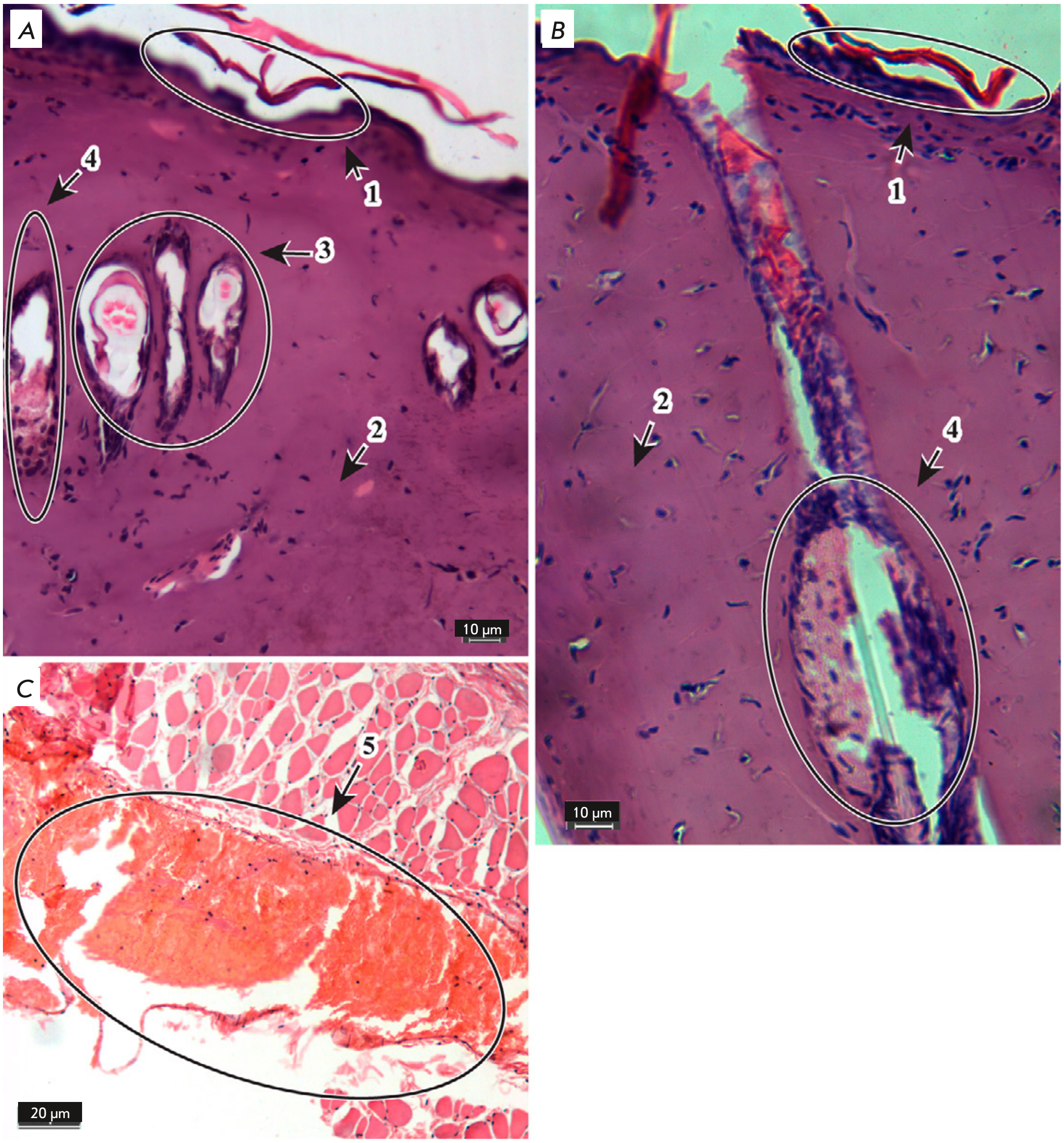

Fig. 3. Morphological changes in the skin 24 h after thermal burn. Hematoxylin and eosin stain. ×20 (*A*, *B*) and ×40 (*C*) objectives. 1 – epidermis, 2 – dermis, 3 – hair follicles, 4 – sebaceous glands, 5 – blood vessels

tact and false stress animals (*Table 1*). In addition, the number of hyperemic vessels, hair follicles, and sebaceous glands was increased in the group of animals with burns compared with that in intact and false stress animals; accordingly, burns caused negative, statistically significant changes in all analyzed parameters (*Table 1*).

A partial restoration of the layered structure of the epidermis was noted 24 h after burning and application of a solution of lecithin liposomes containing 26% of phosphatidylcholine to the burned surface (*Fig. 4*). There was partial formation of dermal bundles, a crimped fiber structure, an increased number of microvessels, and, compared with the skin of the intact animals, a large amount of amorphous substance. The integrity of the hair and hair follicles was preserved, the epidermal root sheath was structured, and the medulla was not expanded. The secretory vesicles of sebaceous glands were damaged, the epithelial cells were loosely located, and intercellular contacts were lost. Large hypodermal vessels were hyperemic, and their walls were partially destroyed.

Following application of a solution of lecithin liposomes containing 90% of phosphatidylcholine, a partial

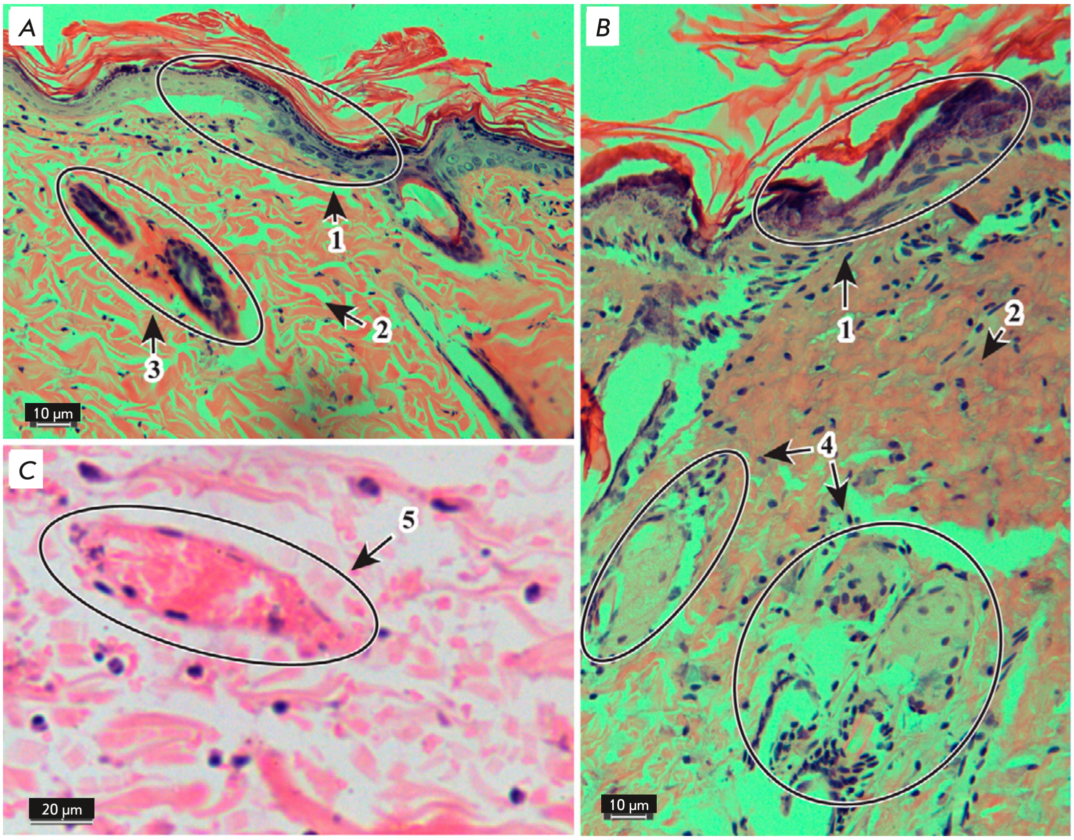

Fig. 4. Morphological changes in the skin with burn injury 24 h after application of liposomes with 26% of phosphatidylcholine. Hematoxylin and eosin stain.
×20 (*A*, *B*) and ×40 (*C*) objectives.
1 – epidermis,
2 – dermis,
3 – hair follicles,
4 – sebaceous glands,
5 – blood vessels

Table 1. Effect of liposomes with various compositions on the parameters of the skin and its derivative 24 h after burn injury

Intact	False stress	Burn	Burn + liposomes with 26% PC	Burn + liposomes with 90% PC
Epidermis thickness, µm				
28.89 ± 3.63	25.95 ± 5.97	13.00 ± 3.87$^{*,\#}$	11.93 ± 2.69$^{*,\#}$	12.25 ± 4.03$^{*,\#}$
Thickness of the stratum corneum of the epidermis, µm				
13.05 ± 2.04	13.42 ± 3.91	5.70 ± 2.20*	4.73 ± 1.49$^{*,\#}$	5.00 ± 2.95$^{*,\#}$
Epidermis thickness (without stratum corneum), µm				
15.84 ± 2.73	12.53 ± 2.46	7.30 ± 2.32*	7.20 ± 2.14$^{*,\#}$	7.25 ± 1.71$^{*,\#}$
Number of hyperemic vessels				
0.00 ± 0.00	0.00 ± 0.00	14.48 ± 4.73$^{*,\#}$	12.00 ± 3.74$^{*,\#}$	7.75 ± 1.22$^{*,\#,v}$
Number of damaged hair follicles				
0.00 ± 0.00	0.00 ± 0.00	2.93 ± 3.47$^{*,\#}$	0.00 ± 0.00^{v}	3.42 ± 0.90$^{*,\#,a}$
Number of damaged sebaceous glands				
0.00 ± 0.00	0.00 ± 0.00	6.78 ± 1.19$^{*,\#}$	6.13 ± 1.13$^{*,\#}$	0.00 ± 0.00^{v,a}

Note. PC – phosphatidylcholine. Statistically significant: * – compared with intact rats; $^{\#}$ – compared with stress; ^{v} – compared with burn, ^{a} – compared with 26% PC.

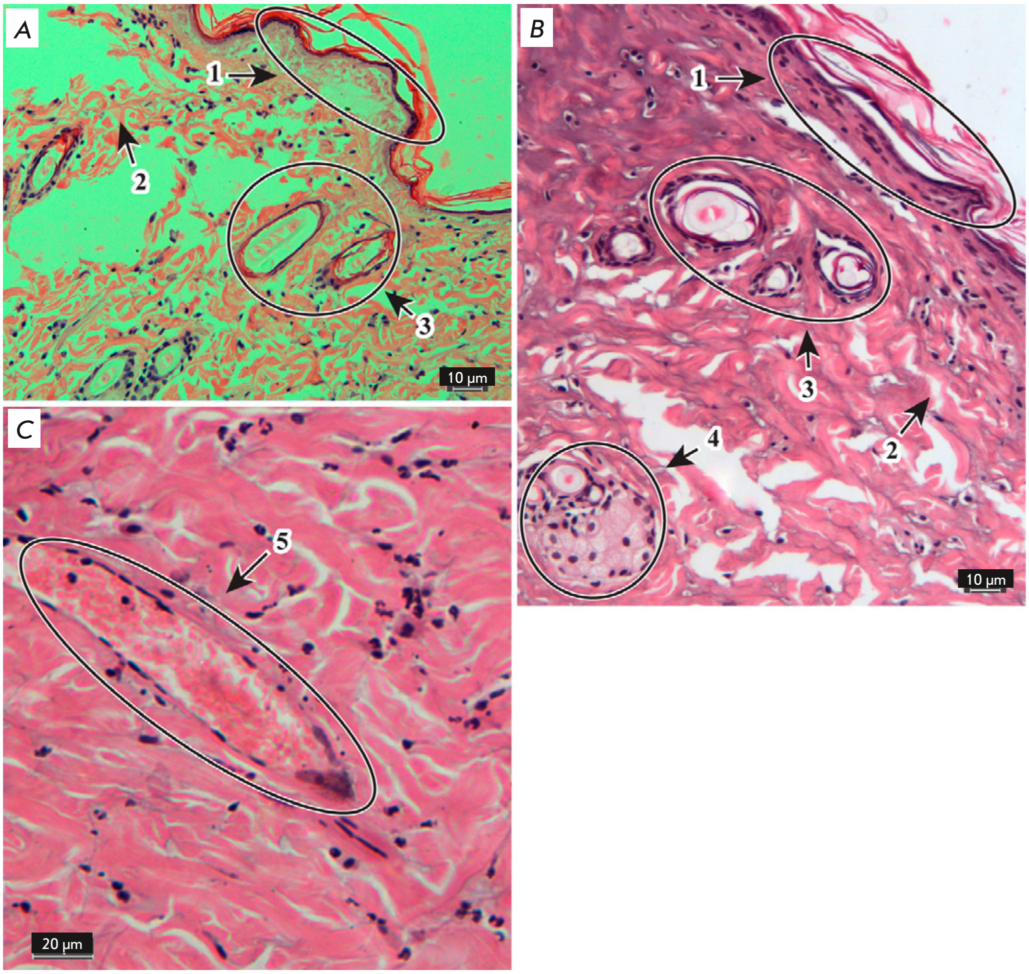

Fig. 5. Morphological changes in the skin with burn injury after application of liposomes with 90% of phosphatidylcholine. Hematoxylin and eosin stain. ×20 (*A*, *B*) and ×40 (*C*) objectives. 1 – epidermis, 2 – dermis, 3 – hair follicles, 4 – sebaceous glands, 5 – blood vessels

restoration of the layered epidermal structure, an increased number of basal layer cells, a decreased number of spinous layer cells, and a damaged granular layer were observed (*Fig. 5*). There was partial formation of dermal bundles, a crimped fiber structure, an increased number of microvessels, and, compared with the skin of the intact animals, a large amount of amorphous substance. The hair root and outer and inner root sheath were destructed, the medulla of the hair root was expanded, the shape of the hair root was changed, and there was a single-layer contour of cells around the root. The integrity of sebaceous glands was preserved, the secretion-containing vesicles were tightly adjacent to each other, and the stratified epithelium of the glands was preserved. Large hypodermal vessels were hyperemic, and their walls had partially thinned.

According to a mathematical assessment, the liposomes of different fatty acid compositions did not have a statistically significant effect on the thickness of the epidermis, stratum corneum of the epidermis, or epidermis without the stratum corneum, but there was a trend towards a partial restoration of the epidermal layers upon using lecithin containing both 26% and 90% of phosphatidylcholine (*Table 1*). However, no damaged hair follicles were detected after the application of liposomes composed of lecithin of 26% phosphatidylcholine content (*Table 1*).

Liposomes composed of lecithin containing 90% of phosphatidylcholine had no effect on the number of damaged hair follicles, but it reduced the number of hyperemic vessels by 47% compared with that in the group of burned animals and eliminated the negative effect of burns on sebaceous glands, whose number was reduced to values observed in healthy animals (*Table 1*).

Therefore, the burns caused negative changes in all studied parameters. Liposomes composed of lecithin containing 26% of phosphatidylcholine prevented the development of damage to hair follicles, which may be due to additional components present in pharmaceutical lecithin.

Liposomes composed of lecithin containing 90% of phosphatidylcholine reduced the number of hyperemic blood vessels and prevented damage to sebaceous glands. In addition, a significant restoration of the dermis structure was observed with liposomes composed of lecithin containing both 26% and 90% of phosphatidylcholine.

DISCUSSION

The barrier function is known to be the main role of the skin. This function is actualized by preventing the physical penetration of foreign components by keratinocytes, due to the unity of their monolayers; the lipid-protective part due to the presence of ceramides, cholesterol, and the free fatty acids present in the intercellular space of corneocytes; lipolytic, proteolytic enzymes, and antimicrobial peptides synthesized by skin cells; and the renewal of lipid and enzymatic components through their secretion by skin cells [41, 42].

Our findings suggest that burns significantly reduce the barrier function of the skin, in particular due to the lipid-protective component of the intercellular space of corneocytes. Probably, inclusion of lipid components into anti-burn agents may reduce the intensity of thermal damage to the skin. Also, phosphatidylinositol 3-kinase/protein kinase B is known to be involved in postburn sepsis [43]. The presence of 12–15% of phosphatidylinositol (phosphatidylinositol 3-kinase/protein kinase B substrate) in 26% of lecithin suggests potentiation of the negative effect of burn injury. However, our experiment revealed no negative effects from the first type of liposomes on the studied parameters, suggesting that phosphatidylinositol does not adversely affect the burn healing process. The positive effect of liposomes composed of 26% of phosphatidylcholine on preventing damage to hair follicles may be due to the phosphatidic acids present in the substance from which the liposomes are made (4–8%). In this regard, the lack of a positive effect from liposomes composed of lecithin with 90% of phosphatidylcholine on hair follicles may be due to the absence of phosphatidic acids in the liposomes. This suggestion requires further research.

The observed decrease in the number of hyperemic vessels is regarded as positive, because the intensity of a skin vessel filling up with blood cells is associated with inflammatory process activity [44]. Thus, liposomes composed of lecithin containing 90% of phosphatidylcholine likely have the ability to reduce inflammatory activity. This effect may be related to the higher content of γ-linolenic acid (C18:3n6c) in lecithin containing 90% of phosphatidylcholine, which is consistent with its positive effects reported in experimental burns in rats [45].

Sebaceous glands are known to release their secretion into hair follicles [46, 47] and synthesize a mixture of lipids, creating a permeability barrier and imparting certain antimicrobial properties to the skin [48, 49]. For this reason, preservation of sebaceous glands by liposomes composed of lecithin containing 90% of phosphatidylcholine is a considerable protective outcome. This effect is most likely due to a higher phosphatidylcholine content and higher contents of linoleic acid (C18:2n6c, 62.88% vs. 56.95%) and oleic acid (C18:1n9c, 11.36% vs. 8.8%) than in pharmaceutical lecithin. This suggestion seems reasonable, because there is evidence that oleic (C18:1n9) and linoleic (C18:2n6) acids are able to accelerate the healing of skin wounds and reduce the intensity of any inflammation in them by inhibiting the production of pro-inflammatory cytokines [50, 51]. Regeneration of auxiliary organs of the skin, such as hair follicles and sebaceous glands, not only accelerates wound healing, but also improves the functionality of regenerated skin. Furthermore, regeneration of sebaceous glands indirectly indicates a regeneration of the hair follicle [52].

CONCLUSION

The presented material suggests that liposomes composed of lecithin containing 90% of phosphatidylcholine are more effective in reducing vascular hyperemia in burn-damaged skin and in preventing damage to sebaceous glands than those composed of lecithin containing 26% of phosphatidylcholine. Nevertheless, liposomes composed of lecithin with 26% of phosphatidylcholine prevent damage to hair follicles, which may be due to the presence of phosphatidic acids, as well as other components. Further research is needed to elucidate the molecular mechanisms of action of liposomes of various compositions. ●

Funding.
This study was supported by the Ministry of Science and Higher Education of the Russian Federation (state scientific program, topic No. 122041100186-2) and the Innovation Promotion Foundation, grant UMNIK, contract 16398GU/2021).

Compliance with ethical standards.
All procedures performed in studies involving animals complied with the ethical standards of the institution, where the studies were conducted, and the principles of the Basel Declaration and recommendations (Permission of the Commission on Bioethics and Humane Treatment of Laboratory Animals used in research and pedagogical process of the educational institution "Vitebsk State Medical University" of January 15, 2021) approved by the legal acts of the Republic of Belarus and the Russian Federation.

Acknowledgments.
The authors are grateful to JSC Design Bureau "Display" (Vitebsk, Republic of Belarus) for creating a device for experimental modeling of thermal burns.

REFERENCES

1. Kreyden O.P., Scheidegger E.P. // J. Invest. Dermatol. 2004. V. 22. P. 40–44.
2. Zhou S.-S., Li D., Zhou Yi.-M., Cao J.-M. // Diabetol. Metab. Syndr. 2012. V. 4. P. 15.
3. Smallridge R.C., Gamblin G.T., Eil C. // Metabolism. 1986. V. 35. P. 899–904.
4. Johnson H.L., Maibach H.I. // J. Invest. Dermatol. 1971. V. 56. P. 182–188.
5. Sato K. // Rev. Physiol. Biochem. Pharmacol. 1977. V. 79. P. 51–131.
6. Cizza G., Marques A.H., Eskandari F., Christie I.C., Torvik S., Silverman M.N., Phillips T.M., Sternberg E.M. // Biol. Psychiatry. 2008. V. 64. P. 907–911.
7. Takemura T., Wertz P.W., Sato K.Br. // J. Dermatol. 1989. V. 120. P. 43–47.
8. Smith K.R., Thiboutot D.M. // J. Lipid Res. 2008. V. 49. P. 271–281.
9. Arck P.C., Slominski A., Theoharides T.C., Peters E.M., Paus R. // J. Invest. Dermatol. 2006. V. 126. P. 1697–1704.
10. Oesch F., Fabian E., Oesch-Bartlomowicz B., Werner C., Landsiedel R. // Drug Metab. Rev. 2007. V. 39. P. 659–698.
11. Slominski A.T., Manna P.R., Tuckey R.C. // Steroids. 2015. V. 103. P. 72–88.
12. Picardo M., Mastrofrancesco A., Tamas B. // Exp. Dermatol. 2015. V. 24. P. 485–486.
13. Wille J.J., Kydonieus A. // Skin Pharmacol. Appl. Skin Physiol. 2003. V. 16. P. 176–187.
14. Thiele J.J., Weber S.U., Packer L. // J. Invest. Dermatol. 1999. V. 113. P. 1006–1010.
15. Zouboulis C.C., Picardo M., Ju Q., Kurokawa I., Torocsik D., Biro T., Schneider M.R. // Rev. Endocr. Metab. Disord. 2016. V. 17. P. 319–334.
16. Paus R., Cotsarelis G. // N. Engl. J. Med. 1999. V. 341. P. 491–497.
17. Cotsarelis G., Sun T.T., Lavker R.M. // Cell. 1990. V. 61. P. 1329–1337.
18. Rochat A., Kobayashi K., Barrandon Y. // Cell. 1994. V. 76. P. 1063–1073.
19. Healthcare in Russia. Statistical compendium. Rosstat. M., 2021. 171 p.
20. van Lieshout E.M., van Yperen D.T., van Baar M.E., Polinder S., Boersma D., et al. // BMJ Open. 2018. V. 8. № 11. P. e023709.
21. Kotronoulas A., Karvelsson S.T., Heijink M. // Prostaglandins Leukot. Essent. Fatty Acids. 2021. V. 175. P. 102358.
22. Silva J.R., Burger B., Kuhl C.M.C., Candreva T., Dos Anjos M.B.P., Rodrigues H.G. // Mediators Inflamm. 2018. V. 2018. P. 2503950.
23. Ancuta E.P. // Acta Sci. Pol. Technol. Aliment. 2016. V. 15. P. 121–129.
24. Stewart M.E., Downing D.T., Pochi P.E., Strauss J.S. // Biochim. Biophys. Acta. 1978. V. 529. P. 380–386.
25. Okuno T., Gijon M.A., Zarini S., Martin S.A., Barkley R.M., Johnson C.A., Ohba M., Yokomizo T., Murphy R.C. // J. Lipid Res. 2018. V. 59. P. 542–549.
26. Savelieva M.I., Sychev D.A. // Phlebology. 2018. V. 12. P. 40–49.
27. Marchio S., Bussolino F. // Bulletin of RSMU. 2018. V. 6. P. 4–14.
28. Baryshnikov A.Yu. // Annals of the Russian Academy of Medical Sciences. 2012. V. 67. P. 23–31.
29. Alyautdin R.N., Iezhitsa I.N., Agarval R. // Vestnik Oftalmologii. 2014. V. 130. P. 117–122. https://doi.org/10.1093/nar/gkl253.
30. Molochkov A.V., Khlebnikova A.N. // Almanac of Clinical Medicine. 2014. V. 34. P. 85–90.
31. Denieva Z.G., Budanova U.A., Sebyakin Yu.L. // Biochem. Cell Biol. 2021. V. 15. P. 21–35.
32. Tazina E.V., Ignatieva E.V., Polozkova A.P., Orlova O.L., Oborotova N.A. // Pharm. Chem. J. 2008. V. 42. P. 30–35.
33. Jenski L.J., Zerouga M., Stillwell W. // Proc. Soc. Exp. Biol. Med. 1995. V. 210. P. 227–233.
34. Kafrawy O., Zerouga M., Stillwell W., Jenski L.J. // Cancer Lett. 1998. V. 132. P. 23–29.
35. Li X.-X., Shi S., Rong L., Feng M.-Q., Zhong L. // Int. J. Nanomedicine. 2018. V. 13. P. 1399–1409.
36. Khoshneviszadeh R.B., Bazzaz S.F., Housaindokht M.R., Ebrahim-Habibi A., Rajabi O. // Iranian J. Pharm. Res. 2015. V. 149. P. 473–478
37. Gimmelfarb G.N. Anesthesia in experimental animals. Tashkent: FAN, 1984. 144 p.
38. Berghof P.K. Small pets. Diseases and treatment: Trans. from German. M.: Aquarium, 1999. 224 p.
39. Bunatyan A.A. Guide to anesthesiology / ed. A.A. Bunatyan. M.: Medicine, 1994. 665 p.
40. Gilpin D.A. // Burns. 1996. V. 22. P. 607–611.
41. Menon G.K., Cleary G.W., Lane M.E. // Int. J. Pharm. 2012. V. 435. P. 3–9.

42. Fujiwara A., Morifuji M., Kitade M., Fujiwara A., Morifuji M., Kitade M., Kawahata K., Fukasawa T., Yamaji T., Itoh H. // Arch. Dermatol. Res. 2018. V. 310. P. 729–735.
43. Luo K., Long H., Xu B., Luo Y. // Int. J. Surg. 2015. V. 21. P. 22–27.
44. Choi S.H., Moon J.S., Jeon B.S., Jeon Y.J., Yoon B.I., Lim C.J. // Biomol. Ther. (Seoul). 2015. V. 23. P. 174–179.
45. Allison F.Jr., Smith M.R., Wood Wb.Jr. // J. Exp. Med. 1955. V. 102. P. 655–668.
46. Karlstad M.D., De Michele S.J., Leathem W.D., Peterson M.B. // Crit. Care Med. 1993. V. 21. P. 1740–1749.
47. Valiveti S., Lu G.W. // Int. J. Pharm. 2007. V. 345. P. 88–94.
48. Li X., Becker K.A., Zhang Y. // Cell Physiol. Biochem. 2010. V. 26. P. 41–48.
49. Wertz Ph.W. // J. Lipids. 2018. V. 2018. P. 5954034.
50. Guidoni M., de Christo Scherer M.M., Figueira M.M., Schmitt E.F.P., de Almeida L.C., Scherer R., Bogusz S., Fronza M. // Braz. J. Med. Biol. Res. 2019. V. 52. P. e8209.
51. Barros Cardoso C.R., Souza M.A., Vieira Ferro E.A., Favoreto S.Jr., Pena J.D.O. // Wound Repair Regen. 2004. V. 12. P. 235–243.
52. Xia Y., You X.-E., Hong C., Chen H., Yan Y.-J., He Y.-C., Ding S.-Z. // Int. J. Clin. Exp. Pathol. 2017. V. 10. P. 7390–7400.

Modern Approaches to *de novo* Synthesis of Extended DNA Fragments: Assembly of a Wide Repertoire of Sequences

T. A. Semashko[1,2*], G. Y. Fisunov[1,2], E. A. Tsoy[1,2], D. R. Kharrasov[1], I. K. Chudinov[1], D. V. Evsyutina[1,2], G. Y. Shevelev[3], V. M. Govorun[1]
[1]Research Institute for Systems Biology and Medicine, Moscow, 117246 Russian Federation
[2]Lopukhin Federal Research and Clinical Center of Physical-Chemical Medicine, Moscow, 119435 Russian Federation
[3]Institute of Chemical Biology and Fundamental Medicine, Novosibirsk, 630090 Russian Federation
[*]E-mail: t.semashko@gmail.com

Received December 27, 2023; in final form, February 28, 2024
DOI: 10.32607/actanaturae.27362

ABSTRACT **The standardization of DNA fragment assembly methods for many tasks of synthetic biology is crucial. This is necessary for synthesizing a wider repertoire of sequences, as well as for further automation and miniaturization of such reactions. In this work, we proposed conditions for the assembly of DNA fragments from chemically synthesized oligonucleotides and we identified the errors occurring in the sequence under these conditions. Additionally, we proposed conditions for further combining synthetic fragments into larger DNA fragments. We showed that the optimized conditions are suitable for the assembly of a wide range of sequences.**

KEYWORDS **DNA synthesis, DNA artificial synthesis, gene synthesis, gene assembly, PCR assembly, polymerase cyclic assembly, spermidine.**

INTRODUCTION

Attempts have been made to obtain synthetic DNA fragments from chemically synthesized short oligonucleotides since the mid-60s of the XX century. However, the assembly of the yeast alanine tRNA gene with a length of 77 bp was successfully completed only in 1970 [1]. The development of techniques for the chemical synthesis of oligonucleotides, as well as the assembly and cloning of extended DNA fragments, currently allows for the creation of entire genomes of viruses [2], prokaryotes [3, 4], and eukaryotes [5], including those designed by researchers – with codon transcoding [6], a four-letter genetic code [7]. Synthetic biology is a rapidly developing field. In many cases, the synthesis of extended DNA sequences is necessary to achieve its ambitious goals of creating organisms with desired properties. The assembly of the whole genome is considered as an achievement of modern technology and is quite an undertaking. In biotechnology, medicine, as well as in fundamental research, the synthesis of *de novo* DNA fragments (containing, as usual, sequences of one or more genes with a length of several kb) with high accuracy and at low cost is of central importance [8], in particular, for heterologous gene expression [9], and their modification [10]. Currently, DNA synthesis *in vitro* is performed hierarchically: first, oligonucleotides are synthesized chemically, and then DNA fragments ranging in size from 0.5 to several kb are assembled from them. If necessary, these fragments are combined with each other to form DNA 2–10 kb long by restriction and ligation, assembly of overlapping fragments, or site-specific recombination [11].

The chemical synthesis of oligonucleotides is an automated, well–rotated process. The main goals are to obtain longer sequences (more than 100 bp), increase the yield of the reaction at all stages of the synthetic cycle, and reduce the number of errors by improving the quality of chemical reagents [12]. Three main strategies for the assembly of oligonucleotides into dsDNA fragments have been developed: *in vitro* assembly using enzymes – ligase cyclic assembly (LCR) [13, 14] and polymerase cyclic assembly (PCR), as well as *in vivo* assembly in yeast cells [15]. The main advantages of PCR assembly are the smaller concentration of the oligonucleotides required for the reaction, the absence of an oligonucleotide phosphorylation stage, and lower labor intensity [16, 17]. Various modifications of PCR have been proposed to assemble long fragments and increase the accuracy of the synthesized sequence [18–20]. At the same time, given the wide variety of target dsDNAs, determination of the optimal conditions for PCR remains relevant, which include the components of the reaction mixture (buffer system, concentrations of salts, magnesium ions, dNTP, oligonucleotides, type of DNA polymerase, the presence of additives), as well as the temperature and time at each stage of PCR. Amides [21], dimethyl sulfoxide [22], betaine [23], glycerin [24], polyethylene glycols, polyamines [25], in particular spermidine [26], are used as additives. Regardless of the type of assembly being performed, successful synthesis requires a rational design of oligonucleotides that takes into account the thermodynamic characteristics of the sequence and the presence of repeating elements and motifs capable of forming secondary structures. The purpose of this work was to design universal conditions for the assembly of DNA fragments suitable for most such tasks.

In this work, we optimized the PCR assembly of DNA fragments from oligonucleotides and we selected the conditions in which DNA fragments up to 1.5 kb with a diverse repertoire of sequences could be efficiently assembled, taking into account product yield and possible errors in the DNA sequence. We optimized the conditions for combining several amplicons into a fragment of up to 7.5 kb.

EXPERIMENTAL

Design and synthesis of oligonucleotides for the assembly of DNA fragments

The oligonucleotide design was made using the SynthBac program [27, 28] with a thermodynamically optimized method. The synthesis of the oligonucleotides for the 1 000 bp model fragment and the BseRI gene was carried out on the AFM-800 synthesizer (Biosset, Russia), and the synthesis of the oligonucleotides for the transposase gene and fragments of the N4 phage was carried out on the Dr. Oligo 768XLc synthesizer (Biolytic, USA).

PCR assembly of DNA fragments from the oligonucleotides

The assembly was carried out in two stages. At the first stage, 2 μl of an oligonucleotide mixture (concentration of 1 000, 100, 10, or 1 nM each) was added to a reaction mixture containing 0.5 μl of polymerase, and a buffer corresponding to the polymerase used; 0.2 mM dNTP (Evrogen, Russia). Additionally, $MgSO_4$ (Fermentas, USA) was added to the reaction to a final concentration of 5 or 10 mM; formamide, to a final concentration of 2%; PEG 4 000 (50%) (Fermentas, USA) to a final concentration of 7.5%; or spermidine, to a final concentration of 0.5 or 2.5 mM. Taq polymerases (5 U/μl, Lytech, Russia), Tersus (50X, Evrogen) with commercial buffers, or Phusion obtained in the laboratory with 1× reaction buffer (10 mM Tris-HCl, pH 8.8, 50 mM KCl, 2.5 mM $MgSO_4$, 0.1% Triton X-100, 0.2 mg/ml of BSA). The activity of the obtained Phusion DNA polymerase matched the activity of commercial Phusion Hot Start II DNA Polymerase (2 U/μl, Thermo Fisher Scientific). The main program for the assembly was: 95°C, 3 min, then 20 cycles – 95°C 30 s, 58°C 30 s and 72°C 1 min, final elongation – 72°C 5 min. Other variants of the program were also used in which the temperature gradient was used at the annealing stage (55, 55.9, 57.6, 60.1, 63.2, 65.8, 67.3 or 68°C), 2 minutes of elongation or 30 reaction cycles.

At the second stage, the completed DNA fragment was amplified. After the first stage of PCR, 2 μl of the reaction mixture was transferred to a reaction mixture containing 20 mM Tris-HCl pH 8.8, 10 mM KCl, 2 mM $MgSO_4$, 6 mM $(NH_4)_2SO_4$, 0.1% Triton X-100, 0.1 mg/ml BSA, Phusion DNA polymerase, 250 nM of each primer, 0.2 mM dNTP. PCR program: 95°C 3 min, then 25 cycles – 95°C 30 s, 58°C 30 s and 72°C 1 min, final elongation – 72°C 5 min.

The assembly of the transposase gene

The gene was assembled in two stages. At the first stage, 2 μl of an oligonucleotides mixture (500, 100, 10 or 1 nM each) was added to the reaction mixture with 0.5 μl of polymerase, and a buffer corresponding to the polymerase used, 0.2 mM dNTP. Additionally, 10 mM $MgSO_4$ or 2.5 mM spermidine was present in the reaction. Taq polymerases (5 U/μl, Lytech) or Phusion obtained in the laboratory with 1× reaction buffer (10 mM Tris-HCl, pH 8.8, 50 mM KCl, 0.1% Triton X-100, 0.2 mg/ml BSA) were used. The activity of the obtained Phusion DNA polymerase matched the activity of commercial Phusion Hot Start II DNA Polymerase (2 U/μl, Thermo Fisher Scientific). The main program for the assembly was: 98°C 3 min, then 20 cycles – 96°C 15 s, 57°C 20 s and 72°C 1 min.

At the second stage, 2 μl of the resulting reaction mixture was transferred to 25 μl of the reaction mixture with 50 mM Tris pH 8.8, 100 mM KCl, 2.5 mM $MgSO_4$, 0.1% Triton X-100, 0.2 mg/ml BSA, DNA polymerase Phusion, 300 nM of each primer, 0.2 mM dNTP. PCR program: 96°C 1 min, then 25 cycles – 95°C 15 s, 57°C 20 s and 72°C 1 min.

Error rate calculations in the assembled DNA fragment

To determine the extent to which the DNA polymerase used affected the frequency of different types of errors in the assembled DNA fragment, the transposase gene was assembled under the conditions described below. Taq (5 U/µl, Lytech) or laboratory-obtained Phusion with 1× reaction buffer (10 mM Tris-HCl, pH 8.8, 50 mM KCl, 0.1% Triton X-100, 0.2 mg/ml BSA) were used as DNA polymerase. The activity of the obtained Phusion DNA polymerase matched the activity of commercial Phusion Hot Start II DNA Polymerase (2 U/µl, Thermo Fisher Scientific). The gene was assembled in two stages. In the first stage, 2 µl of the oligonucleotide mixture was added to the reaction mixture (0.5 µl of polymerase, buffer corresponding to the polymerase used, 0.2 mM dNTP and 2.5 mM spermidine). The main program for assembly was as follows: 98°C 3 min, then 20 cycles – 96°C 15 s, 57°C 20 s and 72°C 1 min.

In the second stage, 2 µl of the resulting reaction mixture was transferred to 25 µl of the reaction mixture with 10 mM Tris-HCl pH 8.8, 100 mM KCl, 2.5 mM $MgSO_4$, 0.1% Triton X-100, 0.2 mg/ml BSA, DNA polymerase Phusion, 300 nM of each primer, 0.2 mM dNTP. PCR program: 96°C 1 min, then 25 cycles – 95°C 15 s, 57°C 20 s and 72°C 1 min.

The gene assembled using Taq DNA polymerase was cloned into the pET15 vector using NEBuilder (NEB, USA) and chemically transformed into *E. coli* Top10 cells. The gene assembled using Phusion DNA polymerase was cloned into the pTZ57RT vector using homologous recombination *in vivo* after chemical transformation into *E. coli* strain Top10 carrying plasmid pKM200 (Addgene) with the Lambda Red recombination system. Some 18 clones of each gene variant were sequenced by the Sanger method on the Honor 1616 genetic analyzer (Nanjing Superyears Gene Technology Co., Ltd., China).

Subsequently, the conditions described above and the laboratory-obtained Phusion DNA polymerase with a 1× reaction buffer were used to assemble DNA fragments up to 1 500 bp long.

Combining DNA fragments using PCR

dsDNA fragments with lengths of 1 009 (fragment 1), 1 152 (fragment 2), and 1 254 (fragment 3) bp, obtained after assembly from oligonucleotides, were combined into pairs (2 and 3) and triples (1, 2 and 3). The amount of matrix added to the reaction was varied. When combining a pair of fragments, the concentration of each of them in the reaction mixture was 3 nM, 300 pM, 30 pM, and 3 pM; for triples it was 2 nM, 200 pM, 20 pM, and 2 pM. The concentration of the fragments was measured using a Qubit fluorimeter (Thermo) and a dsDNA BR Assay Kit (Thermo). During the assembly of three fragments, amplicons were introduced both without purification (in the form of a reaction mixture after assembly from oligonucleotides) and purified on magnetic particles NEBNext Sample Purification beads (NEB) according to the manufacturer's protocol. Each sample contained 0.4 µl of Taq polymerase (5 U/µl, Lytech) or Tersus (50X, Evrogen), an appropriate commercial buffer, 0.2 mM dNTP and a pair of primers with a final concentration of 0.25 µM in the mixture. The amplification reaction was performed at spermidine concentrations of 0, 0.5, and 2.5 mM. Amplification conditions: 95°C 3 min, then 20 cycles – 95°C 30 s, 62°C 30 s and 72°C 5 min, final elongation – 72°C 5 min.

Visualization of the assembly of fragments

Visualization was performed using electrophoretic separation of DNA fragments in a horizontal 1% agarose gel in 0.1 M Tris-borate buffer at 150 V for 20–40 min.

RESULTS

Condition optimization for the assembly of DNA fragments from oligonucleotides

To optimize conditions, we used a fragment of the *Mycoplasma gallisepticum* S6 ribosomal protein operon, consisting of the rpsJ gene and the first half of the rplC gene (1016 bp). Using the SynthBac program developed by our group (manuscript in preparation), the fragment was divided into 47 overlapping thermodynamically optimized oligonucleotides with an average length of 43 bp [27]. The gene was assembled in two PCR stages: in the first stage, the oligonucleotides were extended to assemble the fragment with a complete sequence: in the second stage, when flanked primers were added, the resulting fragment was amplified.

In this work, the PCR conditions of the first stage were optimized (*Fig. 1*). All reaction conditions were applied to the oligonucleotides included into the reaction at four different concentrations (100, 10, 1 and 0.1 nM each in the reaction mixture). According to the results obtained, the optimal range of oligonucleotide concentrations for the assembly of DNA fragments is in the region of tens of nM and varies slightly depending on the composition of the reaction mixture. In the reaction mixture, we varied the concentration of Mg^{2+} ions (2.5, 5 and 10 mM) and found that it has a significant effect on the final product – fragments are much better assembled in the presence of 10 mM Mg^{2+}, although such high concentrations are no lon-

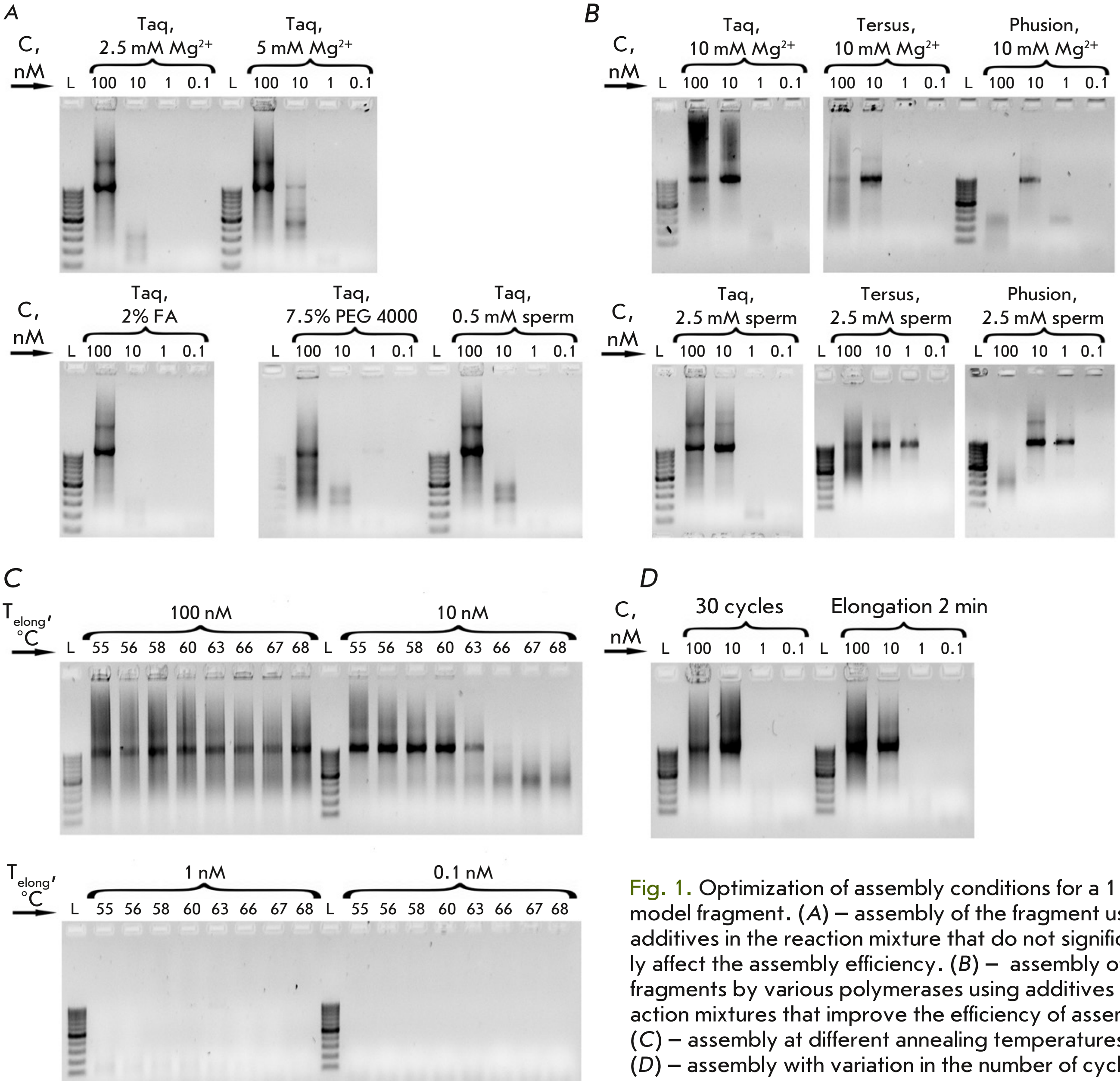

Fig. 1. Optimization of assembly conditions for a 1 kb model fragment. (*A*) – assembly of the fragment using additives in the reaction mixture that do not significantly affect the assembly efficiency. (*B*) – assembly of fragments by various polymerases using additives in reaction mixtures that improve the efficiency of assembly. (*C*) – assembly at different annealing temperatures. (*D*) – assembly with variation in the number of cycles or elongation time. L is the length marker GeneRuler 100 bp (Thermo), sperm is spermidine, C – each oligonucleotide concentration in the reaction mixture

ger used for fragment amplification (*Fig. 1A,B*). The effect of formamide and PEG 4000 in the reaction mixture on the assembly of fragments has also been studied. The addition of these components does not have a significant effect (*Fig. 1A*). Interestingly, the addition of 2.5 mM spermidine to the reaction mixture significantly improved the assembly of DNA fragments (*Fig. 1B*). An increase in the elongation time or the number of cycles in the assembly program also contributed to a better assembly of the fragments (*Fig. 1D*). At high concentrations of oligonucleotides, the assembly reaction proceeds effectively over a wide range of annealing temperatures; however, with a decrease in concentration, a decrease in hybridization, usual for PCR, is observed with an increase in the annealing temperature (*Fig. 1B*). The effectiveness of PCR assembly was also investigated when using different polymerases – Taq, Tersus and Phusion –

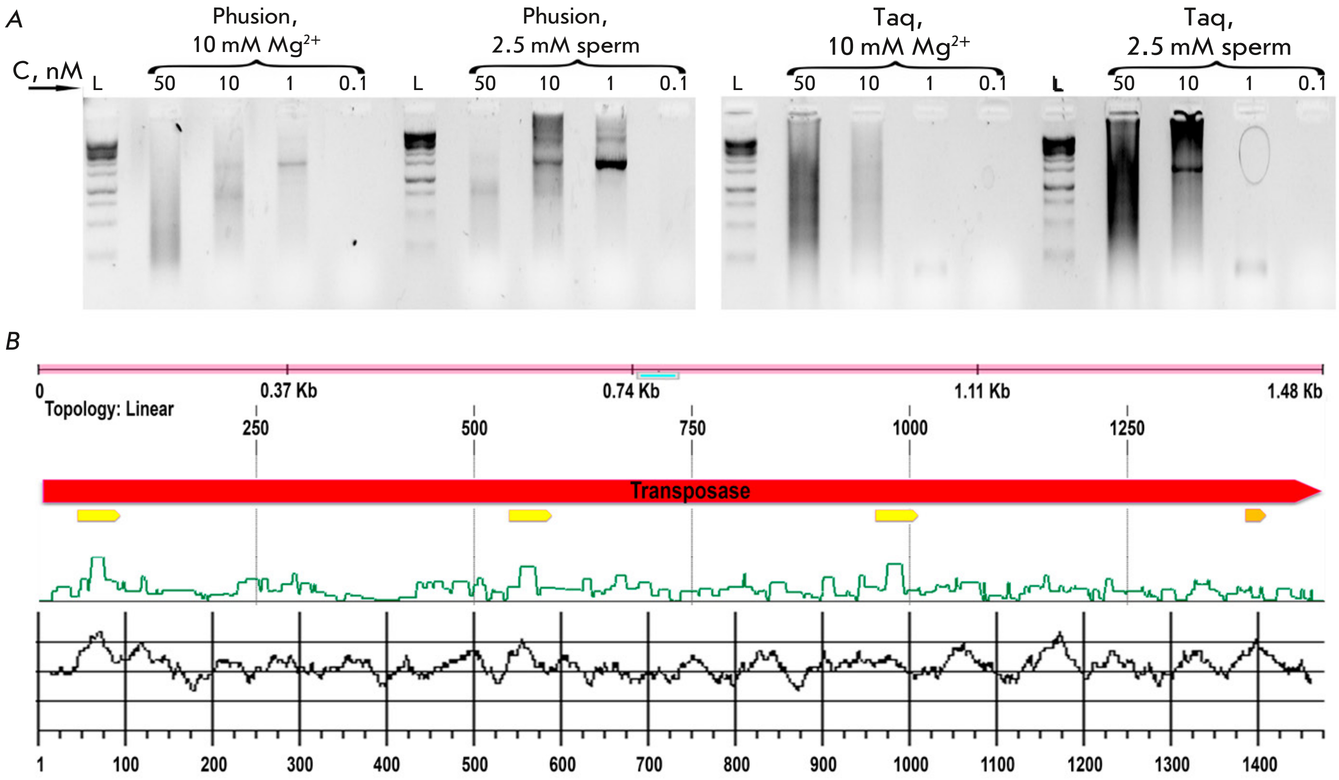

Fig. 2. (*A*) – Optimization of transposase gene assembly conditions. L is the length marker GeneRuler 1 kb (Thermo), sperm is spermidine, C – each oligonucleotide concentration in the reaction mixture; (*B*) – Annotation of the transposase sequence in the SynthBac program window. The red arrow indicates the coding frame of the transposase, the yellow one indicates the hairpin, the dark yellow one indicates the motif with a potential G-quadruplex, and the green line indicates the possibility of formation of a secondary structure. The black line on the bottom panel shows the GC composition calculated in the window of 20 bp

under optimal assembly conditions (with 10 mM Mg^{2+} or 2.5 mM spermidine) (*Fig. 1B*). We showed that all the studied polymerases efficiently collect DNA fragments from oligonucleotides, but that they possess different optimal ranges of concentrations of the oligonucleotides used.

Assembly of the transposase gene

The transposase gene (1,476 bp) was divided into 64 oligonucleotides with an average length of 45 bp using the SynthBac program [27] with an algorithm for thermodynamically optimized oligonucleotides. Most of the genes were successfully assembled using the method we optimized, but the transposase gene possesses an arduous sequence to assemble. We experimentally determined that the difficult fragment is located closer to the 3' end of the gene (data are not provided). Regions of the gene with heterogeneous GC composition, secondary structures such as three identified potential hairpins, or the GGGTGCACTGTGGAGGGCTGGG motif predicted [29] as a potential G-quadruplex proved difficult to assemble (*Fig. 2B*). We were able to obtain the required fragment (full-size (*Fig. 2A*) or divided into two approximately equal parts) only when carrying out an assembly reaction in the presence of 2.5 mM spermidine. Thus, spermidine also increases the specificity of the reaction.

The universality of the proposed conditions for the assembly of various sequences was confirmed by successfully assembling 11 different DNA fragments with a length of about 1.5 kb when adding spermidine to the reaction mixture at the first stage of the assembly *(Fig. 3)*.

Error rate in the DNA sequence identification resulting from the assembly of fragments

We studied the effect of the DNA polymerase type used at the first stage of DNA fragment assembly on the number of various types of errors in the final assembly of the target fragment. (*Table 1*). We demonstrated that the assembly with Taq polymerase yields fragments with an error rate of 8 per 1 kb; and the assembly with Phusion polymerase – three errors

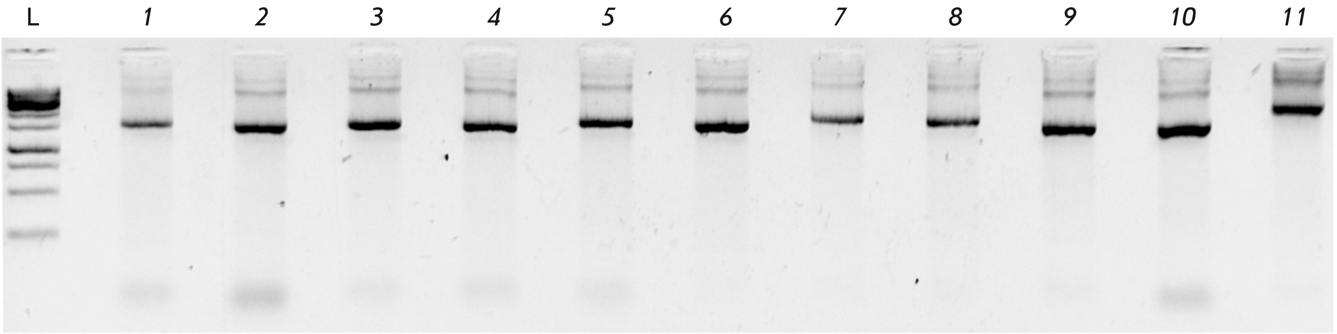

Fig. 3. Validation of the proposed method and conditions for DNA assembly from oligonucleotides on 11 different sequences with a length of approximately 1 500 bp

per 1 kb (total errors in *Table 1*). At the same time, the frequencies of insertions and deletions occurring in fragments were a match, and the main difference when using different polymerases was the number of substitutions, especially the G/C transitions in A/T.

Combining several DNA fragments using PCR

The BseRI restriction endonuclease gene with a length of 3 348 bp was divided into three overlapping fragments with lengths of 1 009 (fragment 1), 1 152 (fragment 2), and 1 254 bp (fragment 3). Each of the fragments was also divided into oligonucleotides using the SynthBac program [27] with an algorithm for thermodynamically optimized oligonucleotides and assembled according to the method optimized by us. The fragments were combined in two (*Fig. 4A*) and three fragments in one reaction (*Fig. 4B,C*). The reaction of combining fragments after preliminary purification was also performed (*Fig. 4B*). In all the selected variants, a full-size product with approximately the same efficiency was obtained. Various reaction conditions were analyzed, such as the assembly with Taq or Tersus polymerase, different concentrations of oligonucleotides, as well as the addition of 0.5 or 2.5 mM of spermidine to the reaction. In this case, the reaction substrates had optimum concentrations of tens of pM for Taq polymerase and hundreds of pM for Tersus, and spermidine did not optimize the reaction.

The genome DNA of vibriophage N4, 38.5 bp long, was divided into fragments about 1.5 kb long using the SynthBac program [27]. Each such fragment was pre-assembled from oligonucleotides using a method optimized by us. It was not possible to assemble longer fragments of up to 7.5 kb from five fragments using a technique optimized for smaller fragments; however, a decrease in temperature and an increase in elongation time allowed us to reproducibly assemble

Table 1. Error rates per 1 kb when assembling the transposase gene using Taq or Phusion DNA polymerase*

Type of error	Assembly using Taq DNA polymerase	Assembly using Phusion DNA polymerase
Substitutions	5.95 ± 0.47	0.90 ± 0.18
Transitions		
G/C to A/T	3.58 ± 0.48	0.26 ± 0.10
A/T to G/C	0.98 ± 0.16	0.08 ± 0.05
Transversions		
G/C to C/G	0.30 ± 0.13	0.19 ± 0.07
G/C to T/A	0.30 ± 0.13	0.19 ± 0.07
A/T to C/G	0.30 ± 0.11	0.11 ± 0.06
A/T to T/A	0.49 ± 0.11	0.08 ± 0.05
Deletions		
Single base	1.17 ± 0.16	1.09 ± 0.22
Multiple bases	0.41 ± 0.15	0.30 ± 0.11
Insertions		
Single base	0.56 ± 0.15	0.49 ± 0.14
Multiple bases	0	0.19 ± 0.07
Total errors	8.09 ± 0.66	2.97 ± 0.30

*The data is presented as mean value for 18 independent samples with a standard error.

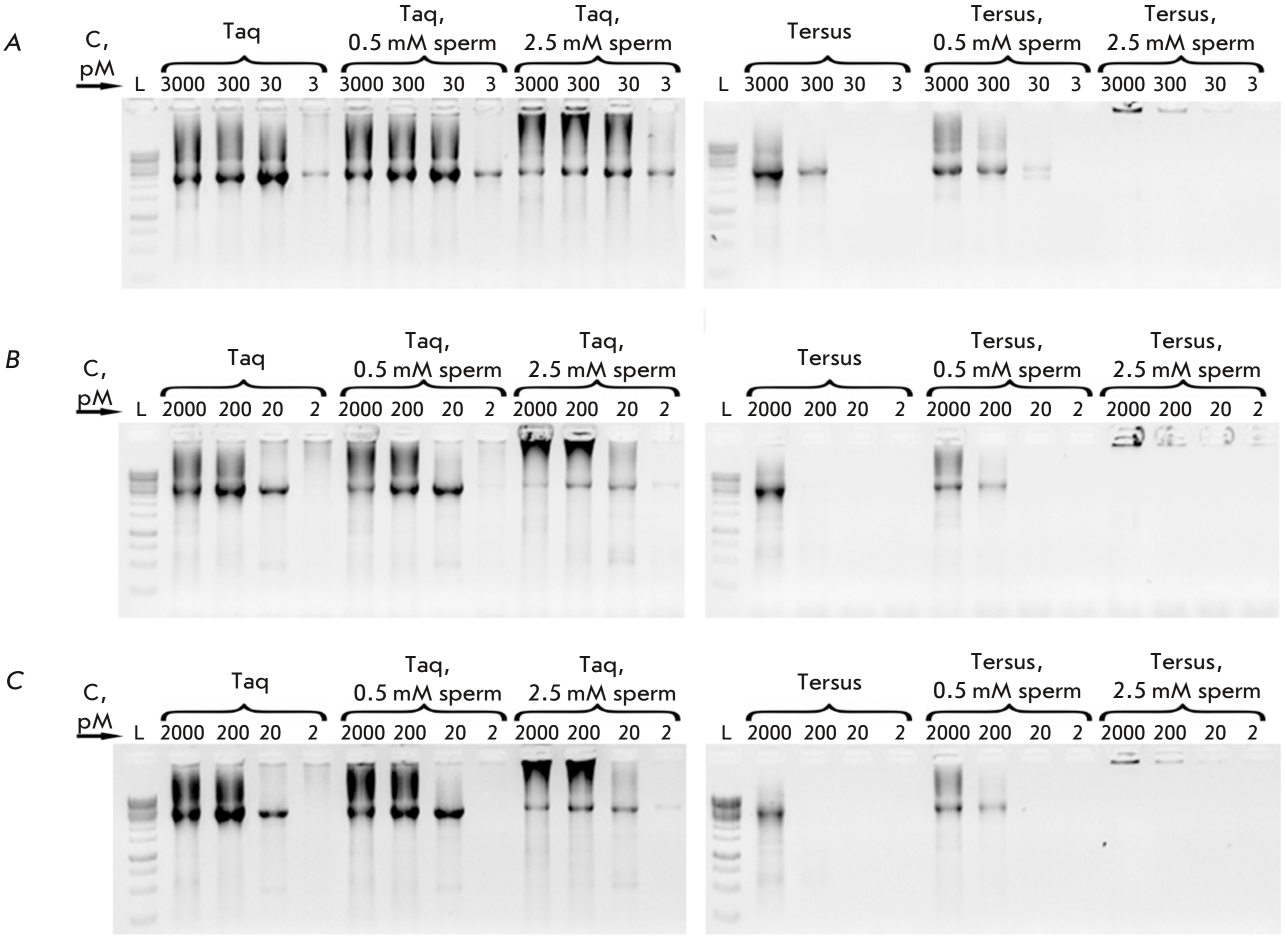

Fig. 4. Optimization of the conditions for combining fragments of the BseRI gene. L is the length marker GeneRuler 1 kb (Thermo), sperm is spermidine, C – each oligonucleotide concentration in the reaction mixture. (*A*) – combining two fragments, 2 and 3; (*B*) – combining three fragments, 1, 2, and 3; (*C*) – combining three previously purified fragments, 1, 2, and 3

DNA fragments of up to 7.5 kb (*Fig. 5*). Fragments of similar length can also be achieved by amplifying the matrix after the Gibson reaction [30].

DISCUSSION

We have chosen the PCR assembly method from the most commonly used methods of DNA assembly from oligonucleotides. The advantages of the PCR assembly method in comparison with ligase-cyclic assembly (LCR) are a lower concentration of oligonucleotides in the reaction, fewer assembly stages, and the use of only DNA polymerase.

The assembly of DNA fragments by PCR consists of two stages. In the first stage, the oligonucleotides hybridize with each other and are extended to form the required fragment, and in the second stage, the full-size fragment is amplified. In this work, the first stage of PCR assembly is optimized – the stage of elongation of the oligonucleotides to a full-size product.

We showed that concentrations of oligonucleotides of about 10 nM, Mg^{2+} 10 mM or 2.5 mM spermidine ions are optimal for DNA assembly. The concentrations of oligonucleotides for different polymerases vary slightly. A wide range of concentrations of the oligonucleotides used in the assembly reaction is described: from 2.5 μM [16], 10–60 nM [31], or from 10 nM [32], and the importance of choosing a polymerase is also indicated [32]. The effect of spermidine on the results of DNA assembly is interesting. The addition of spermidine to the reaction mixture avoids an increase in the concentration of magnesium ions in the reaction, and it increases the specificity of the assembly. There are reports of both an improvement in the efficiency of DNA amplification when using sper-

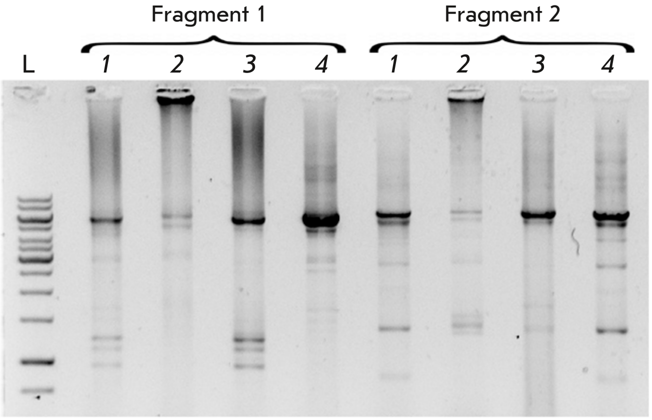

Fig. 5. Optimization of the conditions for combining five 1.5 kb fragments into one. Fragment 1 and fragment 2 are different fragments of vibriophage N4, L is the length marker GeneRuler 1 kb (Thermo), 1 is the usual conditions of combining PCR, 2 is PCR with the addition of 2.5 mM spermidine, 3 is PCR after the Gibson reaction, and 4 is PCR with elongation at 65°C and extended elongation time

midine in the reaction [26, 33] and a lack of an effect [34]. At the same time, spermidine promotes the amplification reaction in complex samples [35, 36]. It has been shown that phosphates are the main target in the interaction of spermidine polycation with DNA in B-form [37]. Presumably, spermidine makes it possible for oligonucleotides to hybridize in dsDNA, neutralizing the negative charge of the phosphate backbone and stabilizing duplexes.

Currently, errors in the obtained matrix are a factor limiting *de novo* DNA assembly, which is associated with both the quality of the oligonucleotides and the accuracy of the polymerases [38–41]. Reducing the number of errors will reduce the complexity that comes with that work and the cost of screening clones and sequencing them to achieve error-free variants. In the case of an optimized technique, the error rate during the assembly of Phusion polymerase was 3 per 1 kb.

We optimized the conditions for combining several DNA fragments 1–1.5 kb long with complementary ends into fragments of up to 7.5 kb long using PCR. The most suitable and widely used methods for combining extended DNA fragments are the Gibson reaction [30] and its variations, as well as homologous recombination in yeast [42, 43]. However, combining multiple amplicons using PCR is a simpler and faster method that uses a smaller variety of enzymes. We showed that a full-size product 2–3 kb long can be obtained under a wide range of conditions common for PCR amplification, and that spermidine does not have a positive effect on reactions of this type, unlike the reaction of DNA assembly from oligonucleotides. With a decrease in temperature and elongation time, fragments of up to 7.5 kb can be combined by amplification.

Thus, in this work, we unified the conditions for the assembly of DNA fragments from oligonucleotides by polymerase chain assembly. We showed that the assembly reaction is efficient at oligonucleotide concentrations in the range of 10 nM, with the addition of 10 mM Mg^{2+} or 2.5 mM spermidine to the reaction mixture. The choice of the oligonucleotide concentration depends on the polymerase. The addition of 2.5 mM spermidine to the reaction mixture makes it possible to increase the specificity of the assembly. The use of a more accurate Phusion polymerase for assembly makes it possible to reduce the number of errors under optimized conditions to 3 per 1 kb, mainly due to fewer substitutions.

To combine DNA fragments obtained from synthetic oligonucleotides, we optimized the conditions for combining several fragments of dsDNA with a size of about 1 kb, with overlapping regions at the ends, into a fragment with a length of up to 7.5 kb. ●

Authors contribution.
T.A. Semashko – writing the draft; D.V. Evsyutina – overview in the introduction, bioinformatic data analysis; T.A. Semashko, G.Y. Fisunov, E.A. Tsoy, D.V. Evsyutina, G.Y. Shevelev – experiments on the assembly of DNA fragments; D.R. Kharrasov, G.Y. Fisunov – obtaining recombinant polymerase Phusion; G.Y. Shevelev – synthesis of a part of oligonucleotides; I.K. Chudinov – sequencing by Sanger; V.M. Govorun – supervision of the project; all authors discussed of the work and editing the manuscript.

Funding.
This work was supported by Russian Foundation for Basic Research (grant 18-29-08043) in terms of optimizing the method of assembling DNA fragments from oligonucleotides and Federal Service for Surveillance on Consumer Rights Protection (grant 122030900107-3) in terms of determining the error rate in the assembly and assembly of large fragments up to 10 kb.

Conflict of Interest.
Authors declare about the absence of any conflicts of interests.

Ethics approval.
This article does not describe any research involving humans or animals as objects.

REFERENCES

1. Agarwal K.L., Büchi H., Caruthers M.H., Gupta N., Khorana H.G., Kleppe K., Kumar A., Ohtsuka E., Rajbhandary U.L., van de Sande J.H., et al. // Nature. 1970. V. 227. № 5253. P. 27–34.
2. Smith H.O., Hutchison C.A., Pfannkoch C., Venter J.C. // Proc. Natl. Acad. Sci. USA. 2003. V. 100. № 26. P. 15440–15445.
3. Gibson D.G., Benders G.A., Andrews-Pfannkoch C., Denisova E.A., Baden-Tillson H., Zaveri J., Stockwell T.B., Brownley A., Thomas D.W., Algire M.A., et al. // Science. 2008. V. 319. № 5867. P. 1215–1220.
4. Venetz J.E., del Medico L., Wölfle A., Schächle P., Bucher Y., Appert D., Tschan F., Flores-Tinoco C.E., van Kooten M., Guennoun R., et al. // Proc. Natl. Acad. Sci. USA. 2019. V. 116. № 16. P. 8070–8079
5. Annaluru N., Muller H., Mitchell L.A., Ramalingam S., Stracquadanio G., Richardson S.M., Dymond J.S., Kuang Z., Scheifele L.Z., Cooper E.M., et al. // Science. 2014. V. 344. № 6179. P. 55–58.
6. Lajoie M.J., Rovner A.J., Goodman D.B., Aerni H.R., Haimovich A.D., Kuznetsov G., Mercer J.A., Wang H.H., Carr P.A., Mosberg J.A., et al. // Science. 2013. V. 342. № 6156. P. 357–360.
7. Chatterjee A., Lajoie M.J., Xiao H., Church G.M., Schultz P.G. // Chembiochem. 2014. V. 15. № 12. P. 1782–1786.
8. Jain K.K. // Med. Princ. Pract. 2013. V. 22. № 3. P. 209–219.
9. Peng R.H., Yao Q.H., Xiong A.S., Cheng Z.M., Li Y. // Plant Cell Rep. 2006. V. 25. № 2. P. 124–132.
10. Xiong A.S., Yao Q.H., Peng R.H., Zhang Z., Xu F., Liu J.G., Han P.L., Chen J.M. // Appl. Microbiol. Biotechnol. 2006. V. 72. № 5. P. 1039–1047.
11. Casini A., Storch M., Baldwin G.S., Ellis T. // Nat. Rev. Mol. Cell. Biol. 2015. V. 16. № 9. P. 568–576.
12. Kosuri S., Church G.M. // Nat. Methods. 2014. V. 11. № 5. P. 499–507.
13. Shevelev G.Y., Pyshnyi D. V. // Vavilov J. Genet. Breed. 2018. V. 22. № 5. P. 498–506.
14. Dietrich R., Wirsching F., Opitz T., Schwienhorst A. // Biotechnol. Techniques. 1998. V. 12. № 1. P. 49–54.
15. Gibson D.G. // Nucl. Acids Res. 2009. V. 37. № 20. P. 6984–6990. http://www.ncbi.nlm.nih.gov/pubmed/19745056.
16. Stemmer W.P.C., Crameri A., Ha K.D., Brennan T.M., Heyneker H.L. // Gene. 1995. V. 164. № 1. P. 49–53.
17. Xiong A.S., Yao Q.H., Peng R.H., Li X., Fan H.Q., Cheng Z.M., Li Y. // Nucl. Acids Res. 2004. V. 32. № 12. P. e98
18. Gao X., Yo P., Keith A., Ragan T.J., Harris T.K. // Nucl. Acids Res. 2003. V. 31. № 22. P. e143
19. Sandhu G.S., Aleff R.A., Kline B.C. // Biotechniques. 1992. V. 12. № 1. P. 14–16.
20. Xiong A.S., Yao Q.H., Peng R.H., Duan H., Li X., Fan H.Q., Cheng Z.M., Li Y. // Nat. Protoc. 2006. V. 1. № 2. P. 791–797.
21. Chakrabarti R., Schutt C.E. // Nucl. Acids Res. 2001. V. 29. № 11. P. 2377–2381.
22. Jensen M.A., Fukushima M., Davis R.W. // PLoS One. 2010. V. 5. № 6. P. e11024
23. Henke W., Herdel K., Jung K., Schnorr D., Loening S.A. // Nucl. Acids Res. 1997. V. 25. № 19. P. 3957.
24. Jurišić V., Obradović J., Tošić N., Pavlović S., Kulić M., Djordjević N. // J. Pharm. Biomed. Anal. 2016. V. 128. P. 275–279.
25. Karunanathie H., Kee P.S., Ng S.F., Kennedy M.A., Chua E.W. // Biochimie. 2022. V. 197. P. 130–143.
26. Wan C.Y., Wilkins T.A. // PCR Methods Appl. 1993. V. 3. № 3. P. 208–210.
27. https://sysbiomed.ru/upload/SynthBac.zip.
28. Garanina I.A., Fisunov G.Y., Govorun V.M. // Front. Microbiol. 2018. V. 9. № NOV. P. 2827.
29. Kikin O., D'Antonio L., Bagga P.S. // Nucl. Acids Res. 2006. V. 34. № suppl_2. P. W676–W682.
30. Gibson D.G., Young L., Chuang R.-Y., Venter J.C., Hutchison C.A., Smith H.O. // Nat. Methods. 2009. V. 6. № 5. P. 343–345.
31. Ye H., Huang M.C., Li M.H., Ying J.Y. // Nucl. Acids Res. 2009. V. 37. № 7. P. e51
32. Wu G., Wolf J.B., Ibrahim A.F., Vadasz S., Gunasinghe M., Freeland S.J. // J. Biotechnol. 2006. V. 124. № 3. P. 496–503.
33. Ahokas H., Erkkilä M.J. // PCR Methods Appl. 1993. V. 3. № 1. P. 65–68.
34. Blanchard M.M., Taillon-Miller P., Nowotny P., Nowotny V. // PCR Methods Appl. 1993. V. 2. № 3. P. 234–240.
35. Roperch J.P., Benzekri K., Mansour H., Incitti R. // BMC Biotechnol. 2015. V. 15. doi: 10.1186/s12896-015-0148-6.
36. Kikuchi A., Sawamura T., Kawase N., Kitajima Y., Yoshida T., Daimaru O., Nakakita T., Itoh S. // Biochem. Genet. 2010. V. 48. № 5–6. P. 428–432.
37. Deng H., Bloomfield V.A., Benevides J.M., Thomas G.J. // Nucl. Acids Res. 2000. V. 28. № 17. P. 3379.
38. Smith H.O., Hutchison C.A., Pfannkoch C., Venter J.C. // Proc. Natl. Acad. Sci. USA. 2003. V. 100. № 26. P. 15440–15445.
39. Sequeira A.F., Brás J.L.A., Guerreiro C.I.P.D., Vincentelli R., Fontes C.M.G.A. // BMC Biotechnol. 2016. V. 16. № 1. P. 86.
40. Carr P.A., Park J.S., Lee Y.J., Yu T., Zhang S., Jacobson J.M. // Nucl. Acids Res. 2004. V. 32. № 20. P. e162–e162.
41. Ma S., Saaem I., Tian J. // Trends Biotechnol. 2012. V. 30. № 3. P. 147–154.
42. Ma H., Kunes S., Schatz P.J., Botstein D. // Gene. 1987. V. 58. № 2–3. P. 201–216.
43. Gibson D.G., Benders G.A., Axelrod K.C., Zaveri J., Algire M.A., Moodie M., Montague M.G., Venter J.C., Smith H.O., Hutchison C.A. // Proc. Natl. Acad. Sci. USA. 2008. V. 105. № 51. P. 20404–20409.

Dimeric Bis-Benzimidazole-Pyrroles $DB_2Py(n)$ – AT-Site-Specific Ligands: Synthesis, Physicochemical Analysis, and Biological Activity

O. Y. Susova[1*], S. S. Karshieva[1], A. A. Kostyukov[2], N. I. Moiseeva[1], E. A. Zaytseva[1], K. V. Kalabina[1], E. Zusinaite[4], K. Gildemann[4], N. M. Smirnov[3], A. F. Arutyunyan[3], A. L. Zhuze[3]
[1]N.N. Blokhin National Medical Research Center of Oncology of the Ministry of Health, Moscow, 115522 Russian Federation
[2]Emanuel Institute of Biochemical Physics, Russian Academy of Sciences, Moscow, 119334 Russian Federation
[3]Engelhardt Institute of Molecular Biology, Russian Academy of Sciences, Moscow, 119991 Russian Federation
[4]Tartu University Institute of Technology, Tartu, 50411 Estonia
*E-mail: o.susova@ronc.ru

Received: November 16, 2023; in final form, January 29, 2024
DOI: 10.32607/actanaturae.27327

ABSTRACT **Its broad spectrum of biological activity makes benzimidazole a fundamental pharmacophore in pharmaceutics. The paper describes newly synthesized AT-specific fluorescent bis-benzimidazole molecules $DB_2Py(n)$ that contain a pyrrolcarboxamide fragment of the antibiotic drug netropsin. Physico-chemical methods using absorption, fluorescence, and circular dichroism spectra have shown the ability of bis-benzimidazole-pyrroles to form complexes with DNA. The new $DB_2Py(n)$ series have turned out to be more toxic to human tumor lines and less vulnerable to non-tumor cell lines. Bis-benzimidazole-pyrroles penetrated the cell nucleus, affected the cell-cycle synthesis (S) phase, and inhibited eukaryotic topoisomerase I in a cell-free model at low concentrations. A real-time tumor cell proliferation test confirmed the molecule's enhanced toxic properties upon dimerization. Preliminary cytotoxicity data for the bis-benzimidazole-pyrroles tested in a cell model with a MDR phenotype showed that monomeric compounds can overcome MDR, while dimerization weakens this ability to its intermediate values as compared to doxorubicin. In this respect, the newly synthesized cytotoxic structures seem promising for further, in-depth study of their properties and action mechanism in relation to human tumor cells, as well as for designing new AT-specific ligands.**

KEYWORDS **bis-benzimidazole-pyrrole, DNA narrow groove binding ligand, cytotoxicity, DNA-binding, topoisomerase I, cell cycle, multidrug resistance.**

ABBREVIATIONS **DMF – dimethylformamide; MDR – multidrug resistance; Topo-I – eukaryotic topoisomerase I; CLCD – cholesteric liquid crystal dispersion; IC_{50} – 50% inhibitory concentration.**

INTRODUCTION

Compounds capable of effectively binding to a narrow DNA groove by forming hydrogen bonds are of interest as agents that can help regulate biological activity. In this respect, the use of bis-benzimidazoles as drugs opens new opportunities for the therapy of socially significant diseases, including malignant neoplasms. The rapidly growing tumor resistance to existing treatment protocols makes it necessary to accelerate the search for new effective DNA-specific ligands, which now represent an important direction in the development of medicinal chemistry [1–4].

DNA-specific compounds based on DNA narrow-groove-binding ligands target the AT pairs of nucleotides in the DNA structure. It is possible to match a molecular structure to a preselected binding site on the DNA, as well as to eliminate any nonspecific interaction with the DNA through complementary interactions between a DNA-specific ligand and a biomacromolecule. In this regard, DNA narrow-

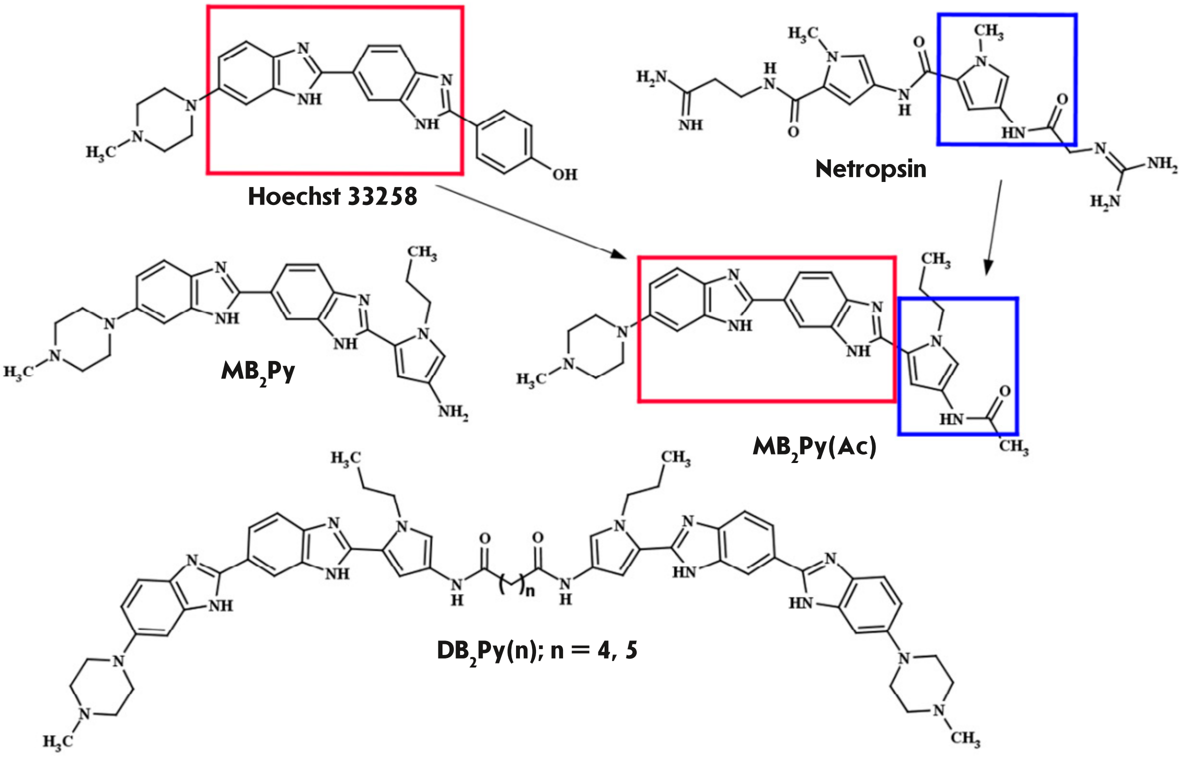

Fig. 1. Structural formulas of **Hoechst 33258**, netropsin, monomeric **MB$_2$Py**, **MB$_2$Py(Ac)**, and dimeric compounds **DB$_2$Py(n)**. In **MB$_2$Py(Ac)**, the bis-benzimidazole fragment is highlighted in red; and the pyrrolecarboxamide fragment, in blue

groove-binding ligands, which are compounds of low molecular weight interacting noncovalently and site-specific with DNA, seem to be quite promising. Such compounds are largely free of the adverse mutagenic side effects characteristic of the low-molecular-weight compounds that intercalate between DNA base pairs. They are able to modulate the expression of genes and DNA-binding proteins, thus exhibiting anti-tumor properties.

Earlier, we obtained **Hoechst 33258**-based fluorescent water-soluble AT-specific dimeric bis-benzimidazole DNA narrow-groove-binding ligands of the **DB(n)**, **DBP(n)**, **DBA(n)**, and **DBPA(n)** series, where n is equal to the number of methylene links in the linker. All the above-mentioned compounds contained two AT-recognizing fragments in their structure, consisting of two bis-benzimidazole units [5–8]. Upon interaction with DNA, each AT-recognizing fragment formed a bifurcation (three-center) hydrogen bond with an O2 thymine atom and/or an adenine atom of two neighboring AT pairs, while covering a region of approximately one and a half base pairs [9]. All the series penetrated cellular and nuclear membranes, stained DNA, and showed significant activity as inhibitors of DNA-dependent enzymes.

In the present study, we synthesized and investigated the biological activity of new DNA narrow-groove-binding ligands containing in their structure an AT-recognizing pyrrolcarboxamide fragment similar to that of netropsin [10], a natural antibiotic never used in practice due to its high cytotoxicity. The new ligands – **MB$_2$Py** and **MB$_2$Py(Ac)** (*Fig. 1*) – consist of three (two benzimidazole and one pyrrolcarboxamide) AT-recognizing units covalently linked to each other, and the dimeric derivatives **DB$_2$Py(n)** (*Fig. 1*) dimerized from **MB$_2$Py** by oligomethylene α,ω-dicarboxylic acids of various lengths (**n** here is the number of methylene links in the linker) to form symmetric head-to-head type compounds. The flexible linker in dimeric compounds allows the molecule to bind to two AT-rich sites located at different distances from each other. As we showed earlier, dimerization of the monomeric ligand of **DB(n)** series increased affinity to the newly structured DNA [11].

Increasing the number of AT-recognizing fragments in the monomeric subunit increases the ligand-

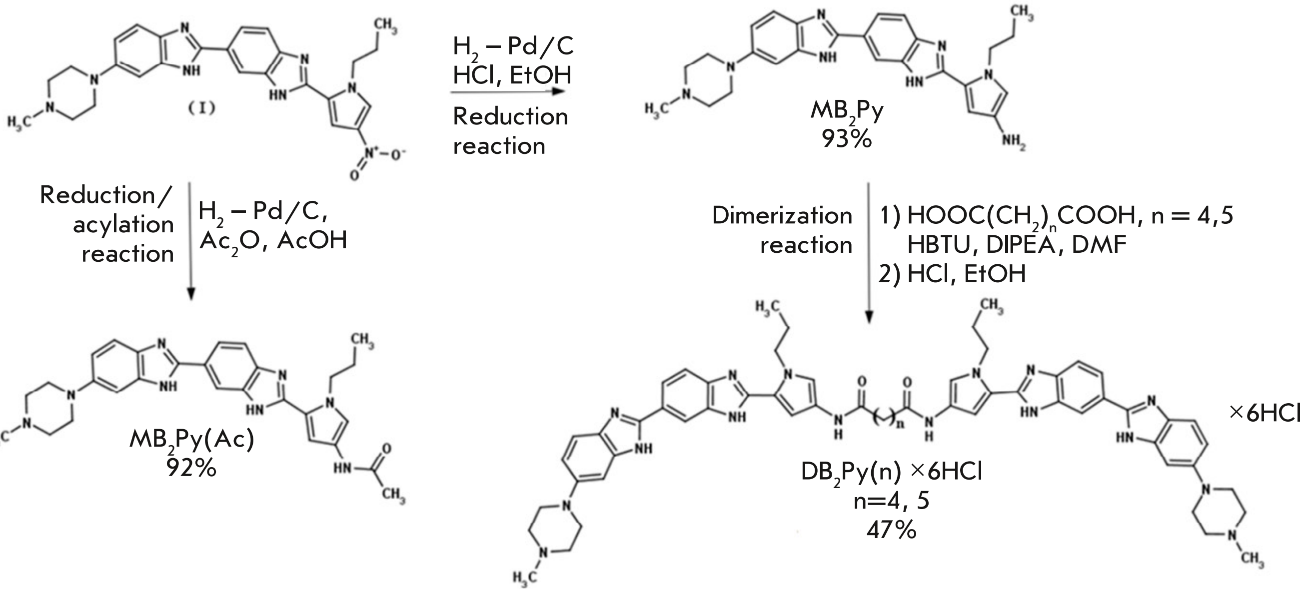

Fig. 2. Synthesis scheme of monomeric (**MB$_2$Py, MB$_2$Py(Ac)**) and dimeric (**DB$_2$Py(4, 5)**) compounds

DNA complexation constant and should decrease the inhibitory concentration against DNA-dependent enzymes. The paper describes the synthesis of two monomeric compounds, **MB$_2$Py** and **MB$_2$Py(Ac)**, and the dimeric compounds **DB$_2$Py(n)** and investigates their biological activity.

The dimeric bis-benzimidazole-pyrroles, **DB$_2$Py(4, 5),** were synthesized from 6-[6-(4-methylpiperazin-1-yl)-1H-1,3-benzodiazol-2-yl]-2-(4-nitro-1-propyl-1H-pyrrol-2-yl)-1H-1,3-benzodiazole **(I)** (*Fig. 2*) obtained in the Laboratory of DNA-Protein Interactions at the Institute of Molecular Biology of the Russian Academy of Sciences. Compound **(I)** was used to obtain the monomeric ligand **MB$_2$Py(Ac)** by reducing the parent compound in a hydrogen current in glacial acetic acid in the presence of acetic anhydride on 10% palladium with carbon as a catalyst. A monomeric unit of **MB$_2$Py** was dimerized into two dimeric compounds **DB$_2$Py(n)** with a series of aliphatic normal α,ω-dicarboxylic acids in the presence of HBTU as a condensing agent and DIPEA as a DMF base, differing in the number of methylene links in the linker: $n = 4, 5$ (*Fig. 2*).

EXPERIMENTAL

In this study, such chemical substances as adipic and pimelic acids, HBTU, DIPEA (Fluka, Switzerland), dioxane, DMF, ice-cold AcOH, Ac$_2$O, iPrOH, acetone (Reachim, Russia) were used. Solutions in organic solvents were dried over Na_2SO_4. The solvents were evaporated on a rotary evaporator in the vacuum of a water jet pump, usually at 30–50°C. The substances were dried in vacuo over P_2O_5 and NaOH. The melting temperatures were determined with a Boethius device (Germany). Hydrogenation was carried out over 10% Pd/C (Merck, Germany) at atmospheric pressure and room temperature until hydrogen absorption ceased. The purity of the obtained compounds was determined by TCX on Kieselgel 60 F$_{254}$ plates (Merck). Substances in chromatograms were detected in UV light by absorbance at 254 nm and/or fluorescence at 365 nm.

^{1}H-NMR spectra were recorded using an Avance III 300 MHz spectrometer (Bruker, Germany) equipped with a cryogenic TCI triple resonance probe (Bruker Biospin, Gmbh, Germany) in DMSO-d_6 at 30°C.

Mass spectra were taken using an AB SCIEX 4800 TOF analyzer (AB SCIEX, USA) in positive-ion detection mode (unless otherwise specifically stated); 2,5-dihydroxybenzoic acid matrix; N_2–laser of 337 nm.

Absorption spectra were recorded in a Cary100 spectrophotometer (Varian, USA).

Fluorescence spectra of the solutions were measured in a PTI spectrofluorimeter (Photo Technology Intern., Canada) using double-stranded DNA of calf thymus (Sigma).

CD spectra were recorded in a portable SKD-2 dichrometer (Institute of Spectroscopy, Russian Academy of Sciences, Troitsk) using DNA of salmon sperm (Technomedservice, Russia) and quartz cuvettes with an optical path length of 1 cm.

Human tumor cell lines were investigated using human non-small cell lung cancer cell lines A549, colon cancer HCT-116, hepatocarcinoma Huh7, pancreatic carcinoma PANC-1, breast cancer SKBR3, MCF7, ovarian cancer SKOV3, osteosarcoma U2OS, a primary culture of human glioblastoma Gbl13n, immortalized epithelial cell line HBL-100 and its doxorubicin-resistant subline HBL-100/DOX, and breast cell line MCF10A of non-tumor origin. As control drugs irinotecan, doxorubicin (Sigma), etoposide, and puromycin (InvivoGen) were applied.

For human tumor cell lines, the DMEM medium (Sigma) containing 10% fetal calf serum (HyClone, South America) and 2 mM *L*-glutamine (PanEco, Russia) was used. Non-tumorigenic MCF10A cells were cultured in a DMEM/F12 medium (Sigma) containing 5% horse serum (Biosera, South America), 100 mg/mL EGF, 1 mg/mL hydrocortisone, and 10 mg/mL insulin (PanEco). Both media contained 100 U/mL penicillin and streptomycin (PanEco), and all cells were cultured at 37°C, 5% CO_2.

The cytotoxic effect was evaluated using the standard microculture tetrazolium test (MTT) measuring the ability of live cell dehydrogenases to reduce uncoated forms of 3-(4,5-dimethylthiazol-2-yl)-2,5-diphenyl-tetrazolium bromide (PanEco) to the blue crystalline pharmasan soluble in dimethyl sulfoxide (DMSO). The coloration was recorded at a wavelength of 570 nm using a spectrophotometer (Multiskan FC, Thermo Fisher Scientific, USA). The optical density in the wells with the cells incubated without the drug was taken as 100%. The optical density values in the wells with each control concentration were averaged, and the percentage of surviving cells for a particular drug concentration was calculated.

Cell cycle measurements were performed using flow cytofluorimetry. To do so, HCT-116 cells were seeded at 500 × 10^3 cells per well in a 6-well plate and grown in the DMEM medium (Gibco, USA) containing 2 mM *L*-glutamine (PanEco) and a 1X antibiotic-antimycotic solution (Gibco) supplemented with 10% (v/v) fetal bovine serum (Gibco) at 37°C and 5% CO_2. In 24 h, the medium was changed to fresh and drugs added at a concentration of 1 μM with no drug added to the control wells. The cells were incubated for 24 and 48 h to be washed in dishes with the Versen (PanEco) and 0.25% trypsin/EDTA(Gibco) solutions. The cell concentration was counted, and equal amounts were selected for the analysis. The selected cells were centrifuged for 5 min at 1,200 rpm to remove the supernatant and washed in 1 ml of cold PBS. The cells were resuspended in 1 ml of cold 96% ethanol and incubated overnight at +4°C to be centrifuged (15 min, 1,900 rpm) and washed 1 time with a cold PBS solution. The precipitate was added, 1 ml of the 3.8 mM sodium citrate solution in PBS containing 500 μg/ml propidium iodide and 1 μl of RNase A (10 mg/ml), and incubated overnight at +4°C. Propidium iodide fluorescence was measured in the FL2 channel using a CytoFlex flow cytofluorimeter. The obtained data were analyzed using the ModFit LT 3.2 software (Verity Software).

Proliferation of the cells exposed to the tested compounds was determined using xCELLigence RTCA (ACEA Biosciences, USA). Every well of a 16-well plate was seeded with 5,000 human osteosarcoma U2OS cells. Each well of the plate had a microelectronic biosensor at the bottom (proprietary E-plates). The cells were incubated for 24 h in a Roche xCELLigence RTCA DP (Roche Diagnostics GmbH, Germany). When cell index 1 was reached, the medium was removed to be added either to the same medium (control) or media with different substance concentrations (0.16, 0.8, 4, 20, 100, 500 μM, respectively).

To determine **the ability of the compounds to penetrate the cell nucleus,** live Gbl13n glioblastoma cells were incubated in the culture medium with the compounds at a concentration of 2 μM for 2 days, washed with phosphate-salt buffer, fixed with formaldehyde, and photographed using a Zeiss Axioplan 2 fluorescence microscope (Carl Zeiss, Germany) in the ultraviolet wavelength range.

Inhibition of Topo-I catalytic activity was assessed in a relaxation reaction of supercoiled DNA (scDNA). The ability to modulate Topo-I activity *in vitro* was studied using a Topoisomerase I Drug Screening kit (TopoGen, Inc., cat. no. 1018-1, www.topogen.com). A single unit of purified Topo-I from calf thymus (Fermentas, USA) and the tested compounds at concentrations of 2.5 and 5 μM; 0.65 and 1.25 μM were incubated with 0. 12 μg of pHOT1 supercoiled plasmid DNA (TopoGen) in ×1 reaction buffer (10 mM Tris-HCl pH 7.9, 1 mM EDTA, 0.15 M NaCl, 0.1% BSA, 0.1 mM spermidine, 5% glycerol). The reaction was run for 30 min at 37°C, stopped by adding SDS to a final concentration of 1%, and treated with proteinase K of final concentration of 50 μg/mL for 30–60 min at 37°C. The reaction products were separated electrophoretically in a 1% agarose gel with TAE buffer (2 M Tris base, 0.05 M EDTA, 1.56 M acetic acid) at a maximum electric field strength of 3–4 V/cm and then stained with an aqueous ethidium bromide solution (0.5 μg/mL). DNA visualization in gel was performed by fluorescence in transmitted ultraviolet light at wavelengths ranging from 240 to 360 nm. In the absence of the inhibitor, Topo-I relaxed scDNA to form a series of topoisomers. Topo-I inhibition effect was detected by the ability of the tested compounds to delay the relaxation reaction of scDNA; i.e., by its preservation. The initial concentration of bis-benzimidazole-pyrroles in DMSO was 5×10^{-3} M.

Cell survival data were processed in the GraphPad Prism 8 software, and the viability curves were compared using Fisher's criterion (F-test). All experiments were repeated 3 times, and the effect on cell proliferation in real time was tested twice. For the purpose of data presentation, the most successful experiment, whose results did not contradict those of the same experiments, was selected.

RESULTS

Synthesis of monomeric bis-benzimidazole-pyrroles MB_2Py and $MB_2Py(Ac)$, and dimeric compounds $DB_2Py(4, 5)$

MB_2Py synthesis. 0.1 g of 10% Pd/C suspended in 20 mL of absolute ethanol was saturated with hydrogen until its absorption ceased. Then, 0.3 mL of concentrated hydrochloric acid and 0.20 g (0.41 mmol) of 6-[6-(4-methylpiperazin-1-yl)-1H-1,3-benzodiazol-2-yl]-2-(4-nitro-1-propyl-1H-pyrrole-2-yl)-1H-1,3-benzodiazole **(I)** was added. The reaction mixture was stirred at room temperature until hydrogen absorption ceased. The resulting solution was filtered off the catalyst and precipitate, the solid precipitate of the target substance was washed off the filter with 2 × 10 mL water, and the water was evaporated under reduced pressure. The **MB_2Py** yield was a green amorphous powder weighing 0.173 g (93%). TLC analysis in a hexane/ethyl acetate solvent system (3 : 1) showed that the obtained substance was homogeneous. Its mass spectrum was 455.26 $[M+H]^+$ and 454.57 ($C_{26}H_{30}N_8$) for the calculated one.

$MB_2Py(Ac)$ synthesis. 0.15 g of 10% Pd/C suspended in 30 mL of glacial acetic acid was saturated with hydrogen until its absorption ceased. Then, 2 mL of acetic anhydride and 0.35 g (0.72 mmol) of the substance **(XII)** were added. The reaction mixture was stirred in a room-temperature hydrogen current for 5 h. The resulting solution was filtered off the catalyst. The resulting solution was evaporated under reduced pressure to be redissolved three times with 30 mL of isopropyl alcohol. The **$MB_2Py(Ac)$** yield was 0.37 g (92.4%) of yellow crystals. TLC analysis in a *i*-PrOH–NH_4OH (5:1) solvent system showed that the obtained substance was homogeneous; and its melting temperature – 219°C. Its mass spectrum was m/z: 496.15 $[M]^+$, 454.13 $[M–NHAc]^+$, and 496.26 ($C_{28}H_{32}N_8O$) for the calculated one.

General synthesis of $DB_2Py(n)$. A α,ω-alkyldicarboxylic acid (0.1 mmol) solution in 2 mL of abs DMF was added to HBTU (0.25 mM), DIPEA (0.50 mM) and stirred at room temperature for 30 min. The resulting solution was added to 0.10 g (0.2 mmol) of MB_2Py, stirred for another hour, and the reaction mixture was left overnight. The solvent was evaporated under reduced pressure, the resulting oil was mashed with abs *i*-PrOH to add 0.5 mL of 35% HCl in dioxane, and the precipitate was filtered off, washed 3 times with 80% aqueous acetone and 2 times with abs *i*-PrOH. The solid residue as a green powder was dried in vacuo over $NaOH/P_2O_5$. TLC analysis in a MeOH-TFA-H_2O (5:1:2) solvent system showed that the obtained substance was homogeneous.

$DB_2Py(4)$·6HCl. Yield 55 mg (48%), melt. temp. > 350°C. Mass spectrum: 1019.57 $[M+H]^+$, calculated Ms: 1018.55 ($C_{58}H_{66}N_{16}O_2$). ^{1}H-NMR (300 MHz, DMSO-d_6): δ 0.85 (6H, t, J = 7.4, 2(–C$\mathbf{H}_3$)), 1.65 (4H, m, (–C$\mathbf{H}_2$–C$\mathbf{H}_2$–)), 1.75 (4H, q, J = 7.2, 2(–CH_2C$\mathbf{H}_2$$CH_3$)), 2.31 (4H, m, 2(–COC$\mathbf{H}_2$–)), 2.77 (4H, s, pip), 3.23 (4H, s, pip), 3.35 (6H, s, 2(N–C$\mathbf{H}_3$)), 4.54 (4H, t, J = 7.0, 2(N–C$\mathbf{H}_2$–)), 7.05–6.84 (4H, m, ArH), 7.10 (2H, s, ArH), 7.36–7.24 (2H, brs, ArH), 7.48 (2H, d, J = 8.6, ArH), 7.58 (2H, m, ArH), 7.97 (2H, m, ArH), 8.26 (2H, d, J = 36.2, ArH), 9.93 (2H, s, 2(–N**H**CO–)).

$DB_2Py(5)$·6HCl. Yeild 61 mg (47%), melt. temp. > 350°C. Mass spectrum: m/z: 1033.42 $[M+H]^+$, calculated Ms: 1032.57 ($C_{59}H_{68}N_{16}O_2$). ^{1}H-NMR (300 MHz, DMSO-d_6): δ 0.87 (6H, t, J = 7.4, 2(–C$\mathbf{H}_3$)), 1.34 (2H, m, –C$\mathbf{H}_2$–), 1.63 (4H, m, –C$\mathbf{H}_2$–CH_2–C$\mathbf{H}_2$–), 1.77 (4H, q, J = 7.2, 2(–CH_2C$\mathbf{H}_2$$CH_3$)), 2.30 (4H, m, 2(–COC$\mathbf{H}_2$–)), 2.87 (8H, brs, pip), 3.35 (6H, s, (–NC$\mathbf{H}_3$)), 4.55 (4H, t, J = 7.2, N–C$\mathbf{H}_2$–), 7.05 (2H, brs, ArH), 7.24 (2H, m, ArH), 7.42–7.28 (4H, m, ArH), 7.75 (4H, dd, J = 20.0, 8.6, ArH), 8.04 (2H, d, J = 8.7, ArH), 8.45 (2H, brs, ArH), 9.93 (2H, s, 2(–N**H**CO–)).

PHYSICO-CHEMICAL ACTIVITY

$DB_2Py(n)$ absorption and fluorescence spectra

Measuring the intensity and absorption maxima of **$DB_2Py(4)$** and **$DB_2Py(5)$** in the absence and presence

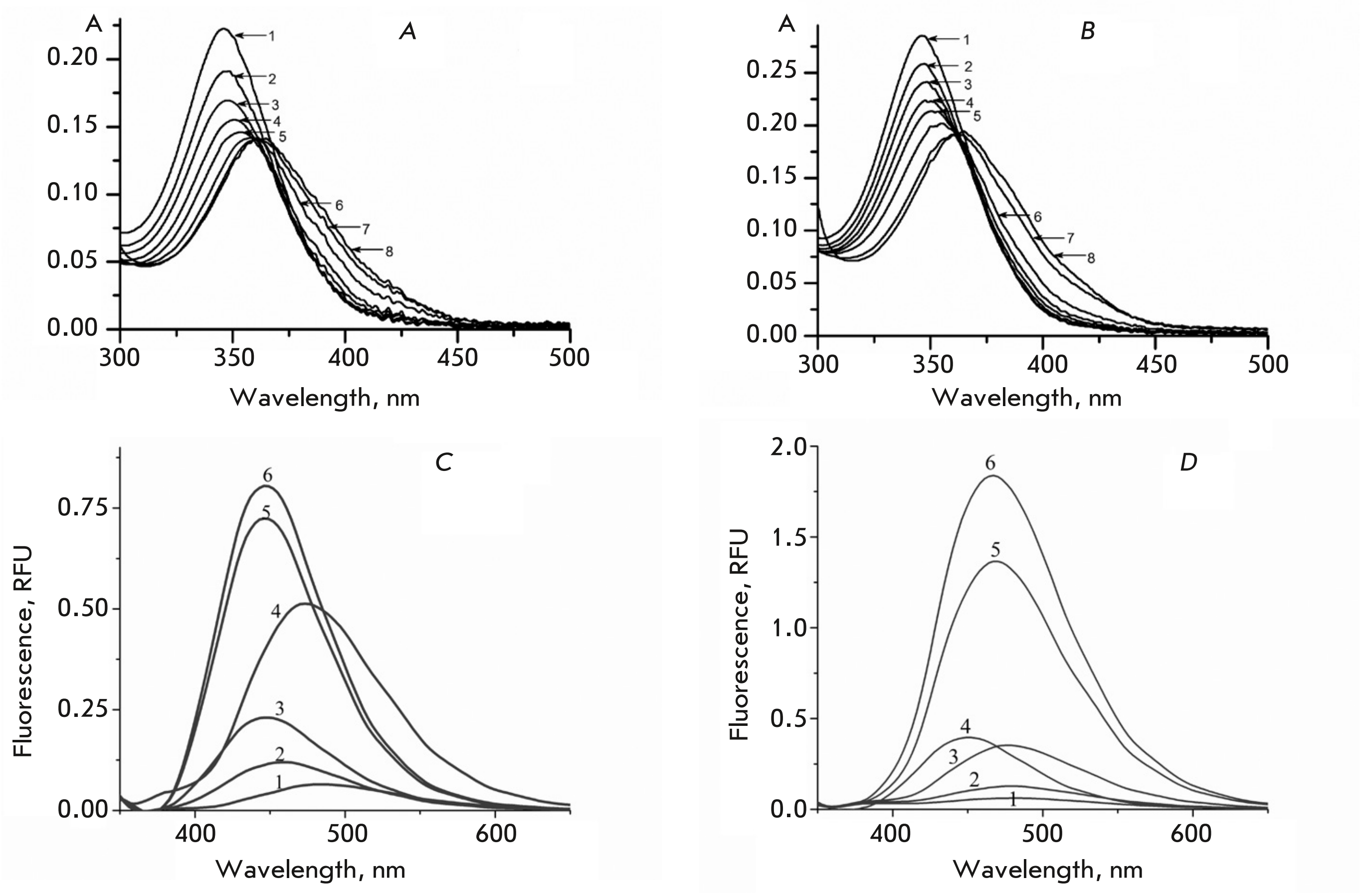

Fig. 3. Absorption and fluorescence spectra of free **DB$_2$Py(n)** and its complex with DNA.
(*A*) – absorption spectra of **DB$_2$Py(4)** in absence (*1*) and presence of DNA (*2–8*); [**DB$_2$Py(4)**] 4.06 × 10^{-6} M; 0.001 M sodium cacodylate. [DNA] *1* – 0; *2* – 0.25; *3* – 0.49; *4* – 0.98; *5* – 1.48; *6* – 2.45; *7* – 14.67; *8* – 121.9 × 10^{-6} M b.p. respectively; optical path length, 10 mm.
(*B*) – absorption spectra of **DB$_2$Py(5)** in absence (*1*) and presence of DNA (*2–8*); [**DB$_2$Py(5)**] 4.29 × 10^{-6} M; 0.001 M sodium cacodylate. [DNA] *1* – 0; *2* – 0.25; *3* – 0.49; *4* – 0.98; *5* – 1.48; *6* – 2.45; *7* – 14.67; *8* – 121.9 × 10^{-6} M b.p. respectively; optical path length, 10 mm.
(*C*) – fluorescence spectra of **DB$_2$Py(4)** in absence (*1*) and presence of DNA (*2*–6). [**DB$_2$Py(4)**] 4.6 × 10^{-6} M; [DNA] *1* – 0; *2* – 3; *3* – 6; 4 – 18; *5* – 30; *6* – 54 × 10^{-6} M b.p. respectively. Buffer: 10 mM PBS (pH 7.4). Excitation wavelength, 320 nm; slot width, 5 nm; cell size 10 × 10 mm; 22°C.
(*D*) – fluorescence spectra of **DB$_2$Py(5)** in absence (*1*) and presence of DNA (*2*–6). [**DB$_2$Py(5)**] 2.3 × 10^{-6} M; [DNA] *1* – 0; *2* – 3; *3* – 6; *4* – 18; *5* – 54; *6* – 78 × 10^{-6} M b.p. respectively. Buffer: 10 mM PBS (pH 7.4). Excitation wavelength, 320 nm; slot width, 5 nm; cell size 10 × 10 mm; 22°C

of DNA at different concentrations and comparison of the obtained spectra enabled us to indirectly confirm the ability of the new dimeric narrow-bridged ligands to form complexes with DNA (*Fig. 3A,B*). As the DNA concentration increased, a drop in the absorption intensity was observed, indicating that the new bis-benzimidazole-pyrroles had formed a complex with DNA. Further increase in the DNA concentration led to a change in the absorption maximum position characterized by a shift to the long-wavelength region of the spectrum (bathochromic shift), as well as an increase in the amplitude of the absorption band. All these processes were indication that several types of complexes had formed depending on the ligand concentration.

In the presence of DNA, the fluorescence spectra of **DB$_2$Py(4)** and **DB$_2$Py(5)** showed increasing fluorescence intensity that grew together with the DNA

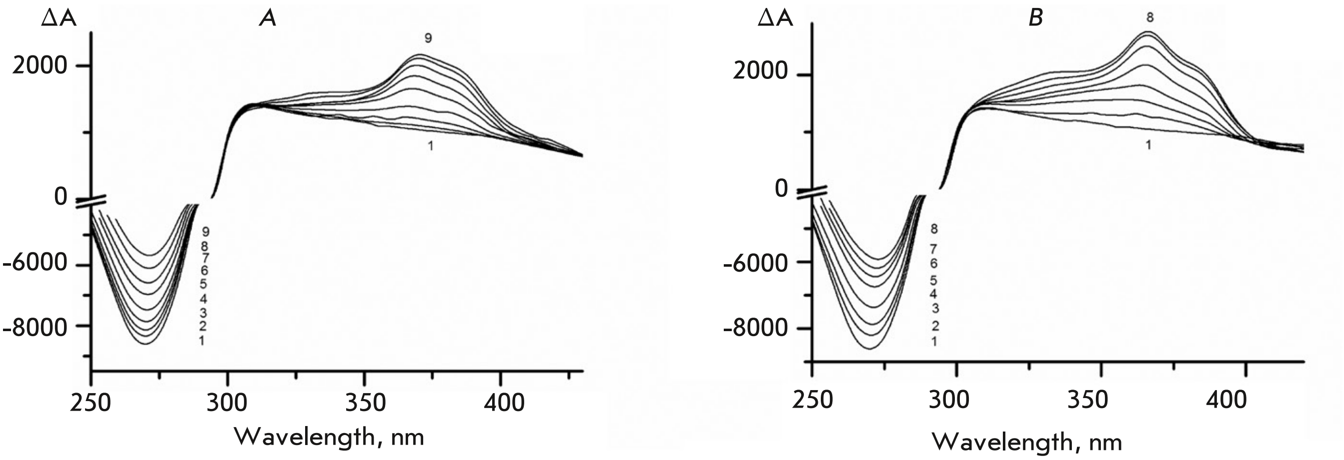

Fig. 4. (*A*) – CD spectra in absence (*1*) and presence of (*2–9*) of **DB$_2$Py(4)**; 0.3 M NaCl + 0.002 M Naphosphate buffer, pH 6.85; 170 mg/ml PEG-4000; [DNA] 4.545 × 10^{-5} M b.p.; [**DB$_2$Py(4)**] *1* – 0; *2* – 0.41; *3* – 0.82; *4* – 1.63; *5* – 3.25; *6* – 4.87; *7* – 6.48; *8* – 8.08; *9* – 10.07 × 10^{-6} M respectively. Optical path length, 10 mm.
(*B*) – CD spectra in absence (*1*) and presence of (*2–8*) **DB$_2$Py(5)**; 0.3 M NaCl + 0.002 M Naphosphate buffer, pH 6.85, 170 mg/ml PEG-4000; [DNA] 4.545 × 10^{-5} M b.p.; [**DB$_2$Py(5)**] *1* – 0; *2* – 0.43; *3* – 0.86; *4* – 1.72; *5* – 3.44; *6* – 5.15; *7* – 6.85; *8* – 8.54 × 10^{-6} M respectively. Optical path length, 10 mm

concentration (*Fig. 3C,D*). This was another sign that the compounds formed complexes with DNA, causing fluorescence ignition through stabilization of the conjugated ligand structure in the narrow DNA groove.

CD spectra of DB$_2$Py(4) and DB$_2$Py(5)/DNA CLCD complexes

The spectra allowed us to confirm that the obtained compounds formed complexes with DNA and detect their localization in one of the DNA grooves.

A similar pattern was observed for compounds **DB$_2$Py(4)** and **DB$_2$Py(5)** (*Fig. 4*): a positive, intense band was detected in the ligand absorption region (300–400 nm), indicating the complexes localized in one of the DNA grooves [12, 13]. Since the X-ray diffraction analysis of the **Hoechst 33258** parent compound localized it in the narrow groove of DNA [9], we had confirmation that our compounds are DNA narrow-groove-binding ligands.

BIOLOGICAL ACTIVITY

Cytotoxicity against human tumor cells

The cytotoxic activity of the compounds was evaluated by the MTT method on six cell lines and one primary human tumor culture to determine the semi-inhibitory concentration (IC_{50}) for non-small cell lung cancer A549, colon cancer HCT-116, hepatocarcinoma Huh7, pancreatic carcinoma PANC-1, breast cancer SKBR3, ovarian cancer SKOV3, and a primary culture of human glioblastoma Gbl13n we had obtained earlier [14, 15]. The data presented in *Fig. 5* demonstrate that the Huh7, PANC-1, and SKBR3 cell lines were more sensitive to the new compounds than to the antitumor agent irinotecan. The cytotoxicity of the dimeric molecules **DB$_2$Py(4)** and **DB$_2$Py(5)** against cell line A549 was significantly higher (5- to 7-fold) than that of monomeric **MB$_2$Py(Ac)** and irinotecan (2.8- to 3.8-fold). However, no significant differences in the cytotoxicity of monomeric and dimeric bis-benzimidazole-pyrroles against the Huh7, PANC-2, SKBR3, and SKOV3 lines were detected.

Table 1. Cytotoxicity of monomeric and dimeric bis-benzimidazole-pyrroles versus irinotecan in a primary culture of human glioblastoma Gbl13n cells

Compound	IC_{50}, μM
MB$_2$Py(Ac)	>100
DB$_2$Py(4)	12.67 ± 2.33
DB$_2$Py(5)	8.78 ± 6.64
Irinotecan	10.02 ± 0.7

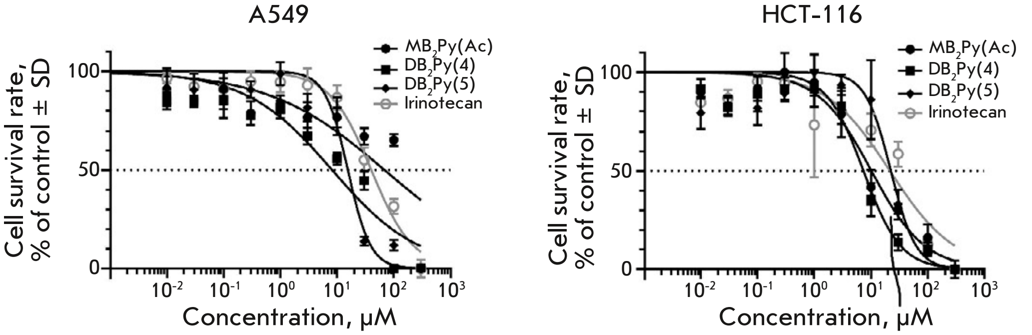

Fig. 5. Cytotoxicity values (IC_{50}) in micromoles (µM) of the monomeric and dimeric bis-benzimidazole-pyrroles compared to irinotecan in various human tumor cell lines.
SD – standard deviation,
SE – standard error,
R^2 – determination coefficient

	A549				HCT-116			
Compound	IC_{50}, µM	SD	SE	R^2	IC_{50}, µM	SD	SE	R^2
MB$_2$Py(Ac)	68.35	1.3E+11	6.5E+10	0.6736	10.13	3.546	1.773	0.9263
BD$_2$Py(4)	8.163	62.48	31.24	0.8911	7.343	1.4048	0.7024	0.9366
DB$_2$Py(5)	15.45	3.202	1.601	0.923	22.32	6.14	3.07	0.8363
Irinotecan	39.95	39.64	19.82	0.9488	21.44	102.08	51.04	0.8267

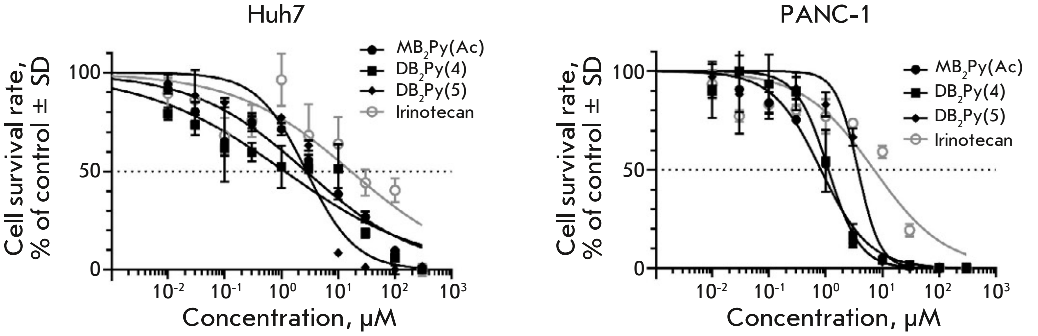

	Huh7				PANC-1			
Compound	IC_{50}, µM	SD	SE	R^2	IC_{50}, µM	SD	SE	R^2
MB$_2$Py(Ac)	2.697	0.10548	0.05274	0.9061	0.8199	0.15072	0.07536	0.9802
BD$_2$Py(4)	1.133	0.09772	0.04886	0.8728	1.105	0.2964	0.1482	0.9421
DB$_2$Py(5)	2.745	0.11036	0.05518	0.9329	3.704	0.8638	0.4319	0.9407
Irinotecan	16.65	0.11536	0.05768	0.7239	7.064	4.46	2.23	0.8915

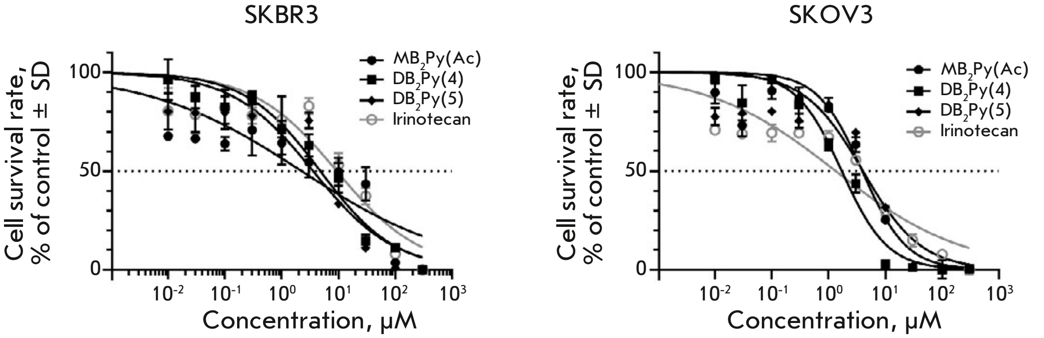

	SKBR3				SKOV3			
Compound	IC_{50}, µM	SD	SE	R^2	IC_{50}, µM	SD	SE	R^2
MB$_2$Py(Ac)	2.22	9.002	4.50	0.8045	3.887	3.11	1.555	0.9313
DB$_2$Py(4)	4.754	6	3	0.947	1.694	1.0884	0.5442	0.9706
DB$_2$Py(5)	3.549	2.54	1.27	0.8604	3.991	2,836	1.418	0.8711
Irinotecan	9.259	12.298	6.149	0.8491	1.318	5.15	2.575	0.8844

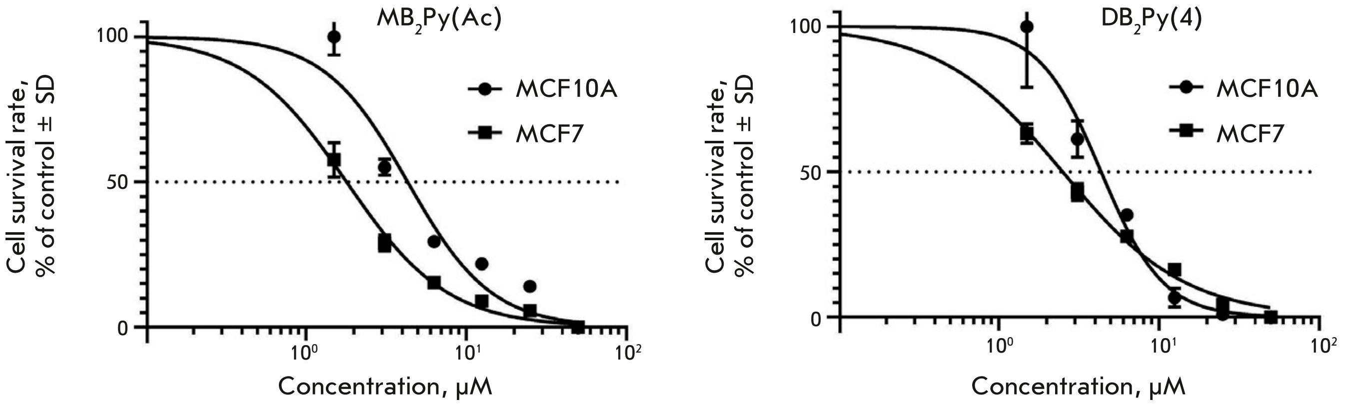

Compound	MCF10A				MCF7				F-test
	IC_{50}, μM	SD	SE	R^2	IC_{50}, μM	SD	SE	R^2	
$MB_2Py(Ac)$	4.316	0.750099	0.5304	0.9225	1.793	0.228678	0.1617	0.9856	*$p<0.0001$
$DB_2Py(4)$	4.355	0.932363	0.5383	0.9432	2.506	0.77388	0.4468	0.9702	*$p<0.0001$

*Statistically significant differences.

Fig. 6. Cytotoxicity of the new bis-benzimidazole-pyrroles in MCF10A (human breast epithelial cells, normal cell line) and on MCF-7 (breast cancer). SD – standard deviation, SE – standard error, R^2 – coefficient of determination, F-test – statistical criterion

Some believe that new drugs should be tested not only on linear, but also on primary cell cultures. In Gbl13n, a primary human glioblastoma cell culture, the cytotoxic activity of the **$DB_2Py(4)$**, **$DB_2Py(5)$** dimers was approximately 10-fold higher than that of the **$MB_2Py(Ac)$** monomer and comparable to that of irinotecan (*Table 1*).

Tumor-cell selectivity

The possible selectivity of the new compounds against tumor cells was determined by the level of their cytotoxicity in tumor and the transformed cell lines.

Breast cancer (MCF7) and conditionally normal mammary epithelial (MCF10A) cell lines were used as models. The tested cell lines were sensitive to the toxic effects of new bis-benzimidazole-pyrroles, with MCF7 being the most susceptible (*Fig. 6*). Therefore, some, approximately twofold, selectivity in the cytotoxic action was observed. At the same time, the monomer **$MB_2Py(Ac)$** and dimer **$DB_2Py(4)$** exhibited similar IC_{50} values for the tested cell lines; so, it can be considered that the doubling of the molecule did not affect cytotoxicity against the investigated pair of cell lines.

Proliferation in an osteosarcoma cell line

The effects the **$MB_2Py(Ac)$** monomer and **$DB_2Py(5)$** dimer had on the proliferation of the cultured U2OS osteosarcoma cells were compared in real time using an RTCA. After the compounds were introduced at concentrations of 0.16–500 μM, cell growth was recorded for 74 h. Puromycin causing complete cell death at a concentration of 10 mg/mL (21 mM) was used as a control (*Fig. 7A*). Lower doses of **$MB_2Py(Ac)$** (0.16, 0.8, and 4 μM) were found to have no effect on U2OS proliferation (*Fig. 7B*). At a concentration of 20 μM, a slowdown in proliferation was observed and 100-500 μM completely stopped cell division. It was demonstrated that **$DB_2Py(5)$** inhibited osteosarcoma cells growth in a concentration- and time-dependent manner (*Fig. 7B*); i.e., the dimer was obviously more toxic than the monomer.

MDR overcome

An important property of a potential drug is its ability to overcome the MDR mediated by the ABC transporter of P-glycoprotein (P-gp). In this respect, the new compounds were tested by MTT in an immortalized, epithelial cell line HBL-100 [16, 17] and in

Table 2. Cytotoxic activities of the novel bis-benzimidazole-pyrroles in the sensitive line HBL-100 and its resistant subline HBL-100/DOX with a MDR phenotype

Compound	HBL-100	HBL-100/DOX	Resilience index*
	IC_{50} ± SD, μM		
Doxorubicin	0.6 ± 0.3	34 ± 6	57
MB_2Py	58 ± 18	125 ± 21	2.1
$MB_2Py(Ac)$	18 ± 11	29 ± 11	1.5
$DB_2Py(4)$	4 ± 4.5	37 ± 11	8.9

*Resilience index is the ratio of IC_{50} in the stable subline HBL-100 and IC_{50} in the sensitive line HBL-100/DOX.

a HBL-100/DOX subline obtained from HBL-100 by prolonged incubation with doxorubicin. It was shown that 95% of HBL-100/DOX cells overexpress the P-gp protein responsible for cell resistance to drugs, including cross-resistance to paclitaxel and vinblastine; in other words, the HBL-100/DOX subline had an MDR phenotype; i.e., it was resistant not only to doxorubicin, but also to other P-gp substrates [18].

The monomers demonstrated a similar cytotoxic effect in the HBL-100 line as in its stable subline; so, the differences in the IC_{50} values did not extend above 2-fold.

The data presented in *Table 2* show that the investigated bis-benzimidazole-pyrroles did not belong to the P-gp substrates. The HBL-100/DOX resistance to **$DB_2Py(4)$** was 9-fold higher if compared to that to HBL-100, whereas the resistance of P-gp-overexpressing cells to such classical P-gp substrates as doxorubicin and paclitaxel increased 50–100 times and more. In this respect, a conclusion can be drawn that **$DB_2Py(4)$** is a weak P-gp substrate; i.e., only the monomeric **MB_2Py** and **$MB_2Py(Ac)$** are able to completely overcome the MDR associated with P-gp overexpression.

Cell-nucleus penetration

How of the new compounds to penetrate within 2 days into the cell nucleus where they, binding to heterochromatin, glow in bright blue dots, was confirmed by fluorescence microscopy (*Fig. 8*).

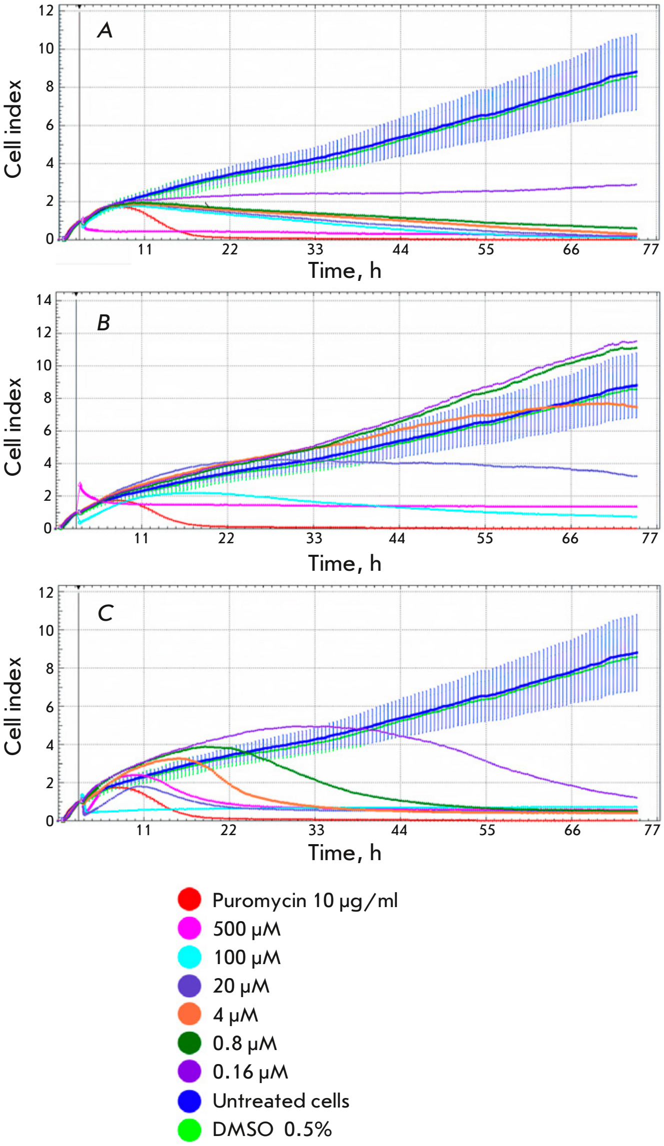

Fig. 7. The effect of the bis-benzimidazoles **$MB_2Py(Ac)$** and **$DB_2Py(5)$** on the proliferation of osteosarcoma cells in real time. Growth curves were measured as the cell index over time. (*A*) – controls: puromycin 10 μg/ml (red line); growth of unexposed U2OS cell line (blue line); 0.5% DMSO (greenline). (*B*) – **MB_2Py** exposure; (*C*) – **$DB_2Py(5)$** exposure

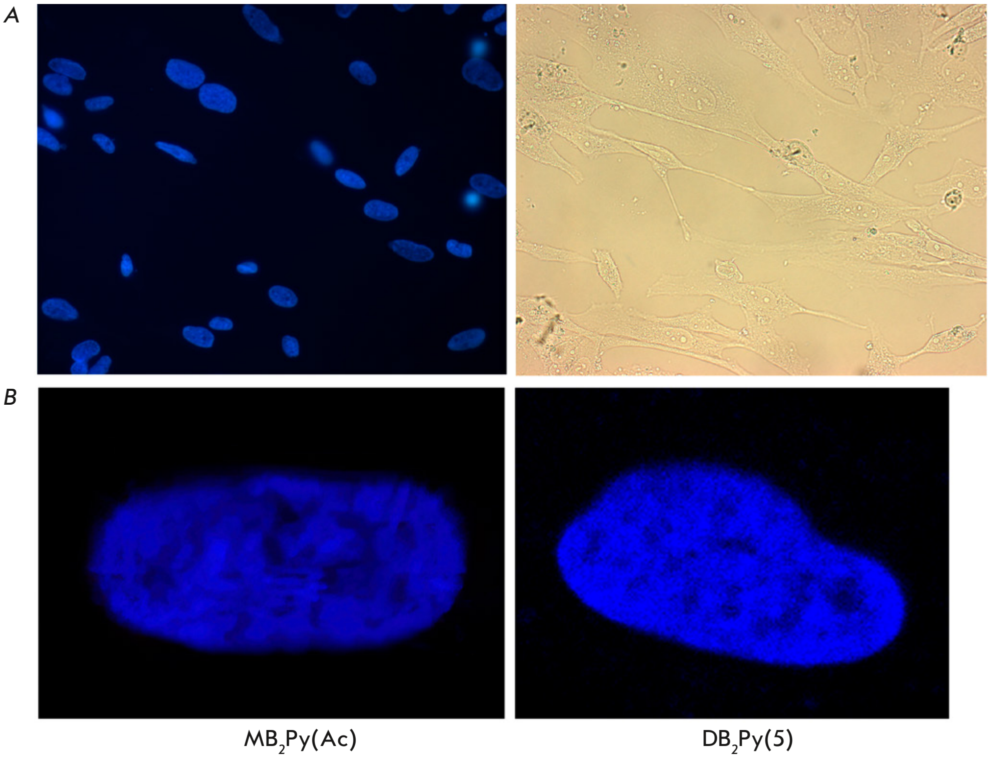

Fig. 8. Fluorescent staining of Gbl13n glioblastoma cells incubated with monomeric and dimeric bis-benzimidazole-pyrroles at a concentration of 2 μM for 48 h.
(*A*) – population of cells stained with the bis-benzimidazole-pyrrole **$DB_2Py(5)$**. On the left is a DAPI filter, on the right is a phase-contrast image. **$MB_2Py(Ac)$** staining looks similar after 2 days;
(*B*) – a picture of stained nuclei obtained using a confocal microscope

Therefore, the synthesized compounds are new promising fluorescent dyes capable of penetrating cellular and nuclear membranes and effectively staining cell nuclei.

Cell-cycle analysis

The way the new substances affect the cell cycle was investigated using two control drugs: etoposide and irinotecan. Etoposide stopped the cell cycle in mitosis as witnessed by the accumulation of cells in the G2/M phase and consistent with [19]. Forty-eight hours after etoposide treatment, the cell population in the G2/M phase had increased from 47 to 70%. Irinotecan arrested the cell cycle in the S-phase, leading to a reduced distribution of cell populations in other phases [20]. The cells exposed to irinotecan accumulated in the S-phase after 24 h and consequently in the G0/G1 phase after 48 h. Apparently, the last accumulation was due to the cells that had time to divide and transit from mitosis to the G0/G1 phase. In 48 h, a slight increase in the proportion of cells in early apoptosis was observed (*Fig. 9*).

Quantification of the cells present in different phases of the cell cycle showed that the effect new bis-benzimidazole-pyrroles had on the cell cycle was similar to that of irinotecan. After 24 h, the cell population had increased in the S-phase up to 62–67% compared to the control.

In 48 h, the cell populations redistributed towards an increase in the G0/G1 phase, proving that the new compounds affected the synthesis phase (S).

On the other hand, **$DB_2Py(4)$** barely induced apoptosis. While the other substances induced early apoptosis, the values exceeded the control by only 2–3 times.

Topo-I as a possible target for novel Hoechst 33258 derivatives

Some tumor types, such as breast, ovarian, and rectal cancers, are characterized by increased activity of Topo-I, an enzyme that plays a key role in cell function by regulating the DNA structure by its transcription, replication, recombination, and repair. Topo-I can relax (unwind) scDNA molecules by forming single-stranded breaks and then ligating them to relax supercoils. That capability currently makes Topo-I a recognized target for tumor targeting therapy [21–23].

Fig. 9. Effect of bis-benzimidazole-pyrroles on the cell cycle in an HCT-116 cell line.
(*A*) – after a 24 h of incubation;
(*B*) – after a 48 h of incubation

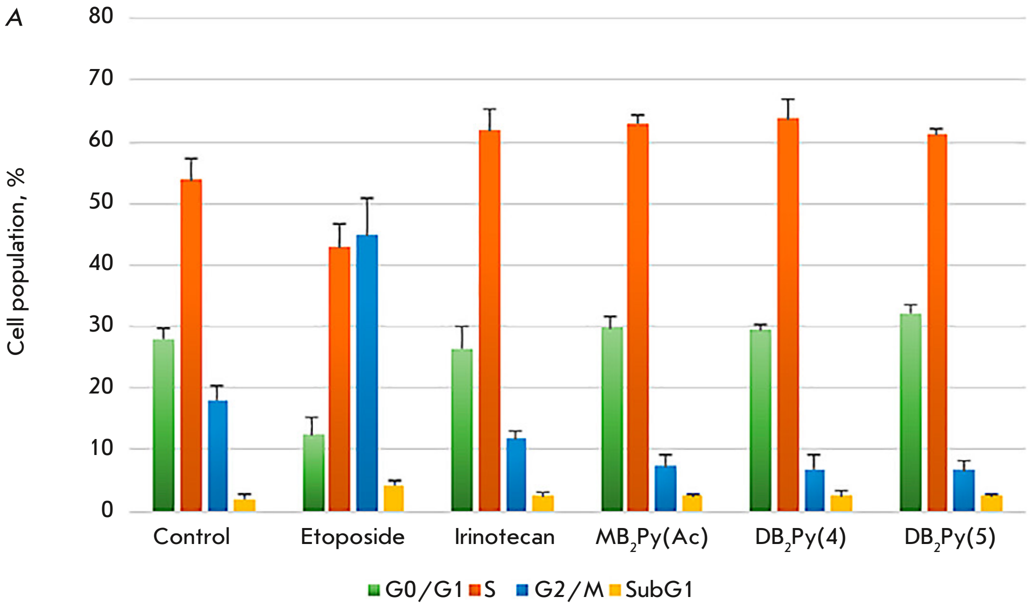

24 h	Control	Etoposide	Irinotecan	$MB_2Py(Ac)$	$DB_2Py(4)$	$DB_2Py(5)$
G0/G1	28.0 ± 1.6	12.4 ± 2.7	26.4 ± 3.7	29.8 ± 1.8	29.5 ± 0.8	32.2 ± 1.2
S	53.9 ± 3.4	42.9± 3.8	61.8 ± 3.5	62.9 ± 1.4	63.7 ± 3.2	61.2 ± 0.9
G2/M	18.1 ± 2.3	44.7 ± 6.2	11.8 ± 1.3	7.3 ± 1.7	6.8 ± 2.5	6.6 ± 1.6
SubG1	2.0 ± 0.8	4.3 ± 0.8	2.4 ± 0.8	2.5 ± 0.2	2.6 ± 0.8	2.6 ± 0.3

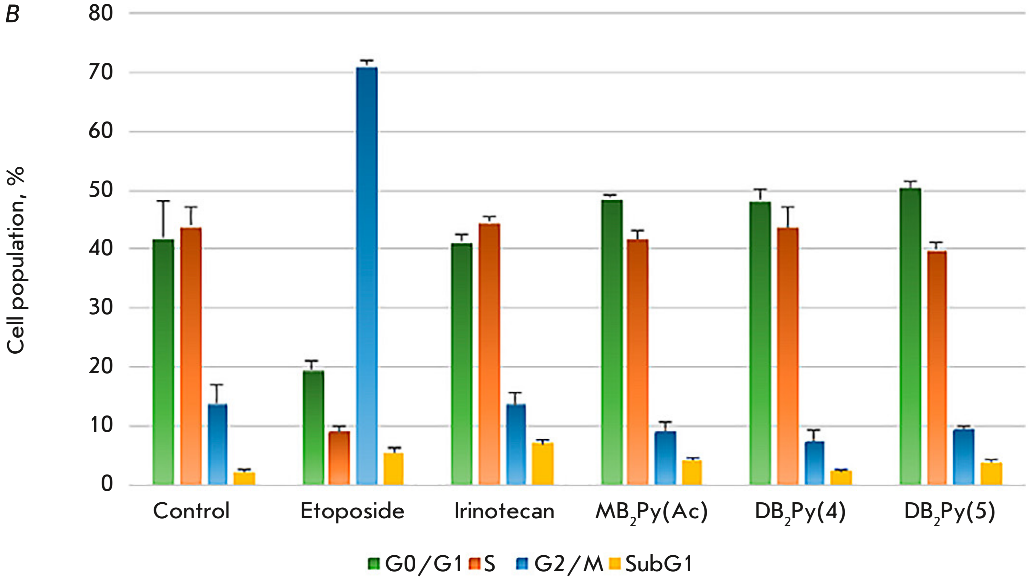

48 h	Control	Etoposide	Irinotecan	$MB_2Py(Ac)$	$DB_2Py(4)$	$DB_2Py(5)$
G0/G1	42.1 ± 6.2	19.7 ± 1.2	41.5 ± 0.9	48.8 ± 0.4	48.5 ± 1.7	50.6 ± 0.9
S	44.0 ± 3.2	9 ± 1	44.8 ± 0.8	41.9 ± 1.3	43.9 ± 3.1	40.0 ± 1.1
G2/M	13.9 ±3.2	71.3 ± 0.7	13.8 ± 1.7	9.3 ± 1.4	7.6 ± 1.6	9.4 ± 0.6
SubG1	2.1 ± 0.4	5.4 ± 0.9	6.9 ± 0.6	4.1 ± 0.4	2.2 ± 0.5	3.8 ± 0.5

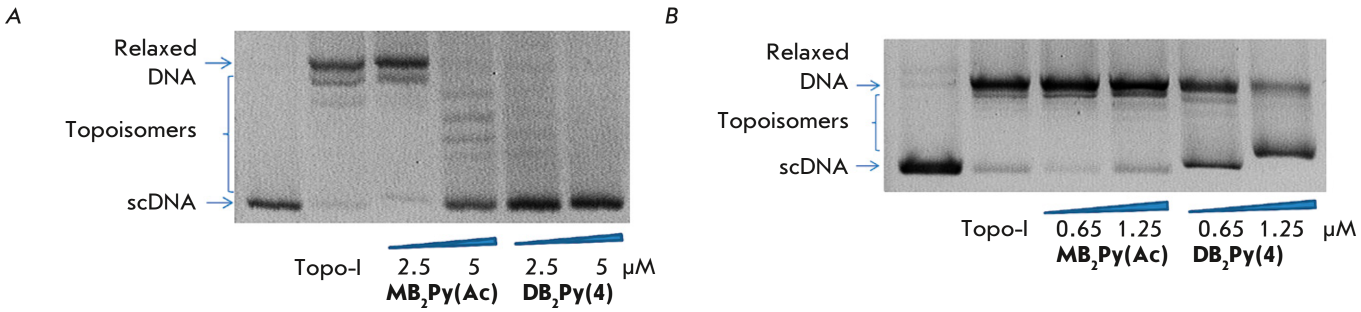

Fig. 10. Calf-thymus Topo-I inhibition by **MB$_2$Py(Ac)** and **DB$_2$Py(4)**. (*A*) – effect of the compounds on Topo-I activity at concentrations of 2.5 and 5 μM. (*B*) – at concentrations of 0.65 and 1.25 μM

DNA narrow-groove-binding ligands are able to compete with Topo-I for AT base-pair binding without covalently linking to DNA and significant changes in its conformation. In our study, Topo-I inhibition was detected through the ability of the tested compounds to delay the DNA relaxation reaction *in vitro*.

The studied compounds (*Fig. 10*) were found to inhibit Topo-I. At monomer and dimer concentrations of 5 and 2.5 μM, respectively, scDNA retention was observed in the DNA relaxation reaction (TopoGen) (*Fig. 10A*). Topo-I catalytic activity was most effectively inhibited by **DB$_2$Py(4)**. If compared to **MB$_2$Py(Ac)**, DNA retention was recorded at a **DB$_2$Py(4)** concentration of just 0.65 μM (*Fig. 10B*).

DISCUSSION

Benzimidazole is a fundamental pharmacophore in pharmaceutics because of its wide range of biological activities [24–27]. When modeling new fluorescent bis-benzimidazole molecules, we hypothesized that the introduction of an AT-specific pyrrole carboxamide fragment with affinity for DNA AT pairs into previously obtained **DB(n)**, **DBA(n)** series would enhance their cytotoxicity. Two bis-benzimidazole units within the new molecule possessed fluorescent properties and interacted with DNA. A flexible linker in the **DB$_2$Py(n)** dimers would allow the molecule to bind to two AT-rich sites located at various distances from each other. Binded with DNA, the new bis-benzimidazole-pyrroles had a planar shape isogeometric to the narrow DNA groove in order to enhance interaction between the new ligands and the DNA.

The tests employing absorption, fluorescence, and CD spectra demonstrated that the new compounds were able to interact with DNA. Since they had been derived from the **Hoechst 33258** molecule known for its localization in a narrow DNA groove, we classified them as DNA narrow-groove-binding ligands [28, 29]. The presence of two bis-benzimidazole fragments in the ligand molecule leads to a significant increase in its affinity towards polynucleotide, which provides an experimental basis for the targeted synthesis of a new class of potential antitumor drugs based on dimeric bis-benzimidazoles.

The new fluorescent compounds have shown their ability to influence the S-phase of the cell cycle; to penetrate into the cell nucleus, and to inhibit Topo-I at low concentrations in a cell-free model. The new series of bis-benzimidazole-pyrroles has turned out to be more toxic against human tumor cell lines than the previously obtained **DB(n)** and **DBA(n)** series and less toxic to a cell line of non-tumor nature. Small (2-fold) but statistically significant differences in cytotoxicity have been demonstrated in a pair (tumorigenic and non-tumorigenic) of human breast cell lines.

Our earlier studies showed that bis-benzimidazole-pyrroles were able to induce Bcl-xl-mediated apoptosis [30]. Since netropsin is known to affect the activity of eukaryotic transcription factors [31, 32], we assumed that the new compounds containing a netropsin fragment in their structure would have a similar action mechanism, which is supported by the data on DNA binding and cell cycle arrest in the synthesis phase at non-toxic concentrations of bis-benzimidazole-pyrroles.

Dimerization of the molecule enhances its affinity to DNA and Topo-I inhibitory properties *in vitro*. However, a MTT analysis of the cytotoxicity of the new compounds in tumor-cell lines did not reveal a clear advantage for the dimeric molecule, despite its ability to penetrate the cell nucleus. Nevertheless, a highly sensitive, real-time proliferation test confirmed the enhanced toxic properties upon bis-benzimidazole-pyrrole dimerization.

The important characteristics of the new compounds as potential antitumor agents are their selectivity and ability to overcome MDR. One of the main reasons for the poor efficacy of modern chemotherapy is the selection of tumor cells with a MDR phenotype that can survive lengthy drug administration. The best known MDR mechanism is overexpression of the P-gp protein, a member of the ABC transporter family. Preliminary detection of bis-benzimidazole-pyrrole cytotoxicity in a cell model with a MDR phenotype showed that dimerization of the molecule may have led to an interaction with the P-gp protein and, as a consequence, to an increase in the resistance of the HBL-100/DOX line to this compound (9-fold on average) compared to doxorubicin (50–100-fold or more); so, it would be interesting to investigate the possibility of direct interaction between the new molecules and the P-gp transporter.

Perhaps the reason why dimeric compounds remain underestimated in terms of their biological activity is their greater tendency to form aggregates as compared to monomeric molecules. Finding a way to overcome the aggregation of dimeric molecules can pave the way to designing significantly more active compounds.

CONCLUSION

The newly synthesized cytotoxic dimeric bis-benzimidazole-pyrroles appear promising for further in-depth study of their properties and action mechanism against human tumor cells, as well as for designing new molecules. ●

This study was supported by the Russian Science Foundation, Grant No. 23-25-00373.
The authors would like to thank A. Zaitsev for help in manuscript preparation.

REFERENCES

1. Venugopal S., Kaur B., Verma A., Wadhwa P., Magan M., Hudda S., Kakoty V. // Chem. Biol. Drug Design. 2023. V. 102. P. 357–376.
2. Wu K., Peng X., Chen M., Li Y., Tang G., Peng J., Peng Y., Cao X. // Chem. Biol. Drug Design. 2022. V. 99. № 5. P. 736–757.
3. Tyagi Y.K., Jali G., Singh R. // Anticancer Agents Med. Chem. 2022. V. 22. № 19. P. 3280–3290.
4. Brishty S.R., Hossain M.J., Khandaker M.U., Faruque M.R.I., Osman H., Rahman S.M.A. // Front. Pharmacol. 2021. V. 12. P. 762807.
5. Ivanov A.A., Salyanov V.I., Strel'tsov S.A., Cherepanova N.A., Gromova E.S., Zhuze A.L. // Rus. J. Bioorg. Chem. 2011. V. 37. № 4. P. 530–541.
6. Koval V.S., Ivanov A.A., Salyanov V.I., Stomakhin A.A., Oleinikov V.A., Zhuze A.L. // Rus. J. Bioorg. Chem. 2017. V. 43. № 2. P. 167–173.
7. Koval V.S., Arutyunyan A.F., Salyanov V.L., Klimova R.R., Kushch A.A., Rybalkina E.Yu., Susova O.Yu., Zhuze A.L. // Bioorg. Med. Chem. 2018. V. 26. № 9. P. 2302–2309.
8. Koval V.S., Arutyunyan A.F., Salyanov V.I., Kostyukov A.A., Melkina O.E., Zavilgelsky G.B., Klimova R.R., Kushch A.A., Korolev S.P., Agapkina Y.Yu., et al // Bioorg. Med. Chem. 2020. V. 28. P. 115378.
9. Teng M.K., Usman N., Frederick C.A., Wang A.H. // Nucl. Acids Res. 1988. V. 16. P. 2671–2690.
10. Finlay A.C., Hochstein F.A., Sobin B.A., Murphy F.X. // J. Am. Chem. Soc. 1951. V. 73. № 1. P. 341–343.
11. Lisitsina E.S., Durandin N.A., Ivanov A.A., Strel'tsov S.A., Susova O.Yu., Shtil A.A., Zhuze A.L., Kuz'min V.A. // Mol. Biol. (Moskow). 2012. V. 46. P. 922–927.
12. Yevdokimov Yu.M., Skuridin S.G., Lortkipanidze G.B. // Liquid Crystals. 1992. V. 12. № 1. P. 1–16.
13. Gromyko A.V., Salyanov V.I., Strel'tsov S.A., Oleinikov V.A., Korolev S.P., Gottikh M.B., Zhuze A.L. // Rus. J. Bioorg. Chem. 2007. V. 33. № 6. P. 613–623.
14. Susova O., Poletaeva A., Lupatov A., Kholodenko I., Karamysheva A., Mitrofanov A.A., Naskhletashvili D., Nasedkina T., Bekyashev A. // Ann. Oncol. 2021. № 32. P. 519.
15. Ammour Y., Susova O., Krasnov G., Nikolaeva E., Varachev V., Schetinina Y., Gavrilova M., Mitrofanov A., Poletaeva A., Bekyashev A., et al // Viruses. 2022. V. 14. № 11. P. 2433.
16. Gaffney E.V. // Cell Tissue Res. 1982. V. 227. P. 563–568.
17. Saint-Ruf C., Nardeux P., Estrade S., Brouty-Boye D., Lavialle C., Rhim J.S., Cassingena R. // Exp. Cell Res. 1988. V. 176. P. 60–67.
18. Rybalkina E.Y., Moiseeva N.I., Karamysheva A.F., Eroshenko D.V., Konysheva A.V., Nazarov A.V., Grishko V.V. // Chem. Biol. Interact. 2021. V. 1. № 348. P. 109645.
19. Chen H., Shan J., Chen D., Wang R., Qi W., Wang H., Ke Y., Liu W., Zeng X. // J. Cell. Physiol. 2018. V. 234. P. 11871–11881.
20. Khader E.I., Ismail W.W., Mhaidat N.M., Alqudah M.A. // Int. J. Hlth Sci. (Quassim). 2021. V. 15. P. 34–41.
21. Pommier Y. // Nat. Rev. Cancer. 2006. V. 6. № 10.

P. 789–802.
22. Li T.-K. // Annu. Rev. Pharmacol. Toxicol. 2001. V. 41. P. 53–77.
23. Pommier Y. // ACS Chem. Biol. 2013. V. 8. № 1. P. 82–95.
24. Verma S., Ravichandiran V., Ranjan N., Flora S.J.S. // Med. Chem. 2020. V. 16. № 4. P. 454–486.
25. Akhtar W., Khan M.F., Verma G., Shaquiquzzaman M., Rizvi M.A., Mehdi S.H., Akhter M., Alam M.M. // Eur. J. Med. Chem. 2017. V. 27. № 126. P. 705–753.
26. Shrivastava N., Naim M.J., Alam M.J., Nawaz F., Ahmed S., Alam O. // Arch. Pharm. Chem. Life Sci. 2017. V. 350. P.e 1700040.
27. Gao C., Li B., Zhang B., Sun Q., Li L., Li X., Chen C., Tan C., Liu H., Jiang Y. // Bioorg. Med. Chem. 2015. V. 23. № 8. P. 1800–1807.
28. Evdokimov Yu.M., Skuridin S.G., Lortkipanidze G.B. // Liquid Crystals. 1992. V. 12. № 1. P. 1–16.
29. Pjura P.E., Grzeskowiak K., Dickerson R.E. // J. Mol. Biol. 1987. V. 20. № 197. P. 257–271.
30. Ianevski A., Kulesskiy E., Krpina K., Lou G., Aman Y., Bugai A., Aasumets K., Akimov Y., Bulanova D., Gildemann K., et al. // Cancers (Basel). 2020. V. 12. P. 1694.
31. Belikov S.V., Grokhovsky S.L., Isaguliants M.G., Surovaya A.N., Gursky G.V. // J. Biomol. Struct. Dyn. 2005. V. 23. № 2. P. 193–202.
32. Dickinson L.A., Gulizia R.J., Trauger J.W., Baird E.E., Mosier D.E., Gottesfeld J.M., Dervan P.B. // Proc. Natl. Acad. Sci. USA. 1998. V. 95. № 22. P. 12890–12895.

Broadly Reactive Nanobody Targeting the H3 Hemagglutinin of the Influenza A Virus

D. V. Shcheblyakov[1], D. V. Voronina[1*], I. A. Favorskaya[1], I. B. Esmagambetov[1], I. A. Alekseeva[1], A. I. Korobkova[1], E. I. Ryabova[1,2], A. A. Derkaev[1], V. Yu. Kan[1], A. Sh. Dzharullaeva[1], A. I. Tukhvatulin[1], A. S. Bandelyuk[1], M. M. Shmarov[1], D. Yu. Logunov[1], A. L. Gintsburg[1]
[1]National Research Center for Epidemiology and Microbiology named after the honorary academician N. F. Gamaleya, Moscow, 123098 Russian Federation
[2]Department of Immunology and Biotechnology, Moscow State Academy of Veterinary Medicine and Biotechnology named after K. I. Skryabin, Moscow, 109472 Russian Federation
*E-mail: daryavoronin2009@yandex.ru

Received: January 24, 2024; in final form, February 09, 2024
DOI: 10.32607/actanaturae.27374

ABSTRACT Monoclonal antibodies and recombinant antibody fragments are a very promising therapeutic tool to combat infectious diseases. Due to their unique paratope structure, nanobodies (VHHs) hold several advantages over conventional monoclonal antibodies, especially in relation to viral infections. Influenza A viruses (IAVs) remain a major threat to public health. The hemagglutinin (HA) protein is the main protective and immunodominant antigen of IAVs. In this study, three broadly reactive nanobodies (D9.2, E12.2, and D4.2) to H3N2 influenza strains were isolated and Fc-fusion proteins (VHH-Fcs) were obtained and characterized *in vitro*. This modification improved the nanobodies' binding activity and allowed for their interaction with a wider range of strains. The D9.2-Fc antibody showed a 100% protection rate against mortality *in vivo* in a mouse lethal model. Furthermore, we demonstrated that the observed protection has to do with Fc-FcγR interactions. These results indicate that D9.2-Fc can serve as an effective antiviral agent against the H3N2 influenza infection.

KEYWORDS nanobody, single-domain antibody, influenza virus, hemagglutinin, Fc region.

ABBREVIATIONS IAV – influenza A virus; HA – hemagglutinin; VHH – variable domain of heavy-chain antibody of *Camelidae* family members; ELISA – enzyme-linked immunosorbent assay; EC_{50} – half-maximal effective concentration; LD_{50} – median lethal dose; mAb – monoclonal antibodies; Fc – fragment crystallizable region; SDS-PAGE – sodium dodecyl sulfate–polyacrylamide gel electrophoresis; HRP – horseradish peroxidase; OD_{450nm} – optical density measured at a wavelength of 450 nm; HI – hemagglutination inhibition; NA – neutralization assay; DTT – dithiothreitol; SEM – standard error of the mean.

INTRODUCTION

H3N2 viruses are one of the pathogens responsible for seasonal influenza epidemics; representatives of this influenza A virus (IAV) subtype have been circulating in the human population since 1968 [1]. A seasonal H3N2 infection typically comes with an unprecedented increase in the number of patients with pneumonia that are hospitalized in intensive care units [2] and in individuals with high mortality and complications [3–5].

Vaccination is one of the most common means used to treat influenza; however, its effectiveness can vary greatly depending on the epidemic season [6, 7]. In addition to the low effectiveness of preventive measures, the activity of modern antiviral drugs has also plummeted due to growing virus resistance [8, 9]. In this context, the development of novel, broadly reactive antiviral drugs and therapeutic monoclonal antibodies (mAb) against influenza becomes crucial. Antigen-binding fragments of *Camelidae* heavy-chain antibodies (nanobodies, VHH) are a promising tool for the early etiotropic therapy of infectious diseases. VHHs present a fully functional domain which binds to an antigen with high affinity and specificity. Nanobodies also demonstrate such outstanding biochemical characteristics as good solubility and thermal/pH stability [10]. Furthermore, VHHs are encoded by a single polypeptide and, thus, can be easily modified: e.g., fused to IgG Fc [11, 12].

The HA glycoprotein is the main immune target. A total of 18 different HA variants are known to date [13, 14]; they form two phylogenetic groups [15]. HA consists of two subunits: HA1 and HA2; these subunits play different roles in the onset of the infectious process. A number of antibodies that specifically interact with H3 HA and the entire phylogenetic group 2 through different mechanisms have been described [16–27]. The Fc-mediated antibody function is one of the mechanisms involved in combating an influenza infection [28, 29].

In this work, we identified three H3-specific VHHs binding to HA of different H3N2 strains isolated in different years. We expanded the VHH binding spectrum and its activity by fusing them to the Fc region. Prophylactic and therapeutic administration of the most promising antibody, D9.2-Fc, protects mice from a lethal H3N2 infection.

EXPERIMENTAL

Cell lines

CHO-S cells were obtained from Thermo Fisher Scientific (USA, cat. No. R80007); MDCK and Caco2 cells were obtained from the Russian collection of vertebrate cell cultures (St. Petersburg, Russia).

Viruses

Mouse-adapted IAV A/Aichi/2/68(H3N2) was used.

Recombinant proteins

The list of antigens used in the study is presented in *Table 1.*

Camel immunization, immune library construction, individual clone selection, and VHH expression and purification

A Bactrian camel was immunized intramuscularly with recombinant H3 HK HA at a dose of 100 μg. Aluminum hydroxide was used as an adjuvant. Blood (50 ml) was collected from the animal to isolate the peripheral lymphocyte fraction 5 days after the final immunization.

Library construction and specific screening of the clones were performed using inactivated A/Aichi/2/68(H3N2) as an antigen according to [30].

Nanobody expression and purification were carried out as previously described [30].

Production of VHH-Fc constructs, expression and purification of modified VHHs

Sequences of the D9.2-Fc, E12.2-Fc, and D4.2-Fc genes encoding the corresponding nanobody fused to the hinge region and Fc of human IgG1 (GenBank: JQ666008.1) were obtained by PCR. The resulting

Table 1. The recombinant HA proteins used in *in vitro* studies

Subtype	Abbreviation	Description	Source	Cat. No.	No. in GenBank/ GISAID databases
H3	H3 HA1 Swiz	HA1 A/Switzerland/9715293/2013 (H3N2)	Sino Biological	40497-V08H1	EPI541659
	H3 HA1 Vic	HA1 A/Victoria/210/2009 (H3N2)	Immune Technology	IT-003-00421p	EPI272062
	H3 Swiz	HA0 A/Switzerland/9715293/2013 (H3N2)	Sino Biological	40497-VNAB	EPI541659
	H3 Aichi	HA0 A/Aichi/2/1968 (H3N2)	Sino Biological	11707-V08H	AAA43178.1
	H3 Perth	HA0 A/Perth/16/2009 (H3N2)	Sino Biological	40043-VNAB	ACS71642.1
	H3 Sing	HA0 A/Singapore/INFIMH-16-0019/2016 (H3N2)	Xema	–	EPI1341068
	H3 HK	HA0 A/Hong Kong/45/2019 (H3N2)	–	–	EPI1691930
H4	H4	HA0 A/mallard/Ohio/657/2002 (H4N6)	Sino Biological	11714-V08H1	ABI47995.1
H7	H7 Anhui	HA0 A/Anhui/1/2013 (H7N9)	Sino Biological	40103-V08H	EPI439507
H10	H10	HA0 A/Jiangxi-Donghu/346/2013 (H10N8)	Sino Biological	40359-VNAB	EPI497477

genes were cloned into the pCEP4 vector for eukaryotic expression (Thermo Fisher Scientific, USA). A similar protocol was used to obtain the pCEP4-D9.2-mG2a plasmid encoding the D9.2 nanobody fused with the hinge region and Fc of murine IgG2a (GenBank: V00798.1). To create the pCEP4-D9.2-mG2a LALA-PG plasmid construct, point mutations were introduced into the pCEP4-D9.2-mG2a plasmid by site-directed mutagenesis [31]. Antibodies were expressed and purified as described in [32]. Antibody purity was assessed by Laemmli polyacrylamide gel electrophoresis (SDS-PAGE) under reducing and non-reducing conditions.

The control VHH-Fc–SD36-Fc, corresponding to the nanobody (SD36) to the stem domain (HA2 subunit) of H3 HA fused to human IgG1 Fc, was prepared and analyzed in a similar manner. The amino acid sequence of the nanobody was taken from [33].

Enzyme-linked immunosorbent assay (ELISA)

ELISA was carried out according to [32]. To detect the antibodies in the serum of camel, anti-Llama IgG conjugated to horseradish peroxidase (HRP) was used (Bethyl, A160-100P). HRP-conjugated secondary anti-c-Myc (ab1326, Abcam), anti-human IgG, and anti-mouse IgG antibodies (A8667 and A9044, MilliporeSigma, USA) were used to detect the antigen-bound VHHs and VHH-Fcs carrying human and murine Fc, respectively. The half-maximal effective concentration (EC_{50}) was calculated using the four-parameter logistic regression in GraphPad Prism 7 (GraphPad Software Inc., USA).

For competitive ELISA, VHH was serially diluted in blocking buffer with a starting concentration of 800 nM (~10 μg/ml). An equal volume of competitive VHH-Fc antibodies (5 nM) was added to wells containing VHH. Bound VHH-Fc was detected using anti-human IgG HRP (A8667, MilliporeSigma, USA). The optical density (OD_{450nm}) in the wells containing only VHH-Fc was considered a 100% signal. Inhibition was expressed as the percentage decrease in OD_{450nm} in the wells containing the VHH/VHH-Fc mixture compared to the VHH-free wells.

Western blotting

Proteins were separated using 10% ready-to-use Mini-PROTEAN® gels (Bio-Rad, USA) and transferred onto an Amersham™ Hybond™ P nitrocellulose membrane (Cytiva, USA). After membrane blocking, VHH-Fc was added to a final concentration of 1 μg/ml. Next, anti-human IgG HRP (A8667, MilliporeSigma, USA) was added. Immunological detection was performed using Clarity™ Western ECL (Bio-Rad) as a substrate.

Hemagglutination inhibition (HI) assay

HI assay was carried out according to [34].

Virus neutralization (VN)

The VN test in the mode of microneutralization was performed in 96-well culture plates as previously described [35]. Non-neutralized viral particles were detected using rabbit polyclonal antibodies to the NP protein and secondary anti-Rabbit IgG HRP antibodies (Cat: 11675-T62 and SSA003, Sino Biological, China).

The ability of antibodies to inhibit the release of viral progeny from the cell and reduce the plaque size was assessed using the techniques described in [16].

Evaluation of the prophylactic and therapeutic effectiveness of the antibodies *in vivo*

All the animal experiments, carried out in accordance with Directive 2010/63/EU, FELASA recommendations [36], were approved by the ethical committee of the Federal State Budgetary Institution National Research Center of Epidemiology and Microbiology n.a. N.F. Gamaleya (protocol No. 19 of 2022).

SPF BALB/c mice aged 6–8 weeks, obtained from the Nursery of Laboratory Animals of the Institute of Bioorganic Chemistry of the Russian Academy of Sciences, were used in all the experiments. The animals were infected intranasally with 5 LD_{50} of the mouse-adapted virus A/Aichi/2/68 (H3N2). The animals were observed for 14 days after infection and weighed daily before they were euthanized. Mice that lost 25% or more of their body weight were euthanized.

Detailed information on the antibody administration regimens is presented in the Results section.

Survival was analyzed using the Mantel–Cox method in GraphPad Prism 7 (GraphPad Software Inc., USA).

RESULTS

To collect nanobodies binding to the H3 subtype HA, a Bactrian camel (*Camelus Bactrianus*) was immunized with the recombinant full-length H3 HK HA0 protein previously obtained in CHO-S cells (*Fig. 1A*). The level of HA-specific antibodies in camel serum was monitored by ELISA (*Fig. 1B*). Unlike the control serum, the immune serum obtained after the entire immunization cycle demonstrated specific activity against the H3 HK protein with a binding titer exceeding 1 : 1 500 000. A 1.4×10^7 phage library was constructed using cDNA encoding the VHH sequences isolated from B cells. H3 HA-specific VHHs were selected using phage display by performing three rounds of bio-panning against inactivated A/Aichi/2/68 (H3N2)

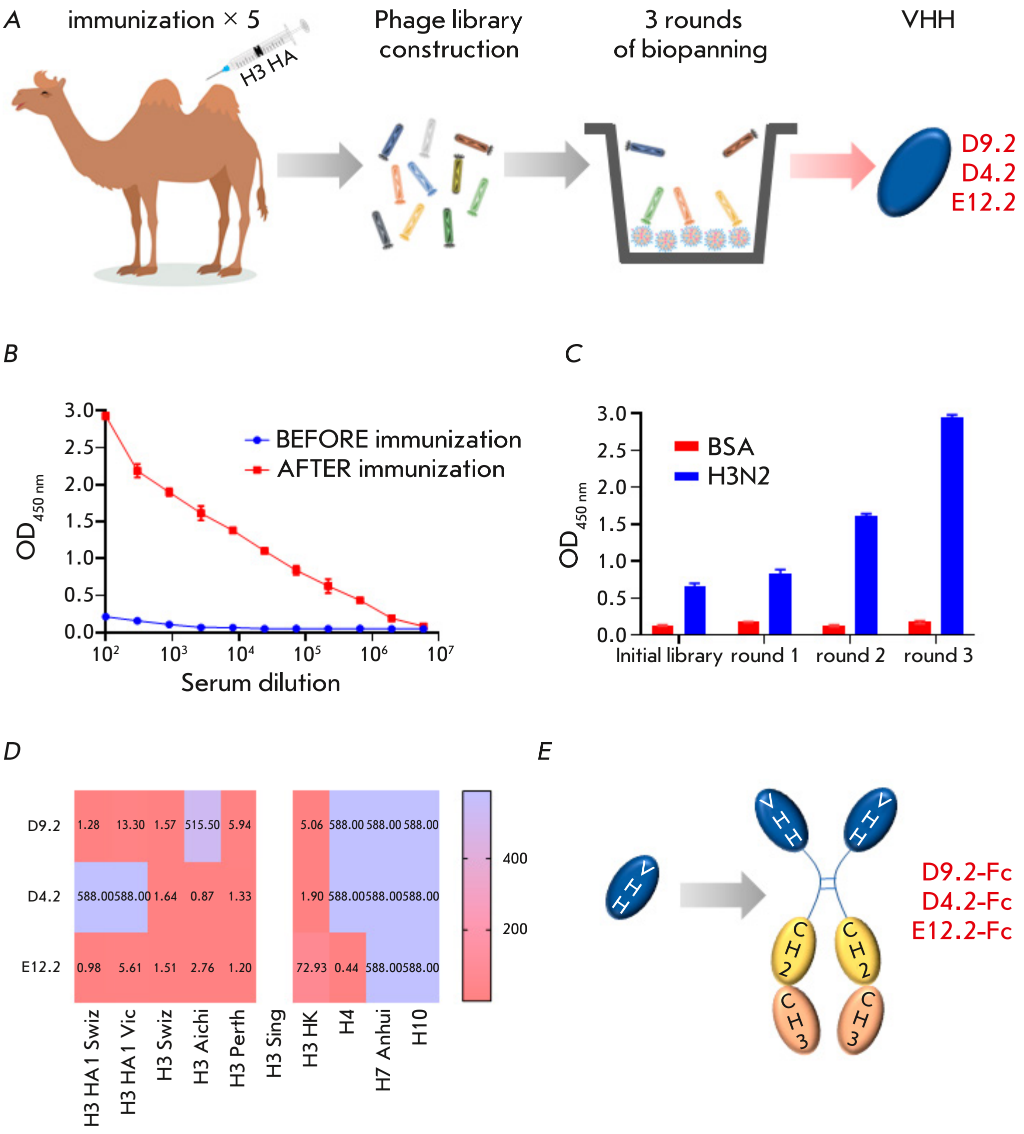

Fig. 1. The schematic process of VHH isolation, characterization of the binding activity of the selected VHHs, and their modification: (*A*) – animal immunization and VHH selection; (*B*) – ELISA signals of H3 HA-binding antibodies in the camel serum before and after the fifth immunization; (*C*) – polyclonal phage ELISA: BSA – bovine serum albumin, H3N2 – inactivated A/Aichi/2/1968 IAV; (*D*) – Group 2 HA-binding activity of the selected VHHs detected by ELISA and expressed as EC_{50} values (nM); (E) – strategy for increasing the potency of VHH modified with the Fc region

(*Fig. 1A*). After the third round of panning, significant enrichment of H3N2-specific VHHs was observed (*Fig. 1C*). Of the resulting panel of antibodies, three VHHs (D4.2, D9.2, and E12.2) binding to H3 HK were selected for further studies (*Fig. 1A*).

VHH immunoreactivity was analyzed by ELISA using recombinant HA of the subtypes H3, H4, H7, and H10 (*Fig. 1D*). All VHHs bound to immobilized HA of different H3N2 strains with high affinity, including isolates obtained in 2009, 2013, and 2019. In addition, E12.2 and D4.2 demonstrated affinity for A/Aichi/2/1968 HA. E12.2 also interacted with H4 HA. Both D9.2 and E12.2 recognized the HA1 subunit of HA. Meanwhile, D4.2 did not bind to HA1 but interacted with full-length HA0.

In order to increase the activity of the selected nanobodies by natural dimerization, extend the serum half-life, and confer Fc-mediated effector functions, we modified VHH with the Fc region (*Fig. 1E*). The selected VHH sequences were fused into the hinge region and the Fc domain of human IgG1. As a result, the following VHH-Fc constructs were obtained: D9.2-Fc, D4.2-Fc, and E12.2-Fc. Dimerization of VHH-Fc was confirmed by electrophoresis (*Fig. 2A*). The band with a molecular mass of approximately 80–90 kDa under non-reducing conditions corresponds to dimeric VHH-Fc.

The scope of the VHH-Fc binding ability was studied by indirect ELISA using recombinant HA0 and HA1 proteins of different IAV strains (*Fig. 2B*). The introduction of the Fc region in the VHH molecule appeared to enhance the binding effectiveness of each of the VHH-Fc selected, although to a different extent. The most pronounced increase in the affinity

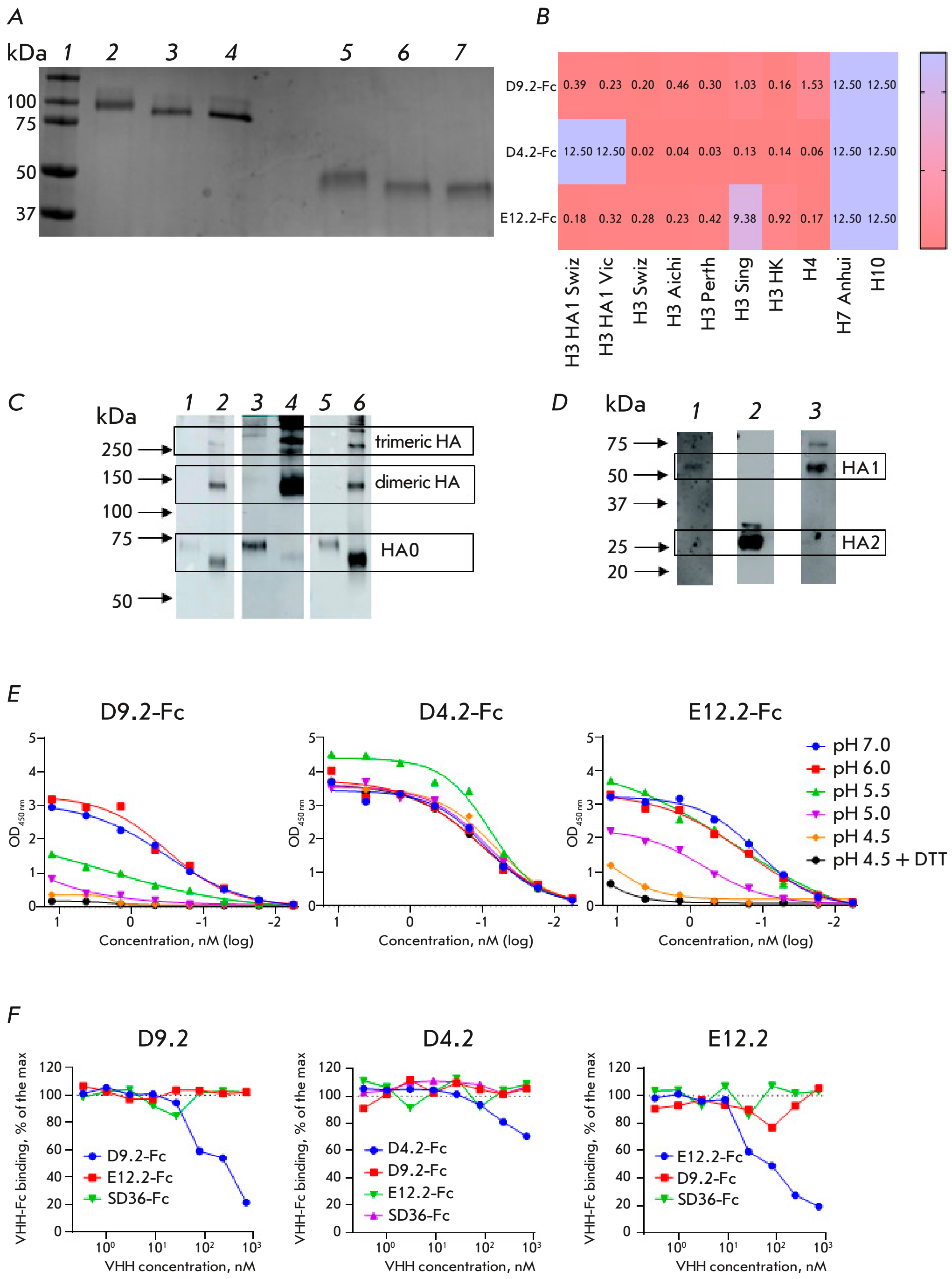

	H3 HA1 Swiz	H3 HA1 Vic	H3 Swiz	H3 Aichi	H3 Perth	H3 Sing	H3 HK	H4	H7 Anhui	H10
D9.2-Fc	0.39	0.23	0.20	0.46	0.30	1.03	0.16	1.53	12.50	12.50
D4.2-Fc	12.50	12.50	0.02	0.04	0.03	0.13	0.14	0.06	12.50	12.50
E12.2-Fc	0.18	0.32	0.28	0.23	0.42	9.38	0.92	0.17	12.50	12.50

Fig. 2. Production of VHH-Fc fusion proteins and their characterization *in vitro*: (*A*) – SDS-PAGE of purified VHH-Fc under non-reducing (*2–4*) and under reducing (*5–7*) conditions: molecular weight ladder (*1*), D9.2-Fc (*2*, *5*), E12.2-Fc (*3*, *6*), and D4.2-Fc (*4*, *7*); (*B*) – binding characteristics of VHH-Fc in relation to different Group 2 HA proteins, expressed as EC_{50} (nM) based on the ELISA assay results; (*C*) – Western blot analysis of the antibody specificity of D9.2-Fc (*1*, *2*), D4.2-Fc (*3*, *4*), and E12.2-Fc (*5*, *6*) to H3 Swiz HA0 under reducing (*1*, *3*, *5*) and non-reducing (*2*, *4*, *6*) conditions; (*D*) – Western blot analysis of VHH-Fc specificity to HA1 and the HS2 subunit of the HA protein: inactivated A/Aichi/2/1968 IAV under reducing conditions, detected using D9.2-Fc (*1*), D4.2-Fc (*2*), and E12.2-Fc (*3*); (*E*) – ELISA demonstrating binding of VHH-Fc to H3 Aichi HA0 cleaved by trypsin-TPCK and incubated in buffer solutions with different pH and DTT; (*F*) – competitive ELISA for identification of VHH-Fc epitopes

was demonstrated for D4.2-Fc: its EC_{50} for H3 Swiz was 22 pM, while the EC_{50} of the monomeric variant was 1,642 pM. Monomeric D9.2 could barely bind to H3 Aichi, while the EC_{50} of the Fc-fusion form for this strain was 0.46 nM. Both D9.2-Fc and D4.2-Fc gained the ability to bind to H4 HA. The least pronounced effect of the Fc modification was shown for E12.2.

Assessment of VHH-Fc specificity by western blotting showed that the selected antibodies recognize mono-, di-, and trimeric HA forms (*Fig. 2C*). Immunoblotting also showed that the antibodies D9.2-Fc and E12.2-Fc specifically bind to the HA1 subunit, while D4.2-Fc has specificity to HA2 (*Fig. 2D*). Next, we analyzed whether the epitopes recognized by the antibodies degrade in decreased pH conditions (*Fig. 2E*). During membrane fusion, HA is known to undergo significant conformational changes due to a decrease in pH in host cell endosomes. Despite the

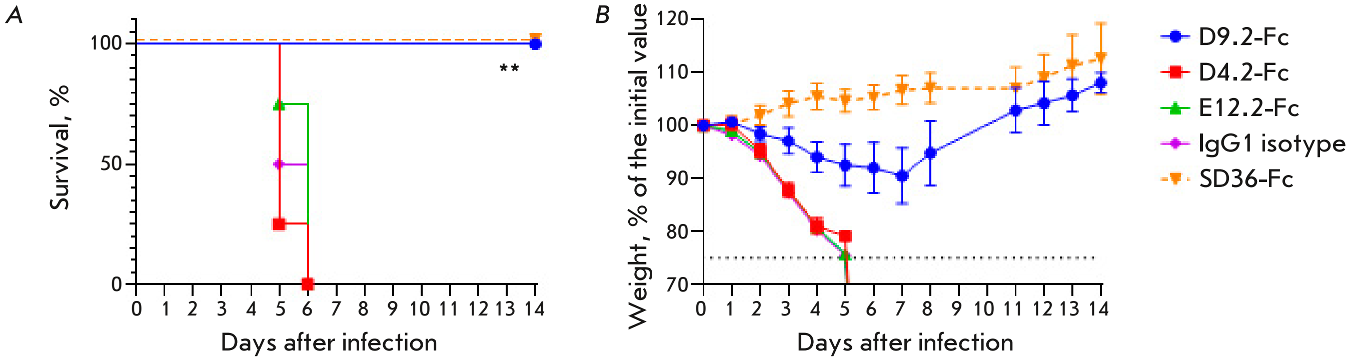

Fig. 3. The preventive effectiveness of VHH-Fc *in vivo*: (*A*) – survival curves, only the differences between the control and D9.2-Fc groups are shown ($^{**}p=0.002$); (*B*) – body weight curves for surviving mice, data are presented as mean values ± SEM

fact that, unlike HA2, the HA1 subunit does not undergo such major rearrangements [37, 38], the activity of HA1-binding antibodies (D9.2-Fc and E12.2-Fc) was reduced with a decrease in pH and completely lost upon DTT addition. This is because the latter eliminates HA1 from HA. However, D4.2-Fc proved to bind equally to HA at different pH values, as well as DTT-treated HA, which confirms that the epitope is located in the HA2 subunit.

Competitive ELISA showed that the three VHH-Fc clones recognize different non-overlapping epitopes on the HA surface (*Fig. 2F*). The HA2-binding antibody D4.2-Fc did not compete with the control VHH-Fc for binding with HA2 (SD36-Fc).

The protective activity of VHH-Fc *in vivo* was studied using a lethal mouse model (*Fig. 3*). BALB/c mice were administered with 1 mg/kg of VHH-Fc intranasally 1 h before infection. The animals in the control group received the IgG1 isotype: an irrelevant VHH-Fc to the SARS-CoV-2 S protein. The SD36-Fc antibody served as a positive control.

The D9.2-Fc antibody protected 100% of the animals from death. Weight loss in this group did not exceed 10% on average. By the end of the experiment, mouse weight exceeded the original weight. Neither E12.2-Fc nor D4.2-Fc demonstrated protective activity. Therefore, D9.2-Fc was selected for further studies *in vivo*.

We further assessed the prophylactic effectiveness of systemic D9.2-Fc administration against a lethal H3N2 infection (*Fig. 4A,B*). Mice were injected with antibodies at a dose of 10 mg/kg intraperitoneally 24 h before IAV infection. The animals treated with D9.2-Fc showed no disease signs; weight loss was either absent or insignificant. The control mice died after 7 days.

In order to estimate the therapeutic effectiveness of D9.2-Fc, mice were intraperitoneally injected with 40 mg/kg of D9.2-Fc 24 h post-infection (*Fig. 4C,D*). Mice from the control group died by day 9 after infection. A total of 80% of the animals receiving D9.2-Fc survived; the change in the body weight did not exceed 15%; the weight of all the mice returned to its initial values by the end of the observation period.

To study the mechanism of D9.2-Fc antiviral action, we assessed the activity of VHH-Fc by HI assay and by different variations of VN. The antibody did not inhibit any hemagglutination activity of IAV in the microneutralization assay and did not exhibit virus-neutralizing activity in the plaque neutralization test. A study of the ability of VHH-Fc to inhibit virus release from the cell also showed no neutralizing properties by D9.2-Fc.

Since D9.2-Fc did not show any ability to neutralize IAV, we assumed that its effectiveness *in vivo* is due to Fc-dependent effector functions. For this reason, we obtained two additional D9.2 variants: VHH fused to murine IgG2a Fc (D9.2-mG2a) and D9.2-mG2a LALA-PG carrying Fc with the mutations L234A, L235A, and P329G (*Fig. 5*). The LALA-PG mutation complex inhibits binding to FcγR and C1q, while interaction with FcRn and Fc stability remained unaffected [39]. ELISA demonstrated that these mutations do not affect D9.2 binding to HA (*Fig. 5B*). To assess and compare the protective properties of the resulting constructs, we injected mice intraperitoneally with antibodies at a dose of 5 mg/kg 24 h prior to infection (*Fig. 5C,D*). Mice (four out of five) receiving D9.2-mG2a were protected from death, while all mice treated with LALA-PG, as well as the control mice, died by day 6. Therefore, the Fc-FcγR interaction is

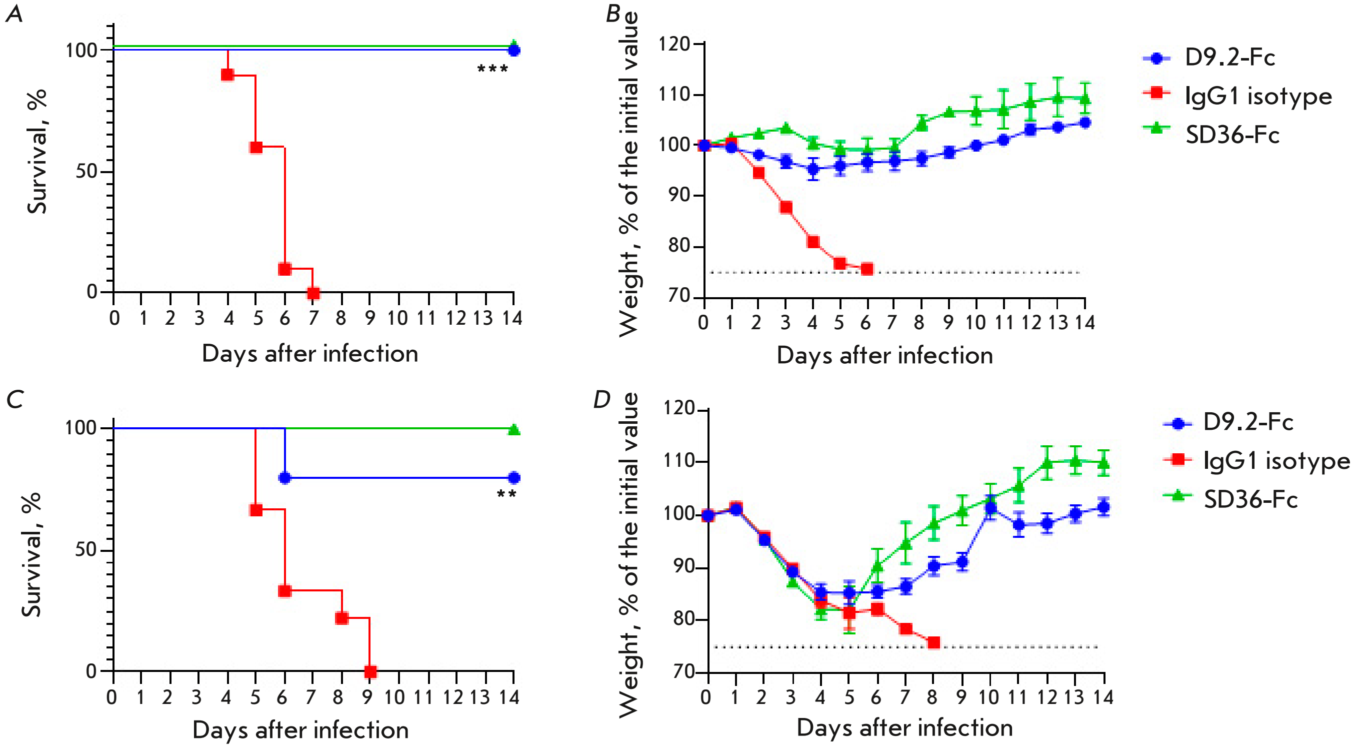

Fig. 4. The effectiveness of D9.2-Fc in preventive (*A*) and (*B*) and therapeutic (*C*) and (*D*) regimens *in vivo*: (*A*) and (*C*) – survival curves ($^{***}p = 0.0002$, $^{**}p = 0.0021$); (*B*) and (*D*) – body weight curves for surviving mice, data are presented as mean values ± SEM

required in order to protect the animals in the presence of non-neutralizing D9.2 antibody *in vivo*.

DISCUSSION

To date, the use of mAbs for infection prevention and treatment has been one of the promising areas of medicine. Nanobodies (VHHs) are considered a reasonable and effective alternative to conventional IgG. The possibility of using VHHs as antibacterial [40, 41] and antiviral antibodies [32, 42, 43] has recently been under active consideration. VHHs consisting of a single polypeptide can be successfully used as a part of adenoviral vectors [44, 45], adeno-associated viral vectors [46, 47], and mRNA [48] for passive immunization. In this work, we identified three VHHs: D9.2, D4.2, and E12.2; these nanobodies are specific to different HA epitopes in H3N2. D9.2 and E12.2 bind to the HA1 subunit, whereas D4.2 interacts with HA2. These VHHs recognize the HA of different H3N2 strains. In addition, monomeric E12.2 can bind to H4 HA.

Enhancement of the VHH antiviral effect by multimerization has been previously reported. VHH P2C5 dimerization has resulted in a 200-fold increase in neutralizing activity against SARS-CoV-2 [49], while the dimer of another anti-S VHH Fu2 was shown to be 10 times more effective in neutralizing the virus compared to its monomeric form [50]. According to Hultberg A. et al., a 4,000-fold increase in VHH activity can be achieved; this was demonstrated for bivalent VHH, which neutralizes the respiratory syncytial virus [12]. A similar observation was made for Fc-fusion VHH, since the introduction of the Fc region to the molecule results in its natural dimerization [51, 52]. Furthermore, an expansion of the binding spectrum of some VHHs due to multimerization was shown. Bivalent anti-influenza VHH R1a-B6 acquired the ability to neutralize H2N2 viruses [53], while Fc-fusion G2.3 neutralized H5N2 and H9N2 [32]. The Fc-fusion VHH active against SARS-CoV-1 demonstrated cross-reactivity with SARS-CoV-2 [54]. In addition, the Fc modification allows for the recruitment of effector functions, including complement activation and/or antibody-dependent cellular cytotoxicity and phagocytosis, which play a crucial role in combating an influenza infection [29]. Therefore, we fused the obtained VHHs to human IgG1 Fc, and Fc-mediated dimerization resulted in increased binding activity and the ability to interact with H4 HA (for VHH D9.2 and D4.2). However, modification of E12.2 resulted in minimal

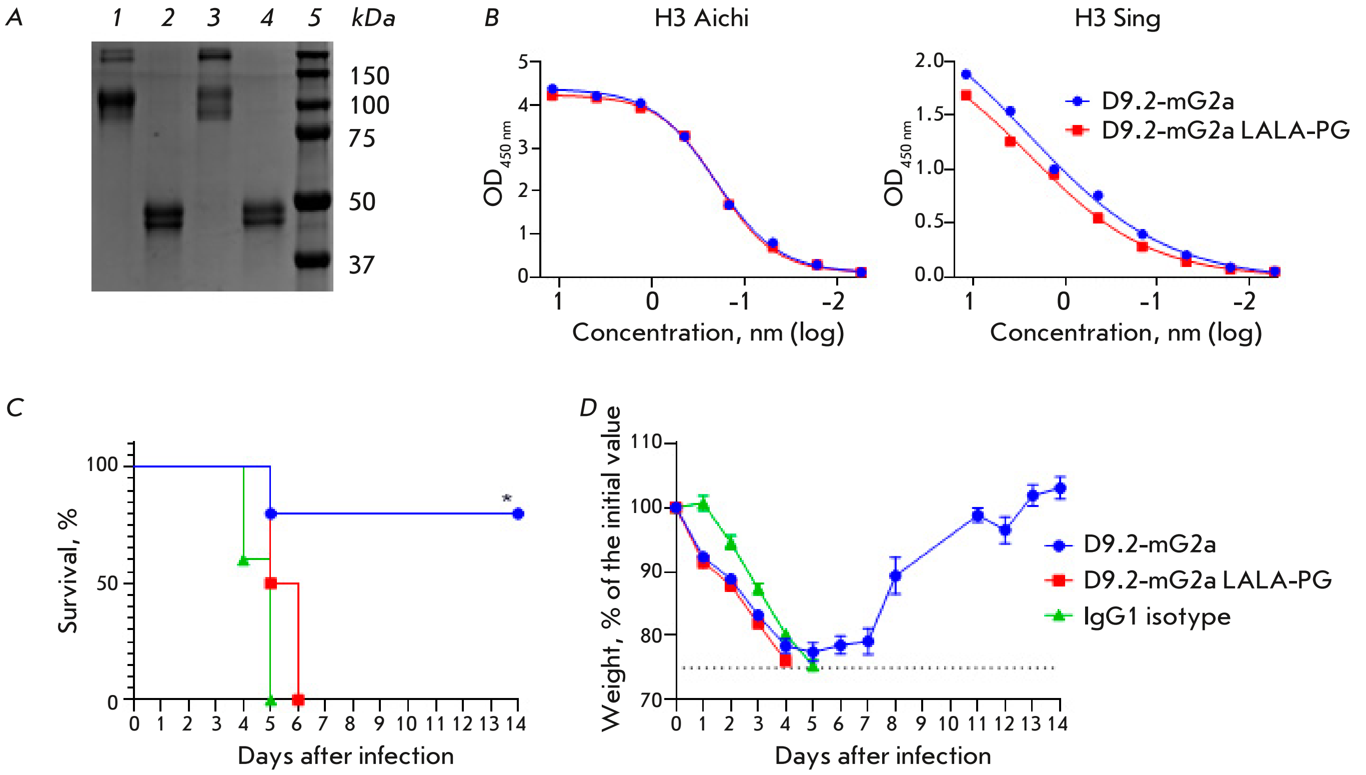

Fig. 5. *In vivo* protection by D9.2 is dependent on Fc-FcγR interactions: (*A*) – SDS-PAGE of the resulting antibody constructs under non-reducing (*1*, *3*) and reducing (*2*, *4*) conditions: D9.2-mG2a (*1*, *2*) and D9.2-mG2a LALA-PG (*3*, *4*), molecular weight ladder (*5*); (*B*) – ELISA demonstrating binding of the above-mentioned antibodies with H3 Aichi and H3 Sing HAs; (*C*) – survival curves (differences between D9.2-mG2a and IgG1 groups: $^{*}p = 0.0361$; differences between D9.2-mG2a and LALA-PG groups – $^{*}p = 0.0116$); (*D*) – body weight curves for surviving mice, data are presented as mean values ± SEM

(compared to other VHHs) increase in binding capacity, suggesting that the potential for enhancing the antibody binding efficiency and spectrum through multimerization depends on the epitope.

We analyzed the effectiveness of the selected antibodies *in vivo* and found that intranasal administration of D9.2-Fc one hour prior to infection fully protects animals from death, while D4.2-Fc and E12.2-Fc do not. Considering these results, D9.2-Fc was selected for further analysis of its prophylactic and therapeutic properties *in vivo*. Systemic administration of D9.2-Fc 24 h prior to infection yielded 100% antibody protection, while antibody injection 24 h after infection resulted in the survival of 80% of the animals.

We also assessed the virus neutralizing activity of D9.2-Fc *in vitro*. However, D9.2-Fc does not have the ability to neutralize H3N2. Thus, we hypothesized that its protective properties *in vivo* depend on the Fc-mediated effector functions of the antibody. The Fc region of human IgG1 is known to be able to bind to murine FcγR [55]. Nevertheless, in certain cases, the IgG subtype plays a crucial role in mAb protection in a lethal mouse model. MAbs with the constant region of the mouse IgG2a heavy chain binding to HA2 and targeting the HA interface were shown to improve protection *in vivo* compared to the original IgG subtype. The reason for this is the higher affinity of the Fc region of the IgG2a subtype for FcγR, compared to IgG1 [56, 57]. Despite the lack of a consensus in researchers' views on the extent to which the antiviral effect of HA1-specific mAbs is determined by the Fc-mediated functions *in vivo*, there is data confirming at least a partial dependence of anti-HA1 mAb protection on the Fc-FcγR interaction [19, 25, 26, 58]. We compared the protective properties of D9.2 fused to murine IgG2a Fc (D9.2-mG2a) and D9.2 carrying LALA-PG mutations (D9.2-mG2a LALA-PG) *in vivo* and discovered that D9.2-mG2a ensured the survival of 80% of the animals, while the entire group of mice receiving LALA-PG died. Thus, we have established that D9.2-Fc protects animals through the Fc-FcγR interaction.

CONCLUSIONS

In this work, we identified three VHH clones that recognize non-overlapping epitopes in the HA structure and exhibit activity against the HA of different H3N2 strains. We expanded the VHH binding spectrum by modifying them with the Fc region. Of the three VHH-Fcs selected, only D9.2-Fc demonstrated protective activity *in vivo* in a murine model of the influenza infection. Despite the lack of neutralizing activity against H3N2, D9.2-Fc can provide effective protection *in vivo* through the Fc-mediated mechanisms. ●

This study was conducted as part of the State assignment of the Ministry of Health of the Russian Federation No. 121031800132-4.

REFERENCES

1. Cockburn W.C., Delon P.J., Ferreira W. // Bull W. Hlth Organ. 1969. V. 41. P. 345–348.
2. Burrell A., Huckson S., Pilcher D.V. // N. Engl. J. Med. 2018. V. 378. № 22. P. 2138–2139.
3. Huang S.Y., Huang W.C., Chen Y.C., Tsai C.Y., Lee I.K. // Am. J. Trop. Med. Hygiene. 2017. V. 97. № 6. P. 1945–1951.
4. Nateghian A., Gouya M.M., Nabavi M., Soltani H., Mousavi S.V., Agah E., Erfani H., Parchami P., Dadras M., Robinson J.L. // J. Clin. Virol. 2020. V. 124. P. 104281.
5. Tekin S., Keske S., Alan S., Batirel A., Karakoc C., Tasdelen-Fisgin N., Simsek-Yavuz S., Işler B., Aydin M., Kapmaz M., et al. // Inter. J. Infect. Dis. 2019. V. 81. P. 6–9.
6. Darvishian M., van den Heuvel E.R., Bissielo A., Castilla J., Cohen C., Englund H., Gefenaite G., Huang W.T., la Bastide-van Gemert S., Martinez-Baz I., et al. // Lancet Respir. Med. 2017. V. 5. № 3. P. 200–211.
7. Lewnard J.A., Cobey S. // Vaccines (Basel). 2018. V. 6. № 2. P. 28.
8. Hayden F.G., Sugaya N., Hirotsu N., Lee N., de Jong M.D., Hurt A.C., Ishida T., Sekino H., Yamada K., Portsmouth S., et al. // N. Eng. J. Med. 2018. V. 379. № 10. P. 913–923.
9. Stephenson I., Democratis J., Lackenby A., McNally T., Smith J., Pareek M., Ellis J., Bermingham A., Nicholson K., Zambon M. // Clin. Infect. Dis. 2009. V. 48. № 4. P. 389–396.
10. Huang K., Ying T., Wu Y. // Viruses. 2022. V. 14. № 6. P. 1162.
11. Hoefman S., Ottevaere I., Baumeister J., Sargentini-Maier M.L. // Antibodies. 2015. V. 4. № 3. P. 141–156.
12. Hultberg A., Temperton N.J., Rosseels V., Koenders M., Gonzalez-Pajuelo M., Schepens B., Ibañez L.I., Vanlandschoot P., Schillemans J., Saunders M., et al. // PLoS One. 2011. V. 6. № 4. P. e17665.
13. Ferrara F., Molesti E., Temperton N. // Future Virol. 2015. V. 10. № 6. P. 731–749.
14. Wu Y., Wu Y., Tefsen B., Shi Y., Gao G.F. // Trends Microbiol. 2014. V. 22. № 4. P. 183–191.
15. Tong S., Zhu X., Li Y., Shi M., Zhang J., Bourgeois M., Yang H., Chen X., Recuenco S., Gomez J., et al. // PLoS Pathog. 2013. V. 9. № 10. P. e1003657.
16. Bangaru S., Lang S., Schotsaert M., Vanderven H.A., Zhu X., Kose N., Bombardi R., Finn J.A., Kent S.J., Gilchuk P., et al. // Cell. 2019. V. 177. № 5. P. 1136–1152.e18.
17. Benjamin E., Wang W., McAuliffe J.M., Palmer-Hill F.J., Kallewaard N.L., Chen Z., Suzich J.A., Blair W.S., Jin H., Zhu Q. // J. Virol. 2014. V. 88. № 12. P. 6743–6750.
18. DiLillo D.J., Palese P., Wilson P.C., Ravetch J.V. // J. Clin. Invest. 2016. V. 126. № 2. P. 605–610.
19. Henry Dunand C.J., Leon P.E., Huang M., Choi A., Chromikova V., Ho I.Y., Tan G.S., Cruz J., Hirsh A., Zheng N.Y., et al. // Cell Host Microbe. 2016. V. 19. № 6. P. 800–813.
20. Iba Y., Fujii Y., Ohshima N., Sumida T., Kubota-Koketsu R., Ikeda M., Wakiyama M., Shirouzu M., Okada J., Okuno Y., et al. // J. Virol. 2014. V. 88. № 13. P. 7130–7144.
21. Kubota-Koketsu R., Mizuta H., Oshita M., Ideno S., Yunoki M., Kuhara M., Yamamoto N., Okuno Y., Ikuta K. // Biochem. Biophys. Res. Commun. 2009. V. 387. № 1. P. 180–185.
22. Lee J., Boutz D.R., Chromikova V., Joyce M.G., Vollmers C., Leung K., Horton A.P., DeKosky B.J., Lee C.H., Lavinder J.J., et al. // Nat. Med. 2016. V. 22. № 12. P. 1456–1464.
23. McCarthy K.R., Watanabe A., Kuraoka M., Do K.T., McGee C.E., Sempowski G.D., Kepler T.B., Schmidt A.G., Kelsoe G., Harrison S.C. // Immunity. 2018. V. 48. № 1. P. 174–184.e9.
24. Son S., Ahn S. Bin, Kim G., Jang Y., Ko C., Kim M., Kim S.J. // Antiviral Res. 2023. V. 213. P. 105591.
25. Tan G.S., Leon P.E., Albrecht R.A., Margine I., Hirsh A., Bahl J., Krammer F. // PLoS Pathog. 2016. V. 12. № 4. P. e1005578.
26. Watanabe A., McCarthy K.R., Kuraoka M., Schmidt A.G., Adachi Y., Onodera T., Tonouchi K., Caradonna T.M., Bajic G., Song S., et al. // Cell. 2019. V. 177. № 5. P. 1124–1135.e16.
27. Yoon A., Yi K.S., Chang S.Y., Kim S.H., Song M., Choi J.A., Bourgeois M., Hossain M.J., Chen L.M., Donis R.O., et al. // PLoS One. 2015. V. 10. № 10. P. e0141312.
28. Gao R., Sheng Z., Sreenivasan C.C., Wang D., Li F. // Viruses. 2020. V. 12. № 3. P. 276.
29. Boudreau C.M., Alter G. // Front. Immunol. 2019. V. 10. P. 440.
30. Voronina D.V., Shcheblyakov D.V., Esmagambetov I.B., Derkaev A.A., Popova O., Shcherbinin D.N. // Acta Naturae. 2021. V. 13. № 4. P. 33–41.
31. Saunders K.O. // Front. Immunol. 2019. V. 10. P. 1296.
32. Voronina D.V., Shcheblyakov D.V., Favorskaya I.A., Esmagambetov I.B., Dzharullaeva A.S., Tukhvatulin A.I., Zubkova O.V., Popova O., Kan V.Y., Bandelyuk A.S., et al. // Viruses. 2022. V. 14. № 11. P. 2485.
33. Laursen N.S., Friesen R.H.E., Zhu X., Jongeneelen M., Blokland S., Vermond J., van Eijgen A., Tang C., van Diepen H., Obmolova G., et al. // Science. 2018. V. 362. № 6414. P. 598–602.
34. Kaverin N.V., Rudneva I.A., Govorkova E.A., Timofeeva T.A., Shilov A.A., Kochergin-Nikitsky K.S., Krylov P.S., Webster R.G. // J. Virol. 2007. V. 81. № 23. P. 12911–12917.
35. He W., Mullarkey C.E., Miller M.S. // Methods. 2015. V. 90. P. 95–100.
36. Mähler M., Berar M., Feinstein R., Gallagher A., Illgen-Wilcke B., Pritchett-Corning K., Raspa M. // Lab. Anim. 2014. V. 48. № 3. P. 178–192.
37. Benhaim M.A., Prasad V.M., Garcia N.K., Guttman M., Lee K.K. // Sci. Adv. 2020. V. 6. № 18. P. eaaz8822.

38. Benton D.J., Gamblin S.J., Rosenthal P.B., Skehel J.J. // Nature. 2020. V. 583. № 7814. P. 150–153.
39. Mausser E., Nador E., Politch J.A., Pauly M.R., Marathe J.G., Moench T.R., Zeitlin L., Whaley K.J., Anderson D.J. // PLoS One. 2023. V. 18. № 3. P. e0282147.
40. Cawez F., Mercuri P.S., Morales-Yãnez F.J., Maalouf R., Vandevenne M., Kerff F., Guérin V., Mainil J., Thiry D., Saulmont M., et al. // Antimicrob. Agents Chemother. 2023. V. 67. № 4. P. e01499-22.
41. Kumar S., Athreya A., Gulati A., Nair R.M., Mahendran I., Ranjan R., Penmatsa A. // Commun. Biol. 2021. V. 4. № 1. P. 836.
42. Esmagambetov I.B., Shcheblyakov D.V., Egorova D.A., Voronina O.L., Derkaev A.A., Voronina D.V., Popova O., Ryabova E.I., Shcherbinin D.N., Aksenova E.I., et al. // Acta Naturae. 2021. V. 13. № 4. P. 53–63.
43. Wang R., Zhang H., Peng C., Shi J., Zhang H., Gong R. // Virol. Sin. 2021. V. 36. № 6. P. 1600–1610.
44. Burmistrova D.A., Tillib S.V., Shcheblyakov D.V., Dolzhikova I.V., Shcherbinin D.N., Zubkova O.V., Ivanova T.I., Tukhvatulin A.I., Shmarov M.M., Logunov D.Y., et al. // PLoS One. 2016. V. 11. № 3. P. e0150958.
45. Tutykhina I.L., Sedova E.S., Gribova I.Y., Ivanova T.I., Vasilev L.A., Rutovskaya M.V., Lysenko A.A., Shmarov M.M., Logunov D.Y., Naroditsky B.S., et al. // Antiviral Res. 2013. V. 97. № 3. P. 318–328.
46. Derkaev A.A., Ryabova E.I., Esmagambetov I.B., Shcheblyakov D.V., Godakova S.A., Vinogradova I.D., Noskov A.N., Logunov D.Y., Naroditsky B.S., Gintsburg A.L. // Front Microbiol. 2022. V. 13. P. 960937.
47. Esmagambetov I.B., Ryabova E.I., Derkaev A.A., Shcheblyakov D.V., Dolzhikova I.V., Favorskaya I.A., Grousova D.M., Dovgiy M.A., Prokofiev V.V., Gosudarev A.I., et al. // Front. Immunol. 2023. V. 14. P. 1129245.
48. Panova E.A., Kleymenov D.A., Shcheblyakov D.V., Bykonia E.N., Mazunina E.P., Dzharullaeva A.S., Zolotar A.N., Derkaev A.A., Esmagambetov I.B., Sorokin I.I., et al. // Front. Immunol. 2023. V. 14. P. 1098302.
49. Favorskaya I.A., Shcheblyakov D.V., Esmagambetov I.B., Dolzhikova I.V., Alekseeva I.A., Korobkova A.I., Voronina D.V., Ryabova E.I., Derkaev A.A., Kovyrshina A.V., et al. // Front Immunol. 2022. V. 13. P. 822159.
50. Hanke L., Das H., Sheward D.J., Perez Vidakovics L., Urgard E., Moliner-Morro A., Kim C., Karl V., Pankow A., Smith N.L., et al. // Nat. Commun. 2022. V. 13. № 1. P. 155.
51. Liu H., Wu L., Liu B., Xu K., Lei W., Deng J., Rong X., Du P., Wang L., Wang D., et al. // Cell Rep. Med. 2023. V. 4. № 2. P. 100918.
52. Schepens B., van Schie L., Nerinckx W., Roose K., Fijalkowska D., Devos S., Weyts W., De Cae S., Vanmarcke S., Lonigro C., et al. // Sci. Transl. Med. 2021. V. 13. №. 621. P. eabi7826.
53. Hufton S.E., Risley P., Ball C.R., Major D., Engelhardt O.G., Poole S. // PLoS One. 2014. V. 9. № 8. P. e103294.
54. Wrapp D., De Vlieger D., Corbett K.S., Torres G.M., Wang N., van Breedam W., Roose K., van Schie L., Hoffmann M., Pöhlmann S., et al. // Cell. 2020. V. 181. № 5. P. 1004–1015.e15.
55. Derebe M.G., Nanjunda R.K., Gilliland G.L., Lacy E.R., Chiu M.L. // Immunol. Lett. 2018. V. 197. P. 1–8.
56. DiLillo D.J., Tan G.S., Palese P.R.J.V. // Nat. Med. 2014. V. 20. № 2. P. 143–151.
57. Bruhns P. // Blood. 2012. V. 119. № 24. P. 5640–5649.
58. Ko Y.A., Yu Y.H., Wu Y.F., Tseng Y.C., Chen C.L., Goh K.S., Liao H.Y., Chen T.H., Cheng T.J.R., Yang A.S., et al. // PLoS Pathog. 2021. V. 17. № 8. P. e1009724.

ELABELA-APJ Axis Enhances Mesenchymal Stem Cell Proliferation and Migration via the METTL3/PI3K/AKT Pathway

D. Xu[1#], J. Fu[1#], X. Liu[1,2], Y. Hong[1], X. Chen[1], S. Li[1], J. Hou[1,2], K. Zhang[1,2], C. Zhou[1], C. Zeng[2], G. Zheng[2], H. Wu[1], T. Wang[1*]

[1]Department of Emergency, the Eighth Affiliated Hospital of Sun Yat-sen University, Shenzhen, Guangdong, 518003 China

[2]Department of Emergency, the Sun Yat-sen Memorial Hospital of Sun Yat-sen University, Guangzhou, Guangdong, 510120 China

[#]Equal contributors.

[*]E-mail: tongwang316@163.com

Received: October 26, 2023; in final form, February 13, 2024

DOI: 10.32607/actanaturae.17863

ABSTRACT **Mesenchymal stem cells (MSCs) possess a strong therapeutic potential in regenerative medicine. ELABELA (ELA) is a 32 amino acid peptide that binds to the apelin peptide jejunum receptor (APJ) to regulate cell proliferation and migration. The aim of this study was to investigate the function of ELA vis-a-vis the MSC proliferation and migration, and further explore the underlying mechanism. We demonstrated that the exogenous supplement of ELA boosts the proliferation and migration ability of MSCs, alongside improved *in vitro* cell viability. These capabilities were rendered moot upon APJ knockdown. In addition, ELA (5–20 μM) was shown to upregulate the expression of METTL3 in a concentration-dependent pattern, a capacity which was suppressed by APJ reduction, whereas the downregulation of METTL3 expression blocked the beneficial effects induced by ELA. ELA was also observed to upregulate the phosphorylation level of AKT. This ELA-induced activation of the PI3K/AKT pathway, however, is inhibited with knockdown of METTL3. Our data indicate that ELA could act as a promoter of MSC proliferation and migration *in vitro* through the APJ receptor, something which might be attributed to the activation of the METTL3/PI3K/AKT signaling pathway. Therefore, ELA is a candidate for optimizing MSC-based cell therapy, while METTL3 is a potential target for its promoting action on MSCs.**

KEYWORDS **ELABELA, METTL3, Mesenchymal stem cells, Apelin receptor, Proliferation, Migration.**

ABBREVIATIONS **MSCs – mesenchymal stem cells; ELA – ELABELA; APJ – apelin receptor; PI3K – phosphatidylinositol 3 kinase; METTL3 – Methyltransferase-like 3; m^{6}A – N^6-methyladenosine; hESCs – human embryonic stem cells; MTC – methyltransferase complex; HSPCs – human hematopoietic stem/progenitor cells; siRNA – small interfering RNA; p-Akt – phosphorylated Akt.**

INTRODUCTION

Mesenchymal stem cells (MSCs) have attracted significant attention in the field of tissue repair and regenerative medicine for their differentiation potential, homing capacity, and self-renewal abilities [1, 2]. Due to their ease of extraction, the not-so-thorny ethical considerations associated with then, and their immunologic privilege, MSCs have become the most widely used stem cells in the regeneration of injured cells and tissues [3]. They can migrate to the sites of damage [4] and differentiate into the desired cell type [5] or contribute beneficial elements [6] such as growth factors. Nevertheless, the curative potential of MSCs remains limited for the following reasons: The insufficient number of MSCs collected from donors [7], the low chance of survival in a hostile environment [8], and the insufficient number of cells capable of migrating to damaged sites [9]. The migration ability is crucial for MSCs, because they better exert their therapeutic effects at the sites of damage [10]. Therefore, exploring ways to improve the *in vitro* expansion and migration capability of MSCs could be key in fulfilling the therapeutic potential of MSCs in cell-based therapy, opening up broader prospects in future regenerative medicine.

ELABELA (ELA, also known as Apela/Toddler) is a small peptide consisting of 32 amino acids that binds to APJ to form an essential signaling axis for modulating cellular events such as migration [11]. For example, ELA is an activator which promotes the movement of mesendodermal cells during the formation of zebrafish gastrulation [12], while ELA-APJ signaling is indispensable for angioblast migration towards the midline during vasculogenesis [13]. Of note, studies have confirmed that ELA expression is rapidly downregulated during the differentiation of human embryonic stem cells (hESCs) [14], and that this manifests itself in paracrine fashion to promote the proliferation of hESCs by accelerating cell-cycle progression. ELA can also activate the PI3K/AKT/mTORC1 signaling cascade, which is required for cell survival [15]. The PI3K/AKT signaling pathway occupies a prominent place in all manners of cellular behavior of MSCs such as proliferation [16], migration [17], and apoptosis [18]. Hence, the question of whether ELA could affect the proliferation and migration of MSCs piqued our interest. We have previously confirmed that ELA reduces MSC apoptosis by stimulating the PI3K/AKT pathway under ischemic and hypoxic conditions [19], but the effect of ELA on the expansion and migration of MSCs remains unclear, with the regulatory mechanisms requiring further investigation, as well.

N^6-methyladenosine (m^{6}A) is a dynamic modification in eukaryotic RNAs that plays a pivotal role in the regulation of cellular processes [20]. A flurry of recent discoveries has pointed to the strong relationship between m^{6}A modification and stem cell regulation [21, 22]. As the main component of the m^{6}A methyltransferase complex (MTC), methyltransferase-like 3 (METTL3) has a direct influence on cell survival, differentiation potential, stem cell maintenance, and more [23]. The depletion of METTL3 was shown to promote cell differentiation and reduce cell proliferation in human hematopoietic stem/progenitor cells (HSPCs) [24]. Conditional knockout of METTL3 in MSCs induced pathological phenotypes of osteoporosis and brought about damaged bone formation, enhanced adipogenic capacity, together with incompetent osteogenic differentiation potential in [25]. Meanwhile, METTL3 participates in the regulation of the PI3K-AKT signaling pathway too. During the osteogenic differentiation process, the protein levels of METTL3 increased, whereas the knockdown of METTL3 suppressed AKT phosphorylation and decreased the osteogenic differentiation of MSCs in [26]. This evidence suggests that METTL3 is closely related to the lineage allocation of MSCs. Nevertheless, the role of ELA and the impact of its interaction with METTL3 on the proliferation and migration of MSCs are poorly understood and require further investigation.

In this study, we investigated the effects of ELA on the proliferation and migration of MSCs *in vitro* and attempted to elucidate the underlining regulatory mechanisms involving METTL3 and the PI3K/AKT signaling pathway.

EXPERIMENTAL PROCEDURES

Cell isolation and culture

MSCs were collected from the bone marrow of Sprague-Dawley (SD) rats (male, weighing between 80 and 120 g) as previously described [19]. All SD rats were purchased from Sun Yat-sen University (Guangzhou, China), and the study procedures were approved by the Animal Ethic Committee of Sun Yat-sen University. Briefly, bone marrow in femurs and tibias from the SD rats were flushed using sterile PBS with 1% penicillin/streptomycin (100 U/mL, HyClone, USA). The cell suspension was centrifuged at 1,000 rpm for 5 min. Then, the supernatant was removed and the cell pellet was resuspended in 4 mL of low-glucose Dulbecco's modified Eagle's medium (DMEM; GIBCO, USA) containing 10% fetal bovine serum (FBS; GIBCO, USA) and 1% penicillin/streptomycin (100 U/mL, HyClone, USA), before being plated in a 25 cm^2 flask. When the confluence of adherent cells reached 90%, digestion passage was performed at a dilution of 1 : 2. MSCs from the third-passage were positive for CD44 and CD29 but negative for CD34 [27], making them useable for subsequent experiments.

ELA treatment

The ELA containing 32 amino acids (sequence: QRPVNLTMRRKLRKHNCLQRRCMPLHSRVPFP) was synthesized by GL Biochem Shanghai Ltd (China). To investigate the effects of ELA on the enhancement of cell proliferation and migration, the MSCs were treated with 5 μM ELA for 24 h. The MSCs were treated with ELA at 0 to 40 μM for 24 h to investigate the relationship between ELA and METTL3 in MSCs. To investigate the signaling pathway downstream of ELA, 5 μM of ELA was added into the culture medium post-transfection for 24 h.

Cell transfection

Small interfering RNA (siRNA) targeting METTL3 (si-METTL3, sequence: CCTACAAGATGACGCACAT), APJ (si-APJ, sequence: GCCTCAGCTTTGACCGATA) and their negative control (NC) were synthesized by RiboBio Co. (Guangzhou, China). Lipofectamine RNAiMax Reagent (Thermo Fisher, USA) was employed for siRNA transfection into the MSCs. Briefly, MSCs were cultured in plates with a penicillin/streptomycin-free medium. The transfection reagent and siRNA (50 nM) were dissolved in DMEM and mixed for 20 min before being dropped onto the culture plate.

CCK-8 assay

The Cell Counting Kit-8 (CCK-8; Dojindo Laboratories, Kumamoto, Japan) was used to detect cell proliferation and viability. The cells were seeded onto 96-well plates (3,000 cells per well) and treated accordingly. Afterwards, the cells were incubated with the CCK-8 working solution for 2 h. The optical density (OD) values at a wavelength of 450 nm were evaluated using a microplate reader (Thermo Varioskan LUX, USA).

EdU staining assay

The 5-ethynyl-2’-deoxyuridine (EdU) assay kit (Ribobio, Guangzhou, China) was applied to evaluate cell proliferation. The MSCs were seeded in a 96-well plate. After the designated treatment, 50 μmol/L of EdU was added to the MSC medium and incubated for 2 h. Afterward, the MSCs were fixed with 4% paraformaldehyde and permeabilized with 0.5% Triton-X 100. After rinsing, the MSCs were incubated with the staining reagent (EdU Apollo) for 30 min. Consequently, all cell nuclei were stained with the Hoechest solution (1 : 1 000) and visualized with a confocal laser scanning microscope (ZEISS, Germany).

Transwell assay

The Transwell system (8-mm pore, Corning, Beijing, China) was applied to analyze the migration capability of MSCs. Cells were incubated with 0.25% trypsin (Gibco, USA) and resuspended in a serum-deficient (0.5% FBS) medium. A cell suspension containing 6×10^4 cells was added to the upper chamber, whereas a 600 μL medium containing 10% FBS was added into the bottom chamber. After incubation for 8h, the cells on the upper surface were wiped with cotton swabs and the cells which had migrated to the lower surface were fixed with 4% paraformaldehyde for 30 min and then stained with 0.1% crystal violet for 20 min. Subsequently, the membrane was air-dried after washing with PBS and 5 fields were randomly examined under the microscope (ZEISS, Germany).

Measurement of the m^6A methylation level

The level of m^6A modification in MSCs was measured using the EpiQuik m^6A RNA Methylation Quantification Kit (Epigentek, USA). Briefly, 200 ng of total RNA was bound to the wells using the Binding Solution. Then, Capture Antibody, Detection Antibody, and Enhance Solution were added into the wells. After washing, Development Solution and Stop Solution were used to complete the reaction. Absorbance at 450 nm was evaluated using a microplate reader (Thermo Varioskan LUX, USA).

Western blot analysis

MSCs were lysed by a RIPA lysis buffer (Beyotime, China) supplemented with a protease inhibitor and a phosphatase inhibitor (CWBIO, China). After 30 min, the cell lysate was centrifuged at 12,000 rpm for 15 min. The supernatant was collected, and the protein concentration was measured by using the bicinchoninic acid (BCA) protein assay (CWBIO, China). After adding the loading buffer, the protein samples were heated for 10 min at 100°C. Equal-sized samples were separated by 10% SDS-PAGE and then transferred onto a polyvinylidene fluoride (PVDF) membrane (0.45 μm, Millipore, USA). Then, after incubation with 5% skim milk for 1 h, the membranes were incubated with the primary antibody at 4°C overnight: GAPDH (1 : 1000; # 2118; Cell Signaling Technology, USA), APJ (1 : 1000; # bs-2430R; Bioss, CHINA), phospho-Akt (Ser473) (1 : 2000; # 4060; Cell Signaling Technology, USA), AKT (1 : 1000; # 4691; Cell Signaling Technology, USA), METTL3 (1 : 1000; # 96391; Cell Signaling Technology, USA). After being washed with 1× TBST (3 times, per 5 min), the membranes were incubated with the secondary antibody (goat anti-rabbit IgG coupled with HRP, 1 : 2000, Cell Signaling Technology, USA) at room temperature for 1 h. About 1× TBST (3 times, per 5 min) was used to rinse the membranes, and chemiluminescence reagents were used to identify the bands by the ChemiDoc™ Touch Imaging System (Bio-Rad, USA).

Statistical analysis

The data were expressed in the form of mean ± SD. All experiments were performed independently at least three times. One-way analysis of variance (ANOVA) was used for multigroup comparisons, and the Tukey’s post-hoc test was used for comparisons between two independent groups. The significance of the difference between the two groups was evaluated by the Student’s *t*- test, with $P < 0.05$ being considered as statistically significant.

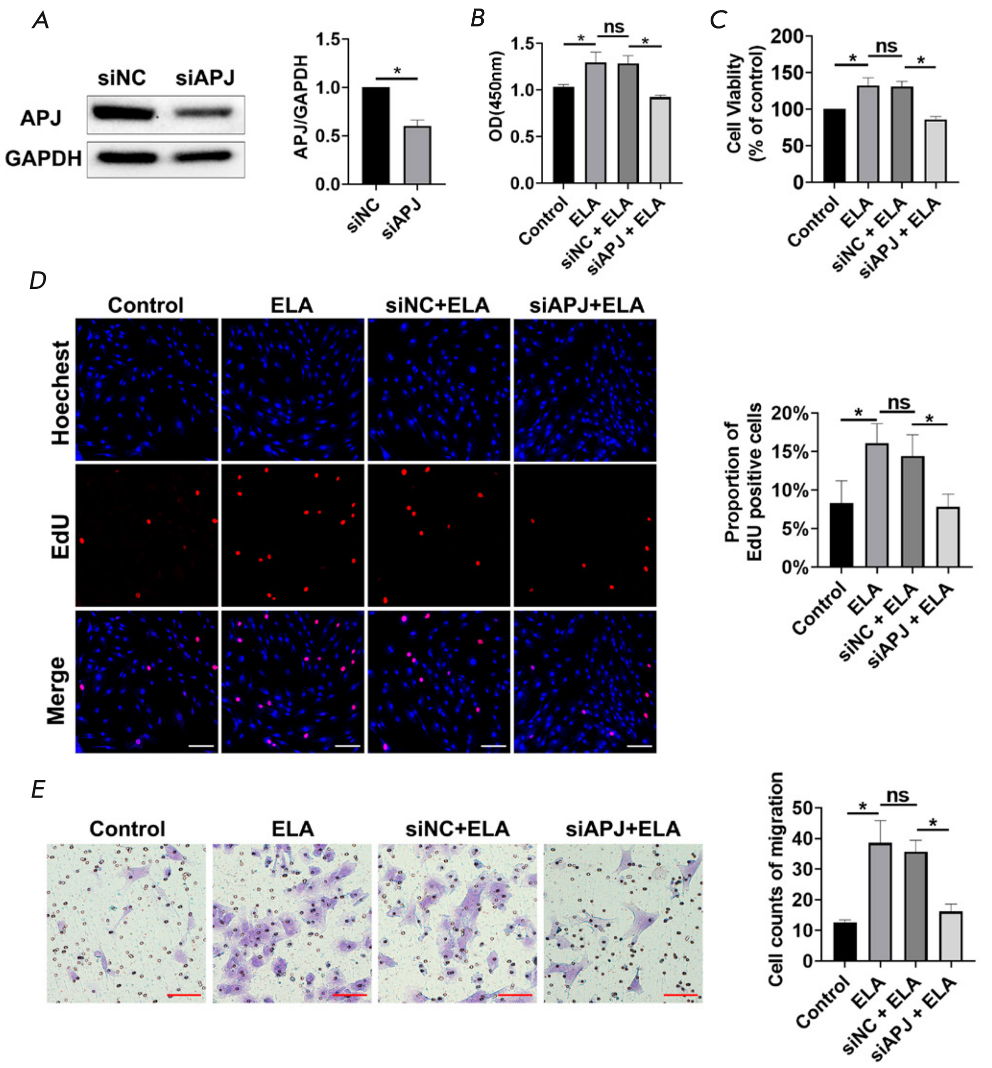

Fig. 1. ELA promotes the proliferation and migration of MSCs in an APJ-dependent manner. (*A*) – Knockdown efficiency of siAPJ evaluated by Western blot. (*B*, *C*) – CCK-8 assay results on MSC proliferation capacity and viability of various experimental groups. (*D*) – The representative images and quantification of EdU assay are shown. Scale bar 100 μm. (*E*) – Transwell assay was performed to detect MSC migration. Scale bar 100 μm. $^{*}P < 0.05$; ns – no significance; siAPJ – APJ knockdown; siNC – negative control

RESULTS AND DISCUSSION

Results

ELA promotes the proliferation and migration of MSCs in an APJ-dependent manner. The MSCs were treated with 5 μM of ELA to investigate the effect of ELA on MSC proliferation and migration. The CCK8 data revealed ELA-treated MSCs to show improved proliferation and viability compared with the control group (*Fig. 1B,C*), while data from the EdU assay indicated the percentage of EdU-positive cells to be markedly increased in the ELA group (*Fig. 1D*). In line with the results of the CCK8 and EdU assays, the migration ability of MSCs was increased after treatment with ELA (*Fig. 1E*). These results appeared to show the ability of ELA to promote MSC proliferation and migration. APJ is a known receptor for ELA. To verify the possible regulatory role of ELA through APJ, the expression of APJ in MSCs was downregulated with small interfering RNAs. The results in *Fig. 1A* demonstrate the successful knockdown of APJ in the siAPJ group. It was discovered that the siAPJ + ELA group exhibited significantly decreased proliferation ability, cell viability, as well as cell migration when compared with the siNC + ELA group (*Fig. 1*). The results between the siNC + ELA and ELA groups showed no significant difference. In summary, it appears that ELA may promote the proliferation and migration capability of MSCs in an APJ-dependent manner.

ELA upregulated the m^{6}A level and the protein level of METTL3 in MSCs. Recent studies have shown that m^{6}A plays an important role in various biological functions of cells, such as proliferation and migration. Therefore, to further explore the mechanism by which ELA promotes the proliferation and migration

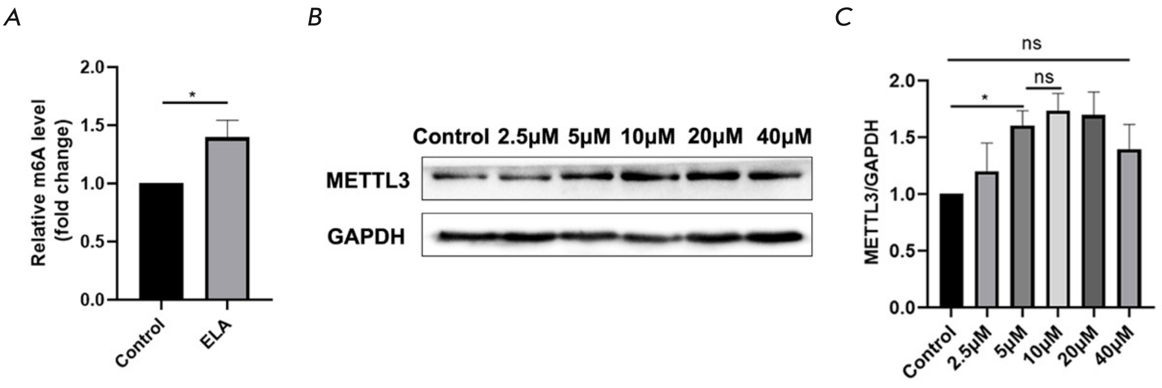

Fig. 2. ELA upregulates the m^{6}A level and the protein level of METTL3 in MSCs. (*A*) – ELA upregulated the level of m^{6}A RNA methylation in MSCs. (*B*, *C*) – ELA increased the protein expression of METTL3 in a concentration-dependent manner ranging from 5–20 μM. $^*P < 0.05$; ns – no significance

ability of MSCs, we sought to establish the m^{6}A level in MSCs. The results showed that, compared with the control group, the m^{6}A level in ELA-treated MSCs was significantly upregulated (*Fig. 2A*).

As the main component of the m^{6}A methyltransferase complex (MTC), METTL3 has a definitve influence on the regulation of stem cell function. Therefore, the expression of METTL3 was measured under increasing concentrations (0–40 μM) of ELA. As shown in *Fig. 2B,C*, the protein level of METTL3 increased in a concentration-dependent fashion within a certain concentration gradient (5–20 μM). No significant difference was observed at 40 μM compared with the control group. These results indicated that ELA could upregulate the expression of METTL3. Based on these results, it appeared reasonable suspect that ELA might affect the proliferation and migration of MSCs by regulating the protein expression of METTL3.

ELA promotes MSC proliferation and migration by regulating the expression level of METTL3. To validate the hypothesis that ELA may promote MSC proliferation and migration by regulating the expression of METTL3, METTL3 knockdown was performed in MSCs and the protein level was examined by Western blot (*Fig. 3A*). The analysis showed ELA to upregulate the METTL3 protein level in MSCs, and this effect was reversed by METTL3 knockdown (*Fig. 3B*).

In *Fig. 3C,D*, cell proliferation and viability were observed to increase in the presence of ELA compared with the control group, while it was significantly decreased in the siMETTL3 + ELA group compared with the siNC + ELA group. Moreover, compared with the control group, the ratio of EdU-positive MSCs increased upon ELA treatment but decreased in the METTL3 knockdown group (*Fig. 3E*). Consistent with the results for proliferation, METTL3 knockdown also appeared to decrease cell migration when compared with the ELA group and the siNC + ELA group (*Fig. 3F*). In addition, no distinct difference was observed between the ELA group and siNC + ELA group (*Fig. 3*). Therefore, it appears reasonable to infer that METTL3 deficiency may block the promotion effect of ELA on MSC proliferation and migration.

ELA/APJ activates the PI3K/AKT pathway by upregulating the expression of METTL3. To explore the regulatory mechanism behind the effects of ELA on the MSC proliferation and migration abilities, the expression level of METTL3 and the key kinase of the PI3K/AKT pathway were further assessed. As shown in *Fig. 4A*, METTL3 was observed to be markedly upregulated in the ELA group compared with the control group, but this effect ceased upon APJ knockdown, indicating the ability of ELA to upregulate METTL3 expression through the APJ receptor. Additionally, previous studies confirmed that ELA could regulate the PI3K/AKT pathway in MSCs [19], and that this pathway is regulated by METTL3 [26]. Therefore, further experiments were carried out to check AKT phosphorylation, with Western blot results confirming increased levels of p-AKT after treatment with ELA. However, METTL3 knockdown reversed this pattern (*Fig. 4B*), suggesting that ELA had activated the APJ receptor, which promotes the proliferation and migration capacity of MSCs, via the METTL3/PI3K/AKT pathway.

Discussion

In this study, the effects and underlying mechanisms of ELA vis-a-vis MSCs were evaluated. Our results revealed that ELA could promote the proliferation, viability, and migration of MSCs *in vitro* in an APJ-

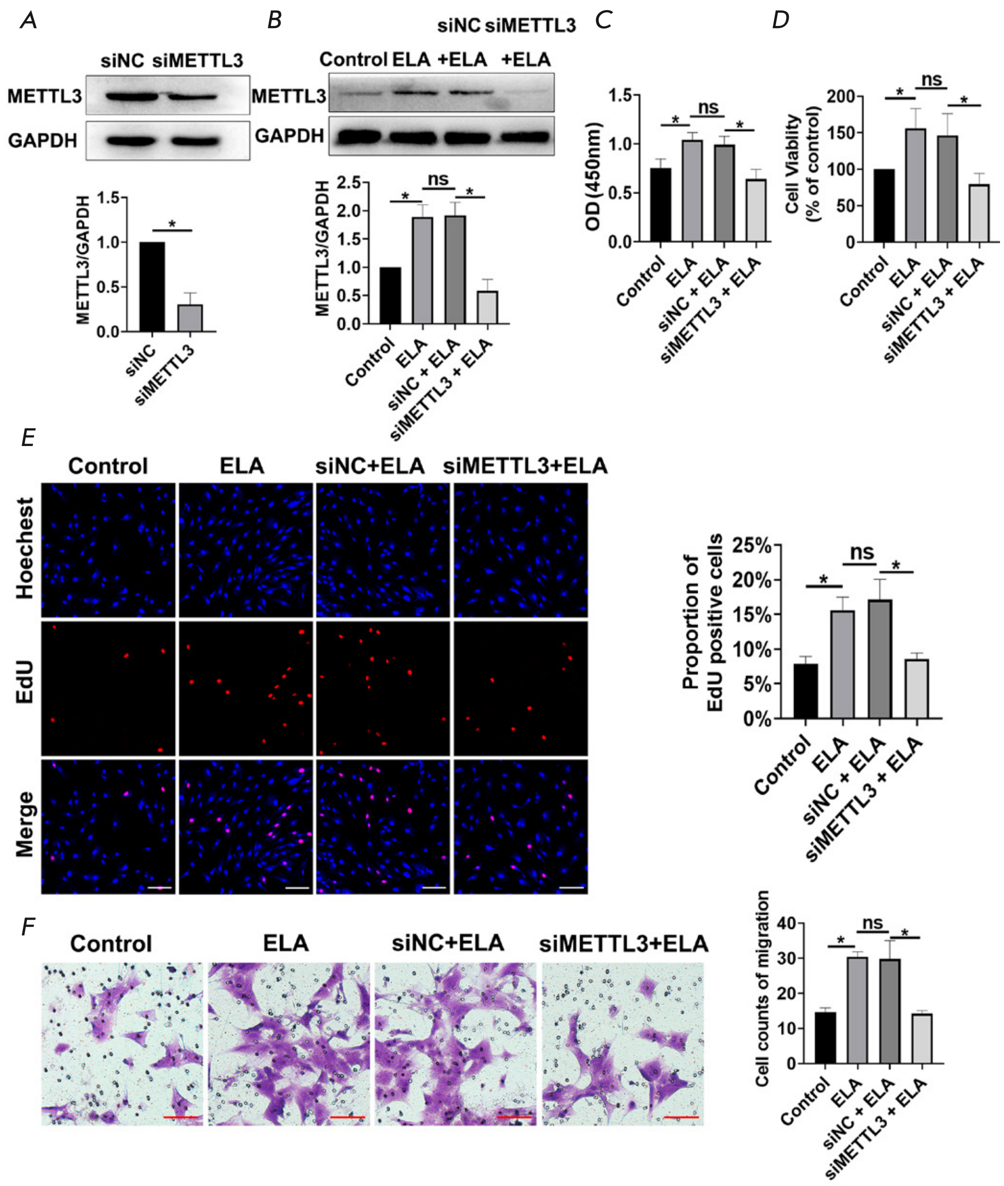

Fig. 3. ELA promotes MSC proliferation and migration by upregulating METTL3. (*A*) – METTL3 knockdown was successfully performed using small interfering RNA. (*B*) – METTL3 knockdown attenuated the upregulation of METTL3 caused by ELA at the protein level. (*C*, *D*) – CCK-8 assay results demonstrate that METTL3 knockdown reversed the synergistic effects of ELA-enhanced MSC proliferation and viability. (*E*) – EdU assay shows that METTL3 knockdown decreases the percentage of EdU-positive MSCs that was increased by ELA. Scale bar 100 μm. (*F*) – Transwell assay results show the inhibitory effects of METTL3 knockdown on cell migration was increased by ELA. Scale bar 100 μm. $^*P < 0.05$; ns – no significance; siMETTL3 – METTL3 knockdown; siNC – negative control

dependent manner. In addition, ELA was shown to upregulate the m^{6}A level and the protein level of METTL3 in MSCs and to activate the PI3K/AKT pathway. METTL3 knockdown not only reversed the effect of ELA on cellular proliferation and migration, but also inhibited the synergistic effect of ELA on p-AKT, suggesting the activation of the METTL3/PI3K/AKT axis as the underlying mechanism. At present, no research has reported any relationship between ELA and m^{6}A, but the results from this study have confirmed that the ELA-APJ signaling pathway may have synergistic effects on the proliferation and migration of MSCs by activating the METTL3/PI3K/AKT axis. This finding provides new strategies for improving the expansion and migration abilities of MSCs *in vitro* and partially sheds light on the potential mechanism of ELA in terms of its promoting effects on MSCs.

The results of this study show that the administration of exogenous ELA can lead to improved proliferation, viability, and migration ability for MSCs. Growing evidence points to the critical role of ELA in the biological functions of the cell [28]. Ho and colleagues confirmed that ELA could improve the proliferation ability of hESCs via the PI3K/Akt pathway [14]. The PI3K/Akt signaling pathway regulates multiple cellular processes of MSCs such as proliferation [16] and migration [17], implying that ELA exerts these effects on MSCs through the PI3K/Akt signaling pathway. Consistent with our results, previous studies have demonstrated that the ELA-APJ signaling pathway stimulates cell motility [12] and influ-

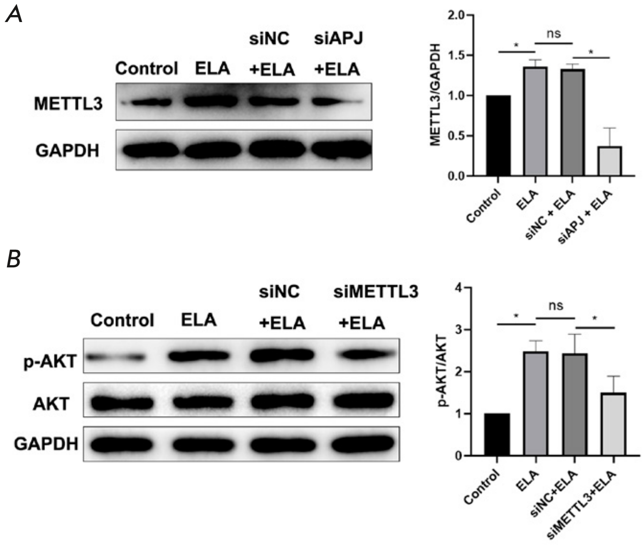

Fig. 4. ELA upregulates the expression of p-AKT by enhancing APJ-associated METTL3 upregulation. (*A*) – Western blot results show that APJ knockdown reversed the upregulation of METTL3 caused by ELA. (*B*) – The downregulation of METTL3 inhibited the increasing ratio of p-AKT / AKT caused by ELA. $^*P < 0.05$; ns – no significance; p-AKT – phosphorylated AKT; siAPJ – APJ knockdown; siMETTL3 – METTL3 knockdown; siNC – negative control

ences angioblast migration [13] during vasculogenesis. Meanwhile, the activation of APJ has been reported to promote cellular proliferation and migration [29]. Thus, the effect of ELA in MSCs is most likely mediated through APJ. Ho and colleagues also suggested that ELA can function through an alternate receptor in hESCs [14]. However, it was observed in this study that APJ knockdown reversed the proliferation and migration abilities induced by ELA in MSCs, making APJ the key receptor of ELA in MSCs. Based on these results, ELA should be considered as a complement for the *in vitro* expansion of MSCs, besides its role as improving MSC migration.

At present, little is known about the molecular mechanisms of ELA in various biological functions. This research confirms that the expression level of the METTL3 protein is considerably upregulated by ELA in a concentration-dependent manner within 5–20 μM. A significant difference was observed from the concentration of 5 μM onward, which was consistent with the concentration used in the cell proliferation experiment. This concentration was thus used in all subsequent experiments. N^6-Methyladenosine (m^6A), which accounts for the most prevalent RNA internal modification in eukaryotes, plays a critical role in various bioprocesses and diseases, such as stem cell self-renewal [30], differentiation [31], and tumorigenesis [32]. METTL3 is the active component in the m^6A methyltransferase complex that has been confirmed to be implicated in biological functions such as cell proliferation and migration [23]. A previous study demonstrated the oncogenic effects of METTL3 in breast cancer [33]. Furthermore, Tian et al. found that Mettl3 knockdown suppressed the activation of the PI3K/AKT pathway during the process of MSC osteogenic differentiation in [26], and this pathway has been confirmed to be initiated by ELA [19]. Therefore, based on these results, it appeared legitimate to speculate that ELA affects MSC proliferation and migration by regulating the expression of METTL3. The protein level of METTL3 was then downregulated, and it was noticed that the promoting effects of ELA on the proliferation and migration of MSCs were significantly attenuated upon METTL3 knockdown. It is thus concluded that ELA futhers the proliferation and migration abilities of MSCs by upregulating the expression of METTL3. This is the first report of the regulatory effect of ELA on the expression of METTL3.

When the mechanism by which the ELA-induced function changes in MSCs was explored, the phosphorylation level of AKT was observed to be upregulated in ELA-treated MSCs. Activation of the PI3K/AKT pathway could enhance cell-cycle progression through the G1/S phase to promote cell proliferation [34], whereas increased expression of MMP-2 and MMP-9 appeared to stimulate cell migration [35]. Additionally, fate determination of bone marrow MSCs could be regulated by METTL3 via PI3K-Akt signaling [26], indicating that ELA might activate the PI3K-Akt signaling by upregulating the expression of METTL3. Therefore, METTL3 expression was downregulated and METTL3 knockdown was found to inhibit the activation of the PI3K/AKT signaling pathway caused by ELA. Based on the results of this study, it can be concluded that ELA/APJ signaling affects proliferation and migration via the METTL3/PI3K/AKT pathway. However, it is worth noting that the downstream target genes of METTL3 have yet to be explored in this study. Therefore, future research should focus on identifying the genes that are regulated by METTL3 to fully clarify the mechanism of ELA action on MSCs, and whether METTL3 functions in an m^6A-dependent manner.

CONCLUSION

Over all, this study provides evidence that support the role of ELA/APJ signaling in promoting the proliferation and migration of MSCs, which may be a result of the activation of the METTL3/PI3K/AKT pathway. ●

This work was supported by the National Natural Science Foundation of China (No. 81070125, 81270213, 81670306, 81700242); Science and Technology Foundation in Guangdong (No. 2010B031600032, 2014A020211002); National Natural Science Foundation of Guangdong Province (No. 2017A030313503); Science and Technology Foundation in Guangzhou City (No. 201806020084); Fundamental Research Funds for Central Universities (No.13ykzd16, 17ykjc18); Futian District Health and Public Welfare Research Project of Shenzhen City (No. FTWS2019001, FTWS2021016) and the Shenzhen Fundamental Research Program (No. JCYJ20190808101405466, JCYJ20210324115003008).

REFERENCES

1. Fan X.L., Zhang Y., Li X., Fu Q.L. // Cell. Mol. Life. Sci. 2020. V. 77. № 14. P. 2771–2794.
2. Szydlak R. // World J. Stem Cells. 2021. V. 13. № 6. P. 619–631.
3. Galipeau J., Sensebe L. // Cell Stem Cell. 2018. V. 22. № 6. P. 824–833.
4. Naji A., Eitoku M., Favier B., Deschaseaux F., Rouas-Freiss N., Suganuma N. // Cell. Mol. Life Sci. 2019. V. 76. № 17. P. 3323–3348.
5. Liu C., Tsai A.L., Li P.C., Huang C.W., Wu C.C. // Stem Cell Res. Ther. 2017. V. 8. № 1. P. 29.
6. Elahi F.M., Farwell D.G., Nolta J.A., Anderson J.D. // Stem Cells. 2020. V. 38. № 1. P. 15–21.
7. Menaa F., Shahrokhi S., Shastri V.P. // Stem. Cells. Int. 2018. V. 2018. P. 5023925.
8. Raziyeva K., Smagulova A., Kim Y., Smagul S., Nurkesh A., Saparov A. // Int. J. Mol. Sci. 2020. V. 21. № 19. P. 7301.
9. Karpov A.A., Udalova D.V., Pliss M.G., Galagudza M.M. // Cell Prolif. 2017. V. 50. № 2. P. e12316.
10. Fu X., Liu G., Halim A., Ju Y., Luo Q., Song A.G. // Cells. 2019. V. 8. № 8. P. 784.
11. Liu W., Yan J., Pan W., Tang M. // Ann. Transl. Med. 2020. V. 8. № 5. P. 243.
12. Pauli A., Norris M.L., Valen E., Chew G.L., Gagnon J.A., Zimmerman S., Mitchell A., Ma J., Dubrulle J., Reyon D., et al. // Science. 2014. V. 343. № 6172. P. 1248636.
13. Liu L., Yi X., Lu C., Wang Y., Xiao Q., Zhang L., Pang Y., Guan X. // Front. Oncol. 2021. V. 11. P. 658253.
14. Ho L., Tan S.Y., Wee S., Wu Y., Tan S.J., Ramakrishna N.B., Chng S.C., Nama S., Szczerbinska I., Chan Y.S., et al. // Cell Stem Cell. 2015. V. 17. № 4. P. 435–447.
15. Dagamajalu S., Rex D.A.B., Suchitha G.P., Rai A.B., Rainey J.K., Prasad T.S.K. // J. Cell Commun. Signal. 2022. V. 16. № 1. P. 145–154.
16. Li J.Y., Ren K.K., Zhang W.J., Xiao L., Wu H.Y., Liu Q.Y., Ding T., Zhang X.C., Nie W.J., Ke Y., et al. // Stem Cell Res. Ther. 2019. V. 10. № 1. P. 247.
17. Samakova A., Gazova A., Sabova N., Valaskova S., Jurikova M., Kyselovic J. // Physiol. Res. 2019. V. 68. № suppl_2. P. S131–S138. doi: 10.33549/physiolres.934345.
18. Mai L., He G., Chen J., Zhu J., Chen S., Hou X., Yang H., Zhang M., Wu Y., Lin Q., et al. // Stem Cells Int. 2021. V. 2021. P. 5555590.
19. Fu J., Chen X., Liu X., Xu D., Yang H., Zeng C., Long H., Zhou C., Wu H., Zheng G., et al. // Stem Cell Res. Ther. 2020. V. 11. № 1. P. 541.
20. Zaccara S., Ries R.J., Jaffrey S.R. // Nat. Rev. Mol. Cell. Biol. 2019. V. 20. № 10. P. 608–624.
21. Dixit D., Prager B.C., Gimple R.C., Poh H.X., Wang Y., Wu Q., Qiu Z., Kidwell R.L., Kim L.J.Y., Xie Q., et al. // Cancer Discov. 2021. V. 11. № 2. P. 480–499.
22. Xie Z., Yu W., Zheng G., Li J., Cen S., Ye G., Li Z., Liu W., Li M., Lin J., et al. // Nat. Commun. 2021. V. 12. № 1. P. 5373.
23. Liu S., Zhuo L., Wang J., Zhang Q., Li Q., Li G., Yan L., Jin T., Pan T., Sui X., et al. // Am. J. Cancer Res. 2020. V. 10. № 6. P. 1631–1646.
24. Vu L.P., Pickering B.F., Cheng Y., Zaccara S., Nguyen D., Minuesa G., Chou T., Chow A., Saletore Y., MacKay M., et al. // Nat. Med. 2017. V. 23. № 11. P. 1369–1376.
25. Chen X., Hua W., Huang X., Chen Y., Zhang J., Li G. // Front. Endocrinol (Lausanne). 2019. V. 10. P. 911.
26. Tian C., Huang Y., Li Q., Feng Z., Xu Q. // Int. J. Mol. Sci. 2019. V. 20. № 3. P. 551.
27. Hou J., Wang L., Wu Q., Zheng G., Long H., Wu H., Zhou C., Guo T., Zhong T., Wang L., et al. // Stem Cell Res. Ther. 2018. V. 9. № 1. P. 109.
28. Ma Z., Song J.J., Martin S., Yang X.C., Zhong J.C. // Heart Failure Rev. 2021. V. 26. № 5. P. 1249–1258.
29. Xu J., Chen L., Jiang Z., Li L. // J. Cell. Physiol. 2018. V. 233. № 9. P. 6472–6482.
30. Wen J., Lv R., Ma H., Shen H., He C., Wang J., Jiao F., Liu H., Yang P., Tan L., et al. // Mol. Cell. 2018. V. 69. № 6. P. 1028–1038.e6.
31. Geula S., Moshitch-Moshkovitz S., Dominissini D., Mansour A.A., Kol N., Salmon-Divon M., Hershkovitz V., Peer E., Mor N., Manor Y.S., et al. // Science. 2015. V. 347. № 6225. P. 1002–1006.
32. Melstrom L., Chen J. // Cancer Gene Ther. 2020. V. 27. № 9. P. 625–633.
33. Cai X., Wang X., Cao C., Gao Y., Zhang S., Yang Z., Liu Y., Zhang X., Zhang W., Ye L. // Cancer Lett. 2018. V. 415. P. 11–19.
34. Vasjari L., Bresan S., Biskup C., Pai G., Rubio I. // Cell Cycle. 2019. V. 18. № 2. P. 204–225.
35. Gao X., Qiao X., Xing X., Huang J., Qian J., Wang Y., Zhang Y., Zhang X., Li M., Cui J., Yang Y. // Front. Oncol. 2020. V. 10. P. 1563.

GENERAL RULES

Acta Naturae publishes experimental articles and reviews, as well as articles on topical issues, short reviews, and reports on the subjects of basic and applied life sciences and biotechnology.

The journal *Acta Naturae* is on the list of the leading periodicals of the Higher Attestation Commission of the Russian Ministry of Education and Science. The journal Acta Naturae is indexed in PubMed, Web of Science, Scopus and RCSI databases.

The editors of *Acta Naturae* ask of the authors that they follow certain guidelines listed below. Articles which fail to conform to these guidelines will be rejected without review. The editors will not consider articles whose results have already been published or are being considered by other publications.

The maximum length of a review, together with tables and references, cannot exceed 50,000 characters with spaces (approximately 30 pages, A4 format, 1.5 spacing, Times New Roman font, size 12) and cannot contain more than 16 figures.

Experimental articles should not exceed 30,000 symbols (approximately 15 pages in A4 format, including tables and references). They should contain no more than ten figures.

A short report must include the study's rationale, experimental material, and conclusions. A short report should not exceed 12,000 symbols (5–6 pages in A4 format including no more than 12 references). It should contain no more than three figures.

The manuscript and all necessary files should be uploaded to www.actanaturae.ru:

1) text in Word 2003 for Windows format;
2) the figures in TIFF format;
3) the text of the article and figures in one pdf file;
4) the article's title, the names and initials of the authors, the full name of the organizations, the abstract, keywords, abbreviations, figure captions, and Russian references should be translated to English;
5) the cover letter stating that the submitted manuscript has not been published elsewhere and is not under consideration for publication;
6) the license agreement (the agreement form can be downloaded from the website www.actanaturae.ru).

MANUSCRIPT FORMATTING

The manuscript should be formatted in the following manner:

- Article title. Bold font. The title should not be too long or too short and must be informative. The title should not exceed 100 characters. It should reflect the major result, the essence, and uniqueness of the work, names and initials of the authors.
- The corresponding author, who will also be working with the proofs, should be marked with a footnote *.
- Full name of the scientific organization and its departmental affiliation. If there are two or more scientific organizations involved, they should be linked by digital superscripts with the authors' names. Abstract. The structure of the abstract should be very clear and must reflect the following: it should introduce the reader to the main issue and describe the experimental approach, the possibility of practical use, and the possibility of further research in the field. The average length of an abstract is 20 lines (1,500 characters).
- Keywords (3 – 6). These should include the field of research, methods, experimental subject, and the specifics of the work. List of abbreviations.
- INTRODUCTION
- EXPERIMENTAL PROCEDURES
- RESULTS AND DISCUSSION
- CONCLUSION
  The organizations that funded the work should be listed at the end of this section with grant numbers in parenthesis.
- REFERENCES
  The in-text references should be in brackets, such as [1].

RECOMMENDATIONS ON THE TYPING AND FORMATTING OF THE TEXT

- We recommend the use of Microsoft Word 2003 for Windows text editing software.
- The Times New Roman font should be used. Standard font size is 12.
- The space between the lines is 1.5.
- Using more than one whole space between words is not recommended.
- We do not accept articles with automatic referencing; automatic word hyphenation; or automatic prohibition of hyphenation, listing, automatic indentation, etc.
- We recommend that tables be created using Word software options (Table → Insert Table) or MS Excel. Tables that were created manually (using lots of spaces without boxes) cannot be accepted.
- Initials and last names should always be separated by a whole space; for example, A. A. Ivanov.
- Throughout the text, all dates should appear in the "day.month.year" format, for example 02.05.1991, 26.12.1874, etc.
- There should be no periods after the title of the article, the authors' names, headings and subheadings, figure captions, units (s – second, g – gram, min – minute, h – hour, d – day, deg – degree).
- Periods should be used after footnotes (including those in tables), table comments, abstracts, and abbreviations (mon. – months, y. – years, m. temp. – melting temperature); however, they should not be used in subscripted indexes (T_m – melting temperature; $T_{p.t}$ – temperature of phase transition). One exception is mln – million, which should be used without a period.
- Decimal numbers should always contain a period and not a comma (0.25 and not 0,25).
- The hyphen ("-") is surrounded by two whole spaces, while the "minus," "interval," or "chemical bond" symbols do not require a space.
- The only symbol used for multiplication is "×"; the "×" symbol can only be used if it has a number to its

right. The "·" symbol is used for denoting complex compounds in chemical formulas and also noncovalent complexes (such as DNA·RNA, etc.).
- Formulas must use the letter of the Latin and Greek alphabets.
- Latin genera and species' names should be in italics, while the taxa of higher orders should be in regular font.
- Gene names (except for yeast genes) should be italicized, while names of proteins should be in regular font.
- Names of nucleotides (A, T, G, C, U), amino acids (Arg, Ile, Val, etc.), and phosphonucleotides (ATP, AMP, etc.) should be written with Latin letters in regular font.
- Numeration of bases in nucleic acids and amino acid residues should not be hyphenated (T34, Ala89).
- When choosing units of measurement, SI units are to be used.
- Molecular mass should be in Daltons (Da, KDa, MDa).
- The number of nucleotide pairs should be abbreviated (bp, kbp).
- The number of amino acids should be abbreviated to aa.
- Biochemical terms, such as the names of enzymes, should conform to IUPAC standards.
- The number of term and name abbreviations in the text should be kept to a minimum.
- Repeating the same data in the text, tables, and graphs is not allowed.

GUIDENESS FOR ILLUSTRATIONS

- Figures should be supplied in separate files. Only TIFF is accepted.
- Figures should have a resolution of no less than 300 dpi for color and half-tone images and no less than 600 dpi.
- Files should not have any additional layers.

REVIEW AND PREPARATION OF THE MANUSCRIPT FOR PRINT AND PUBLICATION

Articles are published on a first-come, first-served basis. The members of the editorial board have the right to recommend the expedited publishing of articles which are deemed to be a priority and have received good reviews.

Articles which have been received by the editorial board are assessed by the board members and then sent for external review, if needed. The choice of reviewers is up to the editorial board. The manuscript is sent on to reviewers who are experts in this field of research, and the editorial board makes its decisions based on the reviews of these experts. The article may be accepted as is, sent back for improvements, or rejected.

The editorial board can decide to reject an article if it does not conform to the guidelines set above.

The return of an article to the authors for improvement does not mean that the article has been accepted for publication. After the revised text has been received, a decision is made by the editorial board. The author must return the improved text, together with the responses to all comments. The date of acceptance is the day on which the final version of the article was received by the publisher.

A revised manuscript must be sent back to the publisher a week after the authors have received the comments; if not, the article is considered a resubmission.

E-mail is used at all the stages of communication between the author, editors, publishers, and reviewers, so it is of vital importance that the authors monitor the address that they list in the article and inform the publisher of any changes in due time.

After the layout for the relevant issue of the journal is ready, the publisher sends out PDF files to the authors for a final review.

Changes other than simple corrections in the text, figures, or tables are not allowed at the final review stage. If this is necessary, the issue is resolved by the editorial board.

FORMAT OF REFERENCES

The journal uses a numeric reference system, which means that references are denoted as numbers in the text (in brackets) which refer to the number in the reference list.

For books: the last name and initials of the author, full title of the book, location of publisher, publisher, year in which the work was published, and the volume or issue and the number of pages in the book.

For periodicals: the last name and initials of the author, title of the journal, year in which the work was published, volume, issue, first and last page of the article, doi. Must specify the name of the first 10 authors. Ross M.T., Grafham D.V., Coffey A.J., Scherer S., McLay K., Muzny D., Platzer M., Howell G.R., Burrows C., Bird C.P., et al. // Nature. 2005. V. 434. № 7031. P. 325–337. doi: 10.1038/nature03440.

References to books which have Russian translations should be accompanied with references to the original material listing the required data.

References to doctoral thesis abstracts must include the last name and initials of the author, the title of the thesis, the location in which the work was performed, and the year of completion.

References to patents must include the last names and initials of the authors, the type of the patent document (the author's rights or patent), the patent number, the name of the country that issued the document, the international invention classification index, and the year of patent issue.

The list of references should be on a separate page. The tables should be on a separate page, and figure captions should also be on a separate page.

The following e-mail addresses can be used to contact the editorial staff: actanaturae@gmail.com, tel.: (495) 727-38-60.

Supplementaries

Table S1. Morphological characteristics of *S. phaeochromogenes* BV-204 growth on different indicative media

Medium	Pigmentation of aerial (AM) and substrate mycelium (SM), presence of soluble pigments (SP)	Medium	Pigmentation of aerial (AM) and substrate mycelium (SM), presence of soluble pigments (SP)
ISP2	AM: Straw SM: Dark-brown SP: None	**ISP5**	AM: Light-straw SM: Dark-brown SP: None
	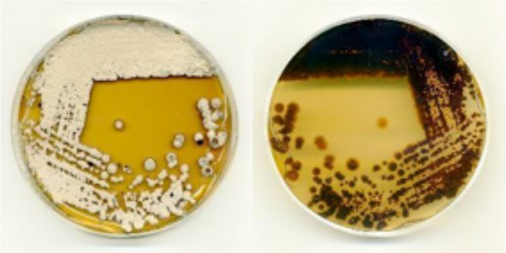		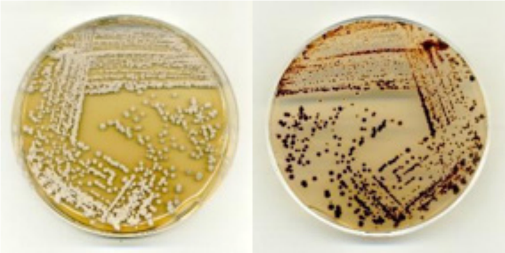
ISP3	AM: Pink-straw SM: Dark-brown SP: Dark-brown	**ISP6**	AM: None SM: Beige SP: None
			

Table S2. Culture characteristics of *S. phaeochromogenes* BV-204 (1) and phylogenetically closest *S. phaeochromogenes* JCM 4958 (2), *S. umbrinus* JCM 4521 (3)

	1	2[*]	3[*]
Morphological and physiological features			
Spore surface	Smooth	Smooth	Smooth
Sporophore shape	Straight and long	Straight or tortoise	Straight or tortoise
Temperature range/ Optimum temperature (°C)	8–37/ 28	ND/28°C	ND/28°C
pH range/ Optimum pH	4.5–8.5/ 7	5–11	5–11
Utilization of carbon sources			
Arabinose	+	+	+
Galactose	+	ND	ND
Glucose	+	+	ND
Inositol	+	+	ND
Xylose	+	+	+
Lactose	+	ND	ND
Maltose	–	ND	ND
Mannitol	+	ND	ND
Raffinose	+	ND	ND
Rhamnose	+	+	+
Sorbitol	–	-	-
Sucrose	+	ND	ND
Fructose	+	+	+
Substrate degradation and enzyme activity			
Starch	+	ND	ND
Gelatin	+	+	+
Carboxymethyl cellulose	+	-	-
Oxidase	+	ND	ND
Nitrate reductase	–	ND	ND
Antibiotic resistance			
Chloramphenicol, 34 μg/mL	+	ND	ND
Streptomycin, 12.5 μg/disc	+	ND	ND
Tetracycline, 10 μg/disc	+	ND	ND
Spectinomycin, 5 mcg/disc	+	ND	ND
Erythromycin, 5 mcg/disc	+	ND	ND
Vancomycin, 5 mcg/disc	37 mm[**]	ND	ND
Levofloxacin, 5 mcg/disc	16 mm[**]	ND	ND

[*] Data on *Streptomyces phaeochromogenes* JCM 4958 and *Streptomyces umbrinus* JCM 4521 were taken from the DSMZ Bacdive database (https://bacdive.dsmz.de/) and publications [31–33].

[**] Diameter of no strain growth zone around an antibiotic disk.

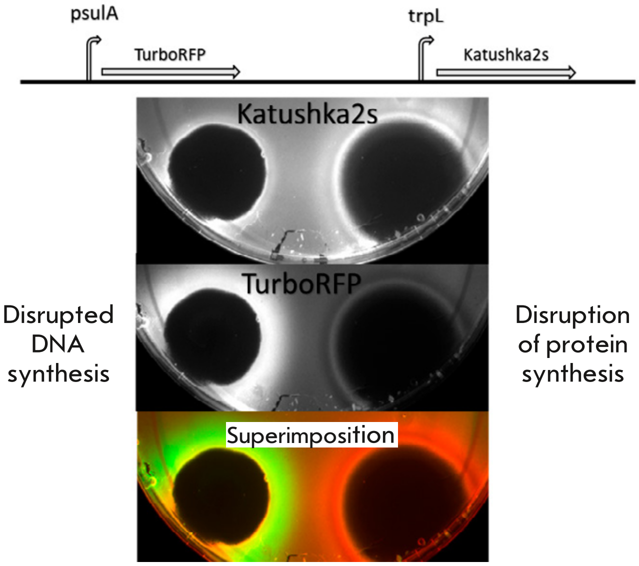

Fig. S7. Reporter system operating principle

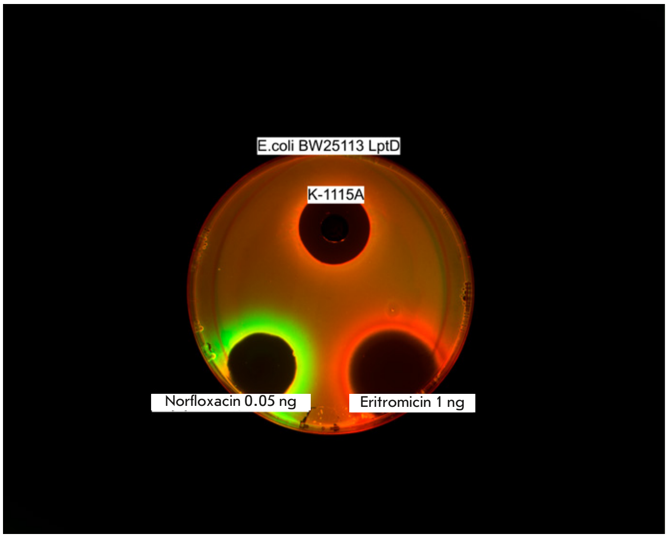

Fig. S8. Activity of purified K-1115A

Species/Abbrv	
1. Streptomyces sp. CM020	RLVGRRAVESCAVERRAAGSRAVERRAAGCRAVGRDAFRLRAPPGEYAFRRAAPHRCHGRAAQRQRFAVERDAAYLLGARHPRMGADLDPVRHPVPGQPPLPRVAHVGLQGRGVPGLHHAHRDMPVRG
2. S.phaeochromogenes	RLVGRRAVESCAVERRAAGCRAVGRDAVGCDAVGRDAVRFRAPPGEYAFRRAAPHRCHGRAAQRQRFAVERDAAYLLGARHPRVGADLDPVRHPVPGQPPLPRVAHVGLQGRGVPGLHHAHRDMPVRG
3. S.phaeochromogenes BV204	RVVESRVVESCAVDRRAAGCRAVGCDAVGRDAVGCDAVRVRAPPGEYALRRAAPHRCHGRAAQRQRLAVERDAAYLLGARHPRVGADLDPVRHPVPGQPPLPGVAHVGLQGRGVPGLHHAHRDMAVRG

Fig. S9. Alignment of the translated amino acid sequence of the *aln5* gene

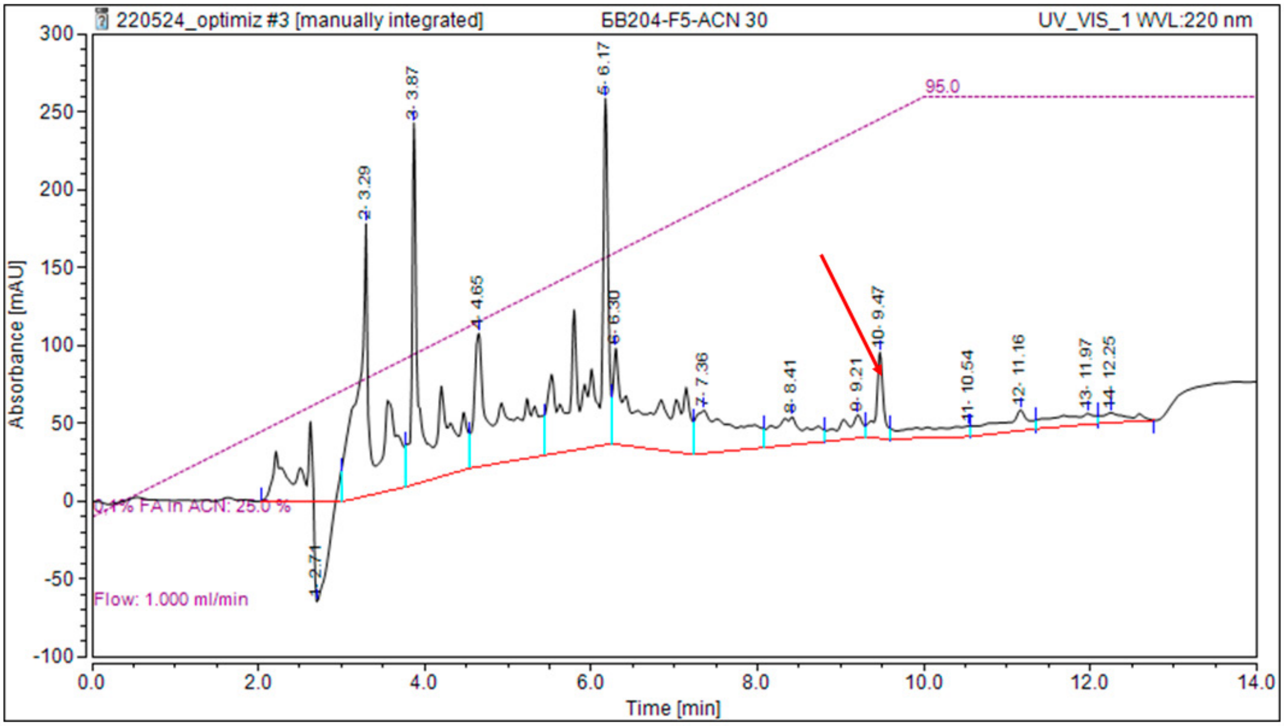

Fig. S10. HPLC profile of the active SPE fraction eluted with 30-40% acetonitrile. The peak is highlighted by the arrow

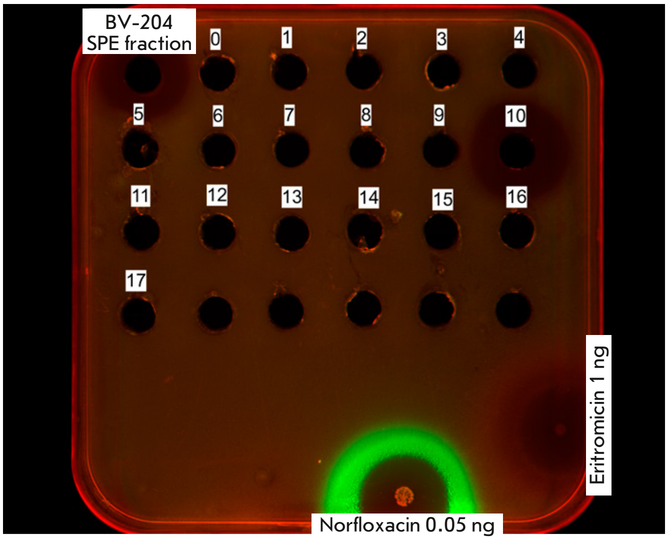

Fig. S11. Verification of HPLC fractions activity

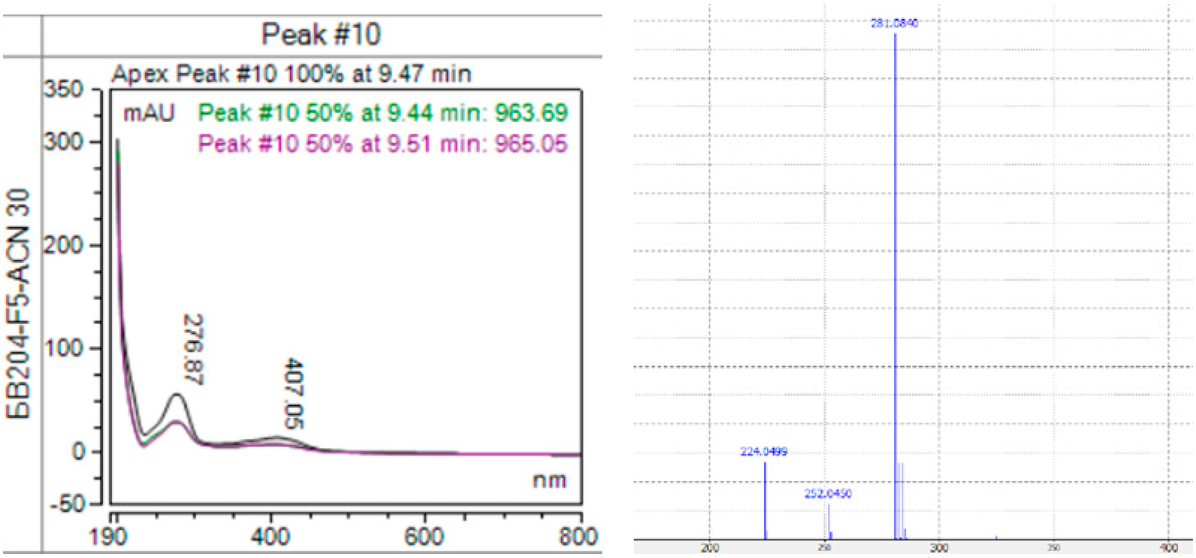

Fig. S12. UV and mass spectrum of the HPLC peak of the active component